UNIVERSITÀ
DEGLI STUDI
DI PADOVA

Sede amministrativa: UNIVERSITÀ DEGLI STUDI DI PADOVA

Dipartimento di Scienze Chimiche

SCUOLA DI DOTTORATO DI RICERCA IN

SCIENZA ED INGEGNERIA DEI MATERIALI

CICLO XXVII

Characterization of CdSe-$Cd_XZn_{1-X}S$ core-shell QDs as active materials for compact micro-cavity lasers

Direttore della Scuola: Ch.mo Prof. Gaetano Granozzi

Supervisore: Dott.ssa Raffaella Signorini

Dottorando: Alessandro Minotto

Abbreviations

AFM: Atomic Force Microscopy
ASE: Amplified Spontaneous Emission
AR: Auger Recombination
BBO: Beta Barium Borate (β-BaB_2O_4)
BT: Benzenthiol
CB: Conduction Band
CM: Carrier Multiplication
CSM: Concentric Shell Model
DADS: Decay Associated Difference Spectra
DFB: Distributed-Feeback
DOS: Density Of States
EADS: Evolution Associated Difference Spectra
EMA: Effective Mass Approximation
ESA: Excited State Absorption
ET: Electron Transfer
fs: Femtosecond
FGR: Fermi's Golden Rule
FON: Film-Over-Nanospheres
GSB: Ground State Bleaching
HH: Heavy-Hole
IRF: Internal Response Function
LH: Light-Hole
LO: Longitudinal Optical (phonon)
MBE: Molecular Beam Epitaxy
MEG: Multi-Exciton Generation
MER: Multi-Exciton Recombination
ML (MLs): Monolayer (Monolayers)
MOCVD: Metal-organic Chemical Vapor Deposition
NA: Numerical Aperture
NIR: Near Infrared
ns: nanosecond
PA: Photo-induced Absorption
PCM: Phonon Confinement Molel
P&P: Pump and Probe
PL: Photoluminescence
ps: Picosecond
PV: Photovoltaics
QC: Quantum Confinement
QD: Quantum Dot
QY: Quantum Yield
QM: Quantum Mechanics
RT: Room Temperature
SADS: Species Associated Difference Spectra
SE: Stimulated Emission
SEM: Scanning Electron Microscopy
SERRS: Surface Enhanced Resonant Raman Scattering
SERS: Surface Enhanced Raman Scattering
SILAR: Successive Ionic Layer Absorption and Reaction
SPAD: Single Photon Avalanche Diode
SVD: Single Value Decomposition
TA: Transient Absorption
TCSPC: Time-Correlated Single Photon Counting
tPL: Transient Photoluminescence
TO: Transverse Optical (phonon)
TEM: Transmission Electron Microscopy
VB: Valence Band
XRD: X-Ray Diffraction

Abstract

Innovation within the field of nanophotonics is fostering the progress in diverse technological fields, spanning light emitting, communication technologies, renewable energies, medical diagnostic and therapy. Among the different classes of nanomaterials that are contributing to such evolution, semiconductor nanocrystals, a.k.a Quantum Dots (QDs), are the most versatile ones. QDs are inorganic semiconductor nanostructures, whose outstanding light emitting performances make them promising competitors to more "conventional" bulk solid-state materials in many commercial applications. The interest on developing QD-based devices spread on a large scale with the development of colloidal synthesis methods. The colloidal approach expedites their processability and integration in light emitting devices with dimensions ranging from the macro- to the nano-scale. In particular, colloidal QDs are suitable active media for the fabrication of compact and flexible solid-state laser sources.

Optical properties of QDs are ruled by the Quantum Confinement (QC) regime. The latter occurs when the size of the material is reduced to levels comparable with the exciton Bohr radius. QC is a size-effect and consequently leads to size-dependent absorption and emission properties. Thanks to QC, QDs exhibit well-defined electronic levels, which enable molecular-like optically allowed absorption transitions. At the same, high absorption cross-sections and stabilities typical of bulk semiconductor materials are preserved.

In this thesis work an emerging class of colloidal QDs, namely CdSe-$Cd_XZn_{1-X}S$ core-shell QDs, is investigated. The attention is mainly focused on the optical gain, which represents one of the most inspected and promising applications for QDs. By investigating the Amplified Spontaneous Emission (ASE) of different series of CdSe-$Cd_XZn_{1-X}S$ heterostructures, this work demonstrates that key properties such as the ASE activation threshold and photo-stability can be optimized by a careful design of the core-shell heterostructure. Guidelines for the synthesis of such best performing optical gain QDs are drawn by means of optical spectroscopy, which provides insights into the correlation between the excitation and relaxation dynamics with the shell thickness, composition and, ultimately, the structure.

Basic parameters such as QD dimensions, size dispersion and photoluminescence quantum yield (QY) can be easily extracted from steady-state absorption and emission spectra. Steady-state absorption and phtoluminescence studies on CdSe-$Cd_XZn_{1-X}S$ QDs were employed as preliminary tools to prove that different shell materials induce distinct exciton confinement, size dispersion and QY.

In a second step, Surface Enhanced Raman Scattering (SERS) technique has been employed, for the first time, as a local probe for the study of the core-shell interfaces. SERS permits the analysis of the nanocrystals with the same structural features and lattice dynamics present when the QDs are employed as emitters in photonic devices. Results of this study revealed that the

composition of the $Cd_XZn_{1-X}S$ shell entails a significant structural difference at the core-shell interface. This structural difference modifies the electronic structure within the QDs, since it directly tailors the QC of the electrons and holes.

The effect of the core-shell interface on optical properties has been unambiguously detected with the use of transient optical spectroscopy. In this thesis work, transient absorption (TA) and transient PL (tPL) techniques were employed to probe the exciton generation and recombination dynamics. The evolution of the exciton population was compared with kinetic models. Differently from steady-state techniques, transient techniques are sensitive to the nature and time-scales of the different radiative and non-radiative relaxation paths, whose control is crucial for guiding the heterostructure engineering process. The kinetic rates obtained revealed a clear dependence on the core-shell interface and the correlation with SERS results is discussed.

The correlation between structure and dynamics was detected from the nanosecond (tPL analysis) down to the sub-nanosecond time scales (TA analysis). A secondary mission of this thesis was also to find a global interpretation of the dynamics of all signals present in TA spectra of the different CdSe-$Cd_XZn_{1-X}S$ QD series. Pump fluence, shell thickness and composition are the coordinates along which the global analysis has been developed. This step is of pivotal importance in order to identify the mechanisms involved in the optical gain process, whose temporal evolution for QDs systems spans from the picosecond to the few nanosecond time-scale.

From the discussion of the results obtained from the different characterization techniques, it emerges that the most efficient way to boost the optical properties of CdSe QDs is the realization of a "graded" $Cd_XZn_{1-X}S$ shell, with Zn concentration (and confinement potential) gradually increasing along the radial direction. In a single entity, this solution should provide suitable confinement of the charge-carriers from the defective outer surface, prevent defect formation at the core-shell interface due the mismatch between the different materials and, eventually, limit the dot dimensions. Low QD dimensions increase the packing density and limits the scattering losses when QDs are included in a thin film and/or in a solid-state matrix. Such aspects have to be taken into serious consideration in order to increase the performances of a QD-based optical amplifier.

Finally, the validity of the hypothesis formulated is experimentally verified by characterizing the bi-exciton radiative recombination, which represents the photo-physical origin of ASE and thus defines the optical gain performances of differently engineered nano-heterostructures. As predicted, best optical gain performances have been achieved from ASE experiments by using CdSe QDs covered with a graded CdS-$Cd_{0.5}Zn_{0.5}S$-ZnS shell. Therefore, the results obtained from the spectroscopic characterization provide a guideline for the engineering of new synthetic approaches, addressed to the preparation of highly stable core-shell QDs with minimal optical

gain activation threshold. Moreover, the rationalization of the dynamics involved in exciton and multi-exciton generation and recombination in core-shell QDs expedites their application in all types of light emitting devices.

Abstract (Italiano)

Il progresso in svariati settori tecnologici, a partire dai dispositivi emettitori di luce, passando per le aree delle telecomunicazioni e delle energie rinnovabili, fino alla diagnostica medica e alla terapia, è favorito dalla ricerca e dallo sviluppo nel campo della nanofotonica. Tra le diverse classi di nanomateriali che stanno contribuendo a questo avanzamento, i nanocristalli di materiale semiconduttore, alias Quantum Dots (QDs) o Punti Quantici, presentano le proprietà ottiche più versatili.

I QDs sono nanostrutture inorganiche di materiale semiconduttore le cui eccezionali prestazioni in termini di emissione di luce li rendono diretti concorrenti dei materiali a stato solido più "convenzionali" in molte applicazioni commerciali. L'interesse a sviluppare dispositivi basati su QDs si è diffuso su larga scala con lo sviluppo di metodi di sintesi di tipo colloidale. L'approccio colloidale facilita la processabilità e l'integrazione in dispositivi emittitori di luce con dimensioni che vanno dal micron a pochi nanometri. In particolare, i QDs colloidali si prestano alla realizzazione di sorgenti laser a stato solido compatte e su substrati flessibili.

Le proprietà ottiche dei QDs sono regolate dal confinamento quantistico (QC). Questo regime si instaura quando la dimensioni del materiale sono comparabili con il raggio eccitonico di Bohr. Il QC, in quanto effetto di taglia, rende le proprietà di assorbimento e di emissione di luce dipendenti dalle dimensioni. Grazie al QC, i QDs possiedono livelli elettronici ben definiti e interagiscono con la luce in maniera simile ai sistemi molecolari. Allo stesso tempo, i QDs dimostrano elevate sezioni d'urto di assorbimento e stabilità al danneggiamento, proprietà tipiche dei semiconduttori inorganici.

Questo lavoro di tesi è incentrato su una classe emergente di QDs colloidali, ossia QDs "core-shell" composti da CdSe-$Cd_XZn_{1-X}S$, aventi cioè un nucleo ("core") di CdSe, ricoperto da un guscio ("shell") di $Cd_XZn_{1-X}S$. L'attenzione è focalizzata principalmente sulle proprietà di guadagno ottico il quale rappresenta per i QDs una delle applicazioni più promettenti e maggiormente studiate. Attraverso la caratterizzazione dell'Emissione Spontanea Amplificata (ASE) di diverse serie di QDs di CdSe-$Cd_XZn_{1-X}S$, questo lavoro dimostra che proprietà chiave come la soglia di attivazione ASE, nonché la stabilità all'irragiamento, possono essere ottimizzate mediante un'attenta progettazione dell'eterostruttura core-shell. Mediante diverse tecniche di spettrocopia ottica è possibile ricavare alcune linee guida per la sintesi di QDs con proprietà di guadagno ottico ottimali. Con queste tecniche è quindi possibile identificare la correlazione tra le dinamiche di eccitazione/rilassamento e la composizione, spessore e, in ultima analisi, struttura del materiale di shell.

Parametri di base come le dimensioni medie dei QDs, la dispersione di taglia e la resa quantica di luminescenza (QY) possono essere facilmente estratti dalle tecniche di assorbimento ed emissione in stato stazionario. Queste ultime sono state impiegate come strumenti preliminari

per dimostrare che, variando la composizione e lo spessore del guscio esterno di $Cd_XZn_{1-X}S$, si altera il grado di confinamento degli eccitoni nel nucleo di CdSe, la dispersione in dimensioni e la QY.

In una seconda fase, la tecnica SERS (Surface-Enhanced Raman Scattering o Scattering Raman amplificato da superfici) è stata impiegata per la prima volta come sonda locale per lo studio dell'interfaccia tra core e shell. La tecnica SERS permette la caratterizzazione dei nanocristalli nelle stesse condizioni strutturali e di dinamica reticolare presenti nei QDs quando impiegati come mezzi attivi in dispositivi fotonici. I risultati di questo studio hanno rivelato che la composizione del guscio di $Cd_XZn_{1-X}S$ comporta delle significative differenze strutturali all'interfaccia core-shell. Questa variazione strutturale modifica la struttura elettronica nei QDs in quanto influenza il grado di confinamento degli elettroni e delle lacune nel core.

L'effetto dell'interfaccia core-shell sulle proprietà ottiche è stato inequivocabilmente rilevato mediante l'uso di tecniche di spettroscopia ottica transiente. In particolare, in questo lavoro di tesi sono stati studiati sia l'assorbimento transiente (TA) sia la luminescenza transiente (tPL) ai fini di esaminare le dinamiche di generazione e di ricombinazione degli eccitoni. L'evoluzione della densità eccitonica è stata quindi confrontata con dei modelli cinetici. A differenza delle tecniche a regime stazionario, le tecniche transienti sono sensibili alla natura e ai tempi caratteristici relativi ai diversi percorsi di rilassamento, radiativi e non radiativi, il cui controllo è fondamentale ai fini dell'ingegnerizzazione dell'eterostruttura. I parametri cinetici ottenuti hanno rivelato una chiara dipendenza dall'interfaccia core-shell e la correlazione con i risultati ottenuti mediante SERS sono stati discussi.

La correlazione tra struttura e dinamica è stata rilevata a partire dalla scala temporale del nanosecondo (tPL) fino alla scala dei picosecondi (TA). Uno scopo secondario di questa tesi è anche quello di elaborare un'interpretazione globale delle dinamiche di tutti i segnali presenti negli spettri transienti per diverse serie di QDs CdSe-$Cd_XZn_{1-X}S$. La densità di eccitazione, lo spessore del guscio e la sua composizione sono le coordinate lungo le quali si è sviluppata tale analisi globale. Questo passo è di cruciale importanza ai fini di identificare i parametri legati al processo di guadagno ottico, i cui tempi caratteristici in sistemi a base di QDs variano dai picosecondi fino a pochi nanosecondi.

Dalla discussione dei risultati ottenuti dalle diverse tecniche di caratterizzazione, emerge che il modo più efficace per aumentare le proprietà ottiche dei QDs di CdSe è la realizzazione di un guscio $Cd_XZn_{1-X}S$ a composizione graduale, in cui la concentrazione di Zn (e di conseguenza il potenziale di confinamento) aumenta gradualmente lungo la direzione radiale. In una sola entità, questa soluzione è in grado di fornire un adeguato confinamento dei portatori di carica dalla superficie esterna, limitare la formazione di difetti all'interfaccia e infine ridurre le dimensioni globali dei QDs. La minimizzazione delle dimensioni permette di aumentare la densità d'impaccamento e limita le perdite dovute allo scattering quando i QDs sono inclusi in una

matrice solida e/o depositati come film sottile. Tali aspetti sono di fondamentale importanza ai fini di migliorare l'efficienza di un amplificatore ottico a quantum dots.

Infine, la validità delle ipotesi formulate è stata verificata sperimentalmente caratterizzando la ricombinazione radiativa bi-eccitonica, la quale rappresenta l'origine fotofisica dell'ASE e quindi definisce le prestazioni di guadagno ottico delle diverse nano-eterostrutture opportunamente ingegnerizzate. Come previsto, dalle misure di ASE le migliori performance dal punto di vista del guadagno ottico sono state raggiunte utilizzando QDs di CdSe ricoperti con uno shell a composizione graduata di CdS-$Cd_{0.5}Zn_{0.5}$S-ZnS. I risultati ottenuti mediante la caratterizzazione spettroscopica forniscono dunque una linea guida per la progettazione di nuove strategie di sintesi che siano orientate alla preparazione di QDs altamente foto-stabili e con una soglia di attivazione ASE minimale. In aggiunta, la razionalizzazione delle dinamiche coinvolte nella generazione e ricombinazione eccitonica e multi-eccitonica in QDs core-shell può accelerare la loro applicazione in tutti i tipi di dispositivi emettitori di luce.

Introduction

In the last three decades nanomaterials have gained a central role in the research and development of new technologies. Much of the success of nanotechnologies stems from the progress in nanophotonics[1]. Depending on the materials, at nanoscale either interaction between charges and surfaces (nano-plasmonic materials)[2] or *quantum confinement* (quantum confined materials)[3] allow the enhancement of a particular photonic function. Moreover, different functions can be combined in a single "nanodevice".

The discovery of quantum dots (QDs)[4] dates back to the early 80's of the last century, thanks to the pioneering works of A. I. Ekimov and A. L. Efros[5] on semiconducting microcrystals, synthesized by ionic segregation and nucleation in glassy matrices. In the same years, L. E. Brus[6] started working on water synthesized colloidal crystallites. Conventionally:

A QD is a semiconductor nanocrystal, composed by a limited number of atoms (100 to 10,000) and with dimensions comparable with the characteristic lengths of the wave functions of charge carriers in either their ground or excited states.

Such condition is known as *quantum confinement*. Spatial localization of electron-hole pairs, *i.e. excitons*, induces a size-dependence of the electronic level structure and photophysical properties. Namely, optical absorption and emission spectra of a given material class shift towards higher energies at smaller sizes[7,8]. Due to their nanoscale dimensions, QDs exhibit properties that bridge those of bulk semiconductors and molecules. Looking at the absorption spectrum of a generic QD, it exhibits discrete absorption bands (like molecular chromophores), which derive from the aforementioned exciton confinement and surge from a continuous absorption proportional to the square root of energy (typical for bulk semiconductors). Alike many molecular dyes, QDs possess photoluminescence (PL) quantum yields (QY) close to unity[9–12], while they share with bulk semiconductors the high absorption cross-sections[13,14] in a broad energy range and high stability to both chemical and photo-induced damage[15,16].

This outstanding optical properties stem from engineered bottom-up synthesis methods. Nowadays, there are two different approaches for QD synthesis. The first class of methods is based on the epitaxial growth of semiconductor nanoislands onto a substrate of either the same or different material. Such *epitaxial QDs* are typically employed as optical materials, such as light

emitters (light emitting diodes, *i.e.* LEDs, LASERs)[17,18] and single photon emitters[19]. Typical semiconducting materials employed are Si, Ge, GaAs, GaP, GaN, InAs, InP and ternary or quaternary alloys of the same compounds. Alternatively, QDs can be colloidally synthesized. Colloidal routes experienced a dramatic widespread after the groundbreaking work[20] by the group of M. G. Bawendi in 1993 and have been progressively engineered for almost every semiconducting material. Success and widespread of *colloidal QDs* is due to their solution processability, low size-dispersion (down to 5%) and high degree of crystallinity. Colloidal QDs are suitable for light emitting (LEDs, LASERs, bio-imaging)[21–25], detection[26,27] and photovoltaics (PV)[28,29] in the visible and NIR spectral range.

Much of the studies on QDs and understanding of their opto-electronic properties have been conducted on CdSe QDs, whose colloidal synthesis has become up-scalable[30–32] and accessible not only to specialized chemists. Besides, most of the strategies that can be applied for boosting CdSe QDs optical performances can be extended also to other materials. Although the next fundamental step will be the switch from CdSe to best performing Cd-free QD-based devices, many open tasks are still seeking a rationalization. First and foremost, recent studies on CdSe QDs highlighted that, in order to push further the understanding of QD photophysics and the efforts to optimize their optical properties, it is largely misleading considering QDs as mere intermediates between molecular and semiconductor materials. NCs, indeed, do not possess a clear individuality as molecules do. The most surprising manifestation is the fact that their optical absorption and emission properties do not depend only on their chemical composition, dimensions and shape: semiconductor NCs exhibit a significant sensitivity to the presence of volume and surface defects[33–35] that may act as traps for charge carriers. Typically, such traps are charged uncoordinated lattice sites, whose concentration is not negligible, especially at the surface of polar semiconductors such as CdSe. Charge-trap interaction is typically detrimental for the optical performances, since traps are involved in processes like non-radiative *Auger recombination* (AR)[36] and single-dot photoluminescence intermittency (phenomenon known as *blinking*)[37,38].

In order to minimize the surface charge-trapping, capping of QDs with an inorganic shell with higher band-gap proved to be the most fruitful approach. However, shell growth entails the creation of a new core-shell interface, which in turn is of key importance for the final optical performances. Shell materials and shell growth methods are chosen in order to reduce the creation of further defects. Namely, a low lattice mismatch with respect to the core material is the most stringent requirement an optimal shell material should satisfy[39]. Such circumstance limits the creation of stacking faults, thus fostering the shell epitaxial growth on core. Nevertheless, a good degree of epitaxy can be achieved even between materials with significant lattice mismatch by tuning synthesis parameters such as reaction time, temperature and ligands. However, the best strategy to minimize core-shell interface defectivity is growing a “graded”

shell, whose composition and lattice parameter are gradually varied along the radial direction. Such configuration can be achieved either by inducing core-shell ion interdiffusion[40–42], *i.e.* creating an alloyed interlayer between core and shell, or by intentionally growing a multi-layered shell with graded composition[43–45]. Both ways proved to be successful in terms of optical performances also for a quantum mechanical reason: a gradual core-shell interface causes a smoothing of the confinement potential, which may result in an order of magnitude reduction of the rate of non-radiative AR, as demonstrated by G. E. Cragg and A. L. Efros in 2010[45].

In the last decade, understanding of QDs photophysics and development of colloidal methods encouraged the synthesis of more complex heterostructures. Nanorods[47], multipods[48], nanoplatelets[49] and relative core-shell derivatives have surpassed QDs in many respects. The reasons for such (apparent) overtaking are several, but all of them derive from a trivial matter of fact: by increasing the volume of a quantum confined structure, issues like charge trapping, AR and blinking, directly related to surface/volume ratio and quantum confinement, are heavily reduced. However, a large single QD volume intrinsically hinders the colloidal stability and, most importantly, limits the packing density of QDs in a neat thin film or composite. On the contrary, graded core-shell QDs demonstrated to be the best performing when embedded in devices. Thanks to the gradual confinement potential provided by the shell, dimensions of graded QDs are maintained low (< 10 nm) and AR is strongly reduced[50].

The necessity to employ such small sized graded QDs forces researchers to "engineer the wave function"[51] in order to minimize the aforementioned issues, which are induced by the low dimensionality. Such *wave function engineering* consists in a careful theoretical design of the nano-heterostructure, which requires a refined synthesis strategy in order to achieve an effective control on the eigenfunctions of quantum-confined charges.

This thesis aims to draw a pathway for the engineering of new synthetic approaches, addressed to the preparation of highly stable core-shell QDs with best performing optical properties. Among the *plethora* of best performing QD materials, different varieties of the archetypal core-shell CdSe-$Cd_XZn_{1-X}S$ QDs have been investigated. Furthermore, CdSe, CdS and ZnS are suitable materials to be combined in a graded core-shell heterostructure. Indeed, most promising and commercial visible light emitting QDs have a CdSe core and a graded CdS-$Cd_XZn_{1-X}S$-ZnS shell. Going from the CdSe core to the ZnS shell the lattice parameter is gradually varied, thus limiting the creation of abrupt or defective interfaces. At the same time, the energy gap is also progressively increased from core to shell, thus protecting excitons from interaction with the majority of traps located at the outmost surface.

In parallel with colloidal synthesis methods, also optical characterization of QDs evolved and gained a key position with respect to other characterization techniques. For instance, basic parameters such as QD dimensions, shape, size dispersion and QY can be easily extracted from

steady-state absorption and emission spectra. These techniques thus represent a convenient tool to control the synthesis process and at the same time to test the QD performances. In addition, transient optical spectroscopy permits to push further the wave function engineering, since transient absorption and PL techniques can selectively probe electron and hole dynamics[52]. Transient PL[35] allows also identifying the nature and time-scales of the different radiative and non-radiative relaxation paths, crucial for guiding the engineering process.

In order to test which shell composition and thickness best matches with the CdSe core, steady-state and transient optical properties of such nano-heterostructures have been correlated with some structural peculiarities.

For the first time, surface-enhanced Raman spectroscopy (SERS) has been employed as a local probe for the study of such core-shell interfaces[41]. The main benefits of SERS in comparison to standard Raman spectroscopy are (i) the Raman signal is highly enhanced by the amplified near field of the plasma resonance close to the exciting laser and signal wavelengths and (ii) the metal presence quenches the residual fluorescence that, due to the high QY of QDs, may dominate over the weak Raman signal. As a result, a high signal-to-noise ratio is obtained with very small laser power, thus avoiding heating damage and allowing room-temperature (RT) measurements. This represents a crucial innovation, since previous Raman studies on QDs were conducted at cryogenic temperature[53]. Namely, the possibility to collect detailed Raman information at RT ensures the analysis of NCs with the same structural features, lattice dynamics, and optical properties present when the QDs are employed as emitters in photonic devices. When studying QDs, an all-optical spectroscopy approach at device operation conditions is also advantageous with respect to more conventional structural characterization techniques, such as transmission electron microscopy (TEM) and X-ray diffraction (XRD), which have also been employed to support the SERS results.

From steady-state absorption and PL studies on CdSe-$Cd_XZn_{1-X}S$ QDs it was possible to verify that different shell materials induce distinct exciton confinement, size dispersion and QY[35]. However, the effect of the core-shell interface on optical properties could be unambiguously detected only with the use of transient optical spectroscopy. Exciton generation and recombination dynamics were probed by means of transient absorption (TA) and transient PL (tPL) techniques. Evolution of exciton population was compared with kinetic models. Regarding the tPL, in literature manifold kinetic interpretations can be found, which does not entail necessarily a clear contradiction between them. Such variety of models arises mainly from the non-stationarity and non-ergodicity[54,55] of individual QDs: single QD PL dynamics is typically treated in the context of PL blinking, whose underlying mechanism remains unclear[37]. In fact, none of the theories currently accounts for all of the key features of blinking. However, for the majority of the light emitting applications, ensembles of QDs are typically employed. A well-

established charge-trapping kinetic model, based on charge-transfer, is usually employed to interpret ~ 10 to 100 ns long PL decays of QDs in their native colloidal dispersion.
A modified version of such model has been employed in this thesis to detect the effect of shell material and core-shell interface on the rates involved in the exciton recombination process. Rates obtained revealed a strong dependence on the core-shell interface, and correlation with SERS results is here discussed.

The correlation between structure and dynamics was detected also at sub-nanosecond time scales by TA analysis. A secondary aim of this thesis was also to find a global interpretation of the dynamics of all signals present in TA spectra of the different CdSe-$Cd_XZn_{1-X}S$ QD series. Pump fluence, shell thickness and composition are the coordinates along which the global analysis has been developed.

Eventually, the attention was focused on optical gain, which represents one of the most investigated and promising applications for QDs. Quantum dots are employed as optical amplifiers[44] and, thanks to the evolution of epitaxial growth techniques, QD lasers can be considered as the state of the art in NIR lasing applications. The advantages offered by a *QD laser* come from the *quantum confinement*, which provides QDs with an atom-like electronic structure. This makes QD laser more similar to gas lasers, since their performances with respect to conventional semiconductor lasers are improved in terms of temperature insensitivity, lasing threshold, intensity oscillations and modulation bandwidth. Furthermore, QD media can be incorporated in *microcavities*, opening to the integration in optical circuits.
The fabrication of QD lasers that operate also in the whole visible spectrum is still an open task. To this end, colloidal CdSe QDs are promising, since the emission region can be tuned from red to blue by just varying the dot size. However, many difficulties have not been overcome yet. First of all, to date lasing from colloidal QD based media has been achieved only by optical pumping. Charge injection and extraction issues in colloidal QDs have hindered the feasibility of an electrically pumped colloidal QD-based laser diode. Other complexities with respect to conventional laser diodes are related with the complex multi-excitonic nature of optical gain in colloidal QDs, which will be discussed in detail in this thesis.

By investigating the *amplified spontaneous emission* (ASE) of different series of CdSe-$Cd_XZn_{1-X}S$ QDs colloidal properties, this work aims to demonstrate that a key property such as ASE activation threshold (comparable with the optical gain threshold) can be optimized by a careful design of the core-shell heterostructure. A laser demands peculiarities for the active medium that go beyond the high QY, stability and properties that unquestionably make QDs promising materials for novel light-emitting devices. The *wave function engineering* approach is here applied to envisage a pathway for the minimization of the activation threshold in a colloidal QD-based laser, operating in the visible range. However, the rationalization of the photophysics

involved in exciton and multi-exciton generation and recombination in core-shell QDs expedites their application in all types of light emitting device.

Outline

This thesis is divided into eight chapters. The first three chapters introduce the theoretical notions and techniques employed in this work:

Chapter 1 focuses on the chemistry of colloidal QDs, providing a brief overview of *materials* and *synthesis* methods. The importance of the *core-shell* approach is here emphasized in terms of passivation of surface traps, here proposed as uncoordinated dangling bonds. Some details about the effects of the shell growth on optical properties will be anticipated and compared with other colloidal nanostructures, such as anisotropic large volume nanocrystals (*quantum rods*, *multi-pods* and *nano-platelets*).

Chapter 2 deals with the effects of *quantum confinement* on bulk semicondutor properties. First of all, some fundamentals about semiconductor photophysics and *exciton* theory are provided. Within the theoretical framework of the Band Theory and Wannier-Mott exciton formalism, solutions of the Schrödinger time-indipendent equation for the quantum confinement problem are provided. In order to obtain the eigenvalues and relative eigenfunctions, the *particle-in-a-sphere* Hamiltonian is employed. Some of the approximations assumed are then relaxed in order to achieve the exciton fine structure for CdSe QDs, whose optical properties are object of investigation in this thesis. Finally, the effects of quantum confinement on optical properties are reviewed.

Chapter 3 presents all the experimental techniques employed for this thesis work. Particular attention is devoted to optical spectroscopy techniques: steady-state absorption and PL, SERS, tPL, TA and ASE.

After these introductive chapters, the remaining chapters present the main experimental achievements of the thesis work:

Chapter 4 provides some details about the colloidal synthesis of the CdSe-$Cd_XZn_{1-X}S$ QDs investigated in this thesis. The basic optical properties (steady-state UV-Vis absorption and PL spectra) of these materials are also provided.

Chapter 5 deals with the SERS characterization of the core-shell interface. CdSe-$Cd_XZn_{1-X}S$ QDs are investigated and the structural variation imposed by the stoichiometric composition of the shell is discussed.

Chapter 6 correlates the structural information, extracted by SERS on different CdSe-$Cd_XZn_{1-X}S$ core-shell series, with results from steady state and transient PL measurements.

Chapter 7 presents the results and discussion obtained by the TA characterization of the different core-shell QD series. Experiments were conducted at different pump fluences in order to investigate the dynamics that rules the optical gain regime in QDs. A global fitting procedure of the TA maps for the optimization of the time-constants involved in exciton and multi-exciton relaxation and relative amplitudes is presented.

Chapter 8 reports the optical gain and ASE performances of CdSe-$Cd_XZn_{1-X}S$ QDs. Activation thresholds and stabilities to laser irradiation are measured and compared with the best performing CdSe QDs with a CdS-$Cd_XZn_{1-X}S$-ZnS graded shell.

PART I:

PHYSICAL CHEMISTRY OF COLLOIDAL QDs

Chapter 1.

Chemistry of Colloidal QDs

Semiconductor QDs have been synthesized by a variety of methods, which can be classified as "physical" or "chemical". To the first category belong all those high-energy input processes such as molecular-beam-epitaxy[56] (MBE) and metalorganic-chemical-vapor-deposition (MOCVD)[57]. The former takes place in high or ultra-high vacuum chambers and exploits the sublimation of ultra-pure elements and successive condensation on the surface of a target substrate. The latter is a chemical vapor deposition method and takes place at moderate pressures (up to 0.01÷1 atm) from the reaction of metalorganic compounds at high temperature. Both methods developed as techniques for the deposition of semiconductor single crystals.

A bridge between the "physical" and the "chemical" is represented by the strategy that gave birth to the first QDs, *i.e.* the microcrystal growth in glasses[58], which is still a high-temperature method. In this case, nanocrystals are obtained by means of solid-state phase segregation and nucleation, followed by growth through diffusion of the nanoparticles through the matrix.

In this thesis the attention will be focused on "freestanding" colloidal QDs, synthesized by "soft" colloidal chemical routes[59]. Such QDs have a nanocrystalline inorganic core, overcoated with a capping layer of organic ligands. Ligands passivate surface dangling bonds and avoid aggregation of the nanocrystals. Furthermore, capping agents govern the solubility of QDs, which can be dispersed in solvents with different polarity by ligand exchange.

A part from the solution processability, the success of the colloidal methods is mainly due the high degree of cristallinity and the size monodispersity. Colloidal QDs have typically sub-15 nm average size, with standard deviations down to 5%, *i.e* about one lattice constant[60].

In this chapter colloidal synthesis methods are reviewed. In section 1.1 conventional QD syntheses are presented and classified in terms of materials and final applications. Section 1.2 provides some fundamentals about the shell growth methods.

1.1 Overview of syntheses, materials and applications

The first strategies to colloidal QD synthesis were based on aqueous chemistry and developed by the groups of Brus and Henglein[6,61,62] in the 1980s. Although the versatility and the simplicity

of the experimental method, it lacked in monodispersity, cristallinity, PL QY and yielded poorly defined absorption and emission bands.

A basic idea of how the colloidal methods work can be provided in terms of La Mer and Dinegar's studies of particle nucleation and growth[63], schematically reported in Figure 1.1.

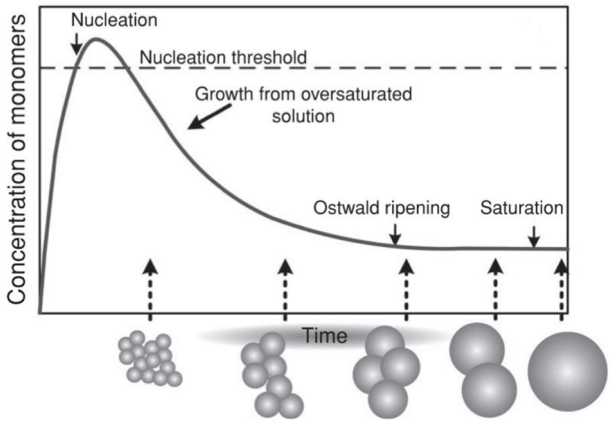

Figure 1.1: Schematic illustration of La Mer's and Dinegar model nanoparticle growth. This figure was adapted from Ref. [64]

These colloidal methods involve a fast nucleation in a coordinating solvent (achieved by quick injection of the precursors into the reaction flask) followed by a rapid growth from monomers and finally slower growth by Ostwald ripening. In 1993, a milestone paper by the group of Bawendi[20] presented a new synthetic route, named *hot-injection method* and based on the pyrolysis of metal-organic precursors with coordinating ligands in a hot organic solvent. Such technique enabled the widespread study and application of colloidal QDs. In Bawendi's work, *cadmium chalcogenide* QDs (CdX; X = S, Se, Te) were synthesized using dimethyl cadmium as metal precursor; and phosphine selenide/telluride, or bistrimethylsilyl sulfide as chalcogenide source. A mixture of trioctylphosphine (TOP) and trioctylphosphine oxide (TOPO) served as coordinating solvent. The latter provided a high boiling point, leading to the higher synthesis temperatures (~ 300 °C) necessary to anneal defects and improve both crystallinity and QY. Reaction temperature served also to control the particle size (size dispersion down to 5%), whose average diameter could be varied from 1 to 12 nm. Colloidal dispersion was maintained also at room temperature thanks to suitable capping agents bound to the QD surface.

An alternative colloidal method (*heating-up method*)[65] entailed the mixing of precursors at a low temperature, leading to supersaturation. The mixture was then gradually heated up to the precursors reaction and decomposition temperature, at which a nucleation burst occurs. Also in this case, the nucleation is a fast and single event and permits to obtain extremely monodisperse QDs.

Such approaches were then adopted by most of the QD community and were further improved and generalized to other binary or ternary semiconducting compounds (II-VI, IV-VI and III-V QDs). A list of materials of the most investigated materials is reported in Table 1.1.

Table 1.1: Most relevant QDs materials and relative stable crystal structure (bulk, RT), group, energy gap (bulk) and lattice parameter (Adapted from Table I on page 46 of Ref [60])

Material	Structure	Group	E_g (eV)	Lattice parameter (Å)
ZnS	Zinc Blende	II-VI	3.61	5.41
ZnSe	Zinc Blende	II-VI	2.69	5.668
ZnTe	Zinc Blende	II-VI	2.39	6.104
CdS	Wurtzite	II-VI	2.49	4.136/6.714
CdSe	Wurtzite	II-VI	1.74	4.3/7.01
CdTe	Zinc Blende	II-VI	1.43	6.482
GaN	Wurtzite	III-V	3.44	3.188/5.185
GaP	Zinc Blende	III-V	2.27	5.45
GaAs	Zinc Blende	III-V	1.42	5.653
GaSb	Zinc Blende	III-V	0.75	6.096
InP	Wurtzite	III-V	0.8	3.545/5.703
InP	Zinc Blende	III-V	1.35	5.869
InAs	Zinc Blende	III-V	0.25	6.058
InSb	Zinc Blende	III-V	0.23	6.479
PbS	Rocksalt	IV-VI	0.41	5.936
PbSe	Rocksalt	IV-VI	0.28	6.117
PbTe	Rocksalt	IV-VI	0.31	6.462

The main drawback of the traditional hot-injection method is the dependence on expensive, hazardous (i.e. dimethyl cadmium) and toxic precursors and solvents.

The introduction of CdO and air-stable Cd precursors represented a first step towards a more sustainable synthesis of high-quality colloidal QDs[66]. Organophosphine-free *non-hot-injection* methods enabled to conduct the synthesis also in air and at lower temperatures (~ 150 °C)[67].

Also room-temperature reactions have been developed. The most successful approaches entail the inverse-micelle[68] and the aqueous-phase growth[69]. The main issues of low-temperature methods are the relatively poor size dispersion and poor PL performances. However, the evolution of QD synthesis strategies toward robust and reproducible "soft-chemistry" procedures is definitely the right way to achieve reaction scale-up and a larger diffusion of QD applications.

1.2 Core-shell QDs: benefits and issues

In the previous subsection it was not mentioned, but most of the QDs nowadays employed for almost every application are core-shell based. Core-shell QDs have been developed to saturate dangling bonds located at QD surface, which intrinsically develop due the high surface/volume ratio and lower coordination of surface atoms with respect to the interior ones. The electronic states associated with the unpassivated orbitals, conventionally defined as *charge-traps*, lie within or in proximity of the band-gap. As suggested by the name, such states act as hole (anion dangling bond) or electron (cation dangling orbital) traps, leading to low QY and significant trap-state PL, which is broader, weaker and red-shifted with respect to the intrinsic PL. Coordination of CdSe QDs with suitable organic ligands has been engineered and reasonable QY values have been reported in literature[70]. However, due to steric hindrance between ligands a non-negligible amount of traps is not passivated. Moreover, organically passivated QDs exhibited limited photostability.

Overcoating of the QD surface with an inorganic wider band-gap semiconductor shell became routine after the work by Hines and Guyot-Sionnest[71]. Thanks to this method, QY values approaching unity have been achieved for almost all kinds of semiconducting materials employed so far [59]. The shell plays a dual role: it passivates both anionic and cationic trap sites and protects the core from chemical and photo-oxidation. Depending on the bands alignment between core and shell, core-shell QD heterostructures can be divided in two main subclasses (Figure 1.2): type-I and type-II [72].

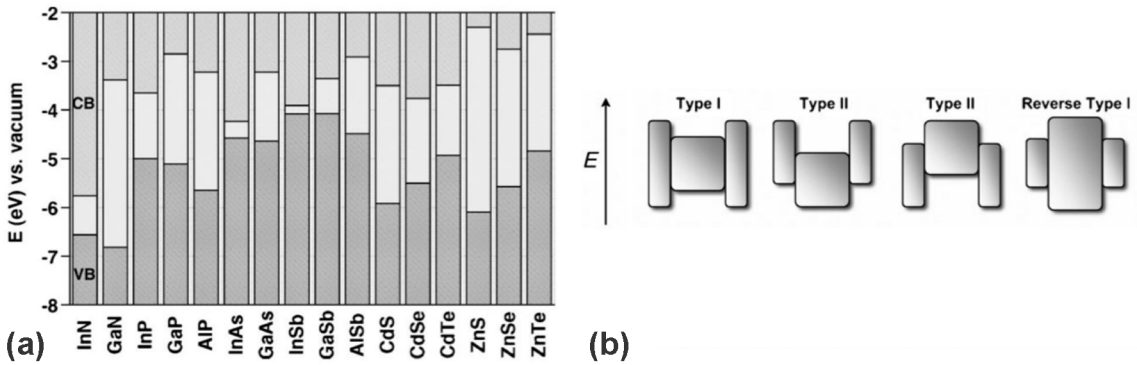

Figure 1.2: (a) Electronic levels for different semiconductor materials; (b) Different core-shell band alignment [Adpted from Ref. [72,73]].

Type-I heterostructures, the most investigated and firstly synthesized, are characterized by a core material whose valence and conduction bands (VB and CB) are located within the shell band-gap. Examples are CdSe-CdS[74] and CdSe-ZnS[75] core-shell QDs. In this configuration, the electron and hole experience a confinement potential that tends to localize both charge carriers

in the QD core, reducing their interactions with surface trap states and enhancing QYs in emission.

In *type-II heterostructures* the lowest energy states for electrons and holes are in different semiconductors. Such configuration induces a separation of electron and hole between core and shell. This arrangement has been widely investigated in the last decade, since charge separation is attractive especially for gain[76] and photovoltaic[77] applications.

A bridge between these two categories is provided by the so-called *"quasi" type-II heterostructures*. Such systems are type-I heterostructures with either the valence or the conduction band of the shell material almost aligned with the corresponding core one. This is the case of the CdSe-CdS core-shell system, which has been deeply investigated in literature. Due to the alignment of the CdSe and CdS CB, electrons tend to delocalize in the shell with a higher probability with respect to the holes[40].

Focusing on the shell growth methods, several routes have been optimized for every semiconductor. All syntheses have been refined in order to respect some quality prerequisites: first of all, the self-nucleation of the shell material has to be minimized. Typically, this is achieved by combining both low shell precursors concentrations and reaction temperatures. High cationic to anionic precursors ratios and the use of ligands with high shell metal affinity also prevent homogeneous nucleation of shell material. Secondly, final core-shell shape and size distribution have to be as more homogenueous and narrower as possible respectively.

The essential condition for a successful shell growth is the final improvement of optical performances with respect to the starting core-only QDs. All such properties depend critically on the degree of epitaxy of shell growth on core. At nanoscale, materials with high bulk lattice mismatch, such as CdSe and ZnS ($\Delta c \sim 12\%$)[39], can be epitaxially combined in a core-shell heterostructure[39,75].

The possible outcomes of shell growth will be meticulously discussed in the second part of this work. Briefly, shell growth is normally accompanied by a red-shift of optical features, due to the delocalization of charge carriers into the shell. A broadening of absorption is also common and mainly due to an unavoidable increase of size dispersion after shell growth. Finally, in the case of extremely mismatched lattices some dislocations may occur at core-shell interface after the growth of multiple shell layers, due to relaxation of the strained heterostrucure. Such defects act as charge-traps, which lower the QY[39,75].

Best quality core-shell QDs can be achieved by three different classes of methods.

The first core-shell structures were synthesized by means of a two-step procedure: cores were preliminarily prepared and purified, while shell was grown in a second phase[75]. To this category belongs the most successful technique for core-shell synthesis, developed originally for thin film deposition: *successive ion layer adsorption and reaction* (SILAR). In 2003 Peng *et al.*[78] extended its application to CdSe-CdS core-shell QD synthesis, depositing one monolayer at a time via

alternating injection of cationic and anionic precursors. After this work, SILAR technique was further improved and extended to other semiconductors[39]. Modified versions of the original SILAR allowed the growth of so called "giant-shell" CdSe-CdS QDs, with up to 20 shell monolayers (ML)[79]. Nowadays, by means of modified SILAR methods it is also possible to carefully control crystalline phases and ion interdiffusion between core and shell materials[80]. Finally, graded shell materials, consisting of layers of different materials can also be obtained[39,44].

A second class of methods includes alternative single step core-shell syntheses, which do not entail any core intermediate purification[30]. This approach was applied to many core-shell systems such as CdSe/CdS[74] and CdSe/ZnSe[76].

Finally, a *cation exchange* strategy has been developed, originally to overcome the inability to grow shells on PbSe and PbS QDs. Conventional high-temperature reaction conditions are too harsh and hamper the integrity of the lead chalcogenide cores[16]. Briefly, in this case only shell slow-reacting metal precursor is added to the reaction flask containing the cores. The reaction is conducted at ~RT and by finely tuning reaction time, temperature and amount of precursor it possible to control the amount of core cations to be replaced. Complete exchange of cations can be also achieved by using highly reactive precursors and cation binding solvents[81].

1.3 Anisotropically shaped quantum confined nanostructures

Shape homogeneity is an important parameter for evaluating the success of a QD synthesis. One of the first order approximations in basic modeling of QD physical properties (Chapter 2) entails spherical shape of semiconductor nanocrystals. However, at nanoscale underlying lattice structure for many semiconductors is either zincblend-like or wurtzite-like. Wurtzite hexagonal lattice induces an unavoidable preferential crystal growth along the c-axis. In general, perfect homogeneity of growth velocity along different axes in different nuclei is difficult to achieve, leading to an intrinsic shape inhomogeneity of the reaction products.

Differential growth along different crystal axes has been also engineered and a variety of uniformly size distributed anisotropic shaped QDs can be synthesized nowadays[82–84]. Reaction conditions, lattice mismatch and differential surface energy for each crystal face are therefore the parameters to be considered to synthesize anisotropic heterostructures such as nanorods, platelets or multi-pods[82,84]. Such structures are metastable nanocrystals, since in the slow growth limit – under thermodynamic control – quasi-spherical QDs are obtained. Therefore, anisotropy can be enhanced only by working in non-equilibrium – under kinetic control – conditions. This is achieved by suitably controlling the symmetry of the underlying crystal phase[85,86], reaction temperature, precursors concentrations and using multicomponent labile ligands[82], which selectively adsorb on different crystal faces.

Due to the anisotropy and higher volume compared to QDs, many issues related to the nanoscale dimensions (Chapter 2 and 4) are reduced for all the *plethora* of non-spherically shaped nanocrystals investigated so far. This makes such structures direct competitors to conventional < 10 nm sized QDs as active media in photonic applications[87]. The main drawbacks are related to the lower colloidal stability and the lower packing density when deposited in a thin film. Compared to spherical QDs, when included in a waveguide their larger volume may enhance the losses due to scattering.

Chapter 2.

Optical Properties of Colloidal QDs

A QD is a nanoscale semiconducting material whose physical properties are governed by a size effect, namely *quantum confinement*. For usual inorganic bulk semiconductors size effects are negligible. But when the material size is of only a few nanometers, electron and hole translational degrees of freedom are limited to a volume whose dimensions are comparable to the length of their characteristic wave functions. In this regime, electron-hole Coulomb interaction is no more screened via the high dielectric constant of the medium; this, together with a profound modification of the band structure induced by the finite translational symmetry, triggers a cascade of novel photo-physical properties. Moreover, at nanoscale surface-related effects become significant due to the high probability of interaction between charges and surface trap-sites, ligands or solvent. This leads to further modifications of the optical response and justifies why so many efforts have been spent so far to engineer the surface chemistry of QDs, as reported in the previous chapter.

This chapter traces the origins of the physics that govern colloidal QDs optical properties: Section 2.1 briefly reviews some bulk semiconductors photo-physics. Thereafter, in Section 2.2 the tools to quantify electron-hole Coulomb interaction are provided, by introducing the concept of exciton. In Section 2.3 quantum confinement is introduced and its effect on electronic properties is illustrated. The remaining Sections 2.4 – 2.5 describe how the optical properties, and in particular optical gain properties, are consequently modified.

2.1 Photophysics of bulk semiconductors

Within a three dimensional periodic crystalline semiconductor the electrons are subject to a periodic potential $V(\mathbf{r}) = V(\mathbf{r}+\mathbf{a})$, where $\mathbf{a}$ represents a generic lattice center. This potential is defined as *Bloch potential* and, by solving the Schrödinger equation, a splitting of the free-electron parabolic energy band[88] is produced, as presented in Figure 2.1 for a one-dimensional lattice.

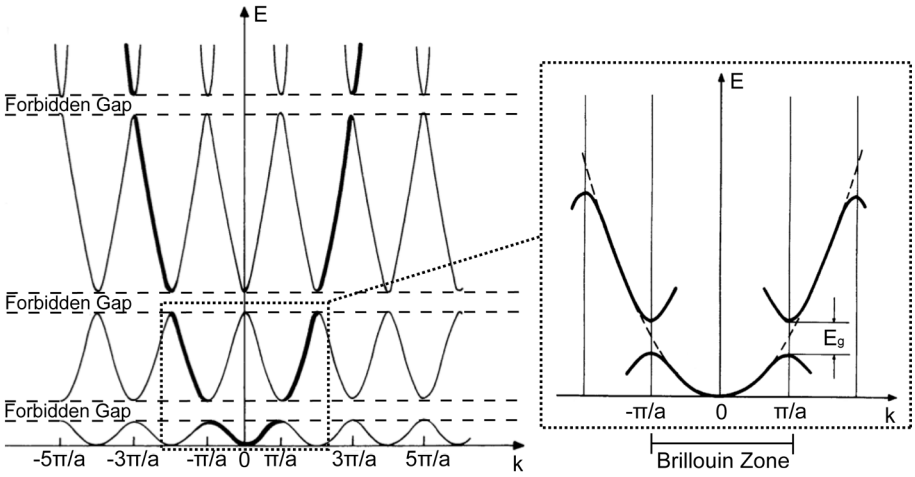

Figure 2.1: Energy dispersion curves for a one-dimensional lattice of constant "a". Thick lines indicate the parts of the band structure corresponding to the parabolic free-electron energy dispersion. The inset highlights the splitting (energy band gap) of the free-electron parabola at the edges of the first Brillouin zone. Adapted from Ref. [89].

This is due to the fact that the eigenfunctions are no more just planar waves as in metals or in general in systems where the potential can be approximated to a constant value. The eigenfunctions are defined as *Bloch functions*:

$$\psi_{n,\mathbf{k}}(\mathbf{r}) = u_{n,\mathbf{k}}(\mathbf{r})e^{i\mathbf{k}\cdot\mathbf{r}} \qquad \text{(Eq. 2.1)}$$

where $u_{n,\mathbf{k}}(\mathbf{r})$ has the same periodic structure as $V(\mathbf{r})$.
By applying the system Hamiltonian to the *Bloch functions* one obtains

$$\left(\frac{(\mathbf{p}+\hbar\mathbf{k})^2}{2m} + V(\mathbf{r})\right)u_{n,\mathbf{k}}(\mathbf{r}) = E_{n,\mathbf{k}}u_{n,\mathbf{k}}(\mathbf{r})\,. \qquad \text{(Eq. 2.2)}$$

In this equation $\mathbf{r}$ can be limited to a single unit cell, due to periodicity of $u_{n,\mathbf{k}}(\mathbf{r})$. The equation resembles the Schrödinger equation for an atom and $\mathbf{k}$ plays the role of a quantum number; $u_{n,\mathbf{k}}(\mathbf{r})$ eigenfunctions correspond to discrete eigenvalues $E_{n,\mathbf{k}}$. As $\mathbf{k}$ is varied the eigenvalues describe energy bands with principal quantum number n = 1, 2, 3, … , with a parabolic dependence on k ($E_{\mathbf{k}} = \hbar^2|\mathbf{k}|^2/2m$). While n is an integer, the allowed values of the wave vector are fixed by the surface boundary conditions and vary with intervals $\Delta k_x = 2\pi/L_x$. Since $L_{x,y,z}$ is much higher than the lattice parameter and corresponds to the macroscopic dimension of the bulk material, bands are quasi-continuous eigenstate dispersions.
Not all energies are accessible to electrons, since bands are separated by *energy gaps* E_g. If the number of electrons per cell is odd, Pauli filling (at T = 0K) leaves at least one band partly unfilled, so that the highest occupied state is on the same band of the lowest unoccupied state. Such low energy separation allows to accelerate the electrons by a weak electric field, therefore the material is a *metal*. On the other hand, if the number of electrons is even and the bands do not overlap the highest occupied state and the lowest unoccupied state lie in different bands,

respectively valence (VB) and conduction (CB) band. If the E_g is narrow enough to permit electron thermal excitation from VB to CB, the solid is a *semiconductor*. Otherwise, the material is an *insulator*.

In order to understand the response of a semiconductor in the presence of light the concept of *hole* need to be introduced: a *hole* is defined as a positively charged quasi-particle representing the lack of an electron from the valence band in an excited semiconductor. Such empty states play a fundamental role in the conduction process and their definition is crucial for the development of the excitonic theory of semiconductors (next section).

Also the curvature of energy bands is relevant, especially for explaining light emitting properties of semiconductors. Bands curvature is governed by the charge carrier mass, which has been treated as a constant parameter in Eq. 2.2, leading to isotropically and parabolically shaped bands. By substitution of *m* with suitable tensorial functions of the wave vector **k**, the real band curvature is obtained. Conveniently, the *effective mass approximation* (EMA) allows to neglect the periodic crystal potential and describe electrons and holes as free particles having a parabolic dispersion and characterized by *effective masses* m_e^* and m_h^* dependent on the crystal material.

Finally, to proceed with the description of semiconductor photophysics, the concept of *density of states* (*DOS*), a.k.a. the number of states per unit energy interval, needs to be introduced. For an electron (or hole) in a real semiconductor the relation does not have a simple analytical form, due to the aforementioned complex curvature of the energy dispersion:

$$DOS(E) \propto \int_{S(E)} \frac{d^2S}{|\nabla_{\mathbf{k}} E|} \qquad \text{(Eq. 2.3)}$$

where *S(E)* represents a constant energy surface of the reciprocal space. Adopting the EMA, proportionality to the square root of energy emerges, similarly to what occurs for a free-electron:

$$DOS(E)_{VB} = 4\pi \left(\frac{L}{\hbar}\right)^3 (2m_e^*)^{\frac{3}{2}} (E - E_{CB})^{1/2} \qquad \text{(Eq. 2.4)}$$

$$DOS(E)_{CB} = 4\pi \left(\frac{L}{\hbar}\right)^3 (2m_e^*)^{\frac{3}{2}} (E_{VB} - E)^{1/2} \qquad \text{(Eq. 2.5)}$$

The probability of the occupation of the energy states by electrons at equilibrium obeys the Fermi statistical distribution:

$$f(E) = \frac{1}{1+e^{(E-E_F)/k_B T}} \qquad \text{(Eq. 2.6)}$$

where E_F is the Fermi level and *K* is Boltzmann's constant. It is possible then to obtain the *density of the occupied states* just multiplying the density of states with the Fermi distribution. This consideration is valid both for the valence and the conduction band.

In the presence of light, a dynamical equilibrium between the electron and hole gases is established. Electrons can be excited from the VB into CB by the absorption of photons, provided the photon energy is higher than the E_g. *Direct-gap* semiconductors (Figure 2.2.a) such as polar CdSe and GaAs have VB top and CB bottom aligned at the same $\boldsymbol{k}$. This condition allows the emission of a photon when an electron recombines with a hole. On the contrary, radiative recombination is forbidden in *indirect-gap* materials (Figure 2.2.b) such as Si, since total momentum needs to be conserved.

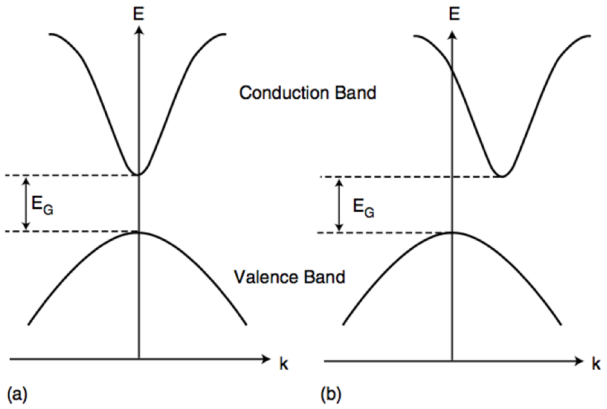

Figure 2.2: Schematic representation of the energy band structure of a direct-gap (a) and indirect-gap (b) semiconductor material.

Non-radiative recombination processes dominate the recombination in indirect-gap materials and compete with radiative recombination in direct-gap semiconductors.

2.1.1 Absorption in semiconductors

When a semiconductor is irradiated with light having an electric field

$$\mathbf{E}(\mathbf{r},t) = \mathbf{E}sin(\omega t - \mathbf{K}\cdot\mathbf{r}) \quad \text{(Eq. 2.7)}$$

$$\omega t > E_g \quad \text{(Eq. 2.8)}$$

electrons can be excited from VB to CB by *absorption* of photons. **E** represents the electric field, orthogonal to the wave vector of light **K**. What we have in this case is a quantum mechanical system subject to a sinusoidal perturbation. Indeed, the Hamiltonian describing the electron-photon interaction has the form

$$H_p = H_p cos(\omega t - \mathbf{K}\cdot\mathbf{r}) =$$
$$= Cexp(i\omega t) - C^{+}\exp(-i\omega t) \quad \text{(Eq. 2.9)}$$

By applying perturbation theory[90] one gets the transition probability from an initial state $|i>$ to a particular final state $|f>$ of higher energy $\hbar\omega_{if} = E_f - E_i$:

$$P_{i\to f}(t) = \frac{4|\langle f|C^{+}|i\rangle|^2}{\hbar^2}\frac{sin^2(1/2)(\omega_{if}-\omega)t}{(\omega_{if}-\omega)^2} \qquad \text{(Eq. 2.10)}$$

which is proportional to the square of the matrix element of the perturbation. The maximum contribution to the probability is when $\omega \sim \omega_{if}$ (Figure 2.3.a), as an expression of the energy conservation for the states of the unperturbed system. This conservation holds only in the limit of weak perturbations and long time scales. As a function of time, the dependence is ruled by a squared sinusoidal function, whose peaks are proportional to $(\Delta\omega)^{-2}$, with $\Delta\omega = \omega - \omega_{if}$. As reported in Figure 2.3.b, at short *t* all curves coincide, while they go out of phase at longer times.

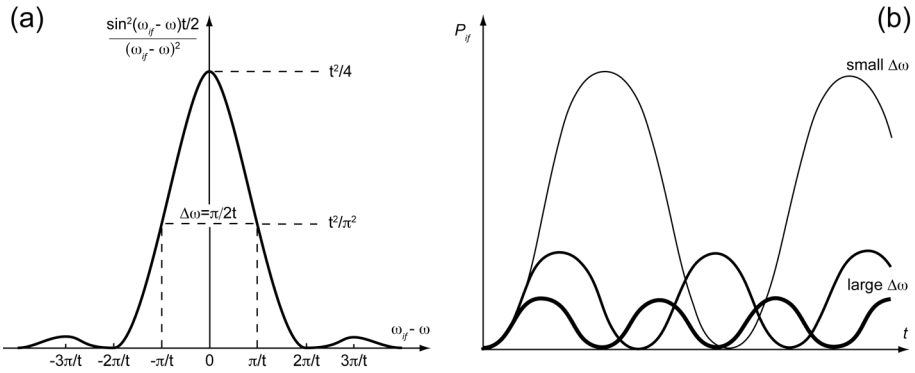

Figure 2.3: (a) Variation of the function $\Delta\omega^{-2}sin^2(\Delta\omega/2)t$ as function of $\Delta\omega = \omega - \omega_{if}$. (b) Variation of the absorption transition probability $P_{i\to f}$ as a function of time for different $\Delta\omega$.

For the case of a semiconductor, the initial state is the VB while the final state is the CB. By adding the concept of joint density of states *DOS(E)**,[i] the total transition probability per unit of time from $|i>$ to one or another of a set of final states close to E_f, *i.e.* the *Fermi's Golden Rule* (FGR), is:

$$W(t) = \frac{2\pi\left|\langle f|C^{+}|i\rangle\right|^2}{\hbar} DOS(E)^* \qquad \text{(Eq. 2.11)}$$

If the initial and final states are replaced by Bloch functions, it is possible to verify that the matrix element also vanishes unless the momentum is conserved, *i.e* $\mathbf{k_f = k_i + K}$. Considering that for photon energy of the order E_g $\mathbf{K << k}$, the selection rule

$$\mathbf{k_f = k_i} \qquad \text{(Eq. 2.12)}$$

is obtained.

[i] From Ref. [91], the joint density of states is expressed as $DOS(E)^* \propto \int_E \frac{dS}{|\nabla_{\mathbf{k}}[E_{CB}(\mathbf{k}) - E_{VB}(\mathbf{k})]|}$, where dS is the element of surface in $\mathbf{k}$ space on the the surface defined by $E = E_{CB}(\mathbf{k}) - E_{VB}(\mathbf{k})$. From this relation it is evident that the $DOS(E)^*$ shows singularities when $\nabla_{\mathbf{k}}E_{CB}(\mathbf{k}) - \nabla_{\mathbf{k}}E_{VB}(\mathbf{k}) = 0$.

From FGR is it possible also to find the relation for the total transition probability per unit of time, by integrating over all VB and CB states. Such total probability is directly related with the absorption coefficient, which has a dependence on energy of the form:

$$\alpha \propto (\hbar\omega - E_g)^{1/2}. \qquad \text{(Eq. 2.13)}$$

Eq. 2.13 describes quite well absorption spectra of *direct-gap* semiconductors, especially at energies close to the band gap, while it is not reliable at higher energies, due mainly to the complex relations for the real DOS at $E \neq E_g$.

2.1.2 Relaxation processes in semiconductors

Photogenerated electron-hole pairs does not live infinitely, but are subject to a series of *recombination processes* that limit the steady increase of charges under continuous irradiation. Such processes play a fundamental role in light emitting devices, light sensitive devices and transistors. They can be categorized is three main classes (Figure 2.4):

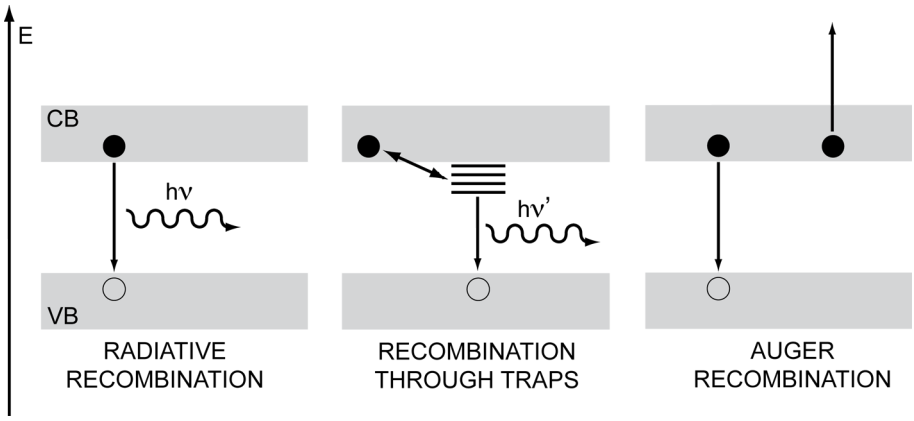

Figure 2.4: Schematic representation of the various recombination processes

- *Radiative interband relaxation*: If the CB bottom and VB top are at the same wave vector, an electron-hole pair can recombine radiatively. As for electron-hole generation by light absorption, also light emission can be explained in terms of light-matter interaction. Radiative rate, in absence of any alternative recombination path (*vide infra*), is related to the absorption coefficient by

$$R \propto \int_0^\infty \frac{n^2(\nu)\alpha(\nu)\beta^2}{e^\beta - 1} d\beta \quad \text{with} \quad \beta = \frac{h\nu}{kT} \qquad \text{(Eq. 2.14)}$$

Such relation demonstrates that it is possible to transform the absorption spectrum $\alpha(\nu)$ into the emission $R(\nu)$ if the refractive index $n(\nu)$ is known. Furthermore, the integral in 2.14 is null except near the fundamental absorption ($h\nu=E_g$). This explains why the light emitted from a semiconductor is very monochromatic. Due to the continuous increase of *DOS* (~ $E^{1/2}$, Eq. 2.4-

2.5) with energy, electron (or hole) intraband relaxation to the CB minimum (VB maximum) is typically phonon assisted (Quessier-Shockley law). On the other hand, phonon-assisted interband relaxation is unlikely, especially in presence of a direct-gap. Only the improbable emission of multi-phonons or phonon combinations can cause electron-hole recombination with a release of thermal energy $\sim E_g \geq 1$ eV.

- *Recombination through traps*: An electron (or hole) in CB (VB) can be captured by a trap whose energy level lies in the band-gap or in proximity of the band. Such traps are typically represented by impurities, lattice defects or surface states due to uncoordinated chemical bonds. From this states charges can radiatively recombine, decreasing the monocromaticity of the total light emitted, or be re-excited to the CB (electron) or VB (hole), slowing down the recombination process.

- *Non-radiative Auger recombination (AR)*: Direct non-radiative interband relaxation can also occur if an electron (or hole) instead of recombining transfers its energy by a scattering process to another electron in the CB (hole in VB), whose intraband energy increases.

2.2 Excitons

Absorption spectra of semiconductors present a peak (Figure 2.5) at energies slightly below E_g, which is not predicted by the considerations reported in the last section.

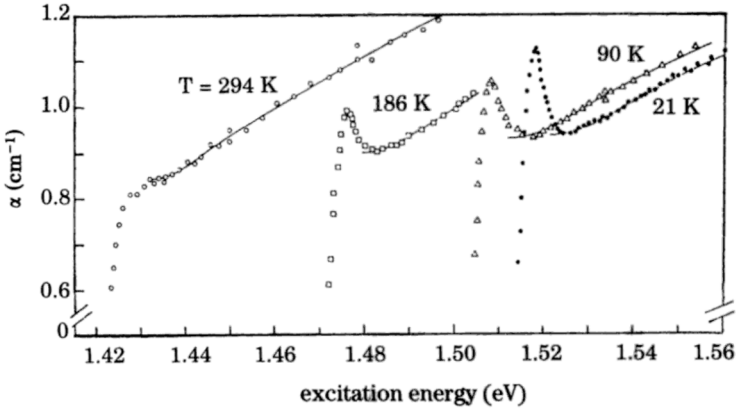

Figure 2.5: Absorption spectra of GaAs near the threshold, at various temperatures. The increase of band-gap is due to the thermal expansion of the lattice, while the peak is due to the generation of excitons. Figure adapted from Ref [90].

Such peak results from the generation through photon absorption of *excitons*, whose peculiarities will be now described.

Excitons are quasi-particles resulting from the quantum mechanical treatment of the collective properties of electrons in crystals. Fundamentals of exciton theory were presented by Frenkel, Peierls, Wannier and Mott as far as 80 years ago.

Their theories justifies absorption of photons at $E < E_g$ as the outcome of Coulomb attraction between electrons and holes, which enters into the total Hamiltonian of the system and generates bound states within the forbidden gap. Such states have a profound influence on absorption and emission properties, but also on energy transfer, charge transfer, photochemical properties, etc.

The first exciton model was provided by Frenkel, who described the case of tightly bound excitons (*Frenkel excitons*) in molecular crystals. In this case delocalization of the excitation is high, due to both strong inter-molecular interactions and the translational symmetry. The latter imposes a degeneration, which is perturbatively lifted by interactions, leading to a wave-like propagation of the excitation.

In terms of the concepts introduced so far, Frenkel excitons are also called small-radius excitons, since they correspond to the situation when the electron and the hole in a bound state are localized in the same lattice cell, with 0.1-1 eV typical binding energies.

A weak-binding approach to excitons was developed by Wannier, and applies to materials with high dielectric constants such as inorganic semiconductors. The medium here acts as a screen for interaction, leading to localized excited states interacting by means of mutual site interactions. Translated in semiconductor language, Wannier-Mott excitons or large-radius excitons (binding energies <0.1 eV) account for the correction of the interband transition energy, due to the interaction between the electron in the CB and the hole in the VB. Here, the radius of the electron–hole bound state is much larger than the lattice constant (a typical size is of the order of tens of lattice constants).

For a two-band model semiconductor, the ground-state electronic wave function for an N-electron system is formally written under Hartree-Fock approximation as Slater determinant of one-electron Bloch functions $\psi_{n,\mathbf{k}}(\mathbf{r})$

$$\phi_0 = 1/N!^{1/2} \begin{vmatrix} \psi_{\mathbf{k_1}}(\mathbf{r_1}) & \psi_{\mathbf{k_1}}(\mathbf{r_2}) & \dots & \psi_{\mathbf{k_1}}(\mathbf{r_h}) & \dots & \psi_{\mathbf{k_1}}(\mathbf{r_N}) \\ \psi_{\mathbf{k_2}}(\mathbf{r_1}) & \psi_{\mathbf{k_2}}(\mathbf{r_2}) & \dots & \psi_{\mathbf{k_2}}(\mathbf{r_h}) & \dots & \psi_{\mathbf{k_2}}(\mathbf{r_N}) \\ \dots & \dots & \dots & \dots & \dots & \dots \\ \psi_{\mathbf{k_h}}(\mathbf{r_1}) & \psi_{\mathbf{k_h}}(\mathbf{r_2}) & \dots & \psi_{\mathbf{k_h}}(\mathbf{r_h}) & \dots & \psi_{\mathbf{k_h}}(\mathbf{r_N}) \\ \dots & \dots & \dots & \dots & \dots & \dots \\ \psi_{\mathbf{k_N}}(\mathbf{r_1}) & \psi_{\mathbf{k_N}}(\mathbf{r_2}) & \dots & \psi_{\mathbf{k_N}}(\mathbf{r_h}) & \dots & \psi_{\mathbf{k_N}}(\mathbf{r_N}) \end{vmatrix} \qquad \text{(Eq. 2.15)}$$

where $\mathbf{r_N}$ are electron position vectors and subscript *h* indicates an electron in the valence band. In the excited state, an electron from the VB is excited to an empty CB state and the resulting excited state wave function is obtained replacing one VB Bloch function $\psi_{\mathbf{k_h}}$ by a CB Bloch function $\psi_{\mathbf{k_e}}$

$$\phi_{ex} = 1/N!^{1/2} \begin{vmatrix} \psi_{\mathbf{k_1}}(\mathbf{r_1}) & \psi_{\mathbf{k_1}}(\mathbf{r_2}) & \dots & \psi_{\mathbf{k_1}}(\mathbf{r_e}) & \dots & \psi_{\mathbf{k_1}}(\mathbf{r_N}) \\ \psi_{\mathbf{k_2}}(\mathbf{r_1}) & \psi_{\mathbf{k_2}}(\mathbf{r_2}) & \dots & \psi_{\mathbf{k_2}}(\mathbf{r_e}) & \dots & \psi_{\mathbf{k_2}}(\mathbf{r_N}) \\ \dots & \dots & \dots & \dots & \dots & \dots \\ \psi_{\mathbf{k_e}}(\mathbf{r_1}) & \psi_{\mathbf{k_e}}(\mathbf{r_2}) & \dots & \psi_{\mathbf{k_e}}(\mathbf{r_e}) & \dots & \psi_{\mathbf{k_e}}(\mathbf{r_N}) \\ \dots & \dots & \dots & \dots & \dots & \dots \\ \psi_{\mathbf{k_N}}(\mathbf{r_1}) & \psi_{\mathbf{k_N}}(\mathbf{r_2}) & \dots & \psi_{\mathbf{k_N}}(\mathbf{r_e}) & \dots & \psi_{\mathbf{k_N}}(\mathbf{r_N}) \end{vmatrix} \quad \text{(Eq. 2.16)}$$

These excited states $\phi_{ex} = \phi_{c\mathbf{k_e},v\mathbf{k_h}}$ are characterized by the wavevector $\mathbf{k_e}$ - $\mathbf{k_h}$ and, due to translational invariance of the electronic Hamiltonian $\widehat{H}_e$, can interact only with states of the same translational symmetry $\phi_{ex} = \phi_{c\mathbf{k_e}',v\mathbf{k_h}'}$ of wavevector $\mathbf{k_e}'$ - $\mathbf{k_h}'$ = $\mathbf{k_e}$ - $\mathbf{k_h}$.

Taking $\langle\phi_0|\widehat{H}_e|\phi_0\rangle$ as the ground state and using the Koopmans' theorem it is possible to evaluate

$$\langle\phi_{ex}|\widehat{H}_e|\phi_{ex}\rangle = E_c(\mathbf{k_e}) - E_v(\mathbf{k_h}). \quad \text{(Eq. 2.17)}$$

Solutions are obtained by linearly combining the excited states wave functions $\phi_{c\mathbf{k_e},v\mathbf{k_h}}$ as:

$$\psi_{\mathbf{K}} = \sum_{\mathbf{k}} A(\mathbf{k})\phi_{c\mathbf{k}+\frac{\mathbf{K}}{2},v\mathbf{k}-\frac{\mathbf{K}}{2}} \quad \text{(Eq. 2.18)}$$

where the Fourier transform $F(\mathbf{r})$ of $A(\mathbf{k})$

$$F(\mathbf{r}) = \sum_{\mathbf{k}} A(\mathbf{k})e^{i\mathbf{k}\cdot\mathbf{r}} \quad \text{(Eq. 2.19)}$$

satisfies the *envelope function equation*:[91]

$$\left(-\frac{\hbar^2}{2m_e^*}\Delta_e - \frac{\hbar^2}{2m_h^*}\Delta_h - \frac{e^2}{\epsilon|\mathbf{r_e}-\mathbf{r_h}|}\Delta_e\right)F(\mathbf{r}) = EF(\mathbf{r}) \quad \text{(Eq. 2.20)}$$

Many approximations have been adopted: exchange term and band mixing are neglected, bands are assumed isotropic and dielectric function is set as constant.

Eq. 2.20 looks like the Schrödinger equation for a hydrogen-like atom. If r = $|\mathbf{r_e}-\mathbf{r_h}|$, solutions for bound states have the form

$$F_{n,l,m,\mathbf{K}} = e^{i\mathbf{K}\cdot\mathbf{R}}\Phi_{n,l,m}(r). \quad \text{(Eq. 2.21)}$$

The first term accounts for the translational invariance of the Coulomb interaction and thus the motion of electron-hole center of mass. **R** is the center of mass coordinate, while **K** is the total quasi-momentum. The second factor $\Phi_{n,l,m}(r)$ is the hydrogen-like eingenfuntion, which governs the relative motion of electron and hole.

Finally, the corresponding eigenvalues are

$$E_n(\mathbf{K}) = -\frac{\mu e^4}{2\hbar^2\epsilon^2 n^2} + \frac{\hbar^2K^2}{2(m_e^*+m_h^*)} = -\frac{R_y^*}{n^2} + \frac{\hbar^2K^2}{2M} \quad \text{(Eq. 2.22)}$$

where μ is the reduced mass and R_y^* is the Rydberg constant. The n = 1 state corresponds to the so-called *band-edge exciton state*. The first term accounts for the exciton binding energy (E_X), while the second term is related to exciton kinetic energy. Such states influence the optical properties of bulk semiconductors, especially at low temperature. At low T it is also possible to detect the fine structure of such exciton states, deriving from the removal of the approximations here employed.

2.3 Quantum confinement

When the size of a semiconductor solid is reduced to values comparable with waves associated to charge carriers, the finite dimensions can't be neglected. Therefore, concepts presented in the previous section need to me reformulated in order to deal with quantum confinement.
The electronic *DOS* changes drastically between systems of different dimensionalities, as is schematically shown in Figure 2.6.

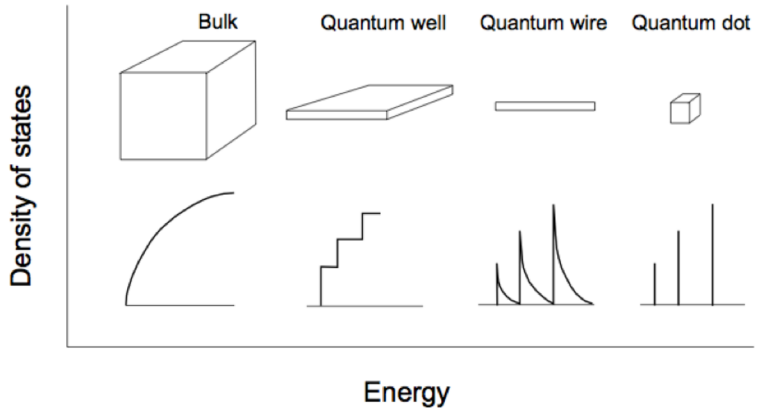

Figure 2.6: Schematic representation of the evolution of the density of states at 0D, 1D, 2D and 3D confinement.

Progressive reduction of dimensionality confines the motion of electrons, leading to quantization along all three directions in space in the case of QDs. QD *DOS* is condensed in a series of Dirac's Deltas, similarly to what is typically observed for molecular systems (Figure 2.6).

Like electrons and holes, also excitons can be confined. Namely, quantum confinement is also defined as the situation in which the solid dimensions are comparable with the *exciton Bohr radius*:

$$a_B = a_0 \frac{m_e}{\mu} \epsilon \qquad \text{(Eq. 2.23)}$$

which represents the scale length of the exciton state. a_0 = 0.0529 nm is the Bohr radius, while m_e is the rest mass of the electron. Almost all materials of interest present a_B of the order of tens

of nanometers. Depending on the nanocrystal size, two confinement regimes can be found (Al. L. Efros and A. L. Efros, Sov. Phys.-Semicond. 1982, 16, 772):

- A *weak confinement* regime ($a<a_B$). This regime can be described neglecting the relative motion of electron and hole: the confinement potential can be considered to act only on the exciton center of mass motion. Uncoupling and neglecting for a while the electron-hole interaction from Eq. 2.20 and considering the confinement potential as an infinite spherical potential barrier (in polar coordinates: $V(r)=0$ at $r<a$, $V(r)=\infty$ at $r>a$), the resulting eigenvalue problem is that of a *particle-in-a-sphere*. The eigenfuctions, expressed in terms of Bessel functions $j_l(k_{n,l}, r)$ and spherical harmonics $Y_l^m(\theta, \phi)$, and the eigenvalues are

$$f_{n,l,m}(r,\theta,\phi) = \frac{C}{r} j_l(k_{n,l}, r) Y_l^m(\theta,\phi), \qquad E_{n,l} = \frac{\hbar^2 k_{n,l}^2}{2M} = \frac{\hbar^2 \alpha_{n,l}^2}{2Ma^2} \qquad \text{(Eq. 2.24)}$$

where $\alpha_{n,l}$ is the nth zero of j_l and a is the dot radius. The spherical symmetry yields atomic-like wave functions, labeled by three quantum numbers: n (1,2,3,...), l (*S,P,D...*) and m. The energies have a parabolic dependence on the wave vector as for the kinetic energy of a free particle, except that the wave vector is quantized by the spherical boundary condition. Moreover, exciton eigenvalues exhibit a strong size dependence ($\propto a^{-2}$).

- *Strong confinement regime* ($a<a_B$). With the development of the synthetic methods QDs with sizes of few nanometers were created. Focusing on colloidal QDs, most studied materials have radii $a<a_B$. This is called the *strong confinement regime*. In the strong confinement ($a<a_B$) limit the confinement potential prevents the uncoupling of exciton and relative electron-hole motion. In other words, in sufficiently small QDs the $1/a^2$ dependence of eigenvalues dominates the Coulomb interaction ($\propto 1/a$). Electron and hole can be thus considered independently, and the two-particle Schrödinger equation becomes:

$$\left(-\frac{\hbar^2}{2m_e^*}\Delta_e - \frac{\hbar^2}{2m_h^*}\Delta_h - \frac{e^2}{\epsilon|\mathbf{r_e}-\mathbf{r_h}|}\Delta_e + V(\mathbf{r_e}) + V(\mathbf{r_h})\right) F(\mathbf{r_e},\mathbf{r_h}) = EF(\mathbf{r_e},\mathbf{r_h}) \qquad \text{(Eq. 2.25)}$$

The eigenvalues of electron and hole are similar to those of Eq. 2.24, with a first order correction due to the Coulomb interaction:

$$F(\mathbf{r_e},\mathbf{r_h}) = F_e(\mathbf{r_e})F_h(\mathbf{r_h}) = C\left(\frac{j_{l_e}(k_{n_e,l_e},r_e)Y_{l_e}^{m_e}}{r_e}\right)\left(\frac{j_{l_h}(k_{n_h,l_h},r_h)Y_{l_h}^{m_h}}{r_h}\right)$$

$$E_{n_e,l_e,n_h,l_h} = \frac{\hbar^2}{2a^2}\left(\frac{\alpha_{n_e,l_e}^2}{m_e^*} + \frac{\alpha_{n_h,l_h}^2}{m_h^*}\right) - C\frac{e^2}{a\epsilon}. \qquad \text{(Eq. 2.26)}$$

In the strong confinement regime the eigenvalues are quantized, with three quantum numbers per charge carrier. The eigenstates are labeled by the quantum numbers n_hl_h-n_el_e. Each level is

shifted in energy by a factor $\propto 1/a$, due to the Coulomb interaction. For example, the lowest pair state is written as $1S_h$-$1S_e$ and is shifted by a Coulomb term $\propto 1.8\frac{e^2}{a\epsilon}$.

2.4 Effect of Quantum Confinement on optical properties of QDs

In light of what presented in the previous section, there are several radical effects of quantum confinement on the linear and non-linear optical properties of QDs:

- Eq. 2.24 and 2.26 point out that as the confinement is increased, the band-gap is also increased. The same trend is expected for absorption and emission peaks.
- The oscillator strength is increased, compared to bulk semiconductors. Energy states are squeezed in Dirac's deltas, fostering also the enhancement of non-linear properties.
- New intra-band NIR transitions may be permitted, between sub-bands with their different quantum numbers. Electrons and holes are now subject also to transitions from one sub-band to the other, without changing any component of its quasi-momentum.
- The exciton (and multi-exciton) binding energy E_X is also increased with respect to typical Wannier-Mott excitons in bulk solids. This makes excitons stable also at RT. However, a non-monotonic increase with decreasing size is expected, since the low dimensionality boosts also the charge tunneling into the potential barrier.

By evaluation of the transition dipole matrix element $|\langle \Psi_{\mathbf{K}} | \mathbf{e} \cdot \hat{\mathbf{p}} | 0 \rangle|^2$, where $\Psi_{\mathbf{K}}$ is calculated by using Eq. 2.18, 2.19 and 2.24, the probability of an optical transition from the ground state and selection rules (Δn = 0, Δl =0) are obtained. However, in order to explain many other aspects of QD photo-physics, such as Stokes shift and the exciton fine structure, some constraints employed in the *particle-in-a-sphere model* have to be relaxed. For example, the richness of the electronic structure has to be taken in account when dealing with the complex band structure of II-VI and III-V semiconductors.

Among all materials, CdSe QDs are considered as an archetypal system and have been deeply investigated both from a theoretical and an experimental point of view.
In Figure 2.7 the band-structure of CdSe is presented.

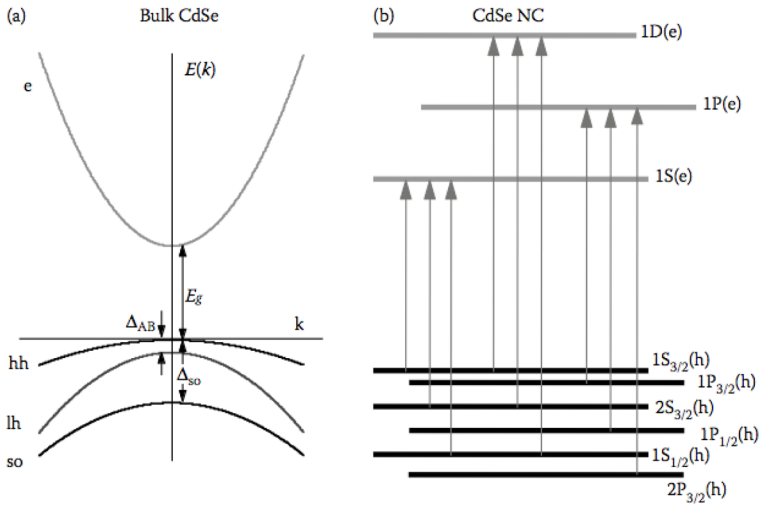

Figure 2.7: (a) Conduction- and valence-band structures near the Brillouin-zone center in CdSe. The valence band is composed of heavy (hh), light (lh), and spin–orbit split-off (so) sub-bands. (b) In the case of NCs, quantum confinement leads to mixing between different valence sub-bands, which produces a complex structure of hole quantized states. Arrows correspond to allowed interband optical transitions. Adapted from Ref. [92].

The conduction band arises from Cd 5s orbitals, is 2-fold degenerate at k = 0 and can be fairly described by a parabolic effective mass dispersion. Complications emerge when looking at the valence band, which originates from the Se 4p orbitals. The 6-fold degeneracy determines a rich valence band sub-structure, leading to a divergence between real and calculated excitonic structure. The strong spin orbit coupling Δ_{so} = 0.42 eV splits the VB degeneracy in $p_{3/2}$ and $p_{1/2}$ at **k** = 0 and away from this point the $p_{3/2}$ is further split into light-hole (LH) and heavy-hole (HH) bands, also called B and A band, respectively. In wurtzite lattices, the crystal field lifts the degeneracy of the LH and HH bands also **k**=0. However, such splitting is only Δ_{AB} = 25 meV and thus typically neglected.

From a computational point of view, the *k·p* pertubative approach, using Luttinger Hamiltonian at k = 0 or Kane model[3], leads to a sufficiently accurate description of the band structure. In order to calculate the excitonic structure, mixing between the valence sub-bands has to be taken into account. The total angular momentum of electrons F_e and holes F_h has both a unit cell contribution J and an envelope function contribution L; for hole states combination of Luttinger Hamiltonian and spherical potential yields a non-conservation of J_h and L_h. The resulting hole states are a mixture of the three valence sub-bands and envelope function with angular momentum L_h and L_h + 2. These effects are referred as *valence band mixing* and *S-D mixing*. The VB states are usually denoted as nL_F (Figure 2.7), where L is the lower of the two total momenta involved in the envelope function, F is the total angular momentum, and n is the number of the state of given symmetry.

Further complications in CdSe QD excitonic structure comes out on relaxing the spherical shape and cubic lattice approximations. In fact within this approximation the band edge exciton

$1S_{3/2}1S_e$ is eightfold degenerate, due to 2-fold spin degeneracy of the first electron quantum confined level and 4-fold total angular momentum degeneracy of the first hole quantum confined level. Lifting of this degeneracy is ascribed not only to non-spherical shape of the dot, but also to hexagonal lattice symmetry[i] and electron-hole exchange interaction. The resulting excitonic structure is usually referred to as *exciton fine structure*, and is schematically represented in Figure 2.8.

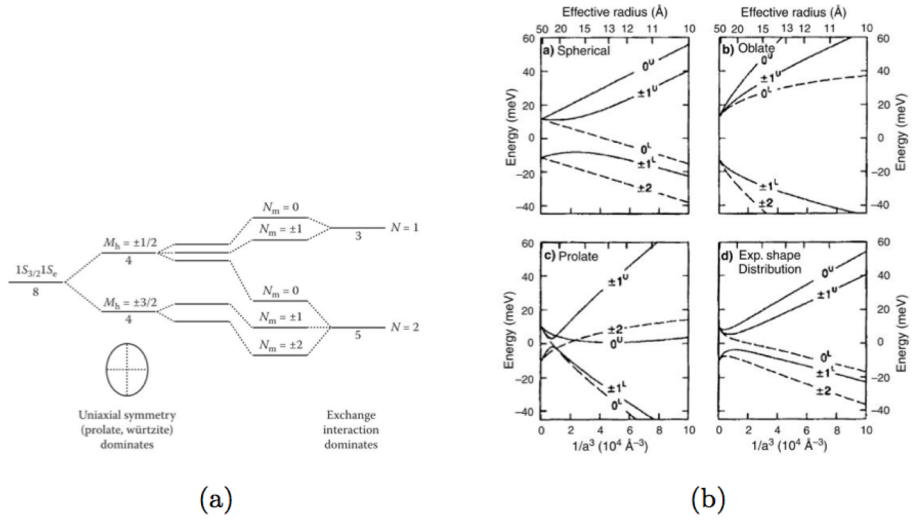

Figure 2.8: (a) Energy-level diagram describing the exciton fine structure. The eightfold degeneracy is split in two fourfold degenerate states by the non-spherical shape of the dots. The hexagonal (wurtzite) lattice and the exchange interaction lead to 5 states: $N_m^u = 0$, $N_m^u = \pm 1$, $N_m^l = 0$, $N_m^l = \pm 1$ and $N_m^l = \pm 2$. $N_m^u = 0$ and $N_m^l = \pm 2$ are dark states. (b) Calculated band-edge exciton structure versus effective radius, for different dot shapes. Adapted from Ref. [93].

The largest contribution to Stokes shift in QDs is due to the energy difference between optical transitions that correspond to the 1U and 0U strong absorbing states and the lower energy 1L and 2 emitting states.

Enhanced Coulomb interaction, due to confinement, affects not only the energetics of QD excitations, but also their characteristic lifetimes. Exciton generation and recombination dynamics diverge from bulk semiconductor behavior illustrated in Section 2.1.

The main difference in II-VI QDs with respect to their bulk counterparts comes from the level spacing, especially for the electron levels: energy separation between states in QDs is larger than typical phonon quanta and multi-phonon relaxation mechanism are hindered, in favor of Auger recombination. Klimov *et al.* demonstrated that AR, *i.e* scattering of electron by a hole, is responsible for the fast hot-electron or intraband relaxation in CdSe QDs. Due to the density of the valence band states, many hole transitions are in resonance with the electron intraband

[i] There are three known CdSe allotropes: the most stable phase is the hexagonal wurtzite, however QDs with zinc blende structure can be synthesized[53]. At high pressures also CdSe with cubic rock salt can be isolated.

transitions. AR interband relaxation is also possible and is one of the main non-radiative paths for exciton recombination. This poses an intrinsic drawback to the application of QDs in light emitting and power conversion applications. While in bulk semiconductors AR is poorly efficient, AR rate increases with decreasing size due to the relaxation of the momentum conservation constrain due to loss of spatial periodicity. Furthermore, strong carrier-carrier interaction affects also multi-exciton decays. The multi-exciton non-radiative AR mechanism is based on release of e-h recombination energy as kinetic energy of a third photoexcited carrier present in the NC. As summarized in Figure 2.4, in bulk solids AR is a three-particle, cubic process, decribed by[3]

$$\frac{dn}{dt} = -Cn^3 \qquad \text{(Eq. 2.27)}$$

where n represents the carrier concentration and C is the Auger constant. If the carrier density is expressed in terms of average exciton concentration per dot ($\langle N \rangle / V_{QD}$) and Poisson distribution of occupancies of multi-exciton states is considered, it is possible to demonstrate that AR scales as $\tau_N^{-1} \sim \frac{CN^3}{V_{QD}^2}$. This cubic proportionality between the Auger rate versus the number of excitons per dot makes AR much faster than the multi-exciton radiative recombination rate. Moreover, due quantum confinement effects the Auger constant C becomes proportional to the volume, thus leading to $\tau_N^{-1} \sim \frac{N^3}{V_{QD}}$,[94] *i.e.* at decreasing QD volume the Auger rate increases.

Such occurrence represents one of the toughest hurdles to overcome for efficient multi-exciton light emission, essential for optical gain applications[3].

As stated before, AR is efficient also in the single exciton regime and its rate is of the order of the radiative rate. Excitons in this case can be scattered by free carriers, which are located at QD core lattice defects or surface trap states (uncoordinated sites). This explains why, in general, charged excitons or *trions*, *i.e.* excitons interacting with free charges, exhibit a high recombination rate[95]. However, trapped charges, as for bulk semiconductors, can also radiatively recombine, leading to a secondary emission peak, typically with weaker intensity with respect to the intrinsic emission[96]. Alternatively, they can be re-excited and reestablish the intrinsic exciton, with the effect of slowing down the recombination process[33,97].

Another process, which is strictly related to the strong carrier-carrier interaction, is carrier multiplication (CM)[98]. Such process, which is the inverse of AR, has been observed in many QD materials, and may be exploited for solar power conversion. Namely, in CM a hot electron can relax to lower energy sub-bands by scattering with a VB electron, promoting the formation of a second exciton in the dot.

In conclusion, quantum confinement effects strongly modify the optical response of semiconductors. In order to expand the application of QDs in light emitting and power

conversion, issues such as AR and charge-trapping need to be circumvented. This can be done by a careful design and synthesis of the nanostructure. In order to tune exciton fine-structure and ensuing optical properties two strategies may be employed: the dot size can be varied or a suitable shell can be grown onto the dot. The latter strategy is the most promising, since it allows the preservation of low dimensionality and is based the control of the exciton dynamics (AR, MEG, MEG, CM) by the wave function engineering.

2.5 QDs as optical gain materials

The theoretical origin of LASER (Light Amplification by Stimulated Emission of Radiation) is commonly assigned to A. Einstein's predictions, in 1917. In his phenomenological dissertation[99] about the interaction between matter and radiation, he demonstrated that this interaction could be explained only in terms of three processes: stimulated absorption, spontaneous emission and stimulated emission. The existence of the latter opened to the possibility to generate amplification of light (*optical gain*) if a sufficient *population inversion* is created in an excited state of the medium.

Laser light emission from a GaAs semiconductor laser diode was demonstrated by Robert N. Hall and Marshall Nathan[100] in 1962, only two years after that Theodore H. Maiman invented the first laser system. During the 50 years long evolution of semiconductor lasers, lots of experimentations have been conducted with the purpose of improving the quality of the coherent light generated, and their success opened the door for the application of these lasers in many commercial devices we daily work with. These devices spans across the following range of applications:

- data recording and reading on CD-ROMs, DVDs, Blu-ray Discs, and holographic data storage media;
- data transmitters in optical fiber communications;
- low power semiconductor used for laser pointers, laser printers, scanners, bar code-readers and for distance measurements;
- surgical and dermatological therapies, optical imaging;
- Pump for secondary lasers

and, of course, in many fields of the scientific research.

Much of the merit of this success is due to properties of the semiconducting gain media, which, coupled with a precise design of the optical cavity, guarantee generally the next linear combination of advantages:

- possibility of bandwidth and wavelength modulation (from IR to visible);
- suitability for both pulsed (mode-locking) and continuous light generation;

- high power conversion efficiency.

Materials adopted as active media, since the beginning, consisted of direct-bandgap inorganic semiconductors (GaAs, AlGaAs, InGaAs, GaN, SiC, InP…). In the course of decades the progress in the field of semiconductor gain media moved towards many directions, in order to fulfill the huge variety of application requests.

The gain regime in a semiconductor medium is usually achieved creating a high carrier density in the conduction band. For a quantitative treatment of the optical response of the semiconductor to light stimulation, Fermi–Dirac distributions for electrons in both valence and conduction band should be considered (Eq. 2.6). In a nutshell, optical gain is obtained when the number of electrons excited in the CB exceeds a threshold value N_{th}, called the transparency threshold.

Among the different research lines undertaken, the development of quantum-confined structures has turn out to be the right choice for both the enhancement of the lasing performances and the implementation in compact resonant microcavities[101]. Thanks to the quantum confinement, quantum well and quantum dot based devices offer improvements in lasing threshold, temperature insensitivity (thanks to the greater spacing between discrete electronic states) and modulation bandwidth. Main achievements in lasing have been obtained by means of epitaxially grown nanostructures[102]. However, in 2000 Klimov group demonstrated that optical gain could be obtained also by using colloidal CdSe QDs, stimulating the interest of many other groups to continue down this path. Since the active volume provided by a single quantum dot is extremely small, a large ensemble of QDs has to be used. Colloidal QD lasing media have been prepared as close-packed films[49] or incorporated into polymers or sol-gel matrices[14,43,44].

As pointed out in the previous section, the excitonic origin of QDs optical properties has to be taken in account. In a simplified two-level system, population inversion (gain) begins when the number of excitons per dot is N_{eh} = 1 with gain saturation (complete population inversion) at N_{eh} = 2. A general overview of the effect of absorption and emission processes in a QD is schematically presented in Figure 2.9.

In a more realistic picture, under photon excitation an average number of carriers per dot $<N_{eh}>$ are pumped in the semi-continuum region, from where they thermally decay to the lowest excited state. Coulomb interaction between two excitons in the same dot leads to a shift E_{XX} of the exciton energy levels (Figure 2.10), defined as *bi-exciton binding energy*. This interaction, enhanced by the quantum confinement, can be either attractive or repulsive, and consequently the emission due to the $\hbar\omega_{xx}$ transition will be shifted with respect to the photoluminescence with photon energy $\hbar\omega_x$. The radiative emission $\hbar\omega_{xx}$ from the bi-excitonic state is then responsible for optical gain generation.

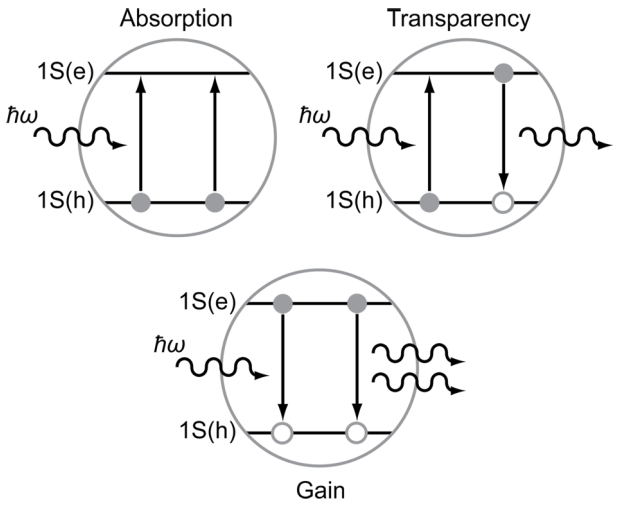

Figure 2.9: Schematic representation of the absorption, transparency and optical gain regimes for an ideal two-level QD system.

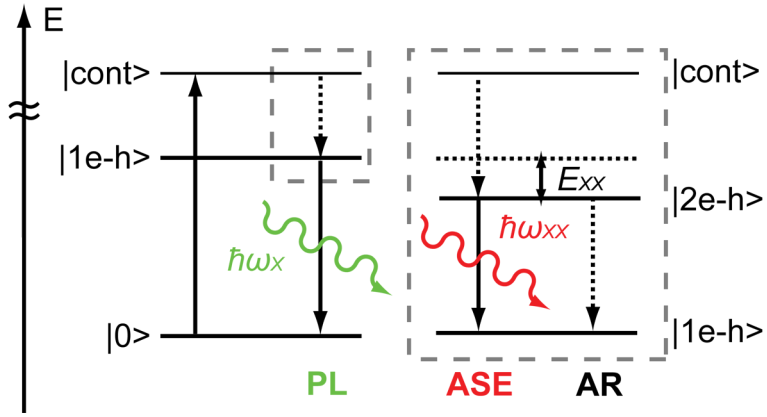

Figure 2.10: Diagram representing the main mechanisms responsible for the exciton and multi-exciton relaxation. Dotted arrows represent a non-radiative decay process. After a QD is excited to the continuum, the system typically relaxes to the bi-exciton state through Auger Recombination (AR) and thermalization. The bi-exciton can recombine radiatively, leading to the emission of a photon with energy $\hbar\omega_{xx} < \hbar\omega_x$, due to the bi-exciton binding energy. Thanks to this energy shift, $\hbar\omega_{xx}$ photons are not re-absorbed by the system and are responsible for the Amplified Spontaneous Emission (ASE). Afterwards, the remaining exciton recombines with the emission of a $\hbar\omega_x$ photon. The ASE process has to compete with the bi-exciton AR, in which an exciton can transfer its energy to a charge carrier.

The energy structure illustrated in Figure 2.10 can be interpreted as a sort of "four-level system"; in such configuration a population inversion from the single-exciton ground state to the upper bi-exciton ground state, necessary for reaching the transparency condition, can be achieved and thus the emission can be amplified. The emission from the bi-excitonic ground state with energy $E_{1S(e)-1S3/2(h)} \pm E_{XX}$ is called Amplified Spontaneous Emission (ASE) and its activation corresponds with the optical gain threshold.

The main obstacle to efficient optical gain in colloidal QDs is represented by AR. The lifetime of the optical gain is intrinsically limited by AR, since Eq. 2.27 states that AR rate is proportional to N^3 and $V_{QD}{}^{-3}$.[94] Due to the strong Coulomb interaction, multi-excitons tend to relax non-

radiatively by exciting a secondary excited charge. Furthermore, another potential complication associated with the realization of the optical-gain regime in semiconductor NC, arises from a second competing phenomenon, which is *excited-state absorption* (ESA), (a.k.a. PA, *photoinduced absorption*)[103]. In this case the stimulated absorption occurs also from the exciton states, slowing down or preventing the creation of the transparency condition. The efficiency of the PA increases in presence of free charges, typically trapped at uncoordinated surface sites.

To overcome the complications connected with both AR and PA, the inorganic coverage of the QDs surface with a different semiconductor demonstrated to be the right treatment. The demonstrated reduction of the AR rate in CdSe/CdS core-shell QDs, coupled with the suppression of PA offered by embedding nanocrystals in a suitable matrix, suggested that such composite systems should be suitable for optical gain applications[104]. Best results were obtained by means of graded core-shell heterostructures, such as CdSe-CdS/$Cd_XZn_{1-X}S$/ZnS core- graded shell QDs [44,49]. As mentioned in the Introduction, gain and light emitting performances in general are boosted in such nano-heterostructures: going from the CdSe core to the ZnS shell the lattice parameter is gradually varied, thus limiting the creation of abrupt or defective interfaces, which would enhance both PA and AR. It was also demonstrated, both from a theoretical[46] and an experimental[40] point of view, that the smoothest the potential barrier, the slowest the rate of AR is. At the same time, maintaining the type-I configuration, the energy gap is also progressively increased from core to shell, thus protecting excitons from interaction with the majority of traps located at the outmost surface.

Chapter 3.

Experimental Techniques

In this chapter the main optical spectroscopy techniques employed in this work are presented. Some theoretical fundamentals and experimental setup for each technique are provided, with an eye to the relevant information that can be extracted from the QD and core-shell QD samples. Sections 3.1 and 3.2 deal with the conventional steady-state absorption and PL techniques. In section 3.2 PL QY determination methods employed in this work are also illustrated. In Section 3.3, after a brief review of Raman scattering and SERS basics, the discussion focuses on how Raman technique can be applied as a local probe for core-shell QDs characterization. Sections 3.4 and 3.5 describe the tPL and TA experimental details, with some remarks on the approaches that have been selected for data analysis. At last, in Section 3.6 the ASE setup for optical gain characterization is presented.

3.1 Steady-state linear absorption

UV-Vis linear absorption measurements were performed using a *Varian Cary-5* spectrometer. Absorption spectra of QDs in solution and embedded in sol-gel films have been collected. From the absorption spectrum exciton transitions, whose nature has been described in the previous chapter, are identified. The size dependence of the exciton states is also verified. Furthermore, the absorption spectra provide also some quantitative information, such as the average dimensions of the QD dispersion and molar extinction coefficients. These quantities can be extracted by examining the spectral position and full-width half maximum of the band-edge exaction state[105].

3.2 Steady-state PL: QY determination

PL spectra from QD colloidal dispersions in 1 cm quartz cuvettes and films have been carried out by using a *Horiba Jobin-Yvon* fluorometer. As illustrated in Chapter 2, PL in QDs is the effect of exciton recombination. Kasha's rule is valid also for QDs, i.e. light emission occurs only from the lowest energy exciton states (N_m = 1L and 2, see Figure 2.8). The full-width at half maximum

(FWHM) of emission spectra depends mainly on size-dispersion, and for colloidal QDs it is typically ~ 100 meV or lower.

One parameter of crucial importance for light emitting materials is the PL QY, which defines the ratio between absorbed and emitted photons. PL QY is related radiative and non-radiative relaxation rate constants k_r and k_{nr} by the relation

$$QY = \frac{k_r}{k_r + k_{nr}}. \qquad \text{(Eq. 3.1)}$$

Eq. 3.1 thus states that, if non-radiative recombination paths are present, QY value is less than unity. Despite such a straightforward relation, interpretation of PL QY in colloidal QDs can be tricky, due to the several factors that can enhance the non-radiative rate: surface-trap interaction, Auger mechanism, inter-dot energy transfer, etc[39]. Moreover, trap states are spread in energy, so depending on the exciting energy a different amount and different trap distributions can be excited. This makes QY also excitation energy dependent[106]. In addition, different dots in a colloidal dispersion may exhibit different emission efficiencies, so the global QY is actually an average of the ensemble. A further complication comes also from the PL blinking effect, which makes the single dot QY randomly intermittent[37].

In this work, PL QY of QD colloidal dispersions in toluene have been calculated, using the relative method introduced by Vavilov in 1924 and reported in many reviews[107,108]. With this method the QY of the sample is calculated relative to reference fluorescent standards with known QY.

The expression here employed comes from the original Vavilov relation:

$$QY_x = QY_{ref}\left(\frac{K_{ref}}{K_x}\right)\left(\frac{D_x}{D_{ref}}\right)\left(\frac{n_x}{n_{ref}}\right)^2 \qquad \text{(Eq. 3.2)}$$

where the subscript *x* (*ref*) stands for the sample (reference standard). *K* accounts for the averaged response of the detector to the emission spectrum, *D* is the detector response and *n* the refractive index of the solution. The explicit relation here employed is:

$$QY_x = QY_{ref}\left(\frac{A_{ref}(\lambda_{ref})}{A_x(\lambda_x)}\right)\left(\frac{I(\lambda_{ref})}{I(\lambda_x)}\right)\left(\frac{D_x}{D_{ref}}\right)\left(\frac{n_x}{n_{ref}}\right)^2 \qquad \text{(Eq. 3.3)}$$

where *I(λ)* is the relative intensity of the exciting light at wavelength λ, *n* is the average refractive index of the solution, *D* is the integrated area under the corrected emission spectrum and *A(λ)* is the absorbance of the solution at the exciting wavelength λ.

Eq. (3.2) is valid if many assumptions are satisfied: the integrated PL intensity is assumed to be proportional to the fraction of absorbed light, all geometrical factors to be identical, the excitation beams to be monochromatic, internal reflection effects to be the same, reabsorption and reemission to be negligible and the emission to be isotropic.

In order to minimize errors, some cautions can be taken. First of all, a maximum absorbance of 0.15 is used for the solutions, in order to minimize the reabsorption effects. Moreover, both solutions are prepared to have similar absorbance at the excitation wavelength: by this way the attenuation of the excitation source along the optical path in the cuvette is analogous in both cases and the number of the excited molecules can be considered similar. To account for the reabsorption of the excitation beam, we consider that the number of absorbed photons is proportional to $(1\text{-}10^{-AL/2})$ instead of AL. L is the optical path of the cuvette and $L/2$ is the thickness across the excited sample. Also the emitted photon can be reabsorbed from the solutions, and we use the Lambert-Beer law to take in account this correction. We consider that the spectrometer measures an apparent corrected emission spectrum of the sample $F_a(\nu)$, which is not the same as the molecular emission spectrum $F(\nu)$. From Beer's law $F_a(\nu)$ and $F(\nu)$ are related by: $F_a(\nu) = F(\nu)10^{-AL/2}$.

These two factors induce a correction of about 5-10% for absorbance lower than 0.2.

3.3 Raman Spectroscopy

Raman spectroscopy is a technique that relies on *Raman effect* or inelastic scattering of an incident monochromatic laser beam, first observed by Raman and Krishnan in 1928[109].

In a Raman spectroscopy experiment the sample is irradiated with a monochromatic beam (typically a continuous wave or CW laser) with frequency ν_L and the diffused light is measured at a defined angle θ with respect to the incident beam direction. The light diffused at the same frequency as the incident radiation is called elastic Rayleigh scattering, while the one at a different frequency is called inelastic Raman scattering. The energy difference between incident and inelastically scattered photons is resonant with a vibrational or rotational mode of the system, which can be in solid, liquid or gaseous state. By contrast with IR absorption spectroscopy, a variation of the polarizability of the molecule with respect to the vibrational motion is responsible for the Raman effect. Light interacts with the polarizability generating an *induced dipole moment*. The radiation scattered by the induced dipole moment is responsible for both Rayleigh and Raman scattering.

As illustrated in Figure 3.1, from an energetic point of view the Raman scattering phenomenon can be divided into two different cases.

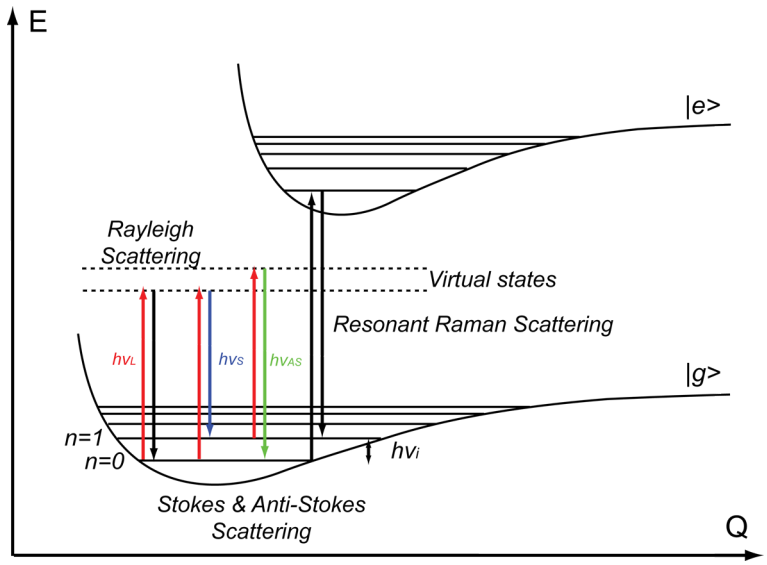

Figure 3.1: Energy level diagram for a generic molecular system, representing four scattering processes: elastic (Rayleigh) Scattering, inelastic (Raman) Stokes and anti-Stokes and resonant Raman Scattering.

Depending on whether incident photons cause transition of a molecule to an *excited virtual state* from its vibrational ground or first- excited state (n = 0 or n = 1), the Raman signal appears shifted to lower or higher energies than the excitation one, respectively. The first case with $\nu_S = \nu_L - \nu_i$, is called *Stokes Raman scattering*, where ν_i is the molecule's vibrational frequency. The second one, where $\nu_S = \nu_L + \nu_i$, is called *anti-Stokes Raman scattering*.

The fundamentals of Raman scattering presented so far can be easily extracted from a classical physics approach. In the zeroth-order approximation, the case of a dilute molecular system (with negligible inter-molecular interactions) is considered. If the system is excited through a monochromatic light with electric field

$$\mathbf{E}(t) = \mathbf{E_0} cos(2\pi\nu_L t) \qquad \text{(Eq. 3.4)}$$

the *induced electric dipole moment* or *molecular polarization* is expressed by

$$\boldsymbol{\mu}(t) = \hat{\alpha}\mathbf{E} = \hat{\alpha}\mathbf{E_0} cos(2\pi\nu_L t). \qquad \text{(Eq. 3.5)}$$

The polarizability tensor $\hat{\alpha}$ is a function of the instantaneous position of the atomic nuclei in the molecular system and oscillates in time because of molecular vibrations.

For small displacements from the nuclear equilibrium position, every single $\alpha_{m,n}$ element of the $\hat{\alpha}$ tensor can be expanded through a Taylor series near the equilibrium nuclear position. For small displacements, considering only the first-order term, the tensor elements are expressed as

$$\alpha_{n,m} = \alpha^0_{m,n} + \sum_i \left(\frac{\partial \alpha_{n,m}}{\partial Q_i}\right) Q_i \qquad \text{(Eq. 3.6)}$$

with $\alpha^0_{m,n}$ representing the tensor elements at equilibrium position and

$$Q_i = Q_{i0}\cos(2\pi\nu_i t) \qquad \text{(Eq. 3.7)}$$

the vibration mode coordinate with amplitude Q_{i0} and frequency ν_i.
Finally, by applying a prosthaphaeresis formula the molecular polarization can be rewritten in terms of the oscillating polarizability:

$$\boldsymbol{\mu}(t) = \alpha^0_{m,n}\mathbf{E_0}cos(2\pi\nu_L t) + \\ +\frac{1}{2}\sum_i\left(\frac{\partial\alpha_{n,m}}{\partial Q_i}\right)_0 Q_{i0}[cos(2\pi(\nu_L+\nu_i)t) + cos(2\pi(\nu_L-\nu_i)t)]. \qquad \text{(Eq. 3.8)}$$

This oscillating dipole moment becomes source of electromagnetic radiation with frequencies ν_L (Rayleigh scattering), $\nu_{AS} = \nu_L + \nu_i$ (anti-Stokes Raman Scattering) and $\nu_S = \nu_L - \nu_i$ (Stokes Raman Scattering). Raman scattering occur only when

$$\left(\frac{\partial\alpha_{n,m}}{\partial Q_i}\right)_0 \neq 0, \qquad \text{(Eq. 3.9)}$$

which is the principal selection rule for Raman active modes.

Given the oscillating electric dipole, the power density emitted by each scattering contribute can be calculated. The following proportionalities are found:

$$\sigma_R \propto \alpha_0^2\omega_L^4 \qquad \text{Rayleigh}$$
$$\sigma_{AS} \propto \left(\frac{\partial\alpha_{n,m}}{\partial Q_i}\right)_0^2 Q_{i0}(\omega_L+\omega_i)^4 \qquad \text{anti-Stokes}$$
$$\sigma_S \propto \left(\frac{\partial\alpha_{n,m}}{\partial Q_i}\right)_0^2 Q_{i0}(\omega_L-\omega_i)^4. \qquad \text{Stokes} \qquad \text{(Eq. 3.10)}$$

From Eq. 3.10 it is clear that Raman scattering is much weaker compared to Rayleigh, since Raman cross-section depends only on the squared derivative of the polarizability, while Rayleigh depends on α_0^2. For traditional Raman scattering, the ratio between the Rayleigh and Raman scattered photons is about 10^6.
Comparing the Stokes and anti-Stokes processes, anti-Stokes is generally less intense. Looking at Figure 3.1, at RT only a small fraction of molecules is in an excited vibrational state. From FGR, the ratio between corresponding anti-Stokes and Stokes band intensities is:

$$\frac{I_{AS}}{I_S} = \left(\frac{\omega_L+\omega_i}{\omega_L-\omega_i}\right)^4 e^{-\frac{\hbar\omega_i}{k_B T}} \qquad \text{(Eq. 3.11)}$$

Finally, an example of Raman spectrum is reported in Figure 3.2.

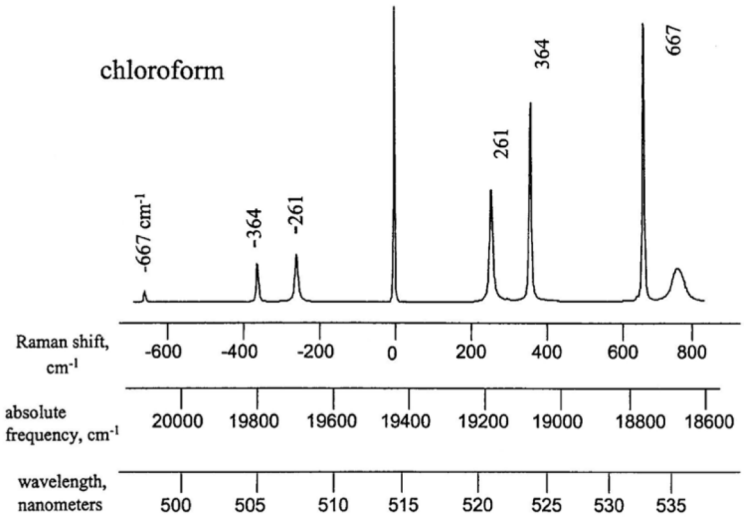

Figure 3.2: Raman spectrum of liquid chloroform at RT. The peak at 0 Raman shift is the attenuated elastic scattering of the 514.5 argon laser line.

Conveniently, in a Raman spectrum the energy of scattered photons is reported in *Raman-shift* $(\Delta\tilde{\nu})$ unities:

$$\Delta\tilde{\nu} = \tilde{\nu}_L - \tilde{\nu}_S = \frac{1}{\lambda_L} - \frac{1}{\lambda_S} = [cm^{-1}] \qquad \text{(Eq. 3.12)}$$

3.3.1 Resonant Raman Scattering

Raman cross-section can be increased if the incident laser light energy is close to a molecular electronic transition. This can be demonstrated by expressing the Raman (Stokes) component of the polarizability with a quantum mechanical approach. The resonant Stokes Raman cross-section becomes

$$\sigma_S(\omega) \propto \frac{\left(\langle g_1|\hat{\mu}_{ge}|e_n\rangle\langle e_n|\hat{\mu}_{eg}|g_0\rangle\right)^2}{\left(\omega_{eg}-\omega\right)^2+{\Gamma_e}^2}\omega^4, \qquad \text{(Eq. 3.13)}$$

where $\omega_{eg} = 1/\hbar(E_e - E_g)$ is the resonance frequency of the electronic transition, Γ_e is the transition damping factor and the two matrix elements represent the dipole momentum of transition from the intermediate state e_n to the final vibrational state g_1, and from the starting ground state g_0 to e_n. From Eq. 3.13 it is clear that scattering cross section rises of several orders of magnitude in resonance conditions, i.e. when $\omega = \omega_L \approx \omega_{eg}$. The main drawback in resonant Raman technique is the increase of the PL emission, which is much intense and wider than Raman features (hundreds versus few cm^{-1}, respectively) and it may hamper the quantitative interpretation of Raman spectra.

3.3.2 Raman Scattering in solid crystals

When dealing with solid-state materials, Raman scattering is due to the inelastic scattering of an electromagnetic wave by low frequency crystal lattice deformations. Such deformations are typically represented as *phonons*, *i.e.* quasi-particles that stand for quanta of oscillation in a crystal lattice[88]. In the case of molecular crystals the two processes coexist, since at higher energies the Raman bands corresponding to *internal molecular vibrations* are observed, while at lower energies the Brillouin scattering by *external lattice vibrations* or phonons is detected.

Raman scattering in solid crystals is interpreted in terms of the electrical susceptibility tensor $\hat{\chi}$, which is the macroscopic counterpart of the molecular $\hat{\alpha}$ tensor. Eq. 3.5-3.10 can be readapted by switching α with χ. The Raman tensor and relative selection rule from Eq. 3.9 become

$$\left(\frac{\partial \chi_{n,m}}{\partial Q_i}\right)_0 \neq 0 \qquad \text{(Eq. 3.14)}$$

and the index i runs over all the coordinates that describe the vibrations of the N atoms in the unit cell. Depending on the class of material, in a solid there can be both *acoustic and optical phonon modes*. Metals are typically primitive, face- or body-centered cubic systems with one atom per unit cell. This is why they display only three acoustic modes (one LA, longitudinal acoustic mode and two TA, transverse acoustic modes). Diamond-, zinc blende- and wurtzite-like lattices, typical for semiconductors, have two atoms per unit cell; hence they exhibit also three optical modes (one LO, longitudinal optical mode and two TO, transverse optical modes). Modes are longitudinally (or transversally) polarized if the atomic oscillations are parallel (or perpendicular) to the wave vector. Figure 3.3 illustrates the phonon dispersions (phonon branches) for the first Brillouin zone of a 2-atoms per cell inorganic semiconductor.

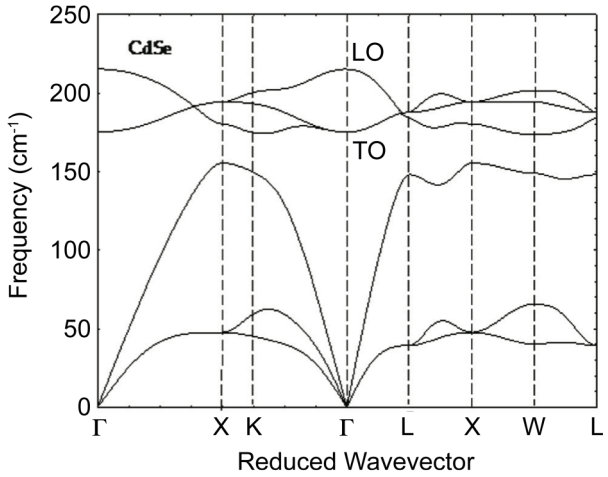

Figure 3.3: Phonon dispersions for the first Brillouin zone of CdSe (wurtzite).

A stringent selection rule for Raman scattering in crystals is the conservation of total momentum (in addition to the energy conservation):

$$\hbar\mathbf{k_L} = \hbar\mathbf{k_S} \pm \hbar\mathbf{q} \qquad \text{(Eq. 3.15)}$$

Since the exciting beam in Raman experiments is in the visible range, the relative $\mathbf{k_L}$ is of the order of 10^5 cm^{-1}. The extension of the first Brillouin zone is 10^8 cm^{-1}, therefore Raman technique allows to study only phonons with $\mathbf{q} \sim 0$, *i.e* in the zone center.

3.3.3 Surface Enhanced Raman Scattering (SERS)

Raman scattering cross sections can be increased more than ten orders of magnitude when the analyte is in proximity to a suitable metal surface. The discovery of the phenomenon dates back to the 70's of the last century[110–112]. Such enhancement is the result of the excitation of *surface plasmons*, which strongly increase the local field felt by the molecules close to the metal surface. The SERS phenomenon is typically observed when the plasmonic substrate is made of colloidal metal nanoparticles or nanostructured metal surfaces, where *localized surface plasmon (LSP) resonance* occurs. Without entering much in the details of the origins of LSPs, they are defined as discrete oscillation modes of the electron density and they are localized since the exciting λ is comparable with the physical dimensions of the nanostructure. In a nutshell, the nature of this kind of electromagnetic modes is explained by considering the problem of a metallic sphere with diameter comparable (dynamic regime) or shorter (quasistatic regime) than the λ of an interacting electromagnetic field, described by Mie[113] in 1908. For the quasistatic regime[114], whose scattered field is that of an electric dipole and is, therefore, radiative, the electric field inside the dot is proportional to the incident electric field amplitude by

$$E_{sph} = \frac{3\varepsilon_d}{\varepsilon(\omega)+2\varepsilon_d} E_0. \qquad \text{(Eq. 3.16)}$$

When $\varepsilon(\omega) = -2\varepsilon_d$, where $\varepsilon(\omega)$ and ε_d represent the dielectric function for the material and the surrounding medium, respectively, a resonance condition is obtained and E_{sph} becomes very large. This condition is possible for metals if the absorption is small, *i.e.* $Im(\varepsilon(\omega)) \approx 0$), and $Re\big(\varepsilon(\omega)\big) = -2\varepsilon_d$. The optical response (absorption and scattering) at this particular frequency is then very large and is called *localized surface plasmon resonance*. As can be observed, this resonance conditions are strongly linked to the metal, the geometry and the dielectric environment.

Not all the metals support plasmon resonances in the visible or NIR region, which is of interest for Raman experiments: silver and gold are the most commonly used, but also copper, aluminum, indium and platinum nanostructures can be employed to enhance the local field.

The enhancement is expressed in terms of the *enhancement factor*

$$EF = \frac{P_{SERS}}{P_{RAMAN}} \qquad \text{(Eq. 3.17)}$$

where P_{SERS} and P_{RAMAN} represent the power of the scattered radiation in presence and in absence of the enhancing material, respectively. Since the local field intensity decay very fast moving away from the nanostructure ($\propto d^{-10}$), crucial parameters to be controlled for maximizing EF are several: excitation λ, polarization and geometry, detection geometry, molecular orientation, absorption efficiency, concentration, distance from the metal surface, etc.

The electromagnetic origin of SERS dominates and accounts not only for the enhancement the local field but also for the enhancement of the scattered light, due to the modified dipole radiation. However, also a chemical enhancement contribution to EF exists, and is given by the interaction between the molecule and the excited surface plasmon oscillation, which can lead to an enhancement in the electronic polarizability of the sample[112]. This contribution is typically lower compared to the electromagnetic one (10^{10} versus 10^{2}) and very difficult to be discriminated.

3.3.4 Raman scattering of QDs

Raman technique can provide a lot of information about composition and structure of QDs. As for their bulk semiconductor counterparts, QDs exhibit optical phonon modes. It is well known from semiconductor physics that the energy of such modes can be modified by several factors. One of them is lattice strain, which can be very high at nanoscale, mainly due to the high surface tension[115]. Furthermore, in the case of epitaxial shell growth, lattice mismatch between core and shell is responsible for phonon band shifts. This makes Raman an alternative tool to monitor the evolution of the epitaxial growth on semiconductor nanostructures[41,53].

However, lattice strain is not the only source for the shift of Raman features. As demonstrated in Section 3.3.2, the conservation of momentum selection rule allows Raman scattering only from phonons in vicinity of the zone center. When the dimensions of the semiconducting material are in the nanoscale the wave vector is no more a good quantum number and the selection rule is relaxed. Therefore, also phonons with $\hbar\mathbf{q} \neq 0$ can inelastically scatter the incident photons. By observing Figure 3.3 and focusing on the represented typical energy dispersions of optical modes, peaked at $\mathbf{q} = 0$, a red-shift of the Raman band is expected as lower energy phonons also contribute to scattering. This phenomenon is typically described and quantified in terms of *phonon confinement*[116], and leads also to a band broadening.

Another effect, related to the high surface/volume ratio, is the appearance of *surface optical phonon modes*[117]; such modes are located at slightly lower energies compared to the optical modes and their integrated area is very sensitive to modifications of the surrounding medium. In the case of colloidal QDs, substantial variations of such bands occur if, for instance, the

passivating ligand is exchanged, a shell is grown on the core or ion interdiffusion occur between core and shell.

The main drawback encountered in a Raman scattering experiment on QDs is the unavoidable presence of PL, due to the high QY of QDs. Laser sources conventionally employed for Raman experiments are often in resonance with QDs absorption bands, further complicating the problem. Such problem can be circumvented by exciting at energies corresponding with non band-edge exciton transitions, where PL contribution is minimized and, at the same time, the Raman cross-section is increased by the resonance condition. If a suitable SERS substrate is employed, it is possible to further improve the signal, since the metal can quench the fluorescence and enhance the Raman cross-section.

Raman and SERS experiments on colloidal QDs have been performed on colloidal CdSe-$Cd_XZn_{1-x}S$, by means of a home-made Micro-Raman setup. The argon ion laser line with λ = 514.5 nm (Spectra Physics Stabilite 2017-output power 1W) was used as excitation light sources. The laser beam was coupled to a microscope (Olympus BX 40) and focused on the sample by a 50x objective (NA = 0.75, Olympus SLMPL). The back-scattered Raman signal was separated from the Rayleigh scattering by an edge filter and analyzed with a 320 mm focal length imaging spectrograph (TRIAX-320 ISA) and a liquid nitrogen cooled CCD camera (Spectrum One, JobinYvon). The typical spot diameter at the focus was between 1 and 3 μm. The CCD detector was calibrated using the optical longitudinal phonon of silicon, centered at 520 cm^{-1}.

3.3.5 SERRS of QDs

Raman spectroscopy is an important tool for the study of interfaces. It has already been used to study Se-CdSe multilayers,[118] CdTe-ZnTe heterojunctions[119] and, as mentioned above, CdSe-CdS core-shell QDs at very low temperature (*i.e.* 3 K).[53] In this work, Surface Enhanced Raman Spectroscopy (SERS) was employed. The main benefits of SERS in comparison to standard Raman spectroscopy have already been mentioned. In the case of SERS on QDs, the metallic substrate is also a quencher for the residual PL, thus increasing the quality of RT Raman spectra. The possibility to collect detailed Raman information at RT ensures the analysis of NCs with the same structural features, lattice dynamics and optical properties present when the QDs are employed as emitters in photonic devices. A high signal-to-noise ratio is obtained with very small laser power (<50 mW), thus avoiding heating damage.

In order to study the bulk and interfacial properties of CdSe and CdSe-$Cd_XZn_{01-X}S$ QDs, in this work Surface Enhanced Resonant Raman Spectroscoy (SERRS, the 514 nm Ar^+ gas laser line employed is resonant with the interband transition for CdSe and CdS) was employed.

An evaluation of the temperature on the substrate is obtaining exploiting Stokes and anti-Stokes Raman signals giving a temperature of about 154 ± 38 °C. However, it has to be taken into account that under resonance SERS conditions, anti-Stokes/Stokes ratio can give only an

approximate estimates of the sample temperature. In fact, different resonance conditions and plasmon enhancement affect differently Stokes and anti-Stokes spectra. Moreover, differences of the coupling of excitons with different phonon modes may yield off-equilibrium phonon distributions.[120]

The well-known silver film over nanosphere (FON) served as plasmonic substrate,[121] whose exemplificative SEM micrograph (Scanning Electron Microscopy) is reported in Figure 3.4.

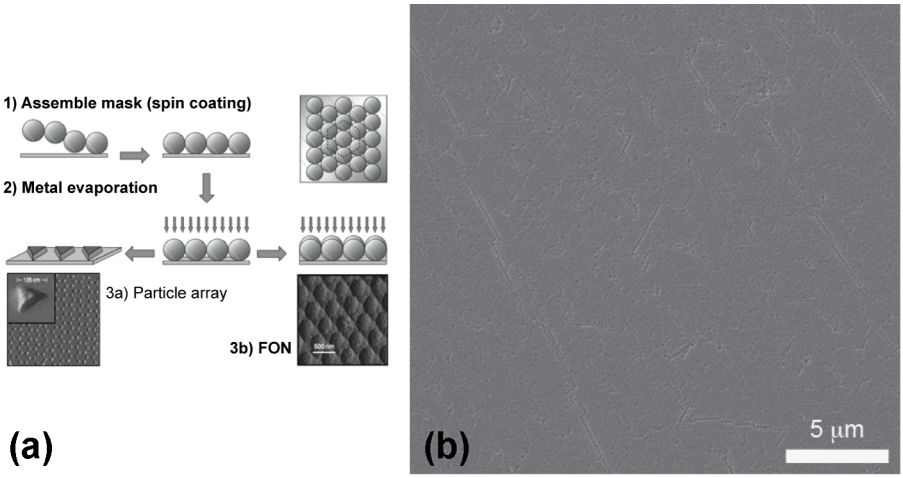

Figure 3.4: (a) Schematic representation of the preparation of a plasmonic substrate based on nanospheres. (b) SEM micrograph of a FON plasmonic substrate employed in this work.

This particular substrate was chosen because of its high enhancement factor (≥ 10^4), high thermal stability up to ~500 K (important for possible damages due to local laser heating during SERS experiments), high electrochemical stability and high shelf life >40 days.[122]

To obtain Film Over Nanosphere (FON) substrates, 2.5x2.5 cm^2 glass slides were cleaned first in acid piranha solution (H_2S0_4:H_2O_2 = 3:1) at ~ 80°C for 1 h and then sonicated in basic piranha solution (NH_4OH(30%):H_2O_2 = 5:1) for 1 h. The substrates were cleaned numerous times and kept in deionized water. Before using, the slides were dried using a N_2 flux. 100 μL of 1% polystyrene nanosphere solution (Fisher Scientific, with 150 nm diameter) in water were spin-coated on top of the glass slides to form a self-assembled mask. Finally Ag thin films were deposited onto the substrates in an Edwards E306A coating system with a bare pressure of 6x10^{-5} mbar. The metal deposition rate was ~ 1 Å/s and the final Ag thickness, evaluated by means of a quartz crystal microbalance, was about 150 nm. Finally, 30 μL of QDs solutions were spun on top of FON substrates at 500 rpm for 1 minute.

To evaluate the enhancement factor (EF)[i] the silver nanostructures were functionalized with benzenthiol (BT) by dipping each sample in a solution of 25 mL of benzenthiol in 25 mL of

[i] The EF was calculated just to test the quality of the various FON substrates, prepared for each QD sample. Only samples with EF~10^4 were employed.

methanol for about 20 hours. Then samples were rinsed repeatedly in methanol and the EF was obtained using the equation:[123]

$$EF = \frac{I^{Raman,ML}}{I^{Raman,Liquid}} \frac{C_V H_{eff}}{C_S} \frac{\sigma_{Toluene}}{\sigma_{BT}} \quad \text{(Eq. 3.18)}$$

where σ_{BT} is the BT differential cross section, $\sigma_{Toluene}$ is the toluene differential cross section and their ratio was directly measured, C_V is the toluene volumetric density ($5.69*10^{21}$ molecules/cm^3), C_S is the BT packing density on the surface ($6.8*10^{14}$ molecules/cm^2) and H_{eff} is the collection efficiency dependent on the collection apparatus and on the effective scattering volume of the sample. Low laser power (≤50 mW) employed for SERS measurements avoided any possible laser damage of FON substrates.

Despite the many advantages of SERS using an FON substrate, this geometry can alter the relative Raman band intensities due to the $1/r^{10}$ field enhancement dependence, r being the distance from the plasmonic surface.[124] In the present study, this problem should have a weak influence because the core/shell interface region is expected to be only up to ~ 1 nm thick (corresponding to approximately 3 ML of shell). Moreover, considering that oleylamine is used as a capping agent, the QD surface is ~ 2 nm away from the substrate. This ensures that the core/shell interfaces of interest here, are spatially located in a less steeply varying regime of the Raman enhancement.[124] Notably, for QDs with very large shells, the difference in the near field enhancement factor can influence the relative longitudinal optical phonon intensity between core and shell materials. For this reason, the discussion of the results is only based on relative intensities from the narrow interface region.

Finally, experimental data reported in this chapter are mean values of many different measurements. Each spectrum was recorded as an average of 10 spectra each one collected with an integration time of 10 s.

3.4 Transient PL

In order to correlate the structural properties extracted by using the Raman technique on colloidal CdSe-$Cd_XZn_{1-x}S$ and the PL efficiency, tPL technique has been employed. Compared to steady-state PL and QY calculation, by investigating the PL dynamics it is possible to get a better insight on the radiative and non-radiative exciton recombination processes and relative k_r and k_{nr} rates (Eq. 3.1). However, in presence of multi-component PL decays, some a priori knowledge about the rates involved is necessary. This is the case of QDs, whose tPL raw data typically need to be interpreted by means of complex kinetic models.

Transient PL data have been collected by means of *Time-Correlated Single Photon Counting technique* (TCSPC)[125]. Basically, this technique measures the times of the individual pulse with

respect to a reference signal, and collects them into a channel "labeled" with the corresponding time. The TCSPC technique makes use of the fact that for low-level high-repetition-rate signals (>MHz) the probability of detecting one emitted photon in one signal period is extremely low. Therefore, this technique does not rely on the number of photons per each time period, but each recorded photon contributes as +1 to the relative channel. Plotting the counts of each channel after a certain acquisition time and at increasing time channel label, what is obtained is a statistical reproduction of the PL decay trace.

The experimental apparatus is based is schematized is based on a scanning confocal microscope (Olympus IX-71) coupled with a TimeHarp 200 TCSPC card (PicoQuant) and a single-photon counting avalanche photodiode (SPAD, MPD, Italy). Excitation was provided by a cavity-dumped frequency doubled Ti:sapphire femtosecond (fs) laser system (Coherent, model Mira Optima 900-F, 400 nm, 1.5 MHz, 100 fs). The excitation beam, suitably attenuated by means of neutral density filters, was focused by a 20× microscope objective into the cuvette containing QD toluene solutions. Fluorescence is collected by the same microscope objective, passed through a dichroic mirror, and focused through a pinhole, to reject out-of-focus light. A band-pass filter was employed in front of the SPAD to select the whole QD PL band. An instrument response function (IRF) of ~150 ps for the whole apparatus was determined by means of scattered light detection. PL decays were measured with a 524 ns (128 ps SPAD binning time) and 65 ns (16 ps SPAD binning time) time window, in order to accurately extract both short and long decay components. Low incident fluence allowed neglecting multiexciton effects: in each experiment the average number of excitons generated per dot was always kept at $\langle N \rangle < 0.01$.

Long and short TCSPC datasets were analyzed by least-squares iterative reconvolution of an N-component multi-exponential decay function with IRF. Acceptable χ^2 and homogeneously distributed residuals were obtained by fitting data with a tri-exponential decay function. Several datasets were collected and independently fitted, leading to negligible statistical uncertainties (typically one percent). Exponential amplitudes (a_N) and lifetimes ($\tau_N = 1/\Gamma_N$) were employed to calculate average lifetimes and lifetime weighted amplitudes; average lifetimes are mathematically defined as

$$< \tau >= \frac{\sum_1^N a_N \tau_N^2}{\sum_1^N a_N \tau_N}, \qquad \text{(Eq. 3.19)}$$

while lifetime weighted amplitudes are calculated using the expression

$$A_N = \frac{a_N \tau_N}{\sum_1^N a_N \tau_N}. \qquad \text{(Eq. 3.20)}$$

The extracted tri-exponential decay was employed in the kinetic model.

3.5 Transient Absorption

Pump and probe technique (P&P), alias transient absorption (TA), has been employed to investigate QD exciton dynamics at the sub-nanosecond time scale. Compared to TCSPC, TA measures the evolution of the absorption spectrum by varying the delay between a short light pulse, named probe, and an initiating pulse, called pump. The pump pulse creates a non-equilibrium vibronic state and a weaker delayed light pulse is used for probing the pump-induced modification of the absorption spectrum at increasing delay time. In this experiment the time resolution is dictated by the pulse duration and not by the detector, as in the case of tPL-TCSPC experiments, allowing the measurement of ultrafast dynamics by using a femtosecond laser as light source.

In TA measurements the pump fluence was also tuned in order to evaluate the dynamics of multiexciton generation (MEG) and recombination (MER) in core-shell CdSe quantum dots.

Since the very short length of the pulses, a quantum mechanical (QM) treatment is needed in order to describe the technique. The generally accepted QM treatment is based on the application of time-dependent perturbative theory to light-matter interaction, within the *density matrix* formalism. TA is a non-linear (NL) spectroscopy which concerns the third order optical polarization $\mathbf{P}^{(3)}(t) = \chi^{(3)}\,\mathbf{E}^3(t)$.[126]

The incoming electric field can be represented as a sum of pump $\mathbf{E}_1(\mathbf{r},t)$ and probe $\mathbf{E}_2(\mathbf{r},t)$ pulse fields, as:

$$\mathbf{E}(\mathbf{r},t) = \mathbf{E}_1(t+\tau)e^{i(\mathbf{k_1}\cdot\mathbf{r}-\omega_1 t)} + \mathbf{E}_2(t)e^{i(\mathbf{k_1}\cdot\mathbf{r}-\omega_2 t)} + c.c. \qquad \text{(Eq. 3.21)}$$

where $\mathbf{E}_j(t)$ are temporal envelopes of pulses and τ is the delay between the two pulses.

The $\mathbf{P}^{(3)}(t)$ dependence involves three fields, and makes this type of experiment a *four-wave mixing*. In principle any linear combination of the 4 individual wavenumbers ($\pm\mathbf{k}_1$, $\pm\mathbf{k}_2$) and frequencies ($\pm\omega_1$, $\pm\omega_2$) associated to the e.m. field can result. This means that many coherent processes can contribute to the signal. However, a good approximation is considering pump and probe pulses well separated in time; in fact, only the long-times surviving terms are diagonal population terms.

Within this incoherent regime it is possible to embody the third-order susceptibility formalism in time dependent population terms and treat the non-linear response term into an effective linear one. Provided that the expected signal is a change in intensity of transmitted probe induced by pump pulse, it is possible to define the trasmittance T in Lambert-Beer approximation and express the absorption coefficient α as a sum of all possible transitions between *i,j* states with absorption cross section $\sigma_{i,j}$ and population N:[127]

$$\alpha = \sum_{i,j} \sigma_{i,j}(\omega)\,(N_i - N_j) \qquad \text{(Eq. 3.22)}$$

where $\sigma_{i,j}$ will be positive-valued for upward transition and negative-valued for downward transitions. If the *i*-state population is changed by the pump pulse excitation so that $N_j^* = N_j + \Delta N_j$ and the probe is delayed by τ the change in absorbance is

$$\Delta A(\omega,\tau) = -log\left(\frac{\int I_{probe}(\omega,t-\tau)e^{-\sum_{k,j}\sigma_{k,j}(\omega)\Delta N_k(t)L}dt}{\int I_{probe}(\omega,t)dt}\right) \qquad \text{(Eq. 3.23)}$$

which, for small signals and pulses shorter than the time scale of ΔN evolution, becomes

$$\frac{\Delta T}{T}(\omega,\tau) = -\sum_{i,j}\sigma_{i,j}(\omega)\,\Delta N_j(t)L\,. \qquad \text{(Eq. 3.24)}$$

Eq. 3.24 says that the probe interrogates the system measuring new transitions associated with the pump induced population redistribution and tracks in time the recovery to equilibrium.

Usually three types of signals are observed in a $\Delta A(\omega)$ spectrum, as presented in Figure 3.5:

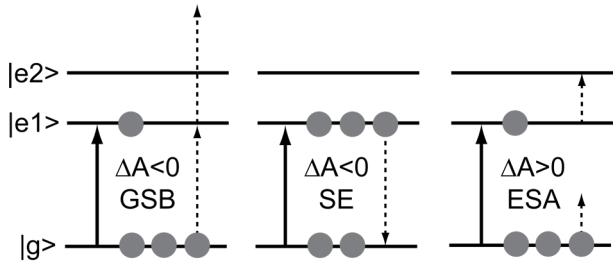

Figure 3.5: Types of signals in transient absorption spectrum.

Ground State Bleaching (GSB), $\Delta A(\omega) < 0$: a fraction of dots are excited to an higher lying energy state by pump pulse, leading to a decrease of the number of dots in ground state and, consequently, to a reduction of absorbers.

Stimulated Emission (SE), $\Delta A(\omega) < 0$*:* Upon population of the excited state there is a non-vanishing probability of having stimulated emission. In this process one probe photon induces emission of one photon from the excited dot, with the effect of increasing the transmitted intensity.

Excited State Absorption (ESA) or Photo-induced Absorption (PA), $\Delta A(\omega) > 0$*:* Excited state dots can also be excited toward higher lying excited states, decreasing the transmitted probe intensity.

Finally, for the colloidal QDs systems investigated in this thesis, signals contained in $\Delta A(\omega)$ can be qualitatively divided into two classes, *many-body effects* and *occupation effects*[128]. The latter embrace changes in optical properties induced by non-equilibrium occupation of excited states. The former encompass energy shift, broadening, and bleaching induced by screening and phase-space filling and depends on the excitation density. When high-fluence pump pulses are used both classes of effects act on the QD electrodynamics.

The TA experimental setup is represented in Figure 3.6.

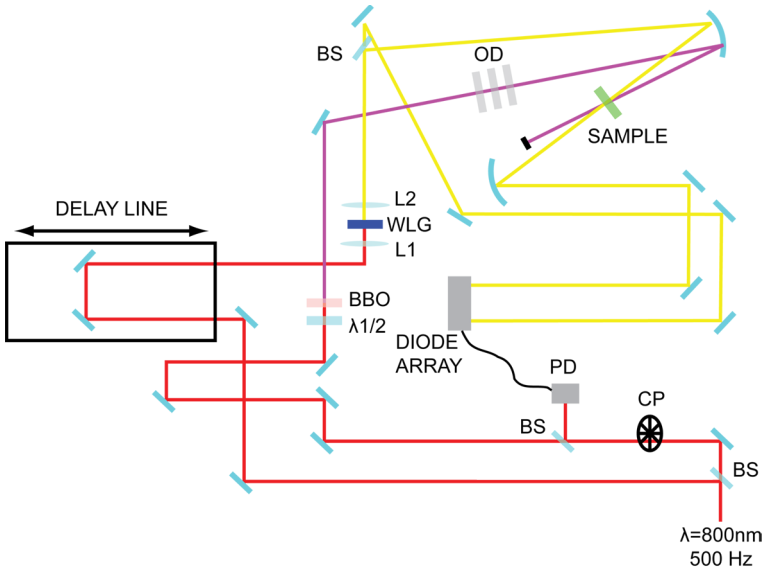

Figure 3.6: Scheme of the experimental set-up or TA experiments. The laser light is provided from a regeneratively amplified Ti:Sapphire fs laser system (λ=800nm, rep. rate 500 Hz). BS: Beam splitter. CP: Chopper. PD: Photodiode. λ1/2: Half-wave plate. L: Lens. WLG: White-light generator.

The excitation source is a Ti:Sapphire femstosecond (fs) laser system, composed by two main units: a fs seed laser system (Mai-Tai SP, Spectra Physics) and a regenerative amplifier (Spitfire, Spectra Physics).

The Mai-Tai system comprises two lasers, a CW diode pumped Nd:YVO_4 laser (Millennia), pumping a mode-locked Ti:Sapphire laser. The whole seed system is set to generate 110 fs pulses at 84 MHz and λ = 806 nm. The energy per pulse is ≈ 5 – 10nJ.

The Mai-Tai output beam (seed) is directed into the Spitfire cavity, designed to stretch, amplify and re-compress the seed pulses by means of *chirped pulse amplification* (CPA). The amplification is obtained by directing the stretched seed into a second Ti:Sapphire rod, which is synchronously pumped by a second harmonic generated Nd:YLF nanosecond laser (Empower). Pulse compression is the last step in CPA and resulting output features are: 110 – 160fs duration, pulse energies up to 1mJ, λ = 800nm and tunable repetition rate (1Hz – 1kHz, here set at 500Hz).

The output beam is splitted in two beams, which are meant to originate a pump and a probe beam. Pump beam repetition rate is halved to 250 Hz, by means of a chopper, and its frequency is doubled to 400nm, by means of NL *second harmonic generation* using a beta-barium borate (BBO) crystal.

On the other hand, the probe beam passes through a computer-controlled motorized delay line and is converted into white light exploiting *super-continuum white light generation* in a sapphire crystal.

Pump and probe beams are then directed toward the sample, where they spatially overlap.

White light transmission spectrum is recorded by means of a detector composed of a diffractive grating and CCD diode array spectrally calibrated system; the difference between transmittance spectrum with and without pump constitutes the transient absorption spectrum.
The delay line is automatically controlled via software, which allows the simultaneous collection of transient spectra at different pump-probe delays and the creation of 2D (wavelength versus delay time) TA maps. The delay line set movement steps and the temporal resolution of the spectrum dictates the temporal resolution. The maximum time delay is determined by the guide rail length, upon which the delay line translates, and space-time conversion yields 800ps. Pulse energy has been determined by using a pyroelectric detector (Molectron J3-05). Knowledge of pulse energy E_p, together with beam diameter d measurements (BeamGage Ophir-Spiricon camera), allow the calculation of the fluence as $F = \frac{E_p}{\pi(d/2)^2}$.

3.5.1 Transient Absorption on QDs

TA studies have been performed on different colloidal dispersions of CdSe-$Cd_XZn_{1-x}S$ QDs. Two different kind of measurement have been performed in order to resolve dynamics operating at different time scales. Namely, TA maps were collected with a 800ps (1ps resolution) and 120ps (200fs resolution) time window.
Optical excitation of quantum dots follows a Poissonian statistics, as a result of the assumption that the probability of exciton generation through photon absorption is independent of the number of excitons already existing in it[36]. The probability of having N e-h pairs in a selected nanocrystal, when the average population is $\langle N \rangle$, is defined as

$$P(N) = \langle N \rangle^N \frac{e^{-\langle N \rangle}}{N!} \qquad \text{(Eq. 3.25)}$$

with $\langle N \rangle = \frac{F}{\hbar\omega} \cdot \sigma$. For each sample different TA maps at different pump fluence have been collected, in order to investigate the ultrafast dynamics in the single ($\langle N \rangle < 1$) and multi-exciton ($\langle N \rangle > 1$) regime.

3.6 Amplified Spontaneous Emission (ASE)

Optical gain properties of CdSe-$Cd_XZn_{1-x}S$ QDs were also characterized. To this aim, QDs were included in sol-gel matrices and deposited on quartz substrates. A high packing density is in fact necessary to observe optical gain and the consequent instauration of the ASE regime. On the other hand, the matrix provides a shield for chemical- and photo-oxidation, as suggested by the band alignment presented in Figure 3.7.

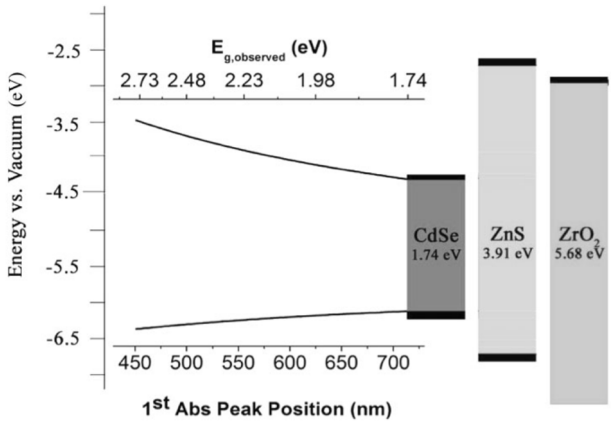

Figure 3.7: Summary of the band-alignment for the different materials employed in this work. CdSe band gap is size dependent and thus the conduction and valence band energies are plotted as a function of the band-edge exciton energy. Both ZnS and ZrO_2 have been employed as matrices for CdSe and CdSe- $Cd_XZn_{1-x}S$ core-shell QDs. The figure has been adapted from Ref. [129].

The bi-exciton origin of the optical gain in QDs systems has already been discussed and the mechanism is schematically summarized in Figure 2.10. A net optical gain is thus produced when the inversion of population from the mono- to the bi-exciton state is sufficient to generate amplified spontaneous emission (ASE). The experimental apparatus for ASE experiments is schematically illustrated in Figure 3.8.

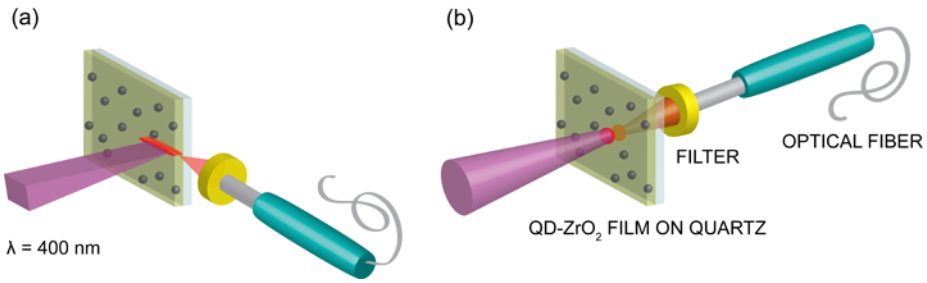

Figure 3.8: ASE setup for (a) waveguide configuration and (b) transmission configuration experiments. The laser light if focused on the sample with a cylindrical and a spherical lens, respectively.

The laser beam is provided by the same regenerative amplifier system employed for the TA experiments. One-photon pumping ASE experiments were carried out by SHG of the 800nm laser output. The intensity of the input beam was tunable by the use of a half wave plate and a polarizer and a set of neutral density filters. The samples were excited in two different configurations:

- *Waveguide configuration*: A cylindrical lens with a 200 mm focal length focused the beam onto the sample. The sample edge emitted beam, in a lateral configuration, was coupled through an optical fibre into a micro-spectrometer (Ocean Optics HR2000), while the spatial profile of the input beam was measured using a CCD camera (BeamGage Ophir-Spiricon camera), placed on the beam focus, and pulse energies were sampled with a pyroelectric detector (Molectron J3-05).

With this experimental configuration the main information obtained from the analysis of spectra, registered at different incident intensities, is the ASE threshold fluence, which is the minimum incident laser fluence necessary to create a sufficient number of couples exciton-exciton to activate ASE. Both spontaneous and multi-exciton emission (ASE) are emitted along the length of the stripe in all directions. For appropriate emission angles the light will be coupled directly into the allowed modes of the asymmetric waveguide constituted by the ZrO_2 QDs films deposited on the quartz slab[130] (Figure 3.8.a) and collected by the optical fiber. Therefore the ASE signal detected by the fiber adds up to the spontaneous emission, whose integrated intensity is linearly dependent on the excitation intensity. Enhancing the incident intensity beyond the threshold, the ASE contribution to the total signal increases exponentially. This phenomenon is commonly considered as the effect of the activation of an optical gain regime.

- *Transmission configuration*: One photon-pumped ASE was also obtained by focusing the beam with a 100mm spherical focal lens and collecting the signal in 0° geometry (Figure 3.8.b), with a cut-off filter in order to remove the residual pumping laser beam. With this configuration waveguide effects are minimized, allowing the measurement on intrinsic QD gain properties.

PART II:

OPTICAL CHARACTERIZATION

OF CdSe-$Cd_XZn_{1-x}S$ QDs

Chapter 4.

CdSe-$Cd_XZn_{1-x}S$ QD Samples

QDs samples under investigation are type-I core-shell CdSe QDs, with variable shell thickness and composition. The main classes of CdSe QDs that have been extensively studied in this thesis are:

- CdSe-CdS core-shell (with 1 to 6 shell ML);
- CdSe-$Cd_{0,5}Zn_{0,5}S$ core-shell (with 1 to 6 shell ML);
- CdSe-ZnS core-shell (with 1 to 6 shell ML);
- CdSe-CdS/$Cd_{0,5}Zn_{0,5}S$/ ZnS graded core-shell.

They have been synthesized by Doct. J.J. Jasieniak and Doct. Francesco Todescato, at CSIRO Division of Molecular and Health Technologies Ian Wark Laboratory, Bayview Avenue, Clayton 3168, Australia. All QDs have been characterized both in solution and in a solid-state sol-gel matrices.

4.1 Synthesis and properties of CdSe cores

CdSe QDs have been synthesized according to the established salt-based method in 1-octadecene (non-coordinating solvent)[12,131]. The capping is a mixture of TMPPA (Bis-(2,2,4-trimethylpentyl)phosphinic acid) and oleic acid (in octadecene solution). Both of them coordinate with Cd atoms, and by combining ligands, the nucleation and ripening of particles can be controlled systematically, enabling the isolation of high yields of nanocrystals with predictable sizes and with a high degree of monodispersity. Following synthesis, QDs are purified through extraction in toluene and with a capping layer of oleyamine.

Different batches of CdSe cores have been investigated and employed as seeds for core-shell heterostructures. In Figure 4.1 the absorption and PL spectra for two different CdSe samples are presented.

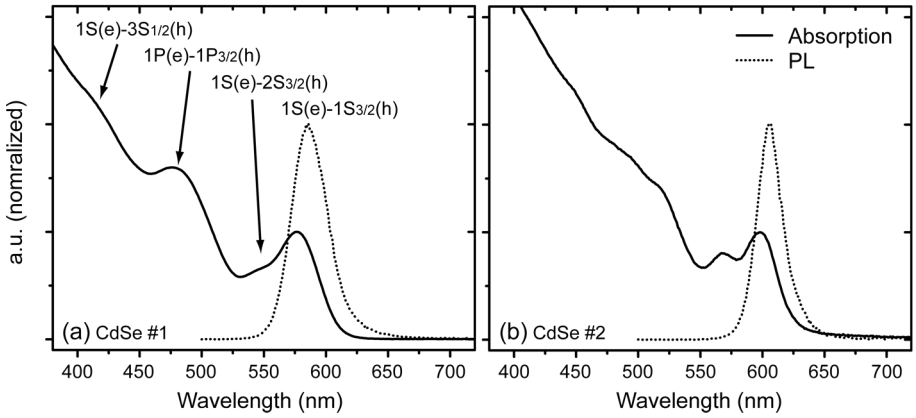

Figure 4.1: Absorption and emission spectra for the two CdSe QD samples investigated in this work. Spectra are normalized at the 1S(e)-$1S_{3/2}$(h) exciton absorption and emission band.

Exciton states can be resolved from the absorption spectra of CdSe#1 and #2 QDs. Absorption and emission spectra are similar, but for CdSe#2 spectra are red-shifted and exciton features are less resolved. Both aspects are due to the different size of the dots, which is increased for the CdSe#2 with consequent decrease of the quantum confinement. The larger size is also responsible for the higher absorption cross-section at higher energies for CdSe#2, with the bulk contribution to the absorption spectrum ($\propto E^{1/2}$, Eq. 2.13) dominating over the excitonic discrete bands.

Also the PL spectrum is shifted and, contrary to the absorption one, it is narrower for the CdSe#2. Such effect is mainly due the different size dispersion and shape homogeneity.

The average core diameters were evaluated from the absorption spectra by means of an empirical calibration curve, provided by Jasieniak *et. al.* [105]:

$$D(\text{nm}) = 59.60816 - 0.54736\lambda + 1.8873 \cdot 10^{-3}\lambda^2 - 2.85743 \cdot 10^{-6}\lambda^3 + 1.62974 \cdot 10^{-9}\lambda^4 \qquad \text{(Eq. 4.1)}$$

In this relation λ represents the wavelength at which the first absorption peak (1S(e)-$1S_{3/2}$(h)) is centered (Figure 4.1). The fourth order polynomial was chosen as the best fitting curve of data obtained by coupling linear absorption analysis to high resolution TEM results and atomistic semiempirical pseudopotential modeling. From Eq. 4.1 CdSe#1 and CdSe#2 cores have D=3.8 nm and D=4.5 nm for CdSe#2, with the 1S(e)-$1S_{3/2}$(h) exciton peak centered at 577 nm and 597 nm, respectively. Although the size is varied by just one lattice parameter (Table 1.1), the absorption and emission are shifted by 20nm.

Such values have been also verified by TEM analysis, which provided also a statistical measurement of the size dispersion. Namely, the values obtained are D_{TEM}=3.9±0.5 nm for CdSe#1 and D_{TEM} =4.2±0.5 nm for CdSe#2. Relative TEM images are reported in Figure 4.2.

From the interplanar distance measured by FFT analysis of the HRTEM, the dominant phase is the CdSe hcp or wurtzite-like (P63mc, cell parameter: a=4.299 Å, c=7.010 Å). The empirical formula thus proved to be a good alternative to time-consuming HRTEM analyses for the

determination of the mean diameter of the QDs in solution. Of course, if size distribution and other structural information about the QDs are required, TEM analyses become necessary.

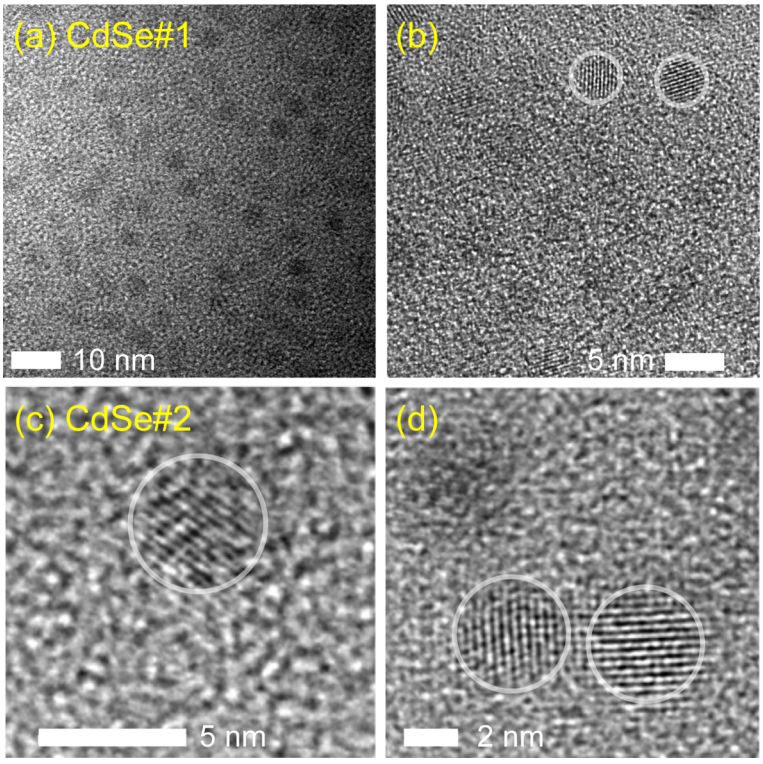

Figure 4.2: TEM images of CdSe#1 and CdSe#2 QDs, provided by Prof. Mattei (Department of Physics and Astronomy, University of Padova) and Doct. Jasieniak.

4.2 Synthesis and properties of CdSe core-shell QDs

To grow CdSe based core-shell nanocrystals a modified SILAR protocol[12] was employed. Briefly, washed CdSe cores were dispersed in a 1:1 mixture of oleylamine (70% purity, Aldrich)/1-octadecene (90% Aldrich) at a concentration of 40 μM. Following degassing at RT for 30 min, the solution was slowly heated to 80 °C under vacuum. The atmosphere was changed to N_2, and the degassed solution was heated to 235 °C. At this point a Cd enriching layer was added, which was the equivalent to a half stoichiometric ML of CdSe. After 5 min, an equivalent quantity of ODE-S was added to form 1 ML of shell material. This was allowed to grow for 10 min prior to the addition of an equivalent amount of Cd, Zn, or CdZn stock solution. After 15 min the solution temperature was reduced to 120 °C to take aliquots of the samples after each ML. The temperature was then increased to a value of between 235 and 250 °C. The exact final temperature was increased by 5 °C every 2 MLs up to a maximum of 250 °C. As-synthesized core– shell QDs were purified through multiple extractions using MeOH, EtOH, and acetone, prior to being dispersed in toluene.

The sulfur stock solution used during shell formation consisted of sulfur (>99.5%, Aldrich) dissolved in 1-octadecene at a concentration of 1 M at 150 °C for 1 h. The metal precursor stocks were prepared by dissolving cadmium, zinc, or 1:1 cadmium/zinc acetate hydrate salts (>98%, Aldrich) in 1- octadecene using a 7:1 excess of oleic acid (Aldrich)/bis(2,2,4- trimethylpentyl)-phosphinic acid (Cytec Specialty Chemicals) at 280 °C for 1 h. The final metal concentration was 1 M.

A 20% excess of the metal layers was used to ensure high PL and high photo-stability of resulting particles[132]. The growth of single layers was verified by monitoring the absorption spectra in the UV-Vis: a gradual increase in the extinction coefficient at high energies is registered as the thickness increases, due to the bulk interband transitions of the shell semiconductors.

The resulting core-shell QDs are finally purified in toluene in a similar manner as cores and finally capped with octadecylamine.

Differently from core CdSe QDs, core-shell QDs final dimensions can't be calculated on the basis of the absorption spectra. However, given the core dimensions, the diameters of the core-shell QDs can be calculated by geometrical considerations. This is possible thanks to the accuracy of the SILAR technique, which allows the precise control of the shell thickness down to the single ML. Namely, in the SILAR technique the amount of shell precursor necessary for the growth of each monolayer is calculated by means of the spherical concentric shell model (CSM)[39]. Through this method the quantity of the injection solution for each monolayer is given by the number of the core surface atoms. Therefore, by simply considering half of the *c*-lattice parameter of the bulk shell semiconductor as the equivalent thickness of one monolayer, dimensions of the core-shell nanocrystals can be calculated.

For CdS 1ML is equal to 0.34 nm, for ZnS 0.31 nm (table 1.1). In literature estimations of the ML thickness of alloyed shells suggest 0.33 nm for $Cd_{0,5}Zn_{0,5}S$ [39]. In order to verify the reliability of the geometrical approximation, some of the core-shell QDs were also studied by TEM, and relative micrographs are reported in Figure 4.3.

From the comparison of calculated and measured mean radii, the validity of the geometrical method was verified within a tolerance of ~5%. The global dimensions calculated for all the samples in solution will be reported in the next sections in the discussion of the results for each QDs series. The diameters of the core-shell QDs thus vary from 3.8 nm for the cores to ~4 nm for the QDs with six monolayers.

In Figure 4.4 the absorption and PL spectra for the different type-I CdSe core-shell QD series are presented.

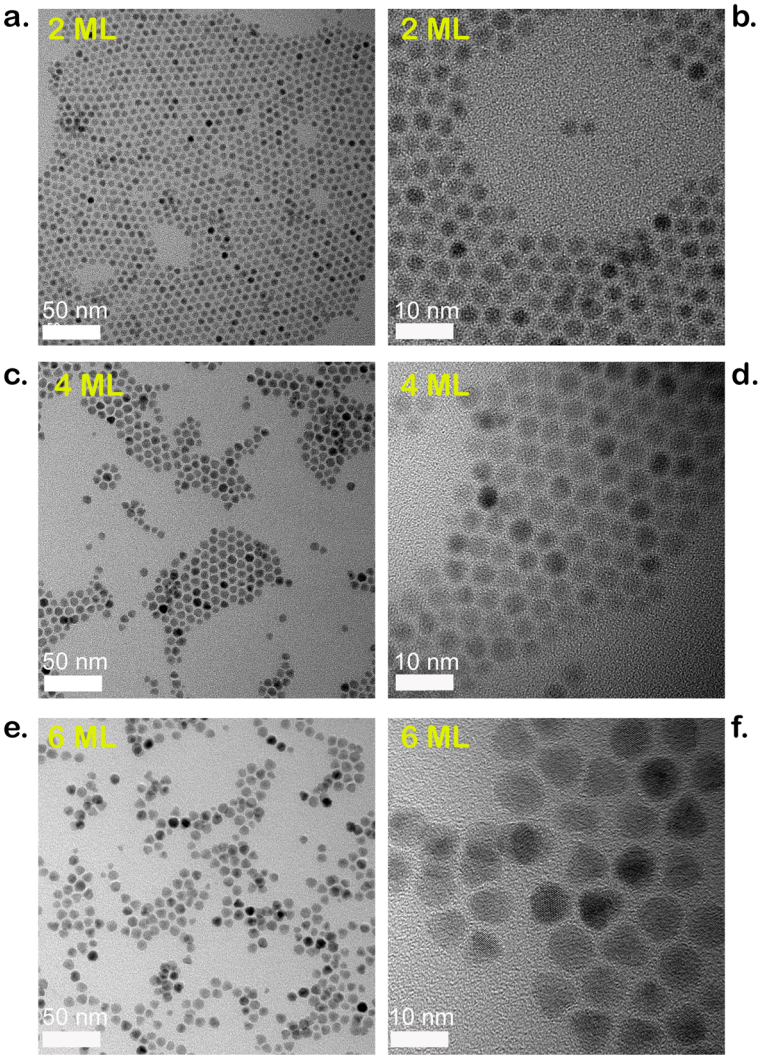

Figure 4.3: Figure 4.2: TEM images of CdSe#1 and CdSe#2 QDs, provided by Jasieniak.

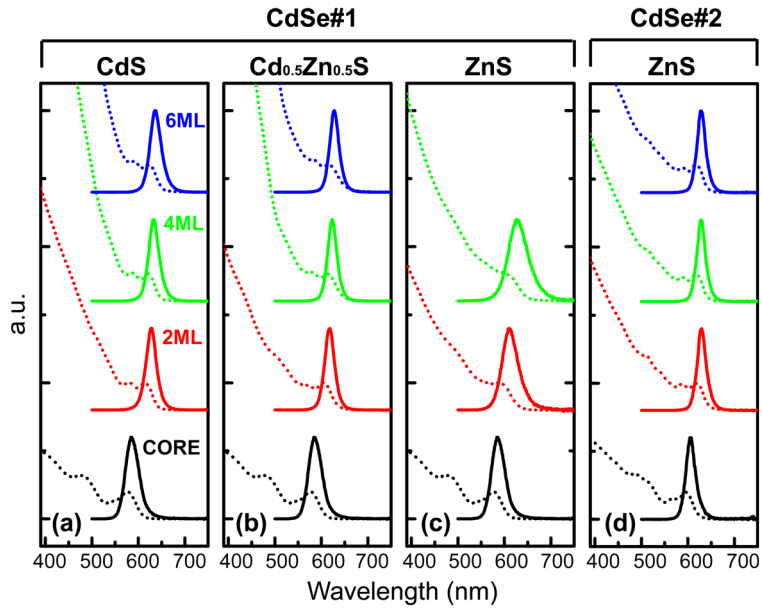

Figure 4.4: (a-c) Absorption (dotted lines) and emission (full lines) spectra of CdSe#1-CdS (a), CdSe#1-$Cd_{0.5}Zn_{0.5}S$, (b) CdSe#1-ZnS (c) and CdSe#2-ZnS (d) core-shell QDs with different number of shell MLs (0, 2, 4, and 6).

Detailed analysis of the effect of shell growth on the optical properties will be provided in the following sections. However, Figure 4.4 stimulates some preliminary observations.

First of all, the excitonic nature of the absorption spectra of CdSe (E_g^{Bulk} = 1.74 eV, Table 1.1) is preserved in all series, even after 6 ML of shell growth. A dramatic increase of the absorbance at λ < 500 nm is also detected and corresponds to the absorption onset by the higher band-gap CdS (E_g^{Bulk} = 2.49 eV) and ZnS (E_g^{Bulk} = 3.61 eV) shell materials. This occurrence is exploited in the SILAR synthesis process for monitoring the advancement of the shell coverage.

Secondly, for all the core-shell series a red-shift of both absorption and PL spectra is discernible. This phenomenon is caused by extensive delocalization of the exciton into the surrounding shell[35]. Close examination of the 1S(h)-$1S_{3/2}$(e) transition with increasing shell thickness reveals that the largest red-shift occurs upon deposition of the first monolayer. The magnitude of the shift then declines for each additional ML, *i.e.* the exciton generated in the CdSe core "feels" the potential barrier imposed by the wider band-gap shell material.

Focusing on the PL spectra, CdSe QDs present a narrow peak with a full-width-half-maximum (FWHM) of ~30 nm. As for linear absorption results, a general red-shift for the 1S(h)-$1S_{3/2}$(e) transition energy can be observed in each series (Figure 4.4) at increasing shell thickness.

Considering now also the shell chemical composition, in "Cd-rich" core-shell series (CdS and $Cd_{0,5}Zn_{0,5}S$) shell growth improves the sharpness of the PL peak compared to the CdSe#1 seed cores. On the other hand, both absorption and PL features for the CdSe#1-ZnS series broaden. The FWHM value of the emission band grows with the thickness of the shell as an effect of lattice mismatch between core and shell[75], which is ~12% for bulk wurtzitic CdSe and ZnS (while for CdSe and CdS the mismatch is 4%). Polycristallinity can also occur, since at RT zinc blende phase is more stable in bulk ZnS (Table 1.1). Therefore, stacking faults and lattice defects may occur and act as nucleation centers for inhomogeneous shell growth, since defects enhance the anisotropy of the surface energy. The direct consequence is the enhancement of the nanocrystal size/shape dispersion, thus leading to the observed peak broadening.

The same shell synthesis, starting from the larger and more monodisperse CdSe#2 cores, does not present any broadening effect. The combination of core crystalline quality and dimensions can thus minimize the effect of lattice mismatch.

Chapter 5.

A SERS Study on the Core-Shell Interface In CdSe-$Cd_XZn_{1-X}S$ QDs

The structural nature of hetero-interfaces in core/shell semiconductor quantum dots (QDs) plays a fundamental role in tailoring their optical properties. This part of the work is focused on using Surface Enhanced Raman Spectroscopy to investigate the structural evolution of such interfaces in CdSe-$Cd_XZn_{1-X}S$ colloidal QDs. A comparison between two systems, namely CdSe-CdS and CdSe-$Cd_{0.5}Zn_{0.5}S$, shows significant structural variation across the core-shell interfaces for the two different materials: a smooth interface for the former and abrupt interface for the latter. This structural difference modifies the electronic structure within the QDs (Chapter 6), which directly dictates the confinement behavior of the electrons and holes. The implications of this translate to a better understanding of why graded CdSe-CdS/$Cd_{0.5}Zn_{0.5}S$/ZnS[44] QDs are so lucrative for linear and non-linear fluorescence based applications.
In Section 5.1 a brief overview about the main concepts and issues related to the core-shell interface is provided, while in Section 5.2 results and discussion are reported. In Section 5.3 some comments and perspectives are collected.

The results presented in this chapter are extracted from a paper published in 2013:
Todescato, F.; Minotto, A.; Signorini, R.; Jasieniak, J. J.; Bozio, R.
Investigation into the Heterostructure Interface of CdSe-Based Core-Shell Quantum Dots Using Surface-Enhanced Raman Spectroscopy
ACS Nano **2013**, *7*, 6649–6657.

5.1 Core-shell interface: State of the art

It is well known from the chemical vapour deposition community that lattice strain at interfaces is responsible for non-epitaxial layer growth and consequently a defective interface.[133] Similar arguments have been made to account for the dependence of QY on shell thickness.[75] In support of this structural picture, empirical experimental evidence from various

core-shell structures has shown that the highest absolute QY values are achieved when minimal lattice strain exists at the core-shell interface.[39] Despite this, the structure of such interface remains largely unknown.

In the last decade, CdSe-CdS QDs represented the most investigated class of core-shell materials.[40,47,87,104,134,135] Recent investigations into CdSe-CdS core-shell QDs by means of fluorescence line narrowing[40] and Raman spectroscopy[53] demonstrated the formation of a "smoothed" interface, due the formation of an alloyed $CdSe_xS_{1-x}$ interlayer. This layer is found to gradually grow during the shelling up to a maximum of 3 CdS ML. As a result, the lattice structure is relaxed and the graded electronic levels create a smooth radial confinement potential. These factors enable for the inherently high QY in this system to be achieved, as well as advantageously enhance the optical gain lifetimes as a result of a reduced Auger recombination rate.[40,46] The main issue with CdSe-CdS QDs is related with the low potential barrier for electron migration provided by the CdS shell.

The optimization of these two counteracting phenomena - the smoothing of the confinement potential and the exciton localization far from the outer surface - can be obtained using "giant" CdSe-CdS QDs with sizes as large as 15 nm.[104] In these nanocrystals (NCs) the trapping role of the external surface is avoided by its large distance from the CdSe core and the potential smoothing is formed by the $CdSe_xS_{1-x}$ interfacial alloy. However, the use of such large nanocrystals for applications like lasers is inherently challenging because of the difficulty to ensure colloidal stability in solution, while maintaining the required high volume fraction of emitters in a neat thin film or composite. An alternate nanocrystal heterostructure, which ultimately enables smaller QDs with high performances to be used, utilizes a radial material grading as recently theoretically proposed by Javaux *et al.*.[45] This structure should provide an initial smoothing of the confinement potential and a gradual enhancement of the electronic barrier to prevent electron-hole migration towards the external surface. Recently, it has been demonstrated that epitaxially grown red-emitting CdSe-CdS-$Cd_{0.5}Zn_{0.5}S$-ZnS graded shell QDs present ASE and lasing thresholds among the lowest reported in literature.[43,44] With the same approach, similar results have been obtained from blue-emitting CdZnS-ZnS QDs.[49] In both cases, the outer high band-gap ZnS shell layer limits the electron trapping at the surface.

Recognized the efficacy of a "graded" approach, in this part of the thesis the interface structure between CdSe cores and two shells, CdS (as a benchmark) and $Cd_{0.5}Zn_{0.5}S$ is studied and compared. Moreover, $Cd_{0.5}Zn_{0.5}S$ is a choice that allows a more strongly electronic confining potential with respect of CdS and can, in principles, partially preserve the smoothness of the confinement potential.

The interfacial lattice strain of CdS and $Cd_{0.5}Zn_{0.5}S$ with respect to CdSe is predicted to be ~ 4 % and ~ 8 %, respectively.[39] By studying the interfaces for each core-shell structure as a function

of shell thickness it is possible to understand how variations to structural properties of the shell material influence the core-shell interface and, eventually, the final optical properties of the NCs.

5.2 Results and discussion of SERS analysis on CdSe-$Cd_XZn_{1-x}S$ core-shell QDs

Figure 5.1.a shows the evolution of the absorption features and the fluorescence band of CdSe-CdS and CdSe-$Cd_{0.5}Zn_{0.5}S$ as a function of increasing number of shell thickness.

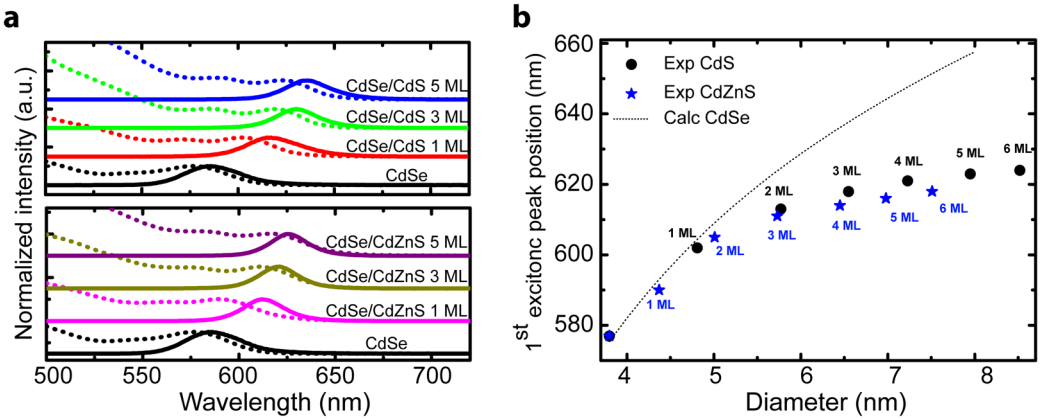

Figure 5.1: (a) Absorption (dotted lines) and emission (full lines) spectra of CdSe/CdS (upper panel) and CdSe/ $Cd_{0.5}Zn_{0.5}S$ core-shell QDs (lower panel) with different number of shell ML (0, 1, 3 and 5). (b) First excitonic absorption peak position for CdSe cores (dotted line, evaluated using Ref. [105]), CdSe/CdS and CdSe/ $Cd_{0.5}Zn_{0.5}S$ (from 1 to 6 ML) QDs as a function of dot diameter.

Table 5.1: CdSe and core-shell QDs average diameter (*d*, nm) and absorption band-edge (peak, nm). In both cases the first excitonic peaks have been measured by means of UV-Visible spectra.

	CdSe-CdS *d* (nm)[a]	CdSe-CdS peak (nm)	CdSe-$Cd_{0.5}Zn_{0.5}S$ *d* (nm)[b]	CdSe-$Cd_{0.5}Zn_{0.5}S$ peak (nm)
0 ML	3.8	577	3.8	577
1 ML	4.8	602	4.4	590
2ML	5.8	613	5.0	605
3ML	6.6	618	5.7	611
4 ML	7.2	621	6.5	614
5ML	8.0	623	7	616
6ML	8.5	624	7.5	618

[a]Radii here reported are obtained from TEM measurements of Ref. [12] for CdSe-CdS QDs synthesized with the same method and with similar CdSe cores. [b]Radii of CdSe-$Cd_{0.5}Zn_{0.5}S$ batch are extracted from TEM images reported in the previous section.

As mentioned before, the first excitonic peak and the emission band of CdSe-CdS and CdSe-$Cd_{0.5}Zn_{0.5}S$ core-shell QDs red-shift on increasing shell thickness. This behaviour is commonly attributed to the difference in the energetic levels (and band gaps) between the three semiconductors (CdSe, CdS, $Cd_{0.5}Zn_{0.5}S$, see Table 1.1), which allows for partial delocalization of

the exciton from the core to the shell. Comparing the positions of the first excitonic peak of CdSe-CdS and of CdSe-$Cd_{0.5}Zn_{0.5}S$ QDs with that of calculated homogeneous CdSe dots with the same overall size (Figure 5.1.b),[105] it is clear that the core/shell interface acts as a more stringent confinement barrier. Moreover, for the same ML number, the exciton confinement in the CdSe-$Cd_{0.5}Zn_{0.5}S$ NCs is higher with respect to that in CdSe-CdS, with both shell types exhibiting saturation at approximately three shell MLs.

Naturally, the difference between pure CdSe cores and the core-shell QDs with the same size stems from the variation of the confinement potentials acting on the photogenerated electrons and holes. When comparing the two types of core-shell QDs, one must additionally take into account the different nature of the interface (abrupt, extended, *etc*...) arising from the changes in the lattice parameters and electronic features across the interface.

5.2.1 SERRS of pure CdSe quantum dots

CdSe#1 QDs with *d*=3.8 nm have been used as cores for all of the core-shell NCs. For this reason, the first step before studying the more complicated core-shell systems is the analysis of the core features. In Figure 5.2.a the Raman spectrum of the CdSe QDs (at RT) deposited on the FON substrate is presented.

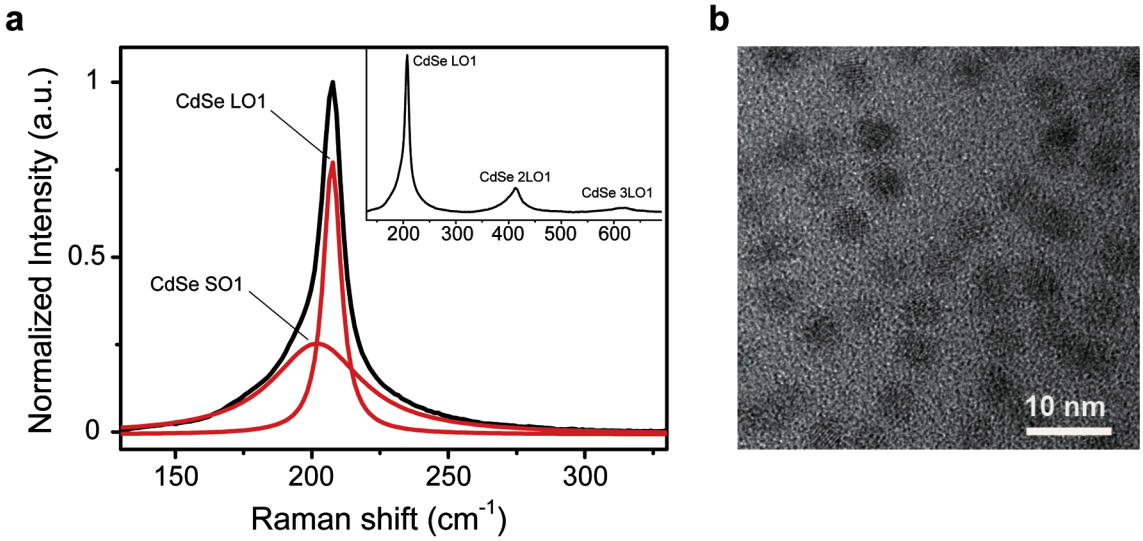

Figure 5.2: a. Raman spectra of CdSe QDs with diameter of 3.8 nm; b. HR-TEM of CdSe QDs shows high sphericity and quality of cores.

The asymmetric band peaked at ~ 207 cm^{-1} is a convolution of two peaks. The fitting with Lorentzian functions identifies to two modes: the principal one, centered at 207.7 cm^{-1}, is the first order longitudinal optical phonon of CdSe (LO1); and a second mode, centred at 201.7 cm^{-1}, originates from the CdSe surface optical phonon modes (SO1).[117,136,137] Two overtones of the

longitudinal optical phonon are also observed around 410 cm^{-1} (2LO1) and 615 cm^{-1} (3LO1) (Figure 5.2.a, inset).

The differences between the Raman features of CdSe QDs and bulk CdSe (LO1 asymmetry, higher FWHM, and different peak position with respect to the 213 cm^{-1} band of the bulk) can be attributed to the spatial confinement of phonons in NCs and, in particularly, to the relaxation of the q=0 selection rule.[115,116] Because of the high sphericity of the core NCs (Figure 5.2.b) it is possible to calculate the theoretical peak position of the CdSe QDs with diameter of 3.8 nm by exploiting the phonon confinement model (PCM).[138] Following this model, our LO1 mode should be peaked at 208.7 cm^{-1}, in good agreement with our experimental value (Figure 5.3).

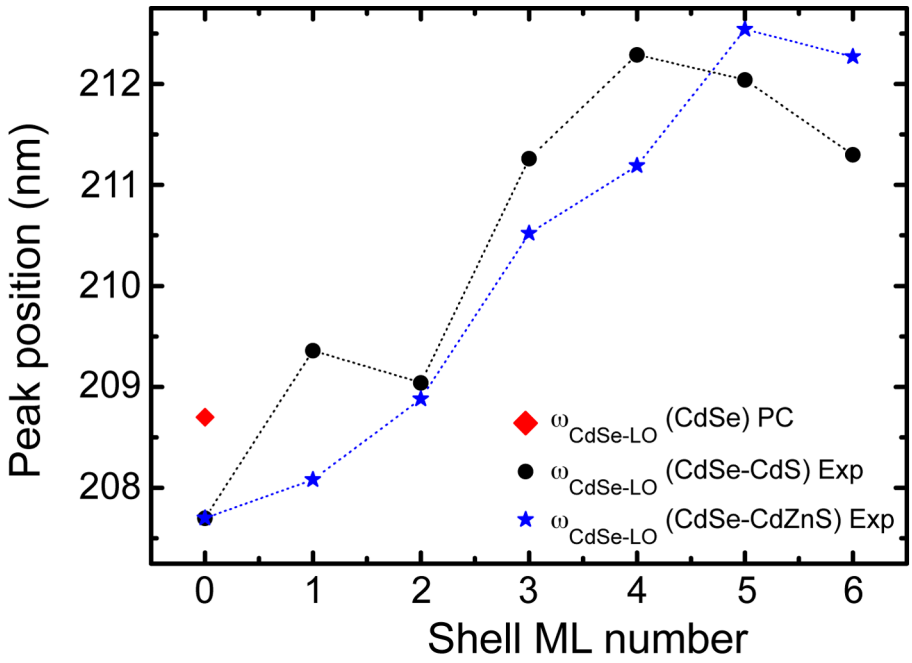

Figure 5.3: Longitudinal optical phonon band position for CdSe in CdSe-CdS and CdSe-$Cd_{0.5}Zn_{0.5}S$ QDs as a function of shell MLs (lines are just guide for eyes). From the peak position shift it is possible to evaluate Dc/c for CdSe cores due to the growth of shell multilayers. The point at 0 ML refers to core CdSe (*i.e.* QDs with 3.8 nm of diameter). The red diamond represents the CdSe expected Raman shift, calculated by PCM.

The PCM and experimental value differ by 1 cm^{-1}, which can be ascribed to the surface tension present on the dot surface. The compressive stress on our NCs surface, evaluated using the Laplace relation,[139] is about 0.67 GPa. When this is considered in accordance with the Grüneisen differential relationship, given by

$$\frac{\Delta\omega}{\omega} = \left(1 + 3\frac{\Delta c}{c}\right)^{-\gamma} - 1, \qquad \text{(Eq. 5.1)}$$

where γ stands for the Grüneisen parameter, which relates the effect of the hydrostatic component of the strain to changes of the phonon frequency, c is the lattice parameter and ω is the original Raman frequency[53].

This gives rise to a shift of the LO1 band by about 1 cm^{-1}.[115] The final difference between the experimental and the PCM LO1 position falls well below our instrumental resolution (~ 1 cm^{-1}).

5.2.2. SERRS of CdSe-CdS quantum dots

SERRS spectra of CdSe-CdS QDs are presented in Figure 5.4.a-c as a function of shell thickness at RT, which accounts for all the possible changes of conduction bands[45] from low temperature used in previous studies.[53]

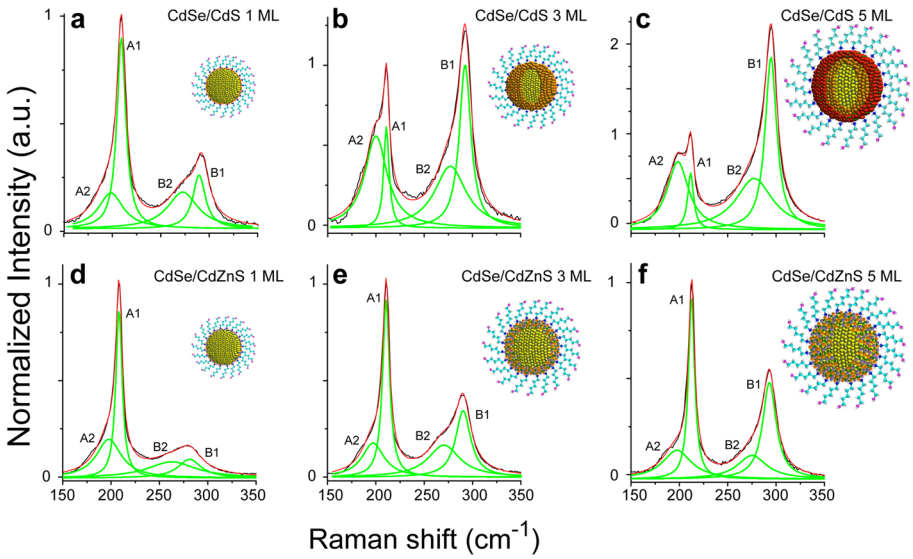

Figure 5.4: SERRS spectra of CdSe and CdS like bands for different number of ML of CdSe-CdS and CdSe-$Cd_{0.5}Zn_{0.5}S$ QDs. All spectra are normalized to the maximum of the A band (note the relative y axes). In the insets, schematic representations of CdSe-CdS and CdSe-$Cd_{0.5}Zn_{0.5}S$ QDs with different shell MLs number are reported.

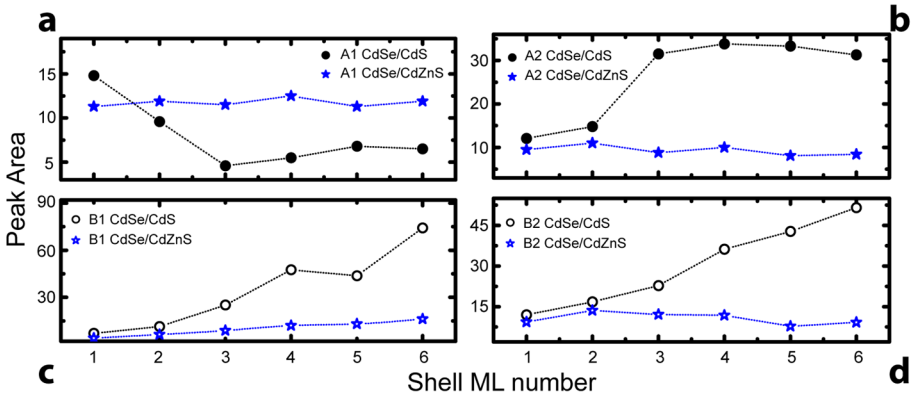

Figure 5.5: Longitudinal CdSe (A1) phonon bands area for CdSe-CdS and CdSe-$Cd_{0.5}Zn_{0.5}S$ QDs; b. CdSe (A2) phonon bands area for CdSe-CdS and CdSe-CdZnS QDs; c. Longitudinal CdS (B1) phonon bands area for CdSe-CdS and CdSe-$Cd_{0.5}Zn_{0.5}S$ QDs; d. CdS (B2) phonon bands area for CdSe-CdS and CdSe-$Cd_{0.5}Zn_{0.5}S$ QDs. In all spectra, lines are just guide for eyes.

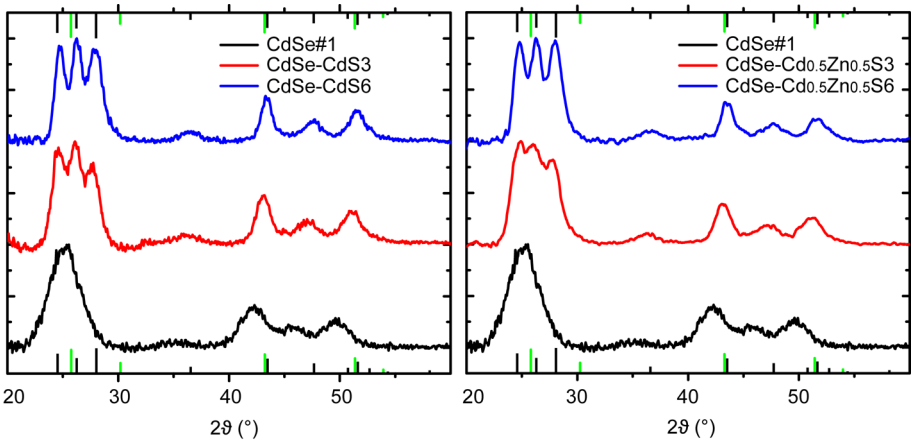

Figure 5.6.a: X-ray diffractograms for CdSe-CdS and CdSe-$Cd_{0.5}Zn_{0.5}S$ for different number of ML. X- ray diffraction was performed on core-shell QDs drop casted onto glass slides from ~ 50 μM solutions. Black and green segments represent the 2ϑ reflections expected from bulk CdSe in its wurtzite and zinc blende phase, respectively. Predominant wurtzite structure of CdSe#1 cores is maintained and reflections shift to higher angles with shell growth. Such phenomena, together with the absence of peak broadening, suggest epitaxial growth with consequent CdS (or $Cd_{0.5}Zn_{0.5}S$) lattice expansion and core lattice compression.

Table 5.2: QDs overall diameter (*d*, nm), experimental CdSe and CdS LO phonon frequencies (in cm^{-1}) and related lattice parameter variation, $\Delta c/c$[140,141] (negative and positive values means compressive and tensile strain, respectively). In table the relative band areas of all the LO and SO Raman features for CdSe-CdS QDs with shell from 1 to 6 ML are also reported.

MLs	*d* (nm)	A1 (cm^{-1})	$\Delta c/c$ CdSe (%)	A1 area	A2 area	B1 (cm^{-1})	$\Delta c/c$ CdS (%)	B1 area	B2 area
1	4.81	208.4	-0.10	14.8 ±0.9	12.1 ±1.1	290.4	0.98	7.1 ±0.9	12.0 ±1.2
2	5.77	209.0	-0.19	9.6 ±0.8	14.8 ±2.3	289.2	1.09	11.4 ±2.0	16.8 ±6.5
3	6.55	211.3	-0.51	4.6 ±1.5	31.5 ±5.1	292.9	0.77	25.1 ±2.4	22.8 ±6.5
4	7.23	212.3	-0.66	5.5 ±2.5	33.8 ±8.7	294.5	0.64	47.5 ±5.9	36.2 ±5.4
5	7.95	212.0	-0.62	6.8 ±1.0	33.3 ±3.4	294.9	0.61	43.7 ±1.9	42.8 ±2.6
6	8.52	211.3	-0.52	6.5 ±0.7	31.3 ±1.7	295.8	0.53	74.2 ±7.8	51.6 ±3.7

Table 5.3: QDs overall diameter (*d*, nm), experimental CdSe and $Cd_{0.5}Zn_{0.5}S$ LO phonon frequencies (in cm^{-1}) and related lattice parameter variation, $\Delta c/c$ (negative and positive values means compressive and tensile strain, respectively). In table the relative band areas of all the LO and SO Raman features for CdSe-$Cd_{0.5}Zn_{0.5}S$ QDs with shell from 1 to 6 ML are also reported.

MLs	*d* (nm)	A1 (cm^{-1})	$\Delta c/c$ CdSe (%)	A1 area	A2 area	B1 (cm^{-1})	$\Delta c/c$ CdS (%)*	B1 area	B2 area
1	4.37	208.1	-0.06	11.3 ±0.5	9.5 ±0.4	281.2	1.80	4.0 ±0.8	9.3 ±1.0
2	5.01	208.9	-0.17	11.9 ±0.4	11.0 ±0.4	286.8	1.29	6.3 ±0.1	13.6 ±1.4
3	5.73	210.5	-0.41	11.5 ±1.2	8.8 ±1.6	290.3	0.99	8.9 ±0.9	12.1 ±1.0
4	6.45	211.2	-0.50	12.5 ±0.4	10.0 ±0.6	292.0	0.85	12.0 ±0.4	11.8 ±1.6
5	6.98	212.5	-0.69	11.3 ±0.3	8.1 ±0.8	293.2	0.75	13.1 ±0.3	7.8 ±1.2
6	7.51	212.3	-0.65	11.9 ±0.4	8.4 ±1.0	294.1	0.67	16.2 ±1.2	9.2 ±1.1

*CdS "like" band

Each spectrum shows prominent Raman bands centered at ~ 209 cm^{-1} (A band) and 290 cm^{-1} (B band). As for the CdSe QDs, the A band is a convolution of two peaks - the longitudinal optical CdSe phonon mode (LO1) centred at ~ 209 cm^{-1} (A1 band) and a surface optical phonon mode (SO1) centred at ~ 200 cm^{-1} (A2 band). A comparison of the integrated intensities of both bands provides insight into the variation of the bulk-to-surface structure. The integral of the A2 band strongly increases with increasing shell thickness and exceeds the contribution of the A1 band above 3 CdS MLs (Figure 5.4.b, Figure 5.5 and Table 5.2). For thicker shell thicknesses, the integral of the A2 band saturates (Figure 5.5.b). This behaviour suggests that such a band is not only due to surface optical phonon modes, but there is also an additional contribution due to the formation of a $CdSe_xS_{1-x}$ alloy that radially extends out by ~ 1 nm (*i.e.*. 3 CdS MLs) from the core, as already described by Tschirner *et al.* and Garcia-Santamaria *et al.*.[40,53] Conceivably, the alloy formation must involve anionic interfacial diffusion from within the CdSe core.[40,142] This is verified by the lowering of the A1 band area up to three MLs of CdS before saturation. The deconvolution of the A2 band (as the B2 band, *vide infra*) is not possible because Raman bands at RT are intrinsically larger with respect to those measured at liquid helium temperature.[53]

The alloy formation is further confirmed by analyzing the second Raman feature peaked at 290 cm^{-1}. This B band also exhibits two main contributions: a longitudinal optical phonon mode originating from CdS, centred at ~ 290 cm^{-1} (B1 band), and a second peak at ~ 275 cm^{-1} (B2 band). The latter peak is composed of two contributions: the surface optical phonon modes of CdS[143] and the interfacial alloy layer formed between the CdSe core and CdS shell.[40,53,144]
As expected, the integrated area of B1 and B2 bands continuously increase with increasing CdS shell thickness (Figure 5.4.a-c and Table 5.2). A comparison of the A1 and B1 peak frequencies shows a gradual blue-shift with an increased shell growth. This behaviour is associated with the variation of the bond length in the CdSe and CdS lattices as caused by interfacial lattice strain. X-ray diffraction (XRD) measurements confirm this finding (Figure 5.6.a).[53]

The variation of the lattice parameter[137] in lattice strained QDs can be evaluated employing the Grüneisen equation.[145] The outcomes of this analysis for different CdS MLs are reported in Table 5.2 ($\Delta c/c$ values) and are consistent with previous results on CdSe/CdS NCs.[53] The lattice parameter of CdSe is about 4% higher with respect to CdS one. Such a difference in lattice constant leads to a compressive strain (negative $\Delta c/c$ values) in the core and tensile one in the shell (positive $\Delta c/c$ values), responsible for the aforementioned lattice parameters variation.

5.2.3 SERRS of $CdSe/Cd_{0.5}Zn_{0.5}S$ quantum dots

In Figure 5.4.d-f the SERRS spectra of CdSe-$Cd_{0.5}Zn_{0.5}S$ as a function of shell thickness are presented. Analogous to that for CdSe-CdS, we observe Raman bands centred at ~ 208 cm^{-1} (A band) and ~ 290 cm^{-1} (B band). The deconvolution of each band with two Lorentzian functions confirm again the existence of the CdSe longitudinal optical phonon band at ~ 208 cm^{-1} (A1

band) and a CdS "like" longitudinal optical phonon mode at ~ 290 cm^{-1} (B1 band). The appearance of this latter contribution has been already reported for CdSe-ZnS QDs.[142,144] It was attributed to the formation of a mixed CdZnS(Se) alloy layer.[146] In this case, the CdS "like" signal is due to the presence of CdS in the shell composition. As is shown in Table 5.3, the integrated areas of the B1 bands exhibit a slight increase with increasing shell thickness. This is consistent with a gradual increase in the Cd-S bond concentration during the shell growth. Meanwhile, the A1, A2 and B2 bands remain almost constant during shell growth (Figure 5.5). This indicates that, unlike for CdS shells, interdiffusion between the CdSe core and the $Cd_{0.5}Zn_{0.5}S$ shell is confined to the first shell ML (~ 0.3 nm).

The abrupt nature of the CdSe-$Cd_{0.5}Zn_{0.5}S$ interface must induce significant stress across the nanocrystals. To better appreciate this, an analogous analysis as for CdSe-CdS was utilized to determine the extent of lattice parameter variation by comparing the frequencies of the A1 and B1 bands (Table 5.3). This analysis shows that the $Cd_{0.5}Zn_{0.5}S$ shell induces strain on the nanocrystals that modifies its bond length – a conclusion that is confirmed by XRD measurements (Figure 5.6). Interestingly, the extent of stress in the nanocrystals appears to level off after ~ 5 MLs of growth. In comparison, the stress is relieved within ~3 MLs in CdSe-CdS. This suggests that for CdSe-CdS QDs the stress for the core is relived more effectively with respect to CdSe-$Cd_{0.5}Zn_{0.5}S$. This is probably due to the lattice mismatch difference between the two shelling materials. The observed $CdSe_xS_{1-x}$ alloy formation, with the associated increase of the lattice parameter, further contributes to the stress relief.

Alloying of CdSe-ZnSe core/shell nanocrystals to form CdZnSe nanocrystals has been previously reported.[147] The transition temperature to induce this behaviour was found to be in excess of 270 ^oC. For the CdZnS case, because of the same ions involved (and the comparable average lattice parameters of $Cd_{0.5}Zn_{0.5}S$ and ZnSe)[148] one may expect similar temperatures for an efficient ions diffusion. For the synthesis of CdSe-$Cd_{0.5}Zn_{0.5}S$ nanocrystals, the growth temperature was limited to 250 ^oC (see Chapter 3.3.5). Notably, this is practically the maximum growth temperature to achieve high quality core-shell nanocrystals. The experimental results show that for QDs obtained with our synthetic route the temperature is insufficient to allow the ions diffusion for any significant interfacial alloying to occur. A direct outcome of this finding is that $Cd_{0.5}Zn_{0.5}S$ cannot be used directly as a material to smooth the confinement potential because it forms an abrupt interface with CdSe.

5.3 A Roadmap for Optimizing Core-Shell QDs - I

A defect free, epitaxially grown shell is instrumental to achieving high fluorescence yields in core-shell QDs. In addition to these linear optical properties, Cragg and Efros[46] have reported that "smoothing out" the confinement potential in NCs results in a reduction of three orders of

magnitude for the Auger recombination rate. Such "smoothing" is well satisfied by $CdSe_xS_{1-x}$ alloy formation in CdSe-CdS QDs. However, for thin shell thicknesses, it also enables sufficient electron and hole delocalization towards the outer surface, which is plagued by surface traps that reduce fluorescence yields.[45] To overcome this problem, "giant" nanocrystals have been grown but, as aforementioned, such large QDs may present problems. On the hand, SERS technique result reported in this chapter demonstrates that the attempt to directly use $Cd_{0.5}Zn_{0.5}S$ (that presents a stronger electronic confining potential with respect of CdS) to obtain smaller QDs does not allow preserving the smoothing of the confinement potential. Namely, SERS has been employed (for the first time) as a tool to study the core-shell interface of CdSe-$Cd_XZn_{1-X}S$ QDs at RT. For both core-shell systems the LO phonon peaks provided insight into the interface formation between the different materials in the QDs. CdSe-CdS QDs were found to exhibit alloy formation with a radial extension of ~ 1 nm (*i.e.* 3 ML). In the CdSe-$Cd_{0.5}Zn_{0.5}S$ case an abrupt interface limited to ~ 0.3 nm (*i.e.* 1 ML) was observed.

The key to obtain small and performing QDs with a smoothed confinement potential resides in the mitigation of excitons delocalization in CdS using $Cd_{0.5}Zn_{0.5}S$ as an over-layer. This solution provides a graded shell composition framed by subsequent higher-bandgap materials thus strongly confining excitons away form the defectives outer surface. This rationalization is likely to explain the origin of the extremely high QY values and the low ASE and lasing[43,44] thresholds observed for CdSe-CdS-$Cd_{0.5}Zn_{0.5}S$-ZnS QDs, where a final ML of ZnS is sufficient to provide a last "electronic" barrier against electron-hole delocalization and ultimately to improve the chemical stability (Figure 5.7).

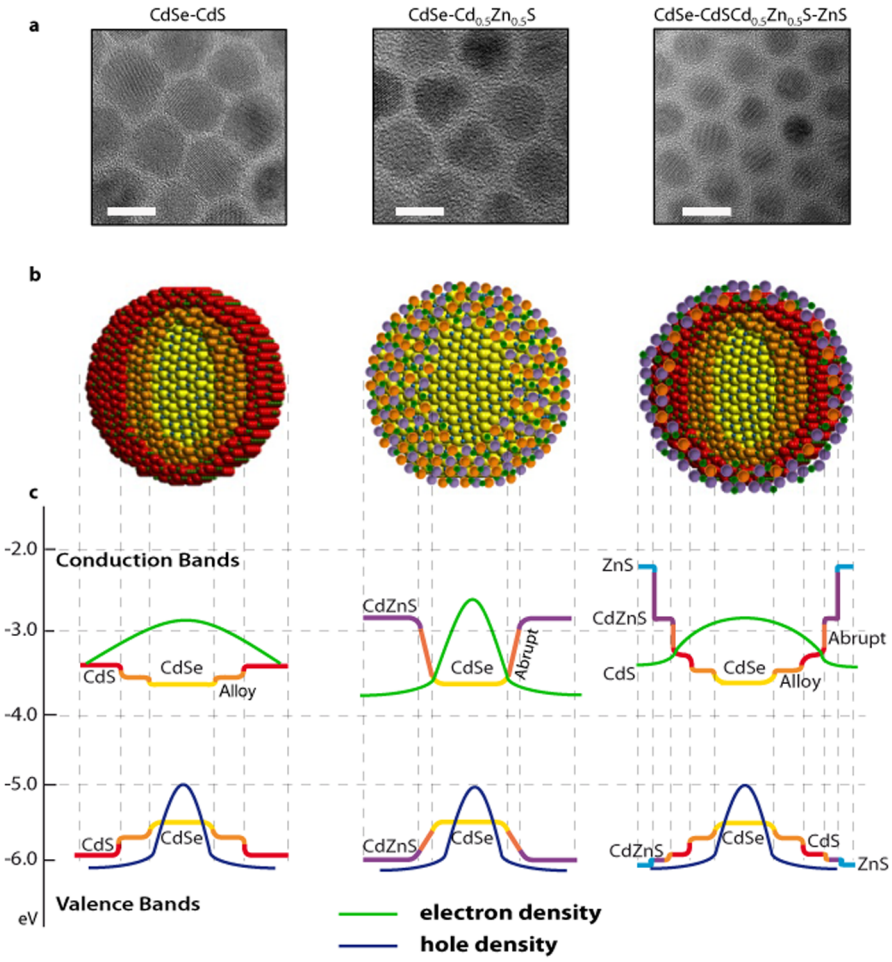

Figure 5.7: HRTEM micrographs (a), cross-sectional core-shell structure depiction (b) and a schematic representation of the electronic (hole) density distribution (c) of CdSe-CdS, CdSe-Cd$_{0.5}$Zn$_{0.5}$S and CdSe-CdS/Cd$_{0.5}$Zn$_{0.5}$S/ZnS QDs. The scale bar in (a) represents a 10 nm length. The vertical scale bar in (c) is relative to vacuum and the represented energy levels are that of the bulk materials.

Chapter 6.

EXCITON DYNAMICS IN CdSe-$Cd_XZn_{1-x}S$ QDs

The Role of the core-shell interface - I

The shell thickness and composition of CdSe-$Cd_xZn_{1-x}S$ core-shell quantum dots are critical parameters for the efficiency of such materials as light emitters. This section provides a detailed study into the optical absorption and PL properties of CdSe-CdS, CdSe-$Cd_{0.5}Zn_{0.5}S$ and CdSe-ZnS QDs with varying shell thickness. The single-exciton recombination dynamics of these systems are analyzed by means of TCSPC technique and directly related to the specific core-shell interfaces of the various QDs studied using a phenomenological kinetic model. This chapter aims to demonstrate the central role of the core-shell interface on both steady state photoluminescence and exciton recombination dynamics in these systems.
Section 6.1 provides some fundamentals about the effects of exciton-surface trap interaction on the exciton recombination. Next, in Section 6.3 results of the preliminary steady-state absorption and PL data are reported, while in Section 6.3 results from TCSPC (tPL) experiments are reported and the kinetic model here used for data fitting is introduced. The results of the fit are discussed in Section 6.4. A concluding Section 6.5 collects some final comments and perspectives.

Main results presented in this section are extracted from a paper published in 2014:
Minotto, A.; Todescato, F.; Fortunati, I.; Signorini, R.; Jasieniak, J. J.; Bozio, R.
Role of Core−Shell Interfaces on Exciton Recombination in CdSe− CdxZn1−xS Quantum Dots
The Journal of Physical Chemistry C **2014**, 118 (41), 24117-24126.

6.1 Charge-Trapping in colloidal QDs: State of the art

The main advances in light emitting performances by QDs have predominantly occurred for the prototypical colloidal CdSe based system, for which high QYs have been achieved[78]. Due to the high surface/volume ratio, numerous surface defects are present in QDs and represent the main source for luminescence quenching. High QY, up to ~100%, can be reached by covering the core surface with an inorganic semiconducting shell, which allows passivation of the so-called surface traps[33,149]. In type-I core-shell hetero-structures[12,75,150] (Chapter 1.2) the band gap of the

shell material is larger with respect to that of the core and the electronic structure is such that the exciton is confined within the core. In this way, the interaction with surface defects is heavily suppressed enhancing, thus, the emitting properties of the QDs.

Due to the high surface to volume ratio, the charge-trapping mechanism has always been considered the main problem to overcome. Understanding what surface traps are, i.e charged uncoordinated surface sites[151,152], and what their effect is on the optical performances has gradually emerged[149,153,154]. Great attention has also been dedicated to determine which mechanisms are responsible for charge trapping, in order to explain the very long (up to μs regime[33,155–158]) QD radiative lifetimes, and to possibly define a guideline to synthesizing trap-unaffected QDs. Jones *et al.* in 2009[33,155] and Mooney *et al.* in 2013[157,158] presented an electron-transfer (ET) kinetic interpretation, based on Marcus ET theory[37,159,160]. Their studies highlighted the main peculiarity of QD exciton recombination dynamics: traps are not infinitely long-living charge accumulators but, especially at RT temperature, de-trapping is energetically favored. De-trapped charges can radiatively recombine, with a delay that is coherent with the long stretched PL decays observed. Moreover, long living charged states, mainly localized on the surface, are the principal source for single QD PL blinking[37,161], Auger non-radiative recombination[36,162]. In non-shell passivated CdSe and CdS QDs trapped excitons can also radiatively recombine, leading to a red-shifted emission band, broader compared to the intrinsic neutral exciton emission band.[157,158]

The structural and photophysical factors that boost QD optical properties are well-known[43,44,79,163]. The best optical performance in terms of radiative recombination rate were achieved by CdSe-CdS core-shell "giant" nanocrystals (up to 20 shell monolayers), in which the interaction of charges with surface traps is heavily reduced by the shell thickness. As already stressed out in the previous Chapters, the main drawback of these CdSe-CdS "giant" QDs is encountered when moving towards the final integration in neat thin films, as their massive size limits the colloidal stability and, intrinsically the packing density. In light of the results of Chapter 5[41] and as suggested by the work of Javaux,[45] development of QD synthesis should aim to a more graded composition at the core-shell interface and a final shell layer with a high band gap (*i.e.* ZnS) to prevent long lifetime electron trapped states. Core-shell graded QDs, with radially increasing concentration of Zn^{2+} ions from core to the outer shell, meet both these requirements in a compact hetero-structure. Results of previous works[43,44,48] show that CdSe-CdS-$Cd_{0.5}Zn_{0.5}S$-ZnS graded core-shell QDs seem to be the best promising candidates to produce RT high performing light emitting devices.

In order to maximize the optical performance of core-shell QDs, it is necessary to understand how the structural properties influence the exciton recombination process. In this section the optical properties of CdSe-$Cd_xZn_{1-x}S$ mixed-composition shell QDs, with x=0, 0.5 and 1, are compared. The present PL study provides a kinetic model that, together with the study of steady

state and tPL (by means of TCSPC), allows the detection of a secondary trap distribution. This result is in favor of what previous theoretical and experimental works already suggested: traps are mainly located at the outer surface[33,151,152], but a considerable amount of traps are also expected at the core-shell interface[33,149]. Shell thickness so far has precluded a satisfactory identification of such traps by means of conventional surface science techniques. Most importantly, combined with the detection of alloying effects at core-shell interface presented in the previous chapter,[40,41,53] the model here employed demonstrates that the evolution of such interface after shell growth is strongly correlated with the dependence of QY, single-exciton radiative lifetime and extent of trap-exciton coupling on shell thickness and composition.

6.2 Steady-State optical characterization of CdSe-$Cd_XZn_{1-x}S$ QDs

CdSe#1 QDs with a 3.8 nm diameter were overcoated by CdS, $Cd_{0.5}Zn_{0.5}S$ or ZnS shells using the SILAR approach[78,105]. The shell thickness ranges from 1 – 6 MLs (Table 6.1).

Table 6.1: CdSe and core-shell QDs average diameter (*d*, nm) and absorption band-edge (peak, nm). In both cases the first excitonic peaks have been measured by means of UV-Visible spectra.

	CdSe-CdS *d* (nm)[a]	CdSe-CdS peak (nm)	CdSe-$Cd_{0.5}Zn_{0.5}S$ *d* (nm)[b]	CdSe-$Cd_{0.5}Zn_{0.5}S$ peak (nm)	CdSe-ZnS *d* (nm)[c]	CdSe-ZnS peak (nm)
0 ML	3.8	577	3.8	577	3.8	5.77
1 ML	4.8	602	4.4	590	4.4	587
2ML	5.8	613	5.0	605	5.0	588
3ML	6.6	618	5.7	611	5.6	597
4 ML	7.2	621	6.5	614	6.2	604
5ML	8.0	623	7	616		
6ML	8.5	624	7.5	618		

[a]Radii here reported are obtained from TEM measurements of ref. [12] for CdSe-CdS QDs synthesized with the same method and with similar CdSe cores. [b]Radii of CdSe-$Cd_{0.5}Zn_{0.5}S$ batch are extracted from TEM images reported in Section 4.1. [c]Dimensions of CdSe-ZnS QDs are estimated by the spherical concentric shell model (CSM), as proposed by ref. [9].

Notably, the ZnS shell thickness was limited to four MLs, likely due to the very high lattice mismatch (12%) with respect to the CdSe#1 core, which did not allow further homogeneous shell growth[39,75]. All QDs were optically characterized at room temperature in toluene colloidal dispersions in order to evaluate the dependence of their optical properties on shell thickness and composition. Particular attention was devoted to PL performances.

6.2.1. UV-Vis absorption

In Figure 6.1a-c we present the absorption spectra of the various core-shell QDs in solution.

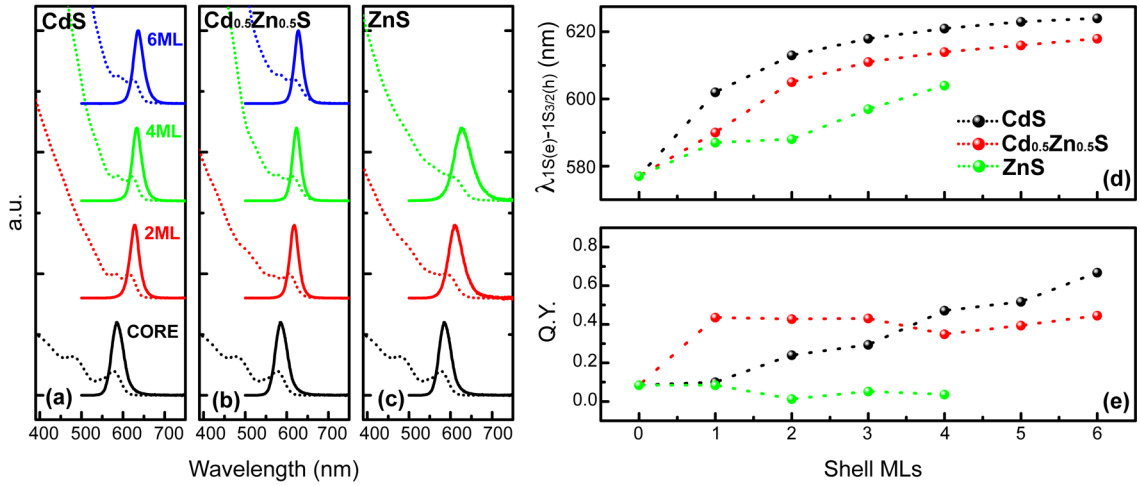

Figure 6.1: (a-c) Absorption (dotted lines) and emission (full lines) spectra of CdSe-CdS (a), CdSe-$Cd_{0.5}Zn_{0.5}S$ (b) and CdSe-ZnS (c) core-shell QDs with different number of shell MLs (0, 2, 4, and 6). (d) First excitonic absorption peak position for CdSe/CdS, CdSe-$Cd_{0.5}Zn_{0.5}S$ and CdSe-ZnS QDs as a function of shell MLs. (e) QY values as at different shell thickness and composition. Dotted lines in (d,e) are just guides for the eyes.

The spectra of these QDs show the typical excitonic structure, discernible in the 400-700 nm (1.77-2.10 eV) range. These bands represent the allowed optical transitions from the CdSe valence subbands[93] to discrete conduction band states. Some general trends connected with the growth of of CdS and ZnS have already been discussed in Section 4.1.

Absorption spectra of core-shell series in Figure 6.1 show other important qualitative results linked to the different chemical composition of QDs. Neglecting, for simplicity, the behavior of samples with only one shell ML, it is clear that in "Zn-rich" materials ($Cd_{0.5}Zn_{0.5}$Sand ZnS shell) the red-shift of the first absorption peak is less pronounced with respect to the "Cd-rich" ones (Figure 6.1). Such behavior stems from the better confinement of charge carriers inside the core of the hetero-structure and is due to the increase of the band gap of the shell moving from CdS to "Zn-rich" materials (Figure 5.7)[39]. A secondary aspect noticed in Figure 1 is the broadening of the characteristic first absorption peak for the CdSe-ZnS QDs, as reported in Figure 6.2.a.

As already mentioned in previous chapters, this broadening is due to imperfections during the growth of the shell and arises from the aforementioned high lattice mismatch between the CdSe cores and ZnS. The particle size dispersion is thus enhanced, and irregular non-spherical particles can be obtained[39,75] because of the anisotropy of the surface energy imposed by lattice defects in the wurtzite crystal structure. Such hypothesis is supported also by the anomalous behavior of the exciton band-edge red-shift versus shell MLs (Figure 6.1.d).

In summary, Zn concentration and lattice mismatch are responsible for the broadening of the absorption peak, but consequences are even more pronounced in the PL performances of the core-shell QDs.

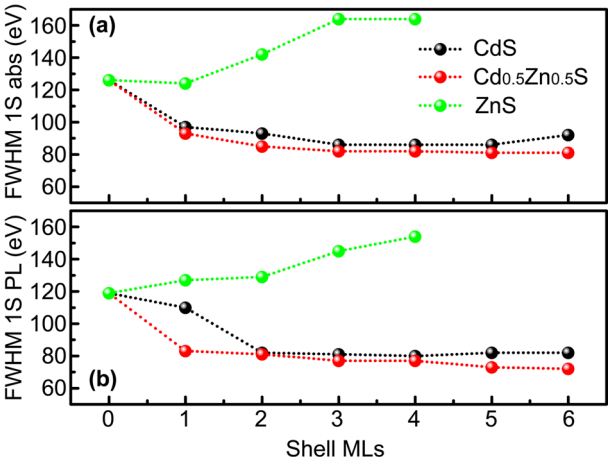

Figure 6.2: FWHM of the band-edge absorption band (a) and PL (b). In order to extract the FWHM of the first excitonic absorption peak absorption spectra were fitted to several Gaussians[164].

6.2.2 Steady-state PL

PL spectra and QY evaluations were performed for all the CdSe core-shell structures. (Figure 6.1). The QDs present a sharp emission peak with a FWHM of ~30 nm. The Stokes shift is ~10 nm (i.e. ~30 meV), consistent with values predicted by theory[93]. Similar to the linear absorption results, a red shift of the 1S(e)-$1S_{3/2}$(h) transition energy can be observed in all series (Figure 6.1.a-c). Additionally, under our experimental conditions no secondary red shifted deep-trap states emission band was registered[158]. Therefore, alternative radiative processes can be neglected in the QDs studied here and the PL spectra originate from the 1S(e)-$1S_{3/2}$(h) transition. Again, a broadening (Figure 6.2.b) of the emission feature is observed in ZnS shell samples, due to the lattice mismatching between CdSe and ZnS[75]. On the other hand, CdSe and CdS have similar lattice parameters (low lattice mismatch, ~4%) allowing an epitaxial shell growth[40,41,53]. As demonstrated by Mews *et al.* in 2005[39], the consequences of the lattice mismatch are even more evident for the QY. In fact, the QY is strongly correlated with the probability of interaction between exciton and charge-traps: higher interaction leads to a lower emission efficiency. Direct evidence of this is the blinking that affects QDs emission[37,161]. Because of such phenomenon, in a certain time-window, across the entire QDs ensemble a certain number of QDs are active emitters and the remaining fraction will be "dark" QDs[33,155,158].

The QY dependence on shell thickness and stoichiometry is reported in Figure 6.1.e. The QY increase with CdS shell growth is well known in literature[39] and is consistent with the above considerations on the structural similarity of core and shell. Additionally, previous studies demonstrated that with conventional synthesis methods it is possible to create and control[40,41,53,165] ions interdiffusion through CdSe core and CdS shell interface. Such diffusion is controlled both by core-shell lattice mismatch[166] (~4% for bulk materials), synthesis temperature[147,167]. Furthermore, refined synthesis methods (cation exchange[81] and modified SILAR technique[80]) allow the control over the extent of the mixed layer. As stated before, a

smooth variation of the interface composition and, consequently, makes core photo-generated charges feel a gradual change of potential when leaking into the shell. This last occurrence also intrinsically lowers AR rate, as already demonstrated theoretically and experimentally[40,46].

As expected, ZnS directly grown on the same bare CdSe cores, with the same synthesis conditions, does not provide any improvement in QY, it rather causes a drop of the efficiency. When lattice mismatch is too large (~12% at CdSe-ZnS interface) and synthesis temperature is too low to permit ion interdiffusion[147], strain is released by defect formation[39,75]. Core-shell epitaxial growth is in fact completely lost following the first monolayer, as shown by the Raman results reported in Figure 6.3.

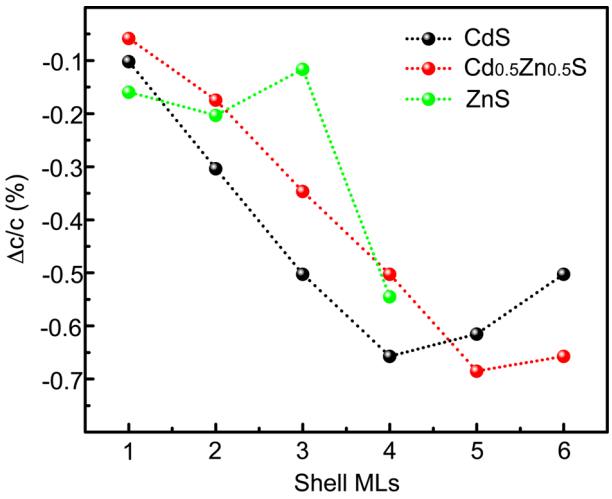

Figure 6.3: CdSe core lattice compression, induced by CdS, $Cd_{0.5}Zn_{0.5}S$ and ZnS shell growth. Lattice strain was measured by Raman technique, with the same procedure reported in the previous section.

For the CdSe-$Cd_{0.5}Zn_{0.5}S$ series a somewhat different behavior was observed: a steep increase of QY is registered after the first shell ML deposition (from 8% to 43%, Figure 6.1.e), then the QY saturated. The steep QY increase can be justified by the fact that $Cd_{0.5}Zn_{0.5}S$ (compared to CdS) provides a higher confining potential, thus minimizing the shell MLs necessary to efficiently confine the exciton from the outer surface. On the other hand, the QY independence on shell thickness can be rationalized by considering the previous Raman study (Chapter 5)[41], which demonstrated that, compared to CdS, $Cd_{0.5}Zn_{0.5}S$ shell provides an abrupt core-shell interface with CdSe, with no progressive ion interdiffusion. At the same time, a good degree of epitaxy is maintained, as demonstrated by both Raman and X-ray diffraction[41] (Figure 5.6). Compared to CdSe-ZnS dots, lattice mismatch is lower, so that the influence of defects on emission performance is limited. However, strain still promotes some defect/trap formation, whose occurrence becomes statistically significant to influence the PL efficiency in a QD ensemble.

Differences in the density and nature of the trap states will modify the extent of their coupling to excitons[33,154], which in turn will influence the QYs of the resulting QD ensembles. By studying

the exciton recombination dynamics (PL decay) it is possible to directly probe the kinetics of charge-traps interaction and gain more information about traps.

6.3 Transient PL

The single dot radiative rate for CdSe nanocrystals was theoretically calculated and experimentally measured in the pioneering works by Efros and Bawendi[93,168]. When the PL decay of an ensemble of QDs is studied, charge trapping/de-trapping and exciton intrinsic recombination add together giving a multi-exponential decay[33], with an average lifetimes ($< \tau >$) that is longer than the intrinsic exciton recombination process[155]. Importantly, by resolving each of the multiple components within the PL decay, one attains a glimpse into each of the recombination processes involved.

In order to understand the influence of core-shell interfaces and shell thickness on exciton recombination dynamics, time-resolved PL experiments were performed by means of technique (Figure 6.4).

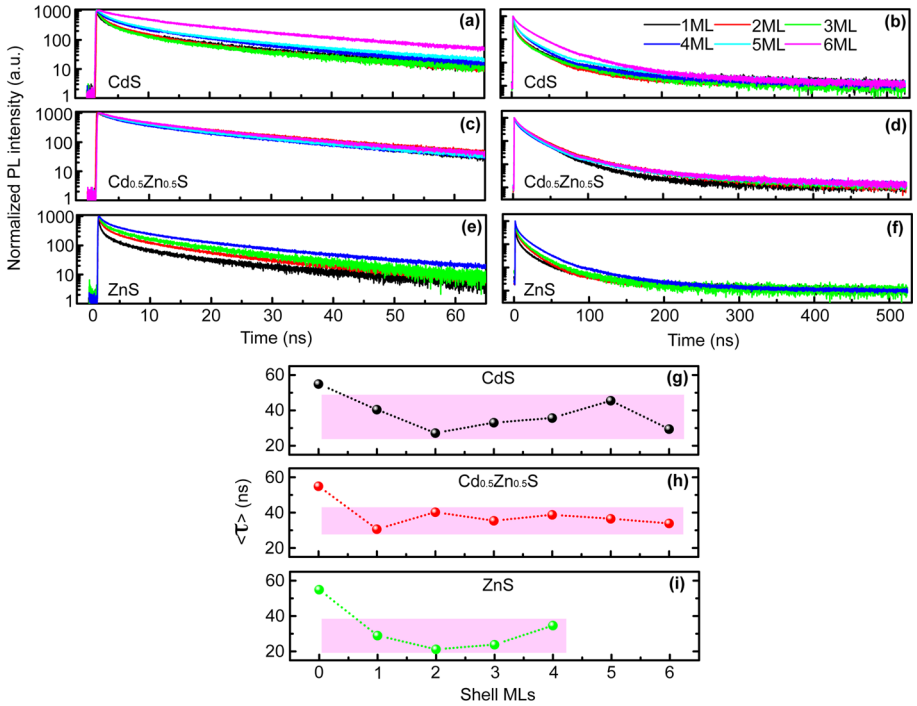

Figure 6.4: (a-f) Normalized time resolved PL decays. (g-i) Average lifetimes, $< \tau >$, as a function of the shell thickness, obtained by a tri-exponential fit of PL decay traces; (a, b) describe CdSe-CdS series, (c, d) CdSe- $Cd_{0.5}Zn_{0.5}S$, (e, f) CdSe-ZnS. Dotted lines in (g-i) are just guides for the eyes.Pink shadows are just to highlight the different $< \tau >$ variability as a function of the shell thickness.

In Figure 6.4.a-f we show the resulting PL transients up to 65 ns and 524 ns for clarity. The PL decays were measured at RT and three exponentials were required for their complete fitting

(fitting procedure was discussed in Chapter 3.4, while an example of tri-exponential fitting for CdSe cores is reported in Figure 6.5).

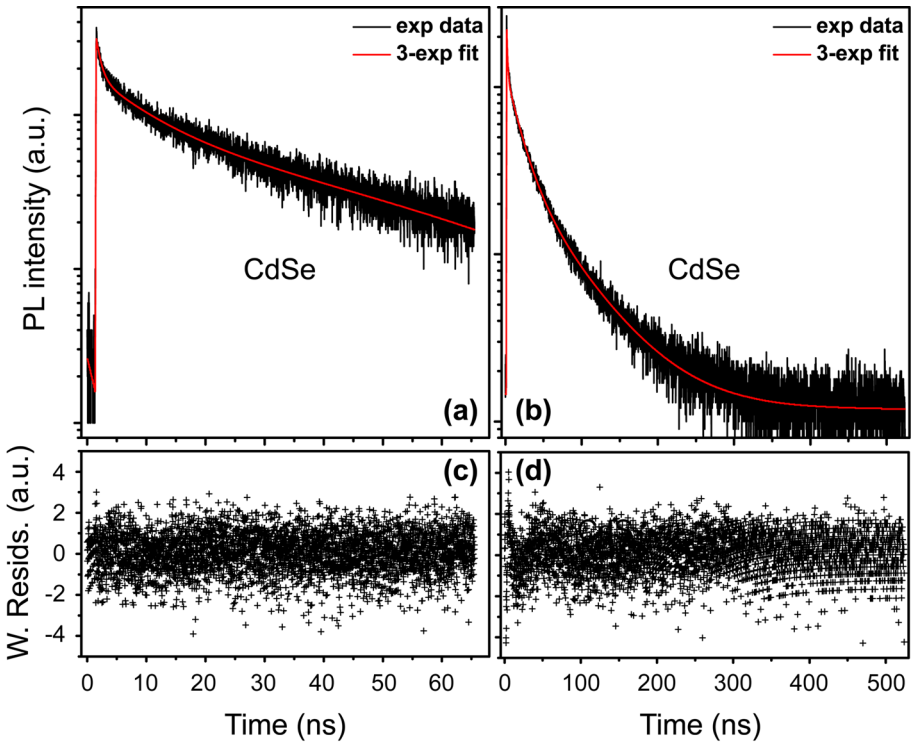

Figure 6.5: (a, b) Time resolved PL decays (black lines) of CdSe cores at two time resolutions: 16 ps SPAD binning time for fast rates accuracy (a) and 128 ps SPAD binning time for slower decay rates (b); red lines represent tri-exponential fit of experimental data. (c, d) Relative weighted residuals after tri-exponential fit of data.

The extracted rates of each exponential decay process, reported in Table 6.2, confirm that the QD PL decay is a combination of different processes, operating at different time scales. The intermediate rate (Γ_2) is consistent with the intrinsic radiative decay, since its frequency scale ($\sim 0.100\ ns^{-1}$) matches the typical exciton recombination rate at RT[33,93]. Meanwhile, the rates Γ_1 and Γ_3 are likely to be associated with traps that modify the PL decay process, with the faster (slower) component Γ_1 (Γ_3) related to a generic trapping (de-trapping) mechanism. However, each rate can't be unambiguously assigned to a definite process: in fact, in some previous works[164], the slowest decay component was associated to the pure radiative rate. Moreover, Γ_n components might have different physical origin moving from bare CdSe cores to different core-shell QDs.

Table 6.2: Lifetime weighted amplitudes (A_N) and exponential rates (Γ_N) extracted from the tri-exponential fit of TCSPC rough data.

QD	*A1*	Γ_1 [ns^{-1}]	*A2*	Γ_2 [ns^{-1}]	*A3*	Γ_3 [ns^{-1}]
CdSe	0.02	**1.201**	0.15	**0.110**	0.83	**0.015**
-CdS 1ML	0.08	**1.086**	0.32	**0.131**	0.60	**0.015**
-CdS 2ML	0.11	**1.004**	0.36	**0.126**	0.52	**0.021**
-CdS 3ML	0.12	**1.000**	0.31	**0.137**	0.57	**0.018**
-CdS 4ML	0.11	**0.559**	0.40	**0.096**	0.49	**0.015**
-CdS 5ML	0.10	**0.517**	0.32	**0.090**	0.58	**0.013**
-CdS 6ML	0.08	**0.267**	0.64	**0.053**	0.28	**0.016**
QD	*A1*	Γ_1 [ns^{-1}]	*A2*	Γ_2 [ns^{-1}]	*A3*	Γ_3 [ns^{-1}]
CdSe	0.02	**1.201**	0.15	**0.110**	0.83	**0.015**
-Cd5Zn5 1ML	0.03	**0.660**	0.46	**0.075**	0.49	**0.020**
-Cd5Zn5 2ML	0.03	**0.550**	0.56	**0.064**	0.51	**0.015**
-Cd5Zn5 3ML	0.05	**0.432**	0.49	**0.060**	0.38	**0.014**
-Cd5Zn5 4ML	0.07	**0.427**	0.53	**0.068**	0.43	**0.013**
-Cd5Zn5 5ML	0.08	**0.320**	0.60	**0.064**	0.38	**0.013**
-Cd5Zn5 6ML	0.09	**0.251**	0.46	**0.057**	0.31	**0.013**
QD	*A1*	Γ_1 [ns^{-1}]	*A2*	Γ_2 [ns^{-1}]	*A3*	Γ_3 [ns^{-1}]
CdSe	0.02	**1.201**	0.15	**0.110**	0.83	**0.015**
-ZnS 1ML	0.09	**2.840**	0.31	**0.188**	0.61	**0.022**
-ZnS 2ML	0.10	**1.481**	0.38	**0.146**	0.52	**0.028**
-ZnS 3ML	0.08	**1.131**	0.36	**0.131**	0.56	**0.026**
-ZnS 4ML	0.06	**0.806**	0.35	**0.104**	0.59	**0.018**

Despite their empirical nature, such exponential rates present some detectable trends. Regarding CdS and ZnS shell based series, Γ_1 and Γ_2 decrease with increasing shell thickness, with a steeper slope after 3MLs for CdS. On the other hand, Table 6.2 shows that for $Cd_{0.5}Zn_{0.5}S$ Γ_2 slightly oscillates around an average value of 0.065 ns^{-1}. Moreover, in terms of relative lifetime weighted amplitudes (A_N, defined in previous subsection and representing the % of photons emitted from the Nth exponential decay component), the intermediate rate Γ_2 gives the largest contribution to $Cd_{0.5}Zn_{0.5}S$ PL decays. Such occurrences have a direct effect on PL decay traces, especially in the 0 – 65 ns time region (Figure 6.4a,c,e): CdSe-CdS and CdSe–ZnS PL decays show a clear variability, both at short and long time range. On the other hand, Figure 6.4c shows that CdSe- $Cd_{0.5}Zn_{0.5}S$ QDs PL decays are almost invariant with the shell growth. The degree of PL decay variability is also highlighted in terms of average lifetimes ($< \tau >$, defined in the TCSPC Measurements subsection), plotted in Figure 6.4.g-i. $< \tau >$ values of the three series do not manifest any explicit trend on the shell thickness and span from 20 ns to 60 ns. The longest $< \tau >$ values are registered for the CdSe-CdS series, shortest for CdSe–ZnS one.

As already noted, the observed PL dynamics is the result of a complex interplay of different processes, possibly occurring on overlapping time scales. Therefore, although the analysis of the empirical PL data could be pushed further, the use of an appropriate kinetic model could be more appropriate to disentangle the different contributions and make possible a comparison among different series of core-shell QDs.

6.3.1 Phenomenological Kinetic Model

As mentioned in the Section 6.1, Jones *et al.*[33] have proposed a quantitative interpretation of the >10ns average PL lifetimes in core-shell QDs on the basis of a kinetic model, which accounts for charge trapping in terms of Marcus theory of electron transfer[159]. This model has been used to fit the experimental PL decay curves of solution samples of CdSe-CdS-ZnS core-shell-shell QDs with varying dimension of the CdSe core, collected in a very broad range of temperatures (77 – 300 K). The model contains adjustable parameters consistent with those of classical Marcus ET theory: the reorganization energy (λ) involved in the ET trapping, the free-energy difference (ΔG) and the electronic coupling integral (V) between exciton and trap states. In a QD solution, trap states are continuously distributed in the energy domain (and so is ΔG), but since traps are more likely located at radial regions (QD interfaces and the external surface) spherical symmetry allows assigning a single λ and V to each radial "trap-shell". Trapping and de-trapping rates are derived from these parameters and, along with trap densities and a radiative decay rate, are used in master equations to yield the time evolution of the exciton population. The model thus provides a link between theory and experiments and allows all the above parameters to be obtained through a best fit of the normalized experimental PL decay curves.
It is worth noting that Jones' phenomenological model assumes that the PL Intensity ($I(t)$) is proportional to the total population of the single exciton state ($\rho_X(t)$), by means of a single radiative rate (k_R), and all non-radiative recombination processes are negligible. This first assumption isn't completely valid, as was demonstrated by Fisher *et al.*[168] who showed that the PL decay of each QD in the ensemble is a single exponential, but its lifetime fluctuates in time. Such fluctuations are correlated with intensity fluctuations, *i.e.* the higher the PL intensity the longer the lifetime. In a TCSPC experiment on a QD ensemble, the final PL decay obtained after time-integration of a huge number of excitation processes shows a multi-exponential behavior[168] resulting from many charge trapping/de-trapping and exciton recombination processes. The second assumption in Jones' model is also tentative as it involves a "dark" QD fraction to account for QYs of less than 100%, while neglecting the numerous alternate non radiative pathways which can exist in QDs[157,169].

With the aim of gaining information on the role of variations in thickness and composition of the shell while maintaining a fixed dimension of a CdSe core, a reduced form of Jones' model was applied to analyze the above reported PL data. In particular, in this work data were collected

only at room temperature, therefore the rate parameters: $\gamma_{X\to N}$ and $\gamma_{N\to X}$ for trapping and de-trapping, respectively, are empirical values of the integrals in Eq. (6) of Ref. [155]. The final rate equations read

$$\frac{d\rho_X(t)}{dt} = \sum_N(\gamma_{N\to X}\rho_N(t) - (\gamma_{X\to N} + k_{NR} + k_R)\rho_X(t)) =$$
$$= \sum_N(\gamma_{N\to X}\rho_N(t) - (\gamma_{X\to N} + k_{NR} + k_R)\rho_X(t)) =$$
$$= \sum_N(\gamma_{N\to X}\rho_N(t) - \left(\gamma_{X\to N} + \frac{k_R}{QY}\right)\rho_X(t)) \qquad \text{(Eq. 6.1)}$$

$$\frac{d\rho_N(t)}{dt} = \gamma_{X\to N}\rho_X(t) - \gamma_{N\to X}\rho_N(t) \qquad \text{(Eq. 6.2)}$$

where N identifies a trap-state distribution with total population $\rho_N(t)$. $\rho_X(t)$ is the total exciton population with k_R and k_{NR} representing radiative and non-radiative decay rate. In this case exciton non-radiative recombination cannot be neglected, since some of the QDs show low QY values (Figure 6.1). The right-hand side of Eqn. 1 is obtained by considering that QY = $k_R/(k_R + k_{NR})$[170]. Scheme 6.1 sums up the different processes involved in the exciton recombination.

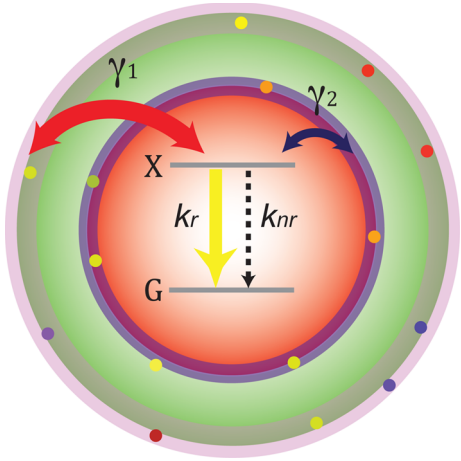

Scheme 6.1: Schematic representation of the exciton recombination process in a prototypical core-shell QD. Double arrows represent the trapping/de-trapping process to/from trap states distributions located at QD outer surface (N=1, pink shaded ring) and core-shell interface (N=2, blue shaded ring). Trap sites are here represented as colored dots. In this scheme N=1 distribution is broader and extends beyond the QD average radius, since surface traps are likely located at surface inhomogeneities related to anisotropic shell growth and ligand binding issues. N=2 here is located at core-shell interface in light of considerations made by us and others. Arrows thickness illustrates the difference in magnitude of trapping (de-trapping) rates to (from) N=1 and N=2 traps distributions.

The k_R and γ values were obtained by non-linear least-square minimization of χ, which is equal to:

$$\chi = \int_0^{t_f}\left(I(t) - K * k_R\rho_X([k_R, \gamma_{X\to N}, \gamma_{N\to X}], t)\right)^2 dt \qquad \text{(Eq. 6.3)}$$

In the last equation, *I(t)* is the multi-exponential fitting function extracted from experimental data. The upper integration limit t_f was set at the maximum time-window of the TCSPC experiment and *K* is a variable scaling factor. A fitting of the tri-exponential function obtained from the experiments could only be obtained by using a minimum of two trap distributions, i.e., N = 1,2 in Eqs. 6.1-6.3. From the peak value of the two trap distributions and their relative reorganization energy and electronic coupling, Jones suggested that the broader one at higher energy originates from surface traps, whereas the narrow one is associated with core/shell interface defects (Scheme 6.1). However some caution should be used as suggested by the same authors and by our results for the PL of the bare CdSe QDs (*vide infra*). Application and accuracy of such phenomenological scheme to model PL decay functions is demonstrated in Figure 6.6.

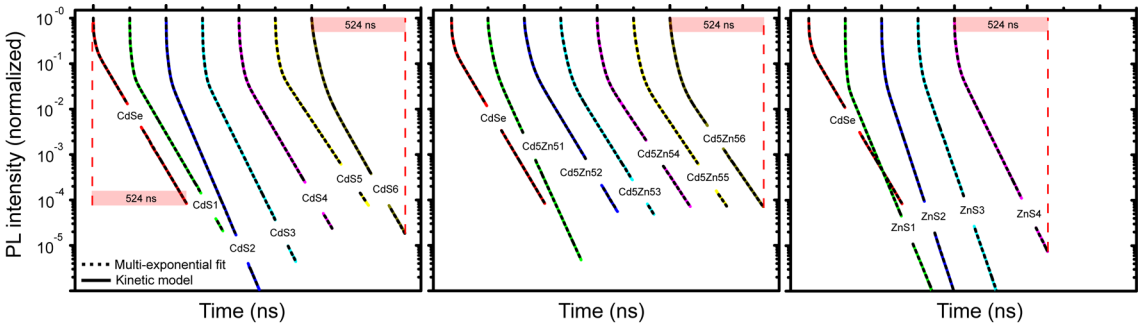

Figure 6.6: Phenomenological model fitting of tri-exponential decay functions, derived from TCSPC data. The model (colored lines) efficiently reproduces decay functions (black dashed lines) for all the samples.

6.4 Discussion of results

The calculated radiative (non-radiative) decay rate k_R (k_{NR}) and the effective trapping (de-trapping) rates, based on modeling of our QD systems, are reported in Figure 6.7 and Table 6.3.

This kinetic model considers the physically realistic QD structure and the associated radial traps states, which unequivocally enables the extraction of the radiative (k_R) and non-radiative (k_{NR}) decay and the trapping/de-trapping rates for different core/shell QDs.

Table 6.3: QDs overall radius (<R> [nm]) and rates calculated using the kinetic model (Eqs. 6.3-5) for CdSe-CdS QDs: trapping ($\gamma_{X\rightarrow 1}$ [ns^{-1}]) and de-trapping $\gamma_{1\rightarrow X}$ [ns^{-1}] rate at outer surface, trapping ($\gamma_{X\rightarrow 2}$ [ns^{-1}]) and de-trapping $\gamma_{2\rightarrow X}$ [ns^{-1}] rate at core-shell interface. R represents the $\gamma_{X\rightarrow N}/\gamma_{N\rightarrow X}$ ratio. 3ML of CdS shell sample is highlighted to underline the global drop of the rates after the corresponding shell thickness. QY [%] is the PL quantum yield.

QD	$\gamma_{X\rightarrow 1}$ [$*10^{-3}$ ns^{-1}]	$\gamma_{1\rightarrow X}$ [$*10^{-3}$ ns^{-1}]	$\gamma_{X\rightarrow 2}$ [$*10^{-3}$ ns^{-1}]	$\gamma_{2\rightarrow X}$ [$*10^{-3}$ ns^{-1}]	R	QY [%]
CdSe	462	685	72	56	0.72	3±1
-CdS 1ML	462	477	124	34	1.15	10±1
-CdS 2ML	430	412	102	39	1.29	24±1
-CdS 3ML	417	391	138	38	1.29	29±2
-CdS 4ML	187	293	58	27	0.77	47±6
-CdS 5ML	178	261	66	28	0.84	52±7
-CdS 6ML	55	193	10	20	0.31	67±8
QD	$\gamma_{X\rightarrow 1}$ [$*10^{-3}$ ns^{-1}]	$\gamma_{1\rightarrow X}$ [$*10^{-3}$ ns^{-1}]	$\gamma_{X\rightarrow 2}$ [$*10^{-3}$ ns^{-1}]	$\gamma_{2\rightarrow X}$ [$*10^{-3}$ ns^{-1}]	R	QY [%]
CdSe	462	685	72	56	0.72	3±1
-$Cd_{0.5}Zn_{0.5}S$ 1ML	163	471	23	32	0.40	43±3
-$Cd_{0.5}Zn_{0.5}S$ 2ML	135	393	22	25	0.38	43±3
-$Cd_{0.5}Zn_{0.5}S$ 3ML	110	297	18	21	0.40	43±3
-$Cd_{0.5}Zn_{0.5}S$ 4ML	124	265	28	21	0.53	35±3
-$Cd_{0.5}Zn_{0.5}S$ 5ML	76	215	21	20	0.41	39±3
-$Cd_{0.5}Zn_{0.5}S$ 6ML	50	180	14	18	0.32	45±4
QD	$\gamma_{X\rightarrow 1}$ [$*10^{-3}$ ns^{-1}]	$\gamma_{1\rightarrow X}$ [$*10^{-3}$ ns^{-1}]	$\gamma_{X\rightarrow 2}$ [$*10^{-3}$ ns^{-1}]	$\gamma_{2\rightarrow X}$ [$*10^{-3}$ ns^{-1}]	R	QY [%]
CdSe	462	685	72	56	0.72	3±1
-ZnS 1ML	1624	769	297	49	2.35	1±1
-ZnS 2ML	702	579	114	50	1.30	4±1
-ZnS 3ML	482	514	88	49	1.01	5±1
-ZnS 4ML	296	434	65	37	0.77	8±1

In order to critically evaluate the extrapolated values reported in Table 6.3 and Figure 6.7 for each QD series, some general considerations about such rates is first necessary. Firstly, the extracted radiative rates are comparable to values calculated by previous works (Supporting Information of Ref. [33]) and span the interval between Γ_2 and Γ_3 exponential decay components (Table 6.3). Discrepancies from the empirical decay rates demonstrate the necessity to employ a kinetic model in order to effectively separate contributions from intrinsic exciton recombination and a trapping/de-trapping mechanism. Furthermore, for the CdSe cores, $k_R \sim 0.002$ ns^{-1} (Figure 6.7), in agreement with the theoretical value for the radiative rate calculated for single excitons in CdSe QDs with 3.9 nm diameter[93]. Therefore, the long $< \tau >$ (Figure 6.4) is due to both the low radiative rate and the trapping process.

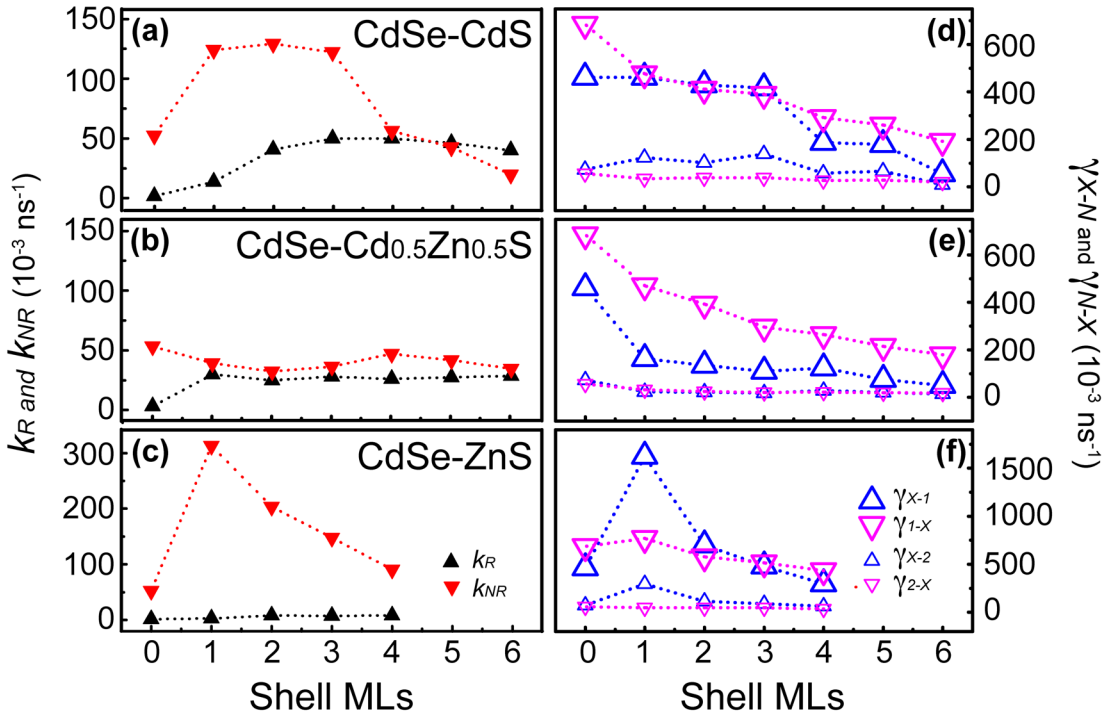

Figure 6.7: (a-c) Radiative (k_R) and non-radiative (k_{NR}) decay rates and (d-f) trapping/de-trapping rates ($\gamma_{X\rightarrow N}$ and $\gamma_{N\rightarrow X}$) as a function of shell thickness, calculated using the phenomenological kinetic model (Eqs. 6.3 and 6.4) and non linear least-square minimization of χ (Eq. 6.5); (a,d) refer to CdSe-CdS, (b,e) to CdSe-Cd$_{0.5}$Zn$_{0.5}$S, (c,f) to CdSe-ZnS. In all graphs, dotted lines are just guides for the eyes.

Focusing on core-shell samples, results cannot be fully understood without recalling what is now well known about CdSe-CdS and CdSe-ZnS core-shell heterostructures. CdSe-CdS, as mentioned above, is a "quasi-type-II" heterostructure (Chapter 1.2). Such band configuration should efficiently confine holes in the core but, at the same time, allow electrons spreading through the shell and, in the case of thin shells, reaching the outer surface. On the other hand, CdSe-ZnS is a typical type-I core-shell structure, which should prevent both hole and electron migration towards the surface. However, in light of the very low QY, the large lattice mismatch between core and shell is expected to bias also the exciton dynamics. Hence, a mixed Cd$_{0.5}$Zn$_{0.5}$S shell might be considered as a compromise between the two, since both lattice mismatch and quasi-type II behavior are reduced.

As predictable, the different core-shell QDs show distinct trends.

i. CdSe-CdS. Previous work[171] has demonstrated that increasing shell thickness decreases k_R if the electron-hole wavefunction overlap is concordantly reduced.

In the case of CdSe-CdS, the asymmetric band alignment[40,171] is expected to heavily reduce k_R for this reason. Despite this prediction, the CdS series prepared here presents an increasing k_R up to 3 MLs, after which a slow diminishing is observed (see Figure 6.7.a). Such a discontinuous trend of the radiative rate is considered to stem from the formation of an interfacial Cd$_x$Se$_{1-x}$S alloy layer up to 3 shell MLs[40,41,53,165]. This layer counteracts the "quasi-type II" behavior of CdSe-CdS

heterostructures[40,171] and increases the CdSe core "effective radius". Considering that k_R grows with CdSe QD volume[93,164], such a scenario is consistent with the initial increase of k_R. As the alloy formation saturates beyond 3 shell ML, the expected k_R attenuation is detected.

On the other hand, k_{NR} experiences a gradual decline with shell growth (Figure 6.7.a), which becomes faster after the alloying saturation (3ML). At 6 ML, the smoothed potential barrier of the CdSe-CdS heterostructure yields the $k_{NR} < k_R$ turning point. This justifies why, for the so-called "giant-shell QDs"[79], non-radiative processes are less effective on emitting performances.

The poor confinement potential presented by the alloyed $Cd_xSe_{1-x}S$ layer allows charge migration towards the surface. This becomes evident by looking at $\gamma_{X\to1}$, *i.e.* the highest trapping rate, which is likely associated in CdSe bare cores to hole surface traps (*vide supra*). Such rate (Figure 6.7.d) in fact shows an almost flat trend with shell thickness up to 3 MLs, while one would expect a decreasing trend at increasing core - surface traps distance. After 3 MLs of alloying, $\gamma_{X\to1}$ experiences an abrupt decrease (Figure 6.7.d and Table 6.3), which means that holes are better confined by the unalloyed CdS outer shell.

Regarding $\gamma_{X\to2}$, such low rate is an effective rate that accounts for an indefinite trap distribution[33], probably located at the core-shell interface region, whose boundary and thickness are smoothed as long as the alloy layer develops. Differently from $\gamma_{X\to1}$, $\gamma_{X\to2}$ slightly increases up to 3 MLs (Figure 6.7.d and Table 6.3), indeed suggesting that traps here involved might have a different physical origin. On the other hand, as for $\gamma_{X\to1}$, $\gamma_{X\to2}$ is reduced by a factor of ≈ 3 and then decreases beyond the 3 MLs limit, suggesting that alloying affects also this secondary rate.

As for the trapping rates, the de-trapping rates $\gamma_{N\to X}$ present a decrease with shell MLs and a step of the slope can be detected again at 3ML (see Table 6.3). But, most notably, while up to 3 MLs the ratio $\gamma_{X\to N}/\ \gamma_{N\to X} > 1$, further shell growth makes de-trapping a more efficient process than trapping. In particular, $\gamma_{1\to X} > \gamma_{X\to1}$ and $\gamma_{2\to X} \approx \gamma_{X\to2}$.

Comparing the different rates at low shell coverage (< 3 MLs), it is evident that trapping processes predominate exciton dynamics ($k_R \ll \gamma_{X\to N}$). Therefore, surface trapping is a preferential process for charge carrier. Conversely, when shell thickness exceeds 3MLs, k_R becomes more competitive versus trapping: k_R in fact increases and, beyond the alloying limit, stabilizes at values comparable to the highest trapping rate, while k_{NR}, $\gamma_{X\to N}$ and $\gamma_{X\to N}/\ \gamma_{N\to X}$ decrease. This is coherent with the suppression of single CdSe-CdS giant shell QDs PL blinking observed by many groups[79,172].

ii. CdSe-ZnS. In contrast to CdSe-CdS, ZnS shell based QDs exhibit a ~5 times lower k_R and very efficient k_{NR} (Figure 6.7.c). High defect concentration in CdSe-ZnS strongly quenches the QY (Figure 6.1e) and may open preferential paths for charges through the shell, probably due to inhomogeneous shell thickness induced by preferential growth upon certain defect sites[173]. Such a hypothesis is supported by the outer trapping rate value $\gamma_{X\to1}$ and the $\gamma_{X\to N}/\gamma_{N\to X}$ ratios,

which are the highest among the three core-shell QDs studied, and by the fact that surface trapping dominates the exciton recombination kinetics ($k_R \ll k_{NR} \ll \gamma_{X\to1}$).

iii. CdSe-$Cd_{0.5}Zn_{0.5}S$. Finally, we focus on $Cd_{0.5}Zn_{0.5}S$ shells. In this series high k_R (and low k_{NR}) are achieved by growing just 1-2 shell MLs. After this steep increase, CdSe-$Cd_{0.5}Zn_{0.5}S$ QDs exhibit an almost constant k_R (and k_{NR}) with increasing shell thickness and the lowest $\gamma_{X\to N}$ among the three QD series (Figure 6.7 and Table 6.3). The effect of trapping is further minimized by the de-trapping rates, since $\gamma_{2\to X} \approx \gamma_{X\to2}$ and, most importantly, $\gamma_{1\to X} \gg \gamma_{X\to1}$. Compared to CdS, both trapping rates are heavily reduced at just one shell monolayer and, similarly to k_R, also $\gamma_{X\to N}$ and $\gamma_{N\to X}$ appear less shell thickness dependent compared to the alloyed CdSe-CdS and mismatched CdSe-ZnS heterostructures. In particular, $\gamma_{X\to2}$ shows an invariant trend on shell thickness. Such behavior is coherent with the results of the previous Chapter, in which Raman spectroscopy was used to show that an abrupt core-shell interface occurs between CdSe and $Cd_{0.5}Zn_{0.5}S$[41]. At the same time, Raman and X-ray diffraction techniques have demonstrated that $Cd_{0.5}Zn_{0.5}S$ grows epitaxially on CdSe (Figure 6.8 and 5.7), suggesting that a negligible number of stacking faults occur at the core-shell interface. Therefore, growing $Cd_{0.5}Zn_{0.5}S$ on CdSe cores causes the exciton to interact with the same number and kind of traps, localized at the core-shell interface, leading to a constant $\gamma_{X\to2}$.

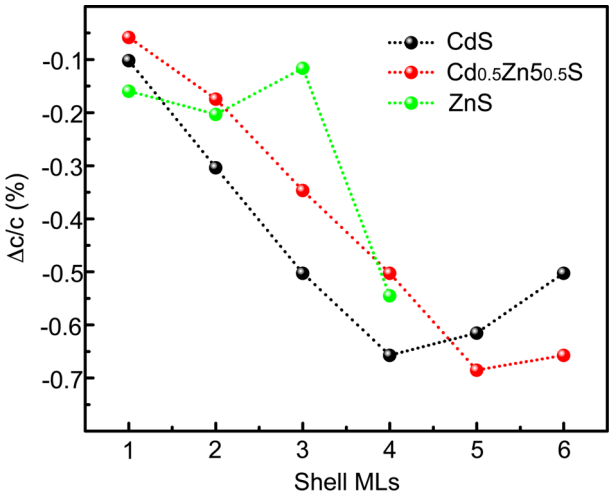

Figure 6.8: CdSe#1 core lattice compression, induced by CdS/$Cd_{0.5}Zn_{0.5}S$/ZnS shell growth. Lattice strain was measured by Raman technique, with the same procedure reported in the previous Chapter. As expected, at 1 shell ML compressive strain induced by ZnS is the highest. While for CdS and $Cd_{0.5}Zn_{0.5}S$ further shell growth is epitaxial and thus enhances the compression on core lattice, for ZnS non-epitaxial growth occurs, i.e. no evolution of the core compression is detected. The abrupt increase of the Δc/c value for the CdSe-ZnS 4 ML sample is probably due to QDs anisotropy, which becomes relevant when thick ZnS shells are grown on CdSe[39,75] and strongly modifies the energy of the LO phonon.

In summary, the influence of the core-shell interface on single-exciton recombination dynamics has been shown to induce different behavior for each core-shell QD investigated. CdS shell based

samples showed increasing radiative performance, which were mainly controlled by k_R. The necessity to overpass a shell thickness of 3 MLs, which corresponds to the $CdSe_xS_{1-x}$ alloy layer thickness, was found to be required for efficiently minimizing trapping and maximize performance. This factor presents a lower limit to the final dimension of the core-shell QD. In contrast, $Cd_{0.5}Zn_{0.5}S$ shelled QDs possess a more strained interface, which limits alloying and effectively confines carries to the core. This causes the radiative decay to be controlled by high de-trapping rates, which minimize both the effects of traps on kinetics and the lower (compared to CdS) k_R.

6.5 A Roadmap for Optimizing Core-Shell QDs - II

Various optical spectroscopy techniques have been employed to study the influence of CdS, $Cd_{0.5}Zn_{0.5}S$ and ZnS shells with a thickness of up to 6 MLs grown on CdSe QDs. Higher QYs were obtained for CdS based samples, but $Cd_{0.5}Zn_{0.5}S$ shells provided better performances at lower shell thicknesses. Due to the high defectivity in the final hetero-structure, ZnS shells provided the lowest QYs, independently of their thickness. In order to detect how different shell compositions and trap-distributions influence exciton recombination, the results from tPL experiments were correlated to a phenomenological kinetic model with radially distributed trap states. In this manner, the influence of a 3ML thick $CdSe_xS_{1-x}$ alloyed layer at the CdSe-CdS core-shell interface on the exciton recombination dynamics is revealed. Moreover, the modeling was equally valid in identifying the abrupt nature of the interface between CdSe cores and a $Cd_{0.5}Zn_{0.5}S$ shell, detected by SERS measurements.

Thanks to its phenomenological formulation, it is envisaged that the same model could be easily adjusted for investigating other QD hetero-structures. By correlating the structural and fluorescence decay properties of QDs in this way, a timelier pathway towards achieving QY values close to unity is envisaged. In particular, the discussion here provided clarifies why graded core-shell CdSe-CdS-$Cd_{0.5}Zn_{0.5}S$-ZnS are high performing QDs for optical applications[44,45,48]: (i) they retain in a single entity the high radiative decay rates of CdS; (ii) they exhibit high de-trapping and low non-radiative decay rates of $Cd_{0.5}Zn_{0.5}S$; and (iii) they possess the superior confinement potential of ZnS.

Chapter 7.

Multi-Exciton Dynamics in CdSe-$Cd_XZn_{1-x}S$ QDs

The Role of the core-shell interface - II

The understanding of the photophysics of excited states in QDs is of great help for the engineering of their optical gain properties. As illustrated in Chapter 3, optical gain and amplified spontaneous emission are the effect of the multi-exciton generation and recombination indeed.

In this chapter the main results obtained by means of the transient absorption (TA) technique are collected. The experimental configuration described in Chapter 3.6 allows the study of QD multi-exciton dynamics, which operates in a much faster (< 1 ns) time scale compared to single-exciton recombination investigated in Chapter 6. The effects of multi-excitons on excitation and recombination dynamics in CdSe-$Cd_XZn_{1-x}S$ core-shell QDs are investigated along different coordinates: shell thickness, shell composition and excitation density. Furthermore, due to the several convoluted mechanisms (*vide infra*) governing the multi-exciton regime, TA data can be interpreted from two points of view: (i) a spectral one, in which the excited state spectral structure is modeled and (ii) a time-trace point of view, which aims to rationalize the excited state dynamics.

After a brief overview of the data analysis techniques and strategies employed (Section 7.1), this chapter will be divided in two, according to the just mentioned dual-level interpretation. Specifically, in Section 7.2 the spectral features occurring in transient absorption spectra will be discussed, while in Section 7.3 their temporal evolution will be examined.

7.1 Experimental data: structure and analysis methods

TA absorption datasets consist of two-dimensional maps resolved both in time delay between pump and probe pulses and wavelength. An example of a TA map is presented in Figure 7.1.

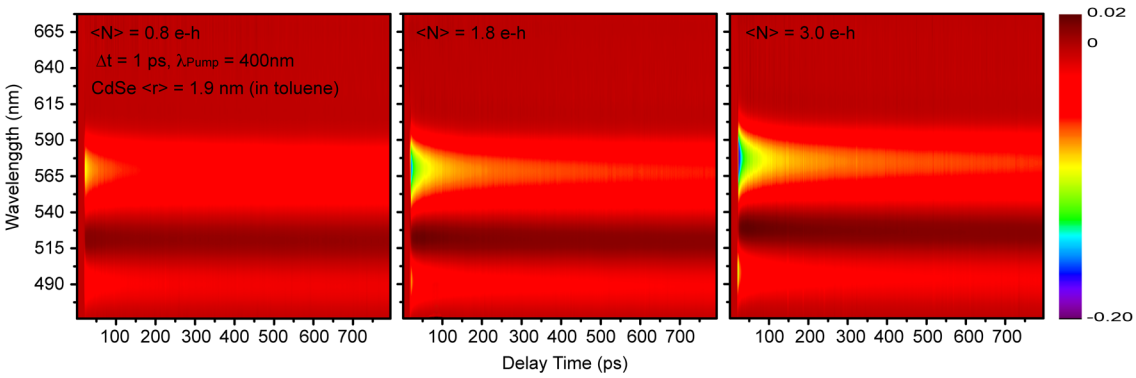

Figure 7.1: TA maps of CdSe#1 cores in toluene solution at increasing pump fluence. TA spectra are collected with pump-probe delay steps of Δt = 1 ps.

The quality of TA signals, i.e. ΔA values (differential absorption), depends on several parameters, such as the sample concentration, white light intensity and stability. In this work, the obtained spectra have been post-processed to minimize noise (when necessary) and white light *chirping* effects, by using a homemade Matlab routine.

7.2 Spectral analysis

The spectral structure, at 1 ps delay, for a CdSe-based core-shell QDs dispersion is presented in Figure 7.2, compared with the linear absorption spectrum:

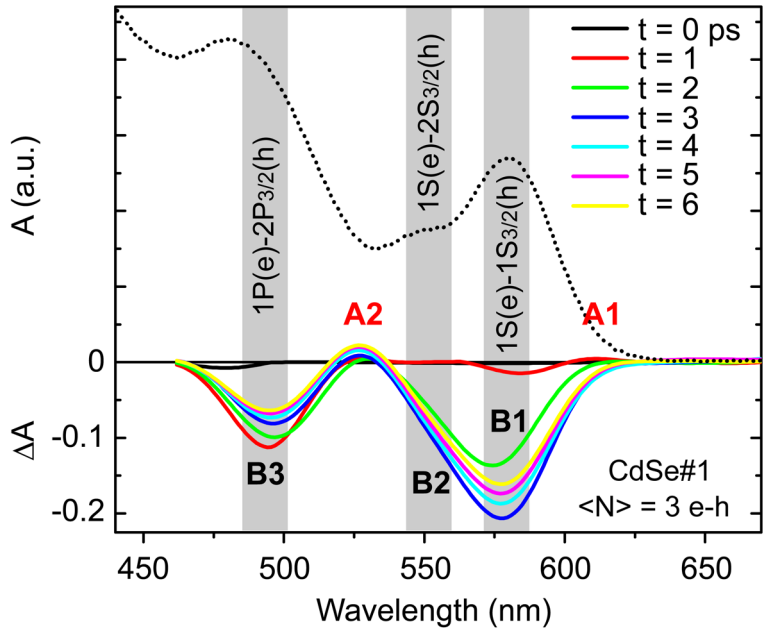

Figure 7.2: Absorption and TA spectra at 0-6 ps pump-probe delays. Grey shadings highlight the main exciton features, while bold labels represent the relative GSB (B-bands, black) and PA signals in TA spectra (red, A bands).

In Figure 7.2 it is possible to identify some specific spectral features. Namely, two excited state absorption (A bands) and three ground state bleaching signals (B bands). The nomenclature here employed for GSB and PA bands is the one introduced by Klimov[92,128].

As mentioned in Chapter 3.5, the excited state spectral structure depends on two overlapping phenomena: the occupation or Pauli blocking effect, originating from state filling, and many-body effects. The main contribution to the latter is the inter-exciton Stark interaction, which causes a shift of the energy levels. At high pump fluences both effects act on the QD electrodynamics.

In literature, the most extensively investigated signal is B1, which represents the GSB of the band-edge 1S(e)-$1S_{3/2}$(h) exciton state. The other bleaching bands correspond to the 1S(e)-$2S_{3/2}$(h) (B2) and 1P(e)-$1P_{3/2}$(h) (B3) absorption transitions. Such bleaching features are induced by state filling; however, the presence of photo-generated carriers creates local electric fields, which modify the spectral position and the oscillator strength of the transitions.

Stark Effect contributions to the TA spectra can be derived by considering the absorption spectrum A as a function of the applied electric field, which can be expressed as a MacLaurin series expansion around $E = 0$[127]:

$$A(\omega, E) = A(\omega, 0) + \left(\frac{dA(\omega,0)}{d\omega}\frac{d\omega}{dE}\right)E + \frac{1}{2}\left(\frac{d^2A(\omega,0)}{d\omega^2}\frac{d^2\omega}{dE^2}\right)E^2 + \cdots \quad \text{(Eq. 7.1)}$$

Expressing the variation of the transition frequency as

$$\omega(E) = \omega_0 - \mu E - \frac{1}{2}\alpha E^2 \quad \text{(Eq. 7.2)}$$

and assuming the absence of permanent dipole moments ($\mu = 0$), from Eq. 7.1 one gets

$$A(\omega, E) - A(\omega, 0) \propto \Delta A \propto \frac{dA(\omega,0)}{d\omega}E^2. \quad \text{(Eq. 7.3)}$$

In Eq. 7.2 α represents the polarizability. In QDs the width of the absorption bands is larger than both the field induced shift and the separation between interacting states. In the small field limit, the Stark difference spectrum is proportional to the second derivative of A[174]. Figure 7.3 compares the second derivative of the absorption spectrum of the CdSe QDs and the normalized a differential absorption spectrum presented in Figure 7.2. As predicted, the two profiles are similar.

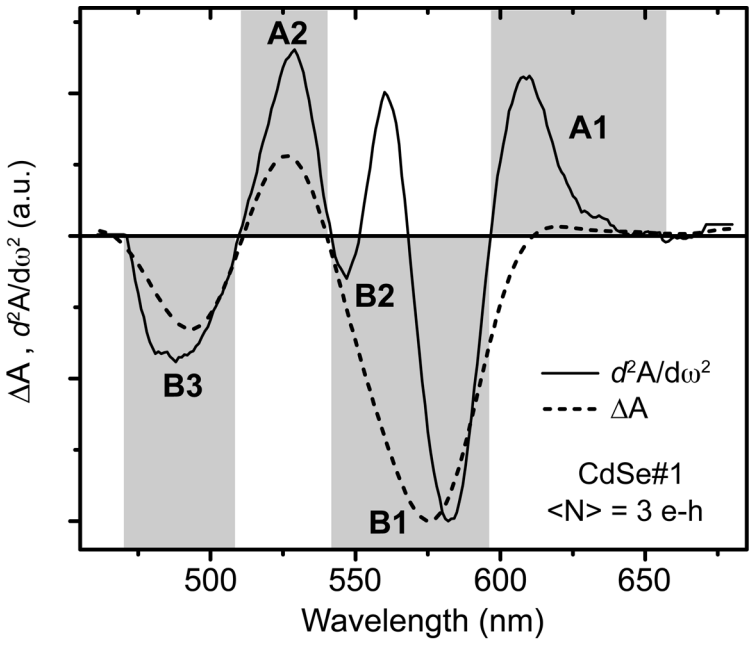

Figure 7.3: Comparison between the second derivative of the linear absorption spectrum versus a TA spectrum for CdSe#1 QDs.

In a neutral QD, the physical source of the Stark field is the dipolar field responsible for the mutual exciton-exciton interaction. However, as discussed in Chapter 6, charge carriers can be trapped at surface or defects at the core-shell interface, especially at high pump fluences (*photocharging*)[175–177]. A trapped charge produces a much more intense monopolar field (~10^5 V cm^{-1})[174], whose magnitude can induce an appreciable Stark shift in dot transition. Scheme 7.1 graphically represents the two situations, with the relative modified energy level structure.

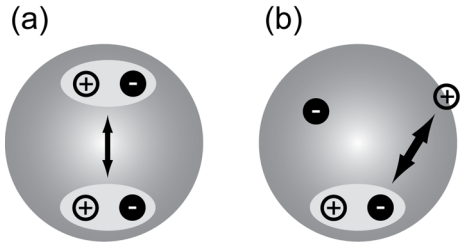

Scheme 7.1: Schematical representation of (a) exciton-exciton and (b) trapped charge-exciton interaction. The thickness of the arrows represents the strength of interaction.

Therefore, the Stark shift of the exciton energy levels also contributes to the bleaching signals, as the oscillator strength of the original exciton states is reduced. Moreover, the same shift is responsible for appearance of new transitions at a different energy, *i.e.* it accounts for the PA (A1 and A2, Figure 7.2) bands. Namely, A1 feature is related with the Stark-shifted |1S> exciton transition and A2 with the Stark-shifted |1P> transition (Scheme 7.2).

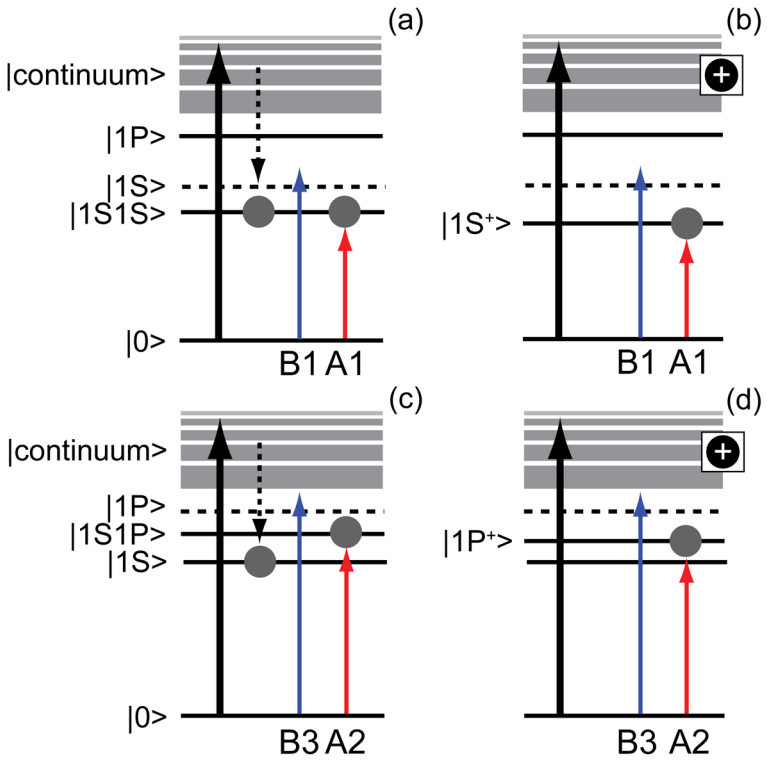

Scheme 7.2: Schematic representation of the Stark induced GSB and PA signals. The black thick arrows stand for the absorption of the pump beam and hot-exciton formation. The dashed arrows represent the hot-exciton relaxation to the lowest unoccupied exciton state (|1S>). (a) B1 and A1 here represent the GSB of the |1S> state due to bi-exciton relaxation and PA to the |1S1S> bi-exciton state, respectively. (b) A1 and B1 signals appear also if a charge carrier is trapped, leading to formation of an energy shifted $|1S^+>$ "trion" state. (c) Same as (a), B3 and A2 represent the GSB of |1P> and PA to the |1S1P> bi-exciton state. (d) Same as (c), B3 and A2 signals are induced by the formation of a $|1P^+>$ "trion" state. B2 is not considered since in the TA spectra B2 is weaker and convoluted with the dominant B1 signal.

It is worth noting that the |1S>, either in its "free" or trapped configuration, is considered as the initial state, since |1S> is the most populated exciton state due to the fast sub-picosecond relaxation processes. On the other hand, the final states are |1S1S> and |1S1P> bi-exciton states (or $|1S^+>$ and $|1P^+>$ trion states). This means that the energy shift associated with the Stark-shift can also be interpreted as either the *bi-exciton binding energy* (E_{xx})[178,179] (Chapter 2.5), in the case of neutral exciton-exciton interaction, or the *"trion" binding energy*,[21,45,180,181] in the case of neutral exciton-trapped charge interaction.

7.2.1 Qualitative interpretation of core-shell TA spectra

In order to provide a straightforward qualitative interpretation for the TA spectra of CdSe-$Cd_XZn_{1-X}S$ core-shell QDs, the discussion will be divided in two subsections: the first will describe TA spectra at short pump and probe delay times (t = 1 ps), the second at long time delay (t = 800 ps), at which most of the multi-exciton effects are expected to have run out.

TA spectra at t = 1ps

When a $Cd_XZn_{1-X}S$ shell is grown on CdSe, as for the steady-state absorption also the transient absorption is modified. First of all, as represented in Figure 7.4, a new bleaching signal can be resolved next to the B3 band. Due its spectral position, it is reasonable to consider this band as the bleaching of some quantum-confined shell transition.

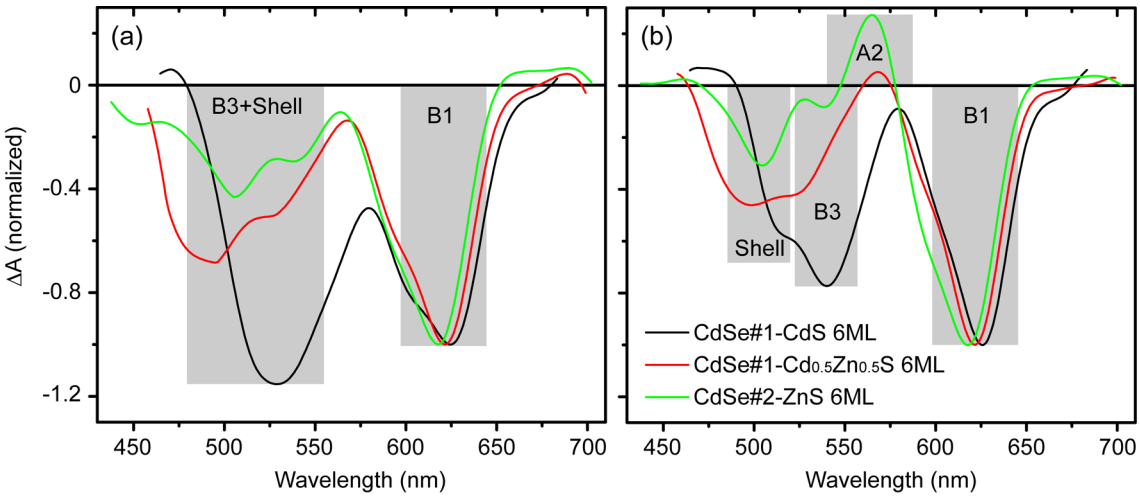

Figure 7.4: Normalized TA spectra of CdSe#1-CdS and –$Cd_{0.5}Zn_{0.5}S$ and CdSe#2-ZnS 6 ML QDs. (a) Normalized TA spectra at Δt = 1 ps and (b) Δt = 800 ps.

The ratio between the different signals varies with the shell composition. One explanation may be related to the fact that also CdS absorbs at λ_{PUMP} = 400 nm. Hence, a considerable fraction of the incident fluence generates excitons in the shell material, which relax by migrating into the lower band-gap CdSe core[165,182]. This CdS to CdSe core transfer yields a shell dependent effective pumping rate of the core and consequently modified relaxation dynamics. If the possibility that the CdS shell generated excitons also interact with surface trap-states is included, the modification of the dynamics gets even more complex.

Additionally, also the influence of the interface defectivity has to be taken into account. Zn-rich shell materials, in light of the results reported in Chapters 5 and 6, are expected to have a higher concentration of lattice defects, especially at the core-shell interface, which may act as localized trap states. The most evident outcome is the increase A2[i] band at increasing Zn concentration. A2 is related to Stark effect, which is more effective when the Stark field is generated by a trapped exciton.

At the same time, for all samples the A1 band is not detected or it extinguishes at a sub-ps time scale. Such PA band is bleached because the pump fluences here employed are high enough to

[i] At t = 1ps A2 is bleached by B1-B2 and B3-shell band. ΔA > 0 at longer pump-probe delays, *i.e* PA becomes evident only when the dominating bleaching signals have recovered.

generate a considerable amount of bi-excitons (given by the Poisson distribution, Eq. 3.25) in the dot. If the absolute value of the |1S1S> bleaching signal grows beyond the limit at which

$$\left(-\frac{\Delta A}{A}\right)_{|1S1S>} = 1, \qquad \text{(Eq. 7.4)}$$

defined as the transparency condition, optical gain, *i.e.* a negative absorption band, is obtained[179]. If $-\Delta A/A > 1$, stimulated emission (SE) contribution to the total (negative) bleaching signal can't be neglected anymore, and, in parallel, amplified spontaneous emission (ASE, see Chapter 8) should be observed. In bare CdSe cores, due to the absence of the passivation provided by the shell, the probability of bi-exciton formation and stability at RT is lower compared to the probability of exciton trapping, leading to a lower bleaching of the |1S1S> state and consequently a higher probability of having PA. However, as it will be discussed in Chapter 8, shell growth or, more generally, an appropriate surface passivation, is not a sufficient condition for obtaining population inversion[179]. Even if minimized, PA to |$1S^+$> (Scheme 7.2) state is still present and does not allow the transparency condition, especially if the QDs are in a diluted solution. ASE emission and optical gain can be obtained only by using high concentrations of QDs, typically obtained by densely packed films of QDs (see Chapter 8).

TA spectra at t = 800 ps

On these timescales multi-excitonic relaxation processes are expected to have run out, therefore, in an exact Poissonian picture, the signal is supposed to be originated by singly excited dots. However, as demonstrated in the previous chapter, photocharging effects influence the exciton dynamics on timescales up to the μs regime.

Figure 7.5 depicts the shell thickness dependence of A2 and B1 ΔA values[i] at 800 ps.

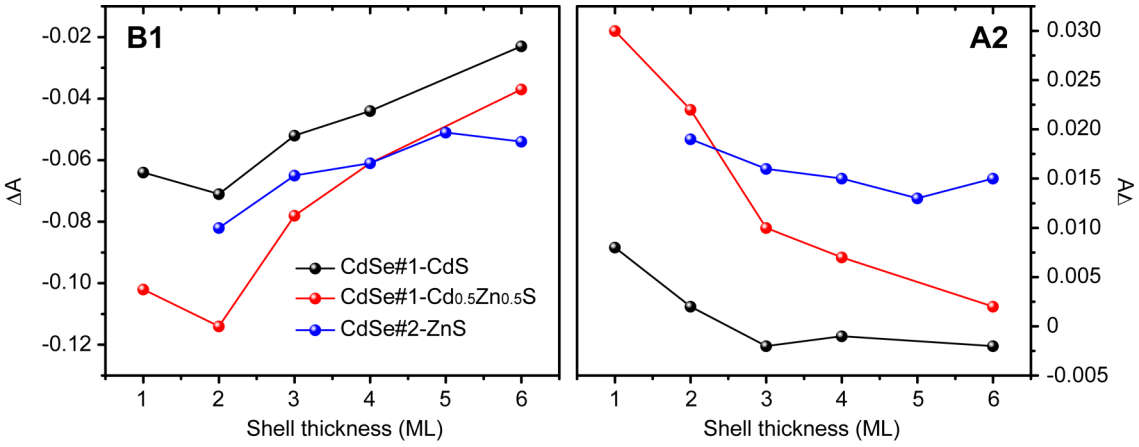

Figure 7.5: ΔA values at t = 800 ps at the B1 (left) and A2 (right) spectral positions (<*N*> = 3 e-h).

[i] Bleaching feature B2 is excluded from the qualitative discussion because is mostly unresolved, and B3 bleaching is excluded as well because of its spectral overlap with a CdS bleaching signal.

The CdSe-ZnS series shows high A2 signals, which exhibit a slowly decreasing trend with shell thickness. This indicates that a non-negligible exciton trapping occurs, and the shell thickness invariance can be explained only by considering much of the defects localized at the core-shell interface. Even if CdSe#2-ZnS samples are expected to be less defective compared to the CdSe#1-ZnS QDs, a non-negligible defect concentration is expected at the first shell MLs.
For all the core-shell series, the trend for A2 is correlated to the B1 shell thickness dependence. This correlation is more evident for the CdSe#1-CdS and $Cd_{0.5}Zn_{0.5}S$ series, where the B1 and A2 variation with shell thickness is steeper. Also in these series A2 decreases with increasing shell thickness. For both series the interfacial defect concentration is lower than for the highly mismatched ZnS shell, so that the excitons are mostly trapped at the outer surface, i.e. farther from the photogenerated core excitons. The gradual decrease in B1 signal with shell thickness can be explained by considering that the TA maps are collected at fixed $<N>$, *i.e.* at a fixed pump induced average number of excitons per dot. Since λ_{PUMP} = 400 nm, part of the pump beam is absorbed also by the CdS shell. The interaction of some shell generated excitons with the high concentration of trap states located at the outmost surface leads to a decrease of the effective CdSe core pumping rate at increasing CdS volume.
In figure 7.5 only the values relative to the pump fluence $<N>$ = 3 e-h are reported. However, at increasing fluence both the absolute value of B1 and the A2 increase, as expected, due to the increase of the |1S> state population (Scheme 7.2).

Finally, from this qualitative overview it emerges that photocharging effects, due to interaction of excitons with surface and core-shell interface localized trap states, strongly modify the spectral structure of TA. Moreover, by considering TA spectra at 1 ps and 800 ps, it is evident that the exciton trapping influences also the temporal evolution of the TA features, *i.e.* the exciton and multi-exciton relaxation and generation processes.
Depending on the core-shell series considered, trap states responsible for the photocharging effects are present with a characteristic concentration and are differently distributed in the QD volume. However, while at long delay time some shell thickness and composition trends may be detected, as suggested by tPL results presented in Chapter 6, at the ultrafast (~ 1ps) time scale exciton-trap interaction is weakly influenced by the shell thickness and composition.
A straightforward demonstration is provided by plotting the $-\Delta A/A$ values of the B1 band at 1 ps[i] versus the expected trend (Figure 7.6), given by the state filling of the two-fold degenerate |1S> exciton state[3]:

$$\left(-\frac{\Delta A}{A}\right)_{|1S>} = 1 - e^{<N>}\left(1 + \frac{<N>}{2}\right) \qquad \text{(Eq. 7.5)}$$

[i] More precisely, ΔA/A values in Figure 7.6 are taken from TA spectra at which |ΔA| for B1 is maximum, whose relative pump-probe delay vary from 1 ps to few ps. Such variation will be discussed more in detail in the next section and is mainly due to the rate of exciton transfer from the shell material to the |1S> CdSe exciton state.

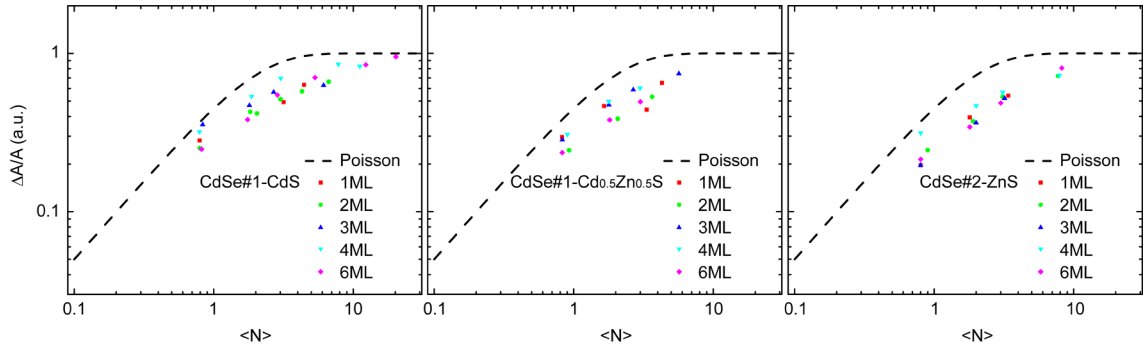

Figure 7.6: Expected trend (dashed line, Eq. 7.5) for */ΔA//A* at the B1 |ΔA| maximum value versus the measured (at t~1ps) */ΔA//A* value for the (left) CdSe#1-CdS series, (center) CdSe#1-$Cd_{0.5}Zn_{0.5}S$ series and (right) CdSe#2-ZnS series.

For all the three sets of core-shell CdSe-$Cd_XZn_{1-X}S$ QDs */ΔA//A* values are below the theoretical expected value. Conventionally, this is largely accepted to be a signature of the presence of carrier trapping.

7.3 Time-trace analysis

Although the most correct description of the spectral structure derives from the exciton level structure, sometimes it is convenient to consider it from an electronic level structure point of view. As presented in Chapter 2, the CdSe the valence band is highly degenerate, while the conduction band states are more energetically separated. This leads to independent relaxation rates for electrons and holes indeed: mainly Auger guided intraband relaxation for electrons, while holes relax through intraband phonon-cooling[36,128,183]. Both processes, for type-I heterostructures, are expected to occur in the sub-ns time scale and can be discerned from TA experiments.

The one just mentioned represents just one among the several reasons for the success of the TA technique in the early studies on QDs. Despite the abundance of information contained in a single TA data set, main achievements reported in literature came from the study of the B1 time-trace. Thanks to the high time-resolution of the technique, by studying the evolution of the |1S> exciton state population intraband, interband and side effects stemming from charge transfer[52] and energy transfer[184] can be detected. However, it is evident that building-up such a complex kinetic model, which takes into account all the possible events that contribute to B1, only on the basis of B1 itself, may lead to some overrating or sometimes erroneous interpretation of the experimental data[177,185]. For this reason, two approaches are employed in this thesis to analyze TA data: first of all an independent study is conducted on the B1 time traces as a function of shell

thickness/composition and pump fluence. This preliminary approach, as an internal standard, allows the comparison of the experimental results with literature data.

In a second step, a multi-wavelength global fitting is reported, which allows a more robust analysis of data. Including all spectral features in the time trace analysis offers the possibility to limit speculations and increase the degree of self-consistency of TA data.

7.3.1 B1-band time trace fitting

As already discussed in this chapter, the B1 band and its time evolution are modeled by both state filling and level shifting of the absorption transition $|0\rangle \rightarrow |1S\rangle$. A typical B1 time trace and relative multi-exponential fitting are shown in Figure 7.7.

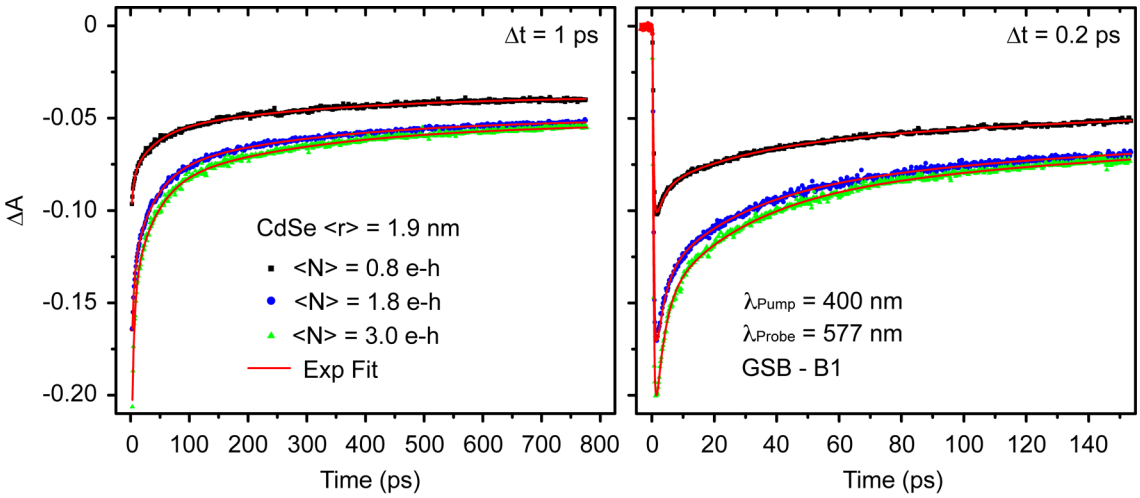

Figure 7.7: Examples of GSB-B1 time traces of the CdSe#1 QDs in toluene colloidal dispersion. Black squares represent TA data collected a <*N*> = 0.8 e-h pump fluence and with pump-probe delay steps of 1 ps (left) and 0.2 ps (right). Blue dots and green triangles represent the evolution of B1 at <*N*> = 1.8 and <*N*> = 3.0 e-h pump fluence, respectively. Red lines represent the multi-exponential curves extracted through the global-fitting of the experimental B1 decay traces at different time resolution and pump fluence.

At time zero t = 0 a fast signal growth is observed, followed by a bleaching recovery. For each sample and pump fluence both "long" (1ps resolution – 800ps time window) and "short" (1ps resolution – 160ps time window) data sets were collected and a multi-exponential global fitting has been conducted. Notably, the bleaching recovery in all data sets never gets to a full completion, since the $|1S\rangle$ exciton average lifetime ($\langle\tau\rangle$, see Chapter 6), is of the order of tens of nanoseconds, much longer than the ~1 ns TA time window. In order to account for this, one of the exponential time constants has been set at the $\langle\tau\rangle$ value extracted by tPL.

On the other hand, the fast initial growth has been modeled with a step function, *i.e.* an exponential component with sub-ps time constant and positive amplitude. This fast growth component took in account all the processes occurring on the sub-ps time scale, namely intra-band exciton relaxation to the |1S> and response of the system to a ~ 150 fs pump-probe auto-

correlation function. The accuracy of this approach was checked by conducting, for some random traces, a multi-exponential fitting with a convoluted Gaussian curve as IRF, initialized with a FWHM = 150 fs[i].

CdSe#1 cores

In Figure 7.7 experimental data and relative fitting for the CdSe#1 cores is presented. A globalized fitting has been conducted using as experimental data all the data sets collected with different time resolution (Δt = 0.2 ps and 1 ps) and at three different pump fluences (<*N*> = 0.8, 1.8, and 3). Multi-exponential time-constants were shared between all the data sets, while the relative amplitudes were let free and optimized by non-linear least-square minimization.

Best fit of data was obtained by using a step function and a minimum of four exponentials, whereof one (τ_1) was fixed at <τ> (<τ> values are reported in Figure 6.4). The bleaching recovery time constants extracted from fit are τ_4 = 5(±1) ps, τ_3 = 30(±2) ps and τ_2 = 240(±5) ps. Despite the good accordance between the experimental data and the multi-exponential curve, the results of such global fitting do not allow clear photo-physical interpretation. At increasing fluence, the amplitudes A_3 and A_4 relative to the fastest decay components (τ_3 and τ_4) also increase with respect to the A_2 and A_1. This occurrence may be due to a combination of effects: multi-exciton recombination[36] and photocharging[175,176].

In the ideal case, *i.e.* in the absence of trapping related effects, the B1 recovery can be interpreted as a pure multi-exciton decay, expressed by a set of coupled rate equations[177]:

$$\frac{dP_N}{dt} = \frac{P_{N+1}}{\tau_{N+1}} - \frac{P_N}{\tau_N}, \qquad \text{(Eq. 7.6)}$$

where P_N stands for population and N for the number of excitons per dot. Considering the twofold degeneracy of the $|1S\rangle$ ($|1S(e)\text{-}1S_{3/2}(h)\rangle$) exciton state, for a certain initial N the individual dot experiences a time-dependent bleach recovery given by:

$$\Delta A_{B1}(t,N) = 0.5 \cdot P_1(t) + \sum_{N=2} P_N(t), \qquad \text{(Eq. 7.7)}$$

with $\sum_{N=1} P_N\,(t=0) = 1$. The theoretical B1 recovery described by Eq. 7.7 for N = 1,2 and 3 e-h are reported in Figure 7.8, where the relative $\tau_{N\text{-}exc}$ values (*i.e* the multi-exciton decay time constants) are approximated as equal to the multi-exciton Auger non-radiative time-constants (much shorter than the radiative multi-exciton time constants) extrapolated from chapter 5 of Ref [3] for CdSe QDs with an average radius of 1.9 nm.

[i] This is due to the fact that the characteristic time constant of the step function is always sub-ps, *i.e.* much shorter than the > 1ps -time constants extracted from the TA time traces.

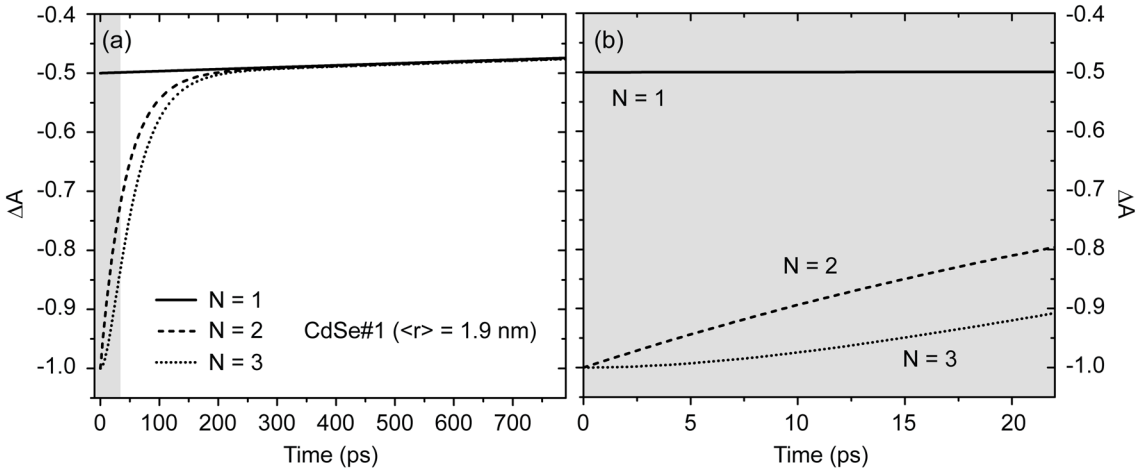

Figure 7.8: Theoretical B1 evolution calculated by solving Eq. 7.6 and 7.7. Single- and multi-exciton recombination rates are taken from Chapter 6 and Ref. [3]. Figures in (a) and (b) illustrate the theoretical B1 traces in the extended time window (800 ps) and short time window (20 ps) respectively.

It is worth noting that for $N > 1$ $\Delta A_{B1}(t = 0)$ does not vary, whilst an induction or delayed onset of the |1S⟩ exciton decay is present at early times (Figure 7.8.b). The induction is due to the transient population of the |1S⟩ exciton state by the |1S1S⟩ and |1S1S1P⟩ multi-exciton states.

Since the pump pulse creates a distribution in population with an average number of excitons per dot proportional to the fluence ($< N >= F \cdot \sigma$), the set of coupled differential equations is initialized by considering the population of each multi-exciton state at given initial $<N>$, given by the Poisson distribution (Eq. 3.25). Therefore, the Poisson averaging of the time-dependent B1 bleaching yields:

$$\Delta A_{B1}(t, < N >) = 0.5 \cdot < N > e^{-<N>} + \sum_{N=2} \langle N \rangle^N \frac{e^{-\langle N \rangle}}{N!}. \qquad \text{(Eq. 7.8)}$$

In Figure 7.9 the experimental B1 time traces reported in Figure 7.7 are compared with the expected $\Delta A_{B1}(t, < N >)$.

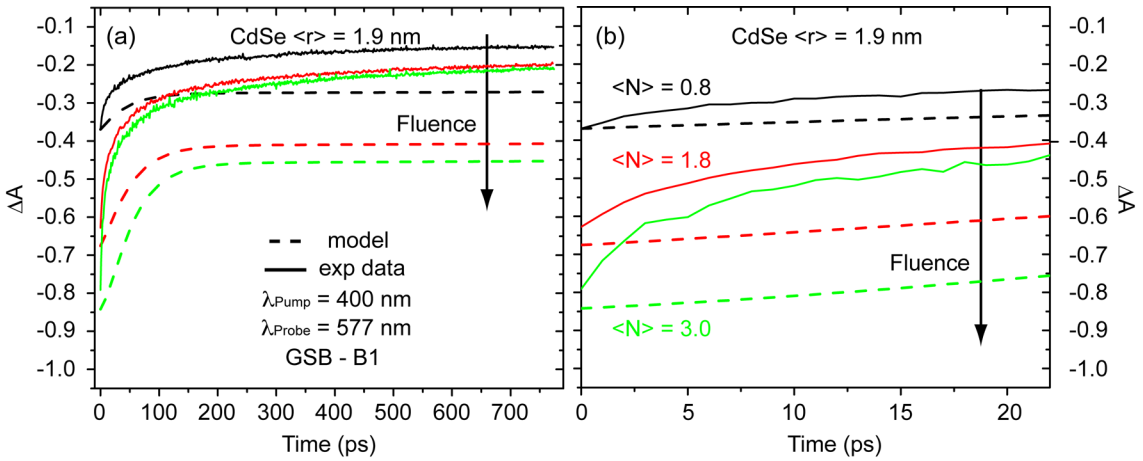

Figure 7.9: Experimental (solid lines) versus expected (dashed lines) B1 normalized time traces for CdSe#1 $<N>$=0.8, 1.8 and 3.0 e-h. Figures in (a) and (b) illustrate the theoretical and experimental B1 traces in the extended time

window (800 ps) and short time window (20 ps) respectively. In the latter the experimental versus the theoretical initial B1 recovery is emphasized. Expected B1 evolution is calculated from Eq. 7.6-7.8 and by using as $\tau_{N\text{-}exc}$ the Auger time constants measured by Ref. [3] for CdSe QDs of the same dimensions as CdSe#1, *i.e.* with an average radius of 1.9 nm[i].

To make clear the relation with the model, experimental data at $<N>$ = 0.8 are normalized and rescaled in order to match the initial theoretical B1 value:

$$\Delta A_{B1}^{experiment}(t = 0, < 0.8 >) = \Delta A_{B1}^{theory}(t = 0, < 0.8 >). \qquad \text{(Eq. 7.9)}$$

The same scaling factor was then used to rescale B1 time-traces at $<N>$ = 1.8 and 3 e-h.
Figure 7.9 shows a general divergence from the expected trend for all the experimental data. The comparison between such a purely multi-exciton relaxation model and the rescaled experimental B1 time traces leads to the following observations:
- For all pump fluences, $\Delta A_{B1}^{experiment}(t = 0) \neq \Delta A_{B1}^{theory}(t = 0)$. If MEG and MER were the only processes controlling the bleaching dynamics, by employing for all the pump fluences the same rescaling factor employed for obtaining Eq. 7.9 a perfect matching with the model at t=0 should be achieved. The discrepancy may be due to the ~ 10% error margin when calculating the initial $<N>$, *i.e.* the accuracy in measuring both the absorption cross-section and the incident fluence. However, the same divergence may be due to a fast charge-trapping process at some unpassivated surface states, which effectively modifies the pump induced $<N>$.
- In the theoretical B1 traces an induction time can be detected in Figure 7.9.b - more clearly at $<N>$ = 1.8 and 3 e-h, as illustrated also in Figure 7.8.b - due to the twofold degeneracy of the $1S(e)\text{-}1S_{3/2}(h)$ exciton state. Experimental B1 traces do not show any induction behavior, since a fast charge-trapping process probably dominates the initial bleaching recovery.
- The long time value of the bleach should be precisely 50% of the early time value of the bleach for high fluence ($<N>$ > 1), since the maximum occupancy of the $|1S\rangle$ exciton state is N=2 and multi-excitons should recombine in hundreds of ps, while the single-exciton lives for tens of ns. On the contrary, the late B1 experimental signal at $<N>$ > 1 is less than 50% of the B1 value at t=0, supporting the existence of some trapping related processes, which compete with the intrinsic exciton recombination. This yields a multi-exponential decay, as demonstrated by the four exponential components extracted from the fit of the data presented in Figure 7.7.

Finally, if a trapping process is included in the interpretation of the data, the adequacy of using a global multi-exponential fit with time constants shared for all the incident pump fluences is called into question. As discussed in the previous section, the Stark interaction between an exciton and a trapped-charge modifies the oscillator strength of the exciton transition.

[i] Multi-exciton recombination (N > 3) rates (up to N = 6) are also considered in the average. Such rates are few ps long and calculated by considering that $\tau_{N\text{-}exc} \sim \tau_{(N\text{-}1)\text{-}exc}/N^2$ [Ref. [92]].

Furthermore, if the incident power is increased, it reasonable to suspect that also the trap density increases. The combination of both leads not only to a re-organization of amplitudes, but also a variation of the characteristic time constants relative to the relaxation processes should be expected. Therefore, from a physical point of view, forcing the fitting to reproduce the data at different pump fluences relying only on a different weighting of the exponential components is inappropriate.

On the other hand, in a multi-exponential fit amplitudes and time constants are correlated parameters. Such correlation may lead to erroneous interpretation of the data when comparing sets of parameters each obtained from an independent fitting procedure. The way out of this paradox is the application of a global fitting of different time-traces from the same TA map relative to other spectral features ($\lambda \neq \lambda_{B1}$) (*i.e* collected simultaneously and at the same experimental conditions). This will be the topic of Section 7.3.2.

Unveiled all the issues related to the B1 fitting, the next sub-sections relative to the core-shell series will just provide some qualitative information, leaving to the following section a more quantitative analysis of the data.

CdSe#1-CdS core-shell QDs

Examples of B1 bleaching time trace for CdS-shelled quantum dots are shown in Figure 7.10. At increasing shell thickness, the pump fluence has been lowered - according to $< N >= F \cdot \sigma$ - in order to counterbalance the increase of the absorption cross section at 400 nm due to the CdS shell material. In this way, the average number of excitons generated in all the core-shell volume is always 0.8, 1.8 or 3.

By comparing the B1 time trace of bare CdSe#1 QDs and CdSe#1-CdS core-shell QDs, some general differences can be noticed: first of all, the fitting of this series has invoked only three exponential components, plus a step function accounting for IRF and sub-ps dynamics. Again, τ_1 was set at the $<\tau>$ value reported in Figure 6.4. τ_2 is longer (>240 ps) compared to CdSe#1, but still < 1 ns and fluence dependent. However, the main difference from CdSe bare cores is that the initial bleaching magnitude seems to endure for longer times (Figure 7.10). This is not due to a longer τ_2 value, it is rather explained by both the absence of a fast τ_4 decay component and the presence of a growth component, occurring during the first 10 ps and with a relative positive amplitude A_3 and time constant τ_3.

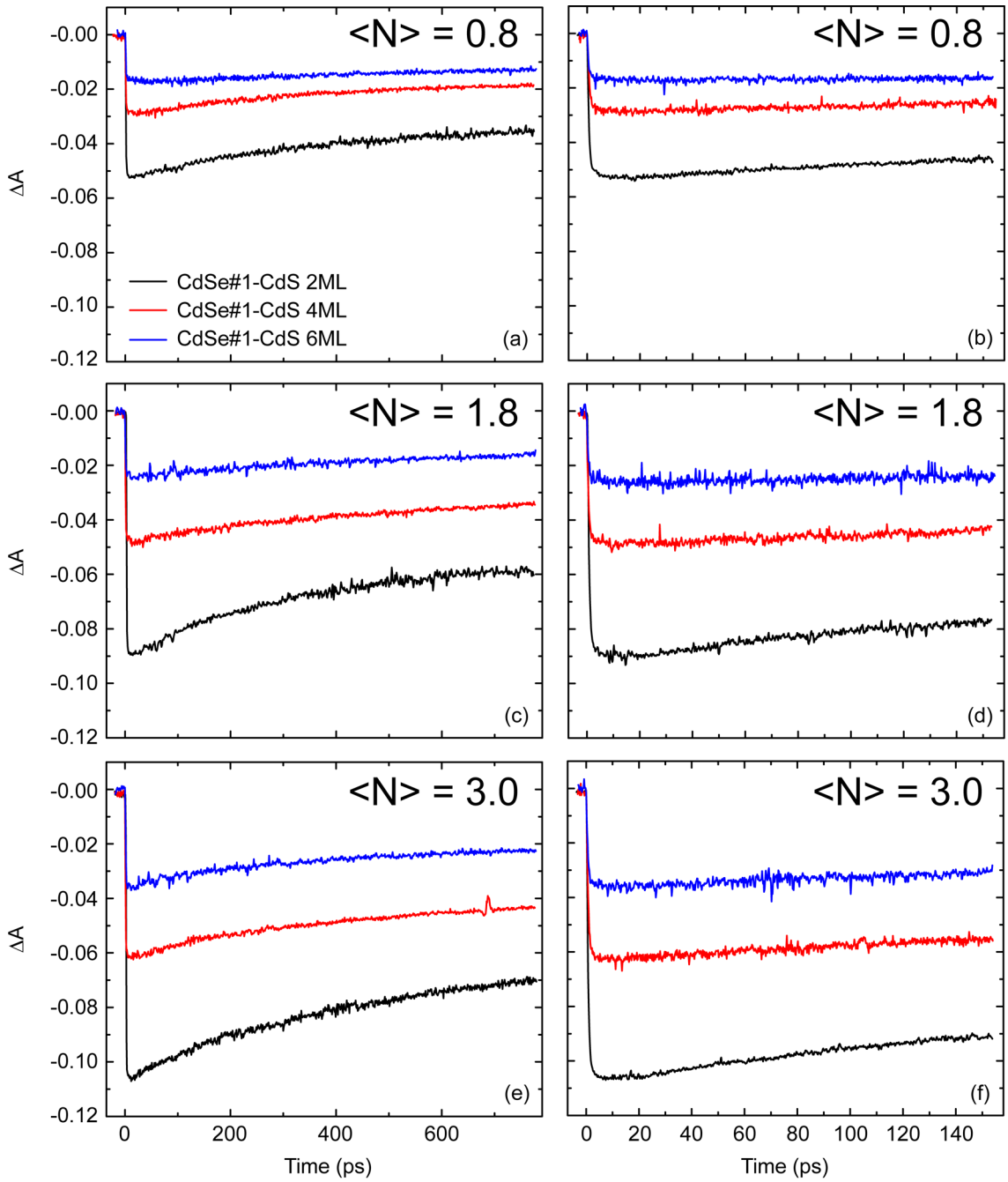

Figure 7.10: B1 TA time traces relative to the series CdSe#1-CdS. 2, 4 and 6 ML samples are here illustrated. (a), (c) and (e) represent the evolution of B1 in the 800 ps time window (Δt = 1 ps) at increasing pump fluence, while (b), (d) and (f) report the B1 time traces in the 160 ps time window collected with a higher resolution (Δt = 0.2 ps).

In Figure 7.11 the same B1 traces have been normalized to the absorbance of the QD solution at the relative spectral position (1S(e)-$1S_{3/2}$(h) exciton state).

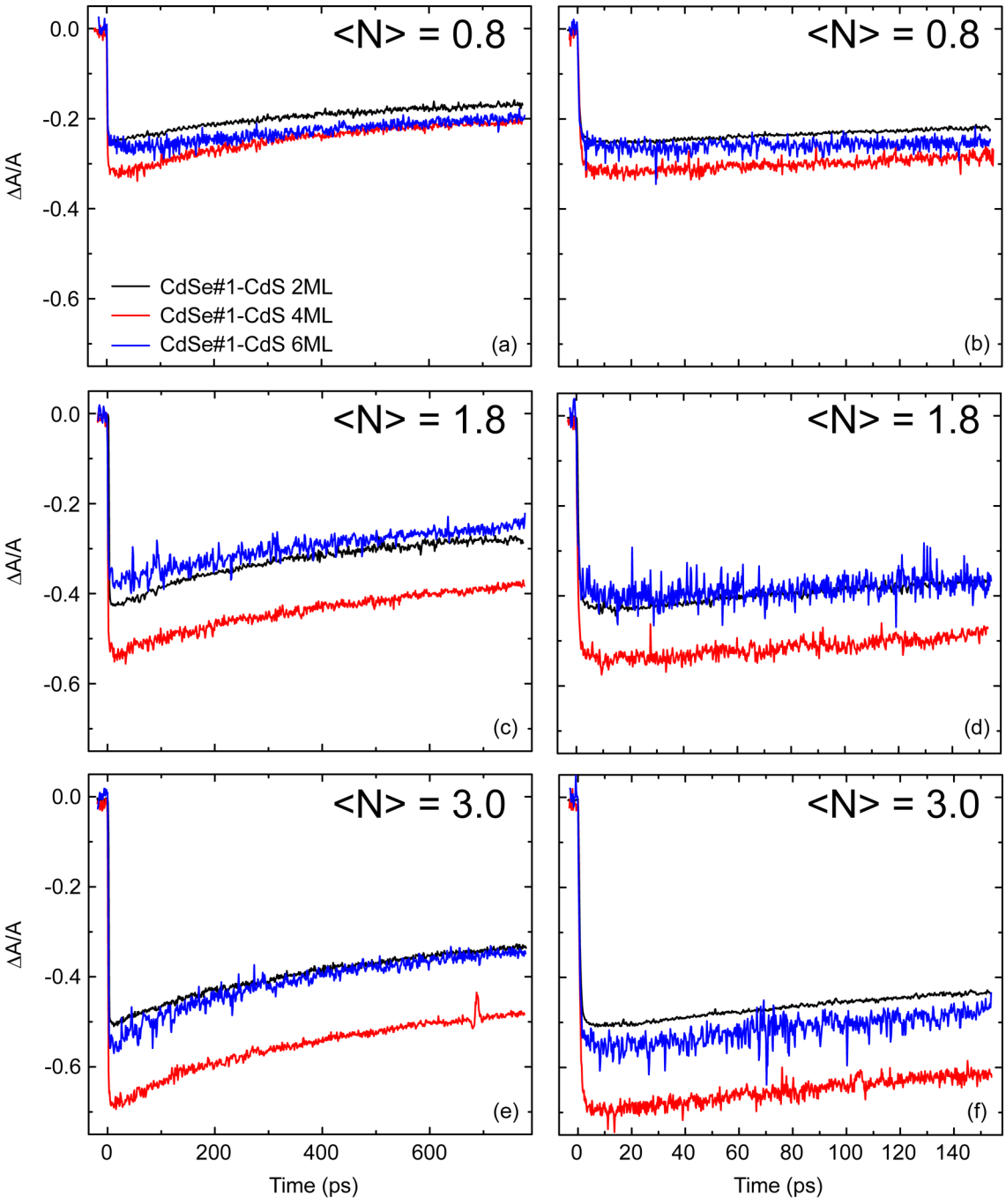

Figure 7.11: B1 *ΔA/A* time traces relative to the series CdSe#1-CdS. 2, 4 and 6 ML samples are here illustrated. (a), (c) and (e) represent the evolution of B1 in the 800 ps time window (Δt = 1 ps) at increasing pump fluence, while (b), (d) and (f) report the B1 time traces in the 160 ps time window collected with a higher resolution (Δt = 0.2 ps).

Figure 7.6 already proved that the B1 TA signal, probably due to photocharging, does not follow the expected Poisson-based trend with pump fluence (Eq. 7.5). On top of that, Figure 7.11 shows that increasing the CdS shell thickness the |*ΔA/A*| B1 signal initially increases, but after few shell MLs it rapidly decreases, thus for all pump fluences the |*ΔA/A*| traces for the 6 MLs sample resemble the 2MLs ones. Shell growth would have been expected to progressively improve the signal and limit the photocharging effects. However, such prediction relies on the assumption that in a type-I core-shell QD all the excitons generated in the large shell volume transfer rapidly

and without any impediment into the core. As it will be discussed in the Section 7.3.2, this might not be true. B1 represents a bleaching signal of a core exciton state; every process that limits the probability of having such state occupied causes a drop of the B1 signal.

CdSe#1-$Cd_{0.5}Zn_{0.5}S$ core-shell QDs

Typical B1 bleaching time traces for the $Cd_{0.5}Zn_{0.5}S$-shelled QDs are reported in Figure 7.12.

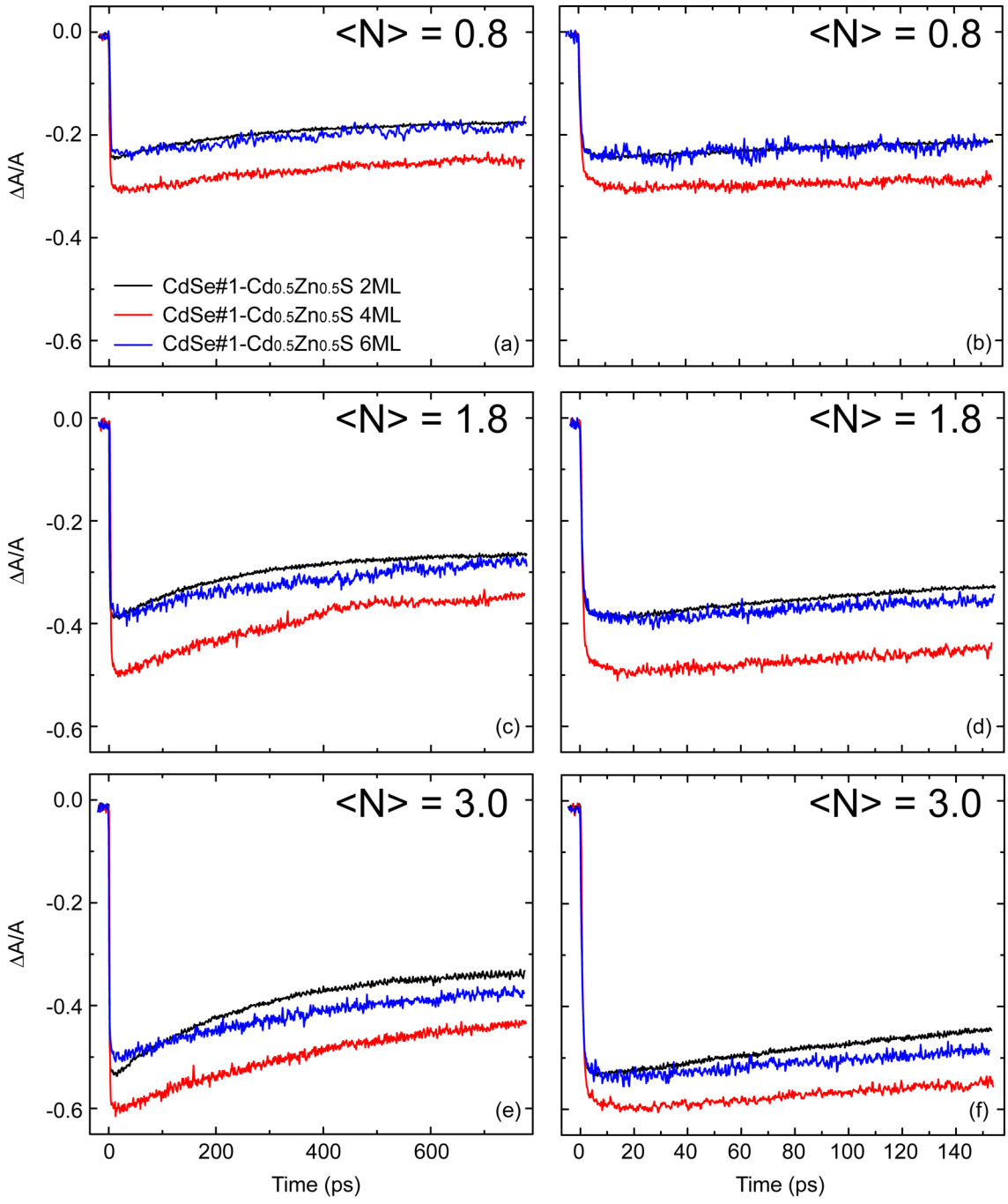

Figure 7.12: B1 *ΔA/A* time traces relative to the series CdSe#1-$Cd_{0.5}Zn_{0.5}S$. 2, 4 and 6 ML samples are here illustrated. (a), (c) and (e) represent the evolution of B1 in the 800 ps time window (Δt = 1 ps) at increasing pump fluence, while (b), (d) and (f) report the B1 time traces in the 160 ps time window collected with a higher resolution (Δt = 0.2 ps).

As for the CdSe#1-CdS series, a tri-exponential function provides the best fit of the data. Again, an induction component to B1 (τ_3) is detected on the short timescale. The τ_2 values are on the same time-scale as for CdS and τ_1 are set also here at the $<\tau>$ reported in Figure 6.4. All extracted rates are fluence dependent.

Alike the CdS series, also here $|\Delta A/A|$ B1 signal initially increases, but after few shell MLs it rapidly decreases.

CdSe#2-ZnS core-shell QDs

B1 Time traces for the CdSe#2-ZnS shelled QDs are reported in Figure 7.13.

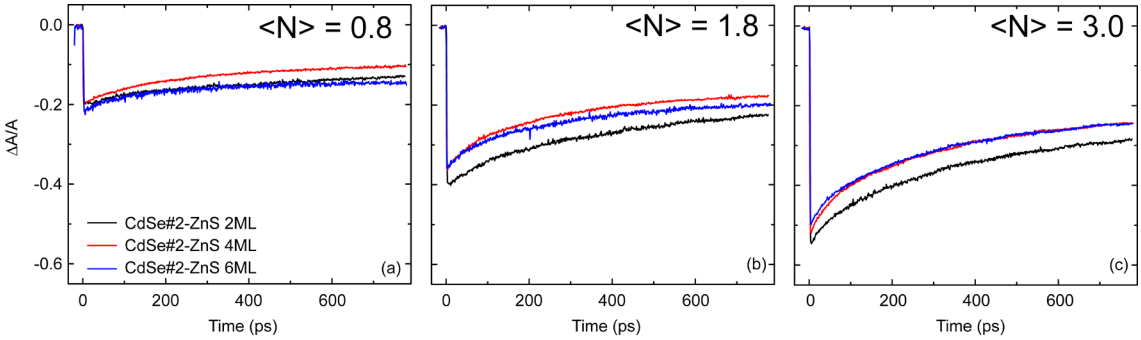

Figure 7.13: B1 $\Delta A/A$ time traces relative to the series CdSe#2-ZnS. 2, 4 and 6 ML samples are here illustrated. (a), (b) and (c) represent the evolution of B1 in the 800 ps time window (Δt = 1 ps) at increasing pump fluence.

Also here, a minimum number of three exponential components was necessary in order to fit the data. In this case, the third component ($\tau_3 \sim 20$ ps) has turned out to be a bleaching recovery (*i.e.* negative amplitude) component instead of an induction.

In this case the pump is not resonant with any shell transition, therefore all excitons are generated in the CdSe core. At increasing shell thickness the deviation from the Poisson expected trend (Eq. 7.5) increases, especially at higher pump fluences. The absorption normalized bleaching ($|\Delta A/A|$) is lowered as more ZnS is deposited on top of the core, and stabilizes as the shell thickness exceeds 2 MLs.

7.3.2 Multi-Wavelength Global Fitting

In order to gain a more quantitative interpretation of the data, a multi-wavelength global fitting of data has been applied and the main results are presented in this section. In order to deal with such analysis, some fundamentals about the method have to be introduced.

First of all, each TA absorption spectrum is the results of the evolution of a several processes, each with a defined characteristic time constant τ_k. By and large, each k^{th}-species may contribute at all the wavelengths, with an extent given by the k^{th} -amplitude α_k. From a mathematical point of view, if the TA data set is considered as a rectangular matrix $\mathbf{D}(t \times \lambda)$, where t-rows represent

the TA spectrum at a fixed time and λ-columns represent the time trace at fixed wavelength, it is possible to express[186]:

$$\mathbf{D} = \mathbf{A}\mathbf{T}^{\mathrm{T}} + \mathbf{R} \qquad \text{(Eq. 7.10)}$$

The $\mathbf{T}(t \times k)$ matrix contains the kinetic profile of the k^{th} pure contribution at t^{th}-time delay, on the other hand the $\mathbf{A}(k \times \lambda)$ matrix contains the amplitude of each component at λ^{th} -wavelength. The $\mathbf{R}(t \times \lambda)$ error matrix contains residuals.

Within this framework, a least squares algorithm can be used to iteratively fit the $\mathbf{A}(k \times \lambda)$ and $\mathbf{T}(t \times k)$ matrices to the experimental data $\mathbf{D}(t \times \lambda)$, thus minimizing $\mathbf{R}(t \times \lambda)$ matrix elements.

From a physical point of view, the description of the original $\mathbf{D}(t \times \lambda)$ data set should be obtained by using the minimum amount of time constants (τ_k) necessary for a good quality fit.

Each row of the globally optimized $\mathbf{A}(k \times \lambda)$ matrix, which stands for the time-independent spectrum of the k^{th} component, may still represent a convolution of different components and then does not reveal a clear physical origin. In all fitting procedures, the optimized parameters (or spectra of parameters) do not have only to describe the experimental data, but they must be meaningful from a physical point of view. Of crucial importance is thus the choice of the model, which has to be as simplest as possible and, possibly, based on prior knowledge of the system.

The simplest model prototypes are the *parallel* and *sequential* models (Scheme 7.3)[186].

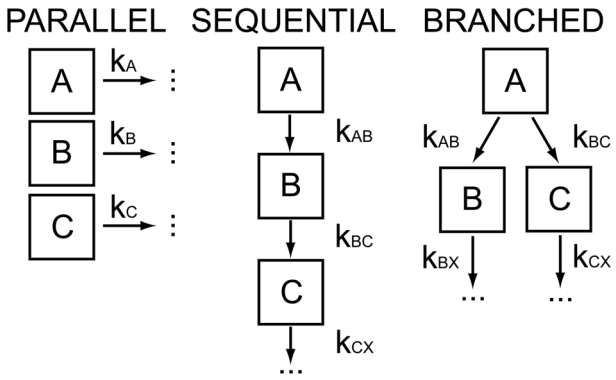

Scheme 7.3: Examples of *parallel*, *sequential* and *branched/target* models. Each compartment represents a distinct physico-chemical species and is a component of the total reaction.

In *sequential* models one component flows into the next compartment with increasing lifetimes. In parallel models each component flows directly to the ground state. The resulting $\mathbf{A}(\lambda)$ spectra are called *evolution associated difference spectra* (EADS) and *decay associated difference spectra* (DADS), respectively. On the other hand, *target* analysis is used if a model different from these is employed (Scheme 7.3); this is typically the case when one or more components communicates with more than one other species. Spectra from this analysis are called *species associated difference spectra* (SADS). The use of a specific target model entails a pre-existing knowledge about the system, which in part can be provided by a preliminary DADS and/or EADS analysis.

For the purpose of this thesis, multi-excitonic theory (Eq. 7.6) would predict that an $(N+1)^{th}$-exciton should recombine into the N^{th} multi-exciton, down to the single exciton state. Therefore, at first glance an EADS analysis may seem the right choice. However, as discussed in the previous section, exciton-exciton and exciton-trapped charge Stark interaction break this sequential picture. Local fields are not only responsible for the energy shift of the states involved, but also influence the population and the recombination rate of exciton species. Moreover, Poisson statistics states that a non-zero probability of having the final single-exciton state already populated t = 0, occurrence which further lowers the accuracy of a sequential interpretation. On the other hand, it can be easily inferred that the individuation of a target kinetic model (SADS analysis), which should take into account also Poisson occupation and Stark effects, would be a very hard task, with the risk of a speculative interpretation of the results.

In this thesis work, the poor knowledge about the kinetic model imposes a global analysis based on a parallel model (DADS analyses), which considers each wavelength independent with respect to others and takes into account the initial population of all the states involved. Independently on the underlying dynamics, DADS relative to a TA spectrum can be considered as loss or gain of absorption with a certain lifetime[186]. If, despite the multi-branched parallel model, a residual sequential behavior is present, DADS will represent the spectra of amplitudes relative to the decay and rise of different intermediate states.

In order to attain to the requirement of maintaining minimal the number components necessary to fit the data and to avoid the occurrence of local minima, a Singular Value Decomposition (SVD) analysis[186] has been used. Without entering into the details of this mathematical technique, SVD provides the minimum number of signal components that can re-construct the original data via a linear combination.

The whole analysis has been performed by using an integrated Matlab routine[187]. Each TA map has been fitted independently, in order to take into account the variation of the different rates at increasing shell thickness, composition and fluence. The fitting parameters were initialized on the basis of the independent B1 fitting, with a long lasting time-constant fixed at $\tau_1 = \langle\tau\rangle$, *i.e.* the single-exciton average lifetime, whose value is reported in the previous chapter. Again, a step-function has been employed in order to account for all the processes occurring on the sub-ps time scale, namely intra-band exciton relaxation to the $|1S\rangle$ and response of the system to a ~ 150 fs pump-probe auto-correlation function.

Henceforth $A_k(\lambda)$ are labeled as α_k to avoid duplicates with A1 and A2 PA bands.

CdSe#1-CdS core-shell QDs

The entire set of data in the CdS series has exhibited the need for a 3-termed multi-exponential decay, as expected from the B1 analysis. An example of fitting results is provided by Figure 7.14, where the DADS, a.k.a. the amplitude spectra α_k relative to each exponential component, are reported.

All the τ_2 and τ_3 values for the CdS are collected in Figure 7.15 (first column of the panel), where they are arranged to enlighten the variation with the shell thickness and pump fluence.

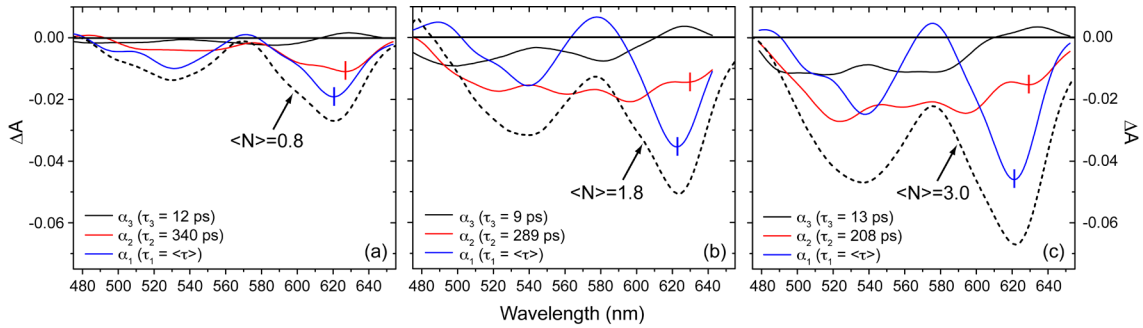

Figure 7.14: Amplitude spectra ($\alpha_k(\lambda)$, DADS) optimized from the TA data of the sample CdSe#1-CdS 4ML. (a), (b) and (c) panels illustrate DADS at pump fluences of <0.8>, <1.8> and <3> e-h, respectively. The dashed curves represent the TA spectra at t = 15 ps and are reported here just for comparison with DADS. The DADS relative to the initial step function are not included in these graphics.

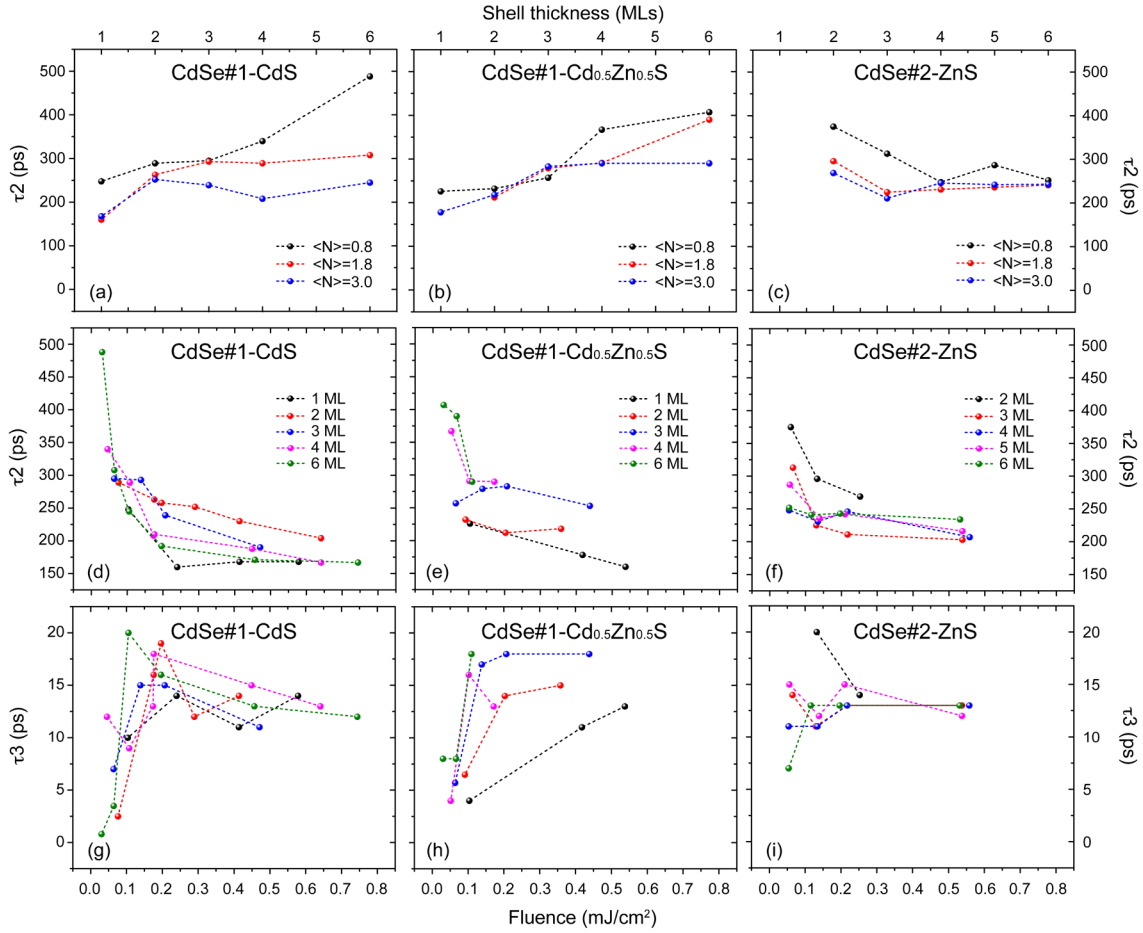

Figure 7.15: Summarizing panel reporting the τ_2 (a-f) and τ_3 (g-h) time-constants extracted from the global fits. The first row (a-c) collects the τ_2 values from the core-shell QD series at all pump fluences in function of the shell thickness. The central (d-f) and bottom (g-i) rows illustrate the dependence of τ_2 and τ_3 on the incident pump fluence, respectively.

The sign (+ or -) of each DADS (α_1, α_2 and α_3) is the most significant element, because it contains the information about the nature of such contribution. In spectral correspondence with ESA or PA (A1 and A2, Figure 7.3), a (-) α indicates that the relative exponential contributes to the growth of the signal, while a (+) α stands for a decay component of the PA signal. For instance, in Figure 7.14.b at the A2 spectral position ($\lambda \sim 570 \div 590$), α_2 and α_3 are (-), meaning that they contribute to the formation of the PA signal, while α_1 is (+) and is responsible for its recovery.

The interpretation for bleaching (B1, B2 and B3, Figure 7.3) signals is basically inverted: a (-)α indicates a recovery of the bleaching while a (+)α indicates a formation of the bleaching signal. Considering B1 ($\lambda \sim 620$), in Figure 7.14 α_1 and α_2 are (-), while α_3 is (+). Therefore, the latter component is responsible for the delayed induction of B1 observed in the previous section (Figure 7.11).

Due to the CdS shell thickness, each QD of the series has a different absorption cross section, therefore to build-up the set of results reported in the first row of Figure 7.15 each sample was pumped at different fluence (mJ/cm^2) levels. On a quality level, at increasing CdS shell thickness the τ_2 component increases, but such trend is mitigated by fluence: at $\langle N \rangle = 3$ τ_2 is almost invariant with the CdS shell volume.

Looking at the Figure 7.15.d and 7.15.g, in these graphics the dependence of τ_2 and τ_3 on the effective pump fluence is reported. As mentioned before, τ_2 decreases with fluence, and this general trend is verified for each CdS sample. On the other hand, τ_3 shows a particular step-like behaviour with fluence. A recurrent result in low fluence experiment ($\langle N \rangle < 1$) is $\tau_3 \sim 5$ps. Conversely, at higher pump fluence, $\tau_3 \sim 15$ps.

Dealing with τ_2, such time constant represents the mean bi-excitonic lifetime, which includes the entire set of processes inducing a bi-exciton recombination, *i.e.* radiative and Auger recombination. In order to support the bi-exciton nature of τ_2, the relative amplitude spectrum (α_2) and fluence/shell thickness dependence will be now discussed.

i. DADS. The analysis can be focused on two of the most significant spectral features: B1 ground state bleaching and A2 excited state absorption. Looking at Figure 7.14, τ_2 relative amplitude α_2 is (-) in the entire spectrum. This means that τ_2 contributes as a bleaching recovery component for B1 and at the same time increases the PA at A2 spectral position.

As stressed out, B1 bleaching arises also from the energy relaxation induced by the bi-exciton formation (Scheme 7.2). Therefore, a bleaching recovery is expected as the bi-exciton density decreases (Scheme 7.2). On the other hand, A2 is the result of a PA to the shifted $|1P\rangle$ state (Scheme 7.2). The $|1S1S\rangle$ bi-exciton recombination increases such PA, as either a trapped (result of bi-exciton AR) or a bound single exciton (product of the radiative bi-exciton recombination)

can generate this shifting. On the other hand, the A2 PA then recovers to zero with τ_1, whose relative amplitude is (+) in that spectral region.

A further verification that τ_2 is related to the bi-exciton relaxation is provided by looking at the B1 spectral region (Figure 7.14), in which it is evident that the minimum of the α_2 amplitude is red-shifted with respect to the α_1 single-exciton component. Such minimum coincides with the bleaching of the |1S1S⟩ state and is consistent with a Stark-shifting interpretation of the spectral features.

ii. Fluence effects. With increasing pump pulse fluence a general decrease of τ_2 is observed in Figure 7.15.d. This is consistent with the photocharging picture outlined in both theoretical and spectral structure sections. An increase in fluence determines the increase of the mean number of exciton generated in a single dot. The presence of non-radiative mechanisms determines then an accumulation of charged and trapped excitons. The net result is a faster bi-exciton recombination, due to the increase of the non-radiative contribution.

iii. Shell thickness effects. The general trend shown in Figure 7.15.a is that of an increase of τ_2 with increasing shell thickness. An increase of the shell thickness reinforces the confinement effect, localizing more efficiently the exciton (or bi-exciton) wave function away from the surface. Being the trapped carriers mainly localized at the surface states reduces the effective non-radiative recombination rate and the photocharging effect.

Focusing on τ_3, this ~10 ps time-constant (Figure 7.15.g) may be related to two different processes: multi-exciton recombination and shell-core exciton transfer. In order to support both the hypotheses, as in the case of τ_2 the relative amplitude spectrum (α_3) and fluence/shell thickness dependence will be now discussed.

i. DADS. A peculiarity of the τ_3 component is that its associated amplitude is (+) in correspondence to B1, which means that it acts as a growth component to the bleaching signal. Such behavior is coherent with a multi-exciton relaxation process, which is responsible for the induction of the B1 signal (Figure 7.8) as a consequence of the kinetic scheme provided by Eq. 7.6. Moreover, the τ_3 time scale (few ps) and the (-) value of α_3 in correspondence of A2 (PA signal growth) are consistent with a multi-exciton relaxation process.

However, the same peculiarities may be justified by a shell to core exciton retarded transfer. By examining the experimental setup, the pump pulse (λ = 400 nm) is resonant with both the CdSe core and the CdS shell. Ideally, excitons generated in the shell material should rapidly transfer to the core states, driven by the type-I band alignment. Actually, CdSe-CdS is a type-II hetero-structure, which forces a differential distribution for electrons and holes. While electrons are delocalized over the whole QD volume, the holes are more concentrated in the core. Such charge misbalance may generate a "Coulomb-blockade[165]" (Scheme 7.4) for the hole-migration into the core and consequently slow down the relaxation dynamics.

ii. Fluence effects. The second hypothesis is supported by the step-like trend of τ_3 with fluence reported in Figure 7.14.g. Above the <N> = 1 threshold the τ_3 increases (on average for all the QDs in the series) from ~ 5 to ~ 15 ps. Therefore, it is confirmed that above a certain fluence the hole-blockade becomes more efficient[165]. In the framework of the Marcus charge-transfer theory[159], the increase of the excitation density in the shell material with increasing fluence modifies the reorganization energy (λ), which is typically ascribed to Coulomb interactions and polarizability differences.

On the other hand, the increase of τ_3 with fluence undermines the first hypothesis. However, multi-exciton recombination occurs, but the hole-blockade process probably covers its effect on the recombination dynamics.

iii. Shell thickness effects. An analysis in terms of the influence of shell thickness on τ_3 reveals the absence of any particular dependence.

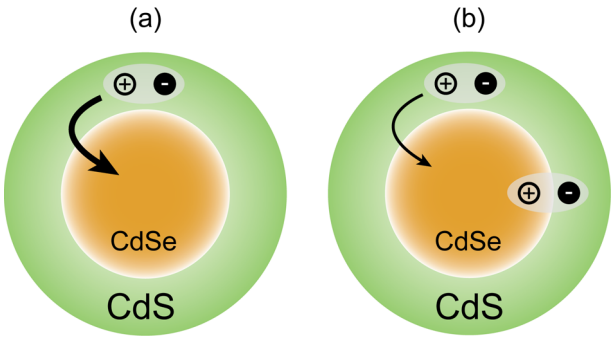

Scheme 7.4: Schematic representation of the photophysics related to the step increase of τ_3 with fluence for the CdSe#1-CdS series. In (a) a single-exciton is generated by the 400 nm pump beam in the CdS shell and transfers rapidly (< 5ps) into the core. Above threshold (b) the differential electron and hole shell-core migration rates may be responsible for the "hole-blockade" process. This leads to a slower shell-core exciton transfer rate, depicted by a thinner arrow in (b).

CdSe#2-ZnS core-shell QDs

Also in this case, the entire set of data in the ZnS series could be fit with a 3-termed multi-exponential decay fit. An example of fitting results is provided by Figure 7.16, where the amplitude spectra $\alpha_k(\lambda)$ relative to each exponential component are reported.

All the τ_2 and τ_3 values for the ZnS are collected in Figure 7.15 (right column of the panel), where they are arranged to enlighten the variation with the shell thickness and pump fluence.

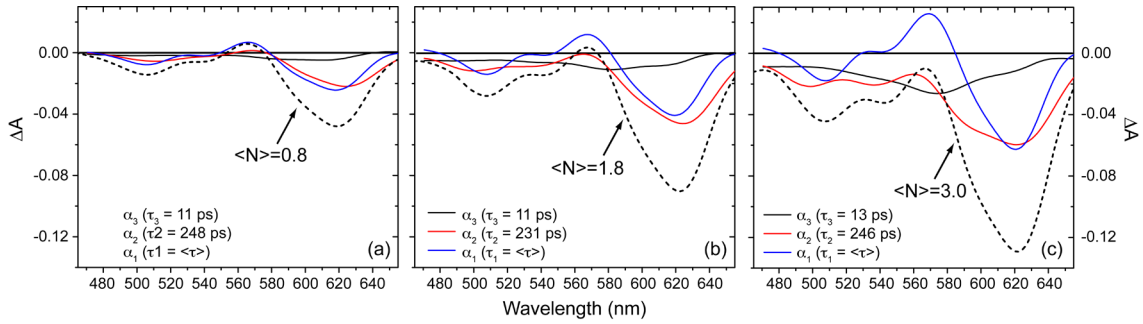

Figure 7.16: Amplitude spectra ($\alpha_k(\lambda)$, DADS) optimized from the TA data of the sample CdSe#1-ZnS 4ML. (a), (b) and (c) panels illustrate DADS at pump fluences of <0.8>, <1.8> and <3> e-h, respectively. The dashed curves represent the TA spectra at t = 3 ps and are reported here just for comparison with DADS. The DADS relative to the initial step function are not included in these graphics.

Regarding τ_2, similar considerations as in the CdSe-CdS series may be made. Again, from the time-scale (200÷350 ps) and the DADS analysis such component can be assigned to the bi-exciton recombination process. Moreover, also in this case τ_2 decreases with incident pump fluence (Figure 7.15.f), while it is almost invariant with shell thickness (Figure 7.15.c). Both occurrences can be rationalized by considering that in this case the pump fluence is not resonant with any shell state, since ZnS has a band-gap of about 3.6 eV. At increasing fluence, the probability for the bi-excitons generated in the core to interact with traps located at the highly strained core-shell interface also increases, thus leading to a faster AR. Excluding QDs with very few shell MLs, the decrease of τ_2 with fluence is however less evident compared to the CdS series. In this case in fact photocharging effects due charged states localized at the outmost surface are minimized thanks to the higher protective barrier provided by the ZnS shell. Further shell growth does not alter the recombination dynamics, most of the exciton and multi-exciton dynamics occur in the core material and are influenced by the traps located at the core-shell interface.

Finally, the higher confinement potential provided by the ZnS shell and the high excitation density in the core material increase the probability of bi-exciton formation, which is evidenced by the high α_2/α_1 ratio at the B1 spectral region. A comparison between Figure 7.14 and 7.16 shows that such ratio is almost doubled passing from a CdSe-CdS 4MLs to CdSe-ZnS 4MLs.

Focusing on τ_3, this exponential component evolves in the same ~ 10 ps timescale as in the CdS series. However, since the ZnS shell is not excited by pump pulse no exciton transfer from come to shell is expected. On the contrary, the defective core-shell interface is expected to play a crucial role in defining the exciton dynamics, also at this initial stage of the recombination process. The association of τ_3 to a fast trapping process (Scheme 7.5) to interface defect states is motivated, first of all, by the necessity to individuate a mechanism which accounts for the low and shell thickness independent PL QY values. A detailed analysis of the DADS analysis enforces such hypothesis.

i. DADS. The α_3 spectrum shows a negative amplitude at every wavelength (Figure 7.16). Therefore, focusing on A2 and B1 features, τ_3 represent a growth contribution to the former PA signal and a decay contribution to the latter bleaching signal. Charge trapping process is indeed expected to reduce $|1S\rangle$ population and therefore population contribution to B1 is reduced. On the other hand, A2 is an inherently Stark-shift generated feature. Charge trapping is expected to generate high electric field, (the dipolar exciton field turns into a more intense free-charge monopolar field) and this is consistent with assignment.

ii. Fluence effects. Figure 7.15.i shows almost no variations of τ_3 with the incident pump fluence. The probability of trapping of a hot-exciton is expected to be proportional to the density of traps, which is not dependent on fluence if the majority of traps is represented by internal lattice defects. Fluence related variations have to be found in the amplitude of the process and not in the rate.

iii. Shell thickness effects. An analysis in terms of the influence of shell thickness on τ_3 reveals the absence of any particular dependence. This is consistent with the fact that the studied phenomenon is supposed to be an interfacial phenomenon and shell volume variations are expected to act only on the amplitudes.

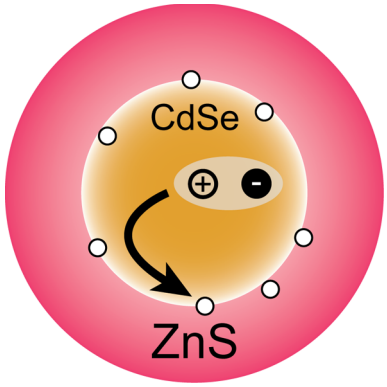

Scheme 7.5: Schematic representation of the photophysics related to the τ_3 decay component for the CdSe#2-ZnS series. The arrow represents the charge trapping at the CdSe-ZnS defective interface ($\tau_3 \sim 10$ ps).

CdSe#1- $Cd_{0.5}Zn_{0.5}S$ core-shell QDs

As for the CdS and ZnS series, also the TA maps of the CdSe-$Cd_{0.5}Zn_{0.5}S$ mixed shell series could be fit with a 3-termed multi-exponential decay. An example of fitting results is provided by Figure 7.17, where the amplitude spectra $\alpha_k(\lambda)$ relative to each exponential component are reported. Time constants τ_2 and τ_3 are collected in the central column of Figure 7.15.

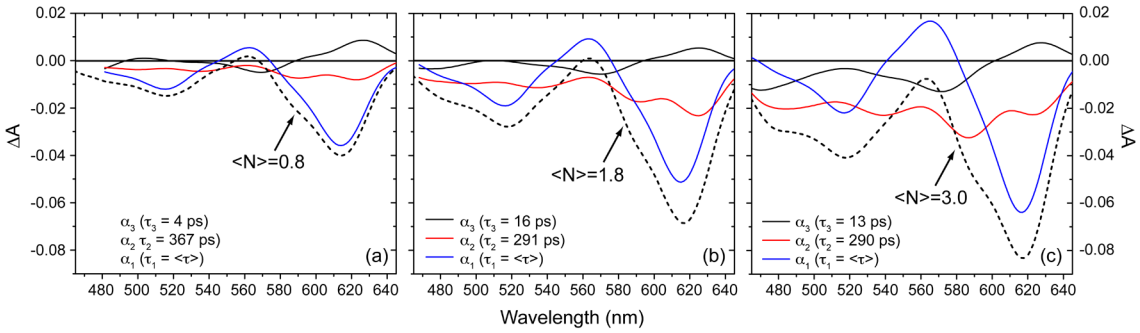

Figure 7.17: Amplitude spectra ($\alpha_k(\lambda)$, DADS) optimized from the TA data of the sample CdSe#1-$Cd_{0.5}Zn_{0.5}S$ 4ML. (a), (b) and (c) panels illustrate DADS at pump fluences of <0.8>, <1.8> and <3> e-h, respectively. The dashed curves represent the TA spectra at t = 15 ps and are reported here just for comparison with DADS. The DADS relative to the initial step function are not included in these graphics.

Considering CdS and ZnS as asymptotic limits, it would be expectable to observe an intermediate behavior for the $Cd_{0.5}Zn_{0.5}S$ sample. However, the observed behavior for the multi-exciton recombination dynamics resembles that of the CdS series. This is primarily due to the fact that the pump pulse excites also the shell material, having the $Cd_{0.5}Zn_{0.5}S$ alloy a lower band-gap than ZnS. The observed trend is similar to that obtained for CdS (Figure 7.15): a step-like increasing trend for τ_3 and a generally decreasing τ_2 with fluence.

Although the shell is excited in these experiments, the presence of interfacial defects can't be excluded. To unveil the nature of each exponential component the relative amplitude spectra need to be investigated (Figure 7.16). The resulting amplitude curves, for both τ_2 and τ_3 resemble those obtained for the CdS series. The τ_2 time constant is again associated to the bi-exciton relaxation process, while τ_3 can be assigned to a core-shell charge transfer process, since it contributes as a growth to both the PA A2 and GSB B1. The step-like increase with fluence is less evident compared to the pure CdS shell, probably due to the counteracting effect of charge trapping at the core-shell interface, which is known to be highly strained (Chapter 5).

Chapter 8.

Amplified Spontaneous Emission from CdSe-$Cd_XZn_{1-x}S$ QDs

In this final chapter the optical gain properties of the QDs series investigated in this thesis work are presented. As already mentioned in Section 2.5, amplified spontaneous emission (ASE) was obtained and characterized by previous works by depositing colloidal QDs in densely packed thin films. Best results in terms of activation threshold fluence and stability were obtained by using CdSe QDs with a graded CdS-$Cd_{0.5}Zn_{0.5}S$-ZnS shell, embedded in a sol-gel matrix[43,44]. The same strategy was also employed by other groups, who achieved low ASE threshold fluences also in the blue spectral region by using graded core-shell QDs of different composition[49].

In Section 8.1 a brief overview of the procedures employed to prepare hybrid QDs-matrix thin films is provided. In the following 8.2 Section results of the ASE characterization, in terms of activation threshold and photo-stability, is presented. In this section a comparative study with the best performing CdSe-CdS-$Cd_{0.5}Zn_{0.5}S$-ZnS graded QDs is also conducted. By using graded CdSe-CdS-$Cd_{0.5}Zn_{0.5}S$-ZnS shell as optical gain materials, the first evidence of a low-threshold microcavity laser operating in the red spectral region was demonstrated[44], with the possibility to optically pump the system both in the linear one-photon and non-linear two-photon regime. This chapter demonstrates that, in order to lower the lasing activation threshold, much of the efforts must be spent on optimizing the ASE threshold and photo-stability. The best way to minimize the threshold is by finely engineering the core-shell heterostructure.

8.1 Preparation of QD-doped solid-state matrices

Since the active volume provided by a single quantum dot is insignificant compared to macroscopic media, a large ensemble of QDs has to be used to achieve optical gain comparable with their bulk counterpart. QD lasing media were first realized in glass matrices via high-temperature precipitation[188], then by epitaxial or self-assembled growth of nanoislands[189] and with the advent of the colloidal synthesis they were prepared as close-packed films[179] or

incorporated into polymers or sol-gel matrices[190]. However, the development of new reliable methods for the dispersion of NCs has to face many drawbacks. For example NCs typically tends to aggregate in polymer-based matrices[191], thus loosing their functional property (i.e., luminescence) rapidly during polymerization steps and the high temperature consolidation process. High temperatures also enhance degradation of QDs and consequently lower their optical properties.

Among most recent QDs embedding methods, incorporation in sol-gel matrices represents the best method to overcome main problems encountered with other attempted solutions. The advantages offered by the sol-gel approach are:

- low annealing temperatures (<300° C).
- high photostability, which is usually limited by carrier traps situated at the surface of nanocrystals. The host matrix can contribute to the surface passivation of QDs, acting as an extra shell.
- homogeneity of QDs dispersion in the matrix[129] and high refractive index, fundamental requirements for an optimal waveguide.

Concerning materials employed as sol-gel matrices for CdSe QDs, recently some comparative studies have been performed on some oxides with high refractive index: ZrO_2, HfO_2 and TiO_2[129,192]. Results obtained in terms of performances as gain media showed that ZrO_2 and HfO_2 are preferable to TiO_2. In fact, zirconia (and hafnia as well) has wide band gap, it can form solely type-I structures in presence of CdSe QDs; titania instead may act as type-II host, depending on the size of the QDs (Figure 3.7). In type-II structures electrons and holes can escape by diffusion through the conduction and valence band of the matrix. This phenomenon leads to corrosion of the nanocrystal and to the quenching of the photoluminescence intensity. The higher probability of carrier losses into the matrix is also considered as the origin of the lower stability of the optical properties (i.e. photoluminescence) in TiO_2 under continuous and pulsed laser action.

Recently, also a non- sol-gel ZnS matrix was employed[193], with the advantage of having a more semiconductive nature and a composition that matches the outer shell of many core-shell QDs. Moreover, in the protocol presented in Ref. [193] the annealing temperature of the film is almost halved compared to ZrO_2 and QDs are directly embedded in the matrix precursor from their native solvent (toluene). Good results were obtained in terms of ASE threshold values and stabilities (comparable with the QD-ZrO_2 hybrid system). The drawbacks of employing such matrix, compared to ZrO_2, is the lower resistance to ageing and the necessity to operate in an O_2-free atmosphere when conducting both the film deposition (spin-coating) and annealing processes.

In this work mainly ZnS and ZrO_2 matrices were tested by embedding different CdSe core-shell QDs. Optimization and ASE characterization of QD-doped ZnS films is ongoing and only preliminary results have been obtained so far.

In this manuscript only the results obtained by using ZrO_2 will be provided. ZrO_2 is, at the moment, the matrix that provided the best compromise of performances, stability (to both irradiation and ageing) and reproducibility.

8.1.1 Dispersion of CdSe QDs in ethanol

In order to have particles compatible with sol-gel materials, the original hydrophobic ligands of the core-shell CdSe QDs, in $CHCl_3$ solutions, are exchanged with an appropriate ligand[129] and re-dispersed in EtOH. For CdSe cores and core-shell nanocrystals, a surface ligand exchange with 5-Amino-1-pentanol (AM) is performed, to make QDs soluble in ethanol (EtOH) solutions.

The protocol followed for the ligand substitution and redispersion in EtOH is similar to that utilized by Petruska *et al.*[44,190]. The target of this procedure was to prepare 160 µL solutions of QDs in EtOH with a concentration of ~80 µM, passing through the following steps:

1. NCs were firstly precipitated from chloroform by adding some drops of AP solution in $CHCl_3$ 1M. To help the phase separation solutions were centrifuged until visible precipitation of QDs.
2. Nanocrystals were then re-dispersed in 1ml EtOH and 300µL of AM in $CHCl_3$ 1M to allow homogeneous dispersion. This solution was left overnight.
3. QDs were re-precipitated with a minimum amount of hexane.
4. The residual solvent was removed and finally QDs were re-dispersed in 160 µL of EtOH, getting to the required ~80 µM concentration of QDs, at that point capped by AM.

8.1.2 Preparation of sol-gel QDs/ZrO_2 hybrid matrices

Nanocrystals, after the separation in EtOH, were ready to be inserted in the sol-gel matrix. The method adopted for the preparation of the zirconia sol is similar to that suggested by Urlacher[44,194]:

1. As matrix precursor Zr-isopropoxide, $Zr(OPr)_4$ (0.5 mL, 2.26 mM) was employed, while acetylacetone (AcAc) (0.13 mL, 2.26 mM) was chosen as chelating agent. The sol solution in isopropanol (i-PrOH) (3 mL) was thus obtained.
2. To ensure chelation of the metal cations by AcAc, the sol solution was stirred for about 1 h and then passed through a 0.2 µm PTFE filter prior to its use.
3. 80 µL of sol solution are then added to each batch of QD solution in EtOH, previously prepared in the way reported above, with a volume of 160µL and a concentration of ~80 µM.
4. Sol-gel QDs doped thin films are obtained by spin-coating (in Ar atmosphere to prevent degradation) at 3500 rpm for 20s on quartz glasses.
5. Films were treated at 100°C for 2 min and at 250°C for a further 5 min. These temperatures offer the best compromise between the creation of a QDs doped waveguide with a high refractive index (increased by high temperature annealing) and photoluminescence activity (better preserved by low temperature treatments).

Steps 4 and 5 were repeated for other two times, in order to deposit 3 individual layers.

To conclude the description of the procedure followed to obtain the QDs/ZrO_2 hybrid matrices, a final remark has to be reported. For some reason, yet not fully rationalized, the process of re-dispersion of QD from $CHCl_3$ to EtOH didn't work with some of the QDs solutions; in fact, at the moment of re-dispersion in EtOH (step 4 of the protocol), for some samples a considerable fraction of QDs was not dispersed in solution and thus not included in the matrix. Different strategies and separation methods were attempted in order to overcome this problem, but the problem persisted, especially for the CdSe cores and both CdSe#1- and CdSe2#-ZnS series. The origin of such a difficulty in the re-dispersion may be attributed to an unsuccessful adequate capping of the QDs with octadecylamine after the QDs synthesis. This could have caused residuals of ligands from the synthesis mixture that boost the precipitation of QDs in alcoholic solution and can't be substituted by aminopentanol with the soft method employed in this work. For the problem reported above, only for samples reported in Table 8.1 the inclusion in matrix was successful in terms of photoluminescence and optical gain properties.

Table 8.1: Core-shell QDs embedded in ZrO_2 sol-gel matrix. The final film thickness (t [nm]) and the relative QD average radius are reported.

QD	t [nm]*	<r> [nm]†
CdSe-CdS 2ML	122 ±5	2.5
CdSe-CdS 4ML	166±4	3.2
CdSe-CdS 6ML	224±3	3.9
CdSe-$Cd_{0,5}Zn_{0,5}S$ 2ML	135±5	2.5
CdSe-$Cd_{0,5}Zn_{0,5}S$ 4ML	188±5	3.2
CdSe-$Cd_{0,5}Zn_{0,5}S$ 6ML	230±5	3.8

* Film thickness was evaluated by ellipsometric measurements, while † the average radii are estimated by TEM analyses (Chapter 4).

8.2 ASE characterization of CdSe-$Cd_xZn_{1-x}S$ QDs

Amplified spontaneous emission experiments were conducted both in waveguide and in transmission configuration (Section 3.6). Results obtained by means of the waveguide configuration will be presented in the first sub-section, while the transmission method will be discussed in the following one.

8.2.1 ASE: Waveguide configuration

In Figure 8.1 the photoluminescence spectra and ASE of the QD-doped ZrO_2 films are presented.

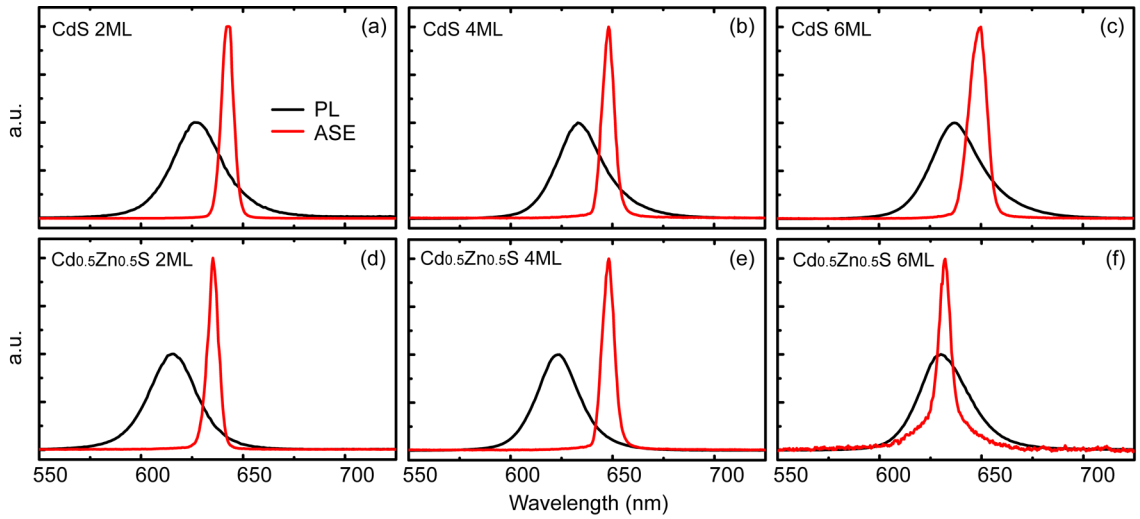

Figure 8.1: (a-c) PL (black lines) and ASE spectra (red) of CdSe#1-CdS with 2, 4 and 6 shell MLs embedded in ZrO_2 films. (d-f) PL (black lines) and ASE spectra (red) of CdSe#1-$Cd_{0.5}Zn_{0.5}S$ with 2, 4 and 6 shell MLs.

Table 8.2: PL maximum (PL max [nm]) spectral position of QDs in toluene dispersion and in ZrO_2 matrix. Amplified PL maximum (ASE [nm]) and bi-exciton binding energy (E_{XX} [meV]). Absorption cross section at λ = 400 nm (σ [cm^2]). ASE threshold fluence (F [mJ/cm^2]). Stability to irradiation, expressed in terms of time necessary to halve the ASE signal ($t^{50\%}$ [min]).

CdSe-	PL max (sol) [nm]	PL max (film) [nm]	ASE [nm]	E_{XX} [meV]	σ [cm^2]	F [mJ/cm^2]	$t^{50\%}$ [min]
CdS 2ML	629	627	639	-37	5.2E-15	0.17	30
CdS 4ML	633	634	646	-36	8.6E-15	0.05	150
CdS 6ML	637	637	647	-30	1.3E-14	0.03	>180
$Cd_{0.5}Zn_{0.5}S$ 2ML	615	615	632	-54	5.1E-15	0.14	20
$Cd_{0.5}Zn_{0.5}S$ 4ML	625	623	645	-69	8.7E-15	0.07	50
$Cd_{0.5}Zn_{0.5}S$ 6ML	631	631	633	-6	1.4E-14	0.09	>180

No substantial PL shift is registered after matrix inclusion of QDs (Figure 8.1 and Table 8.2), although the capping with aminopentanol and the sol-gel solid ZrO_2 matrix provide a different dielectric confinement of the core-shell CdSe QDs with respect native toluene solution. On the other hand, as predicted in Chapter 2, ASE peaks are red-shifted with respect to the PL maximum. Therefore, the bi-exciton nature of ASE and exciton-exciton interaction is verified. The red-shift is due mainly to an attractive interaction between the hole-electron couples, *i.e.* an energy stabilization of the bi-exciton in the type-I core-shell nanostructure. The lifetime of the bi-exciton state (τ_2) varies with the shell thickness and is ~ 200÷500 ps, as reported in Chapter 7.

Another contribute to the ASE red-shift is the interference with the 1S(e)-$1S_{3/2}$(h) band-edge absorption, which contributes also to the narrowing of the amplified emission with the respect to the PL emission. The reduced width of the ASE band (FWHM ~ 10 nm, Figure 8.1) is thus due

not only to its stimulated/coherent origin, but also to the re-absorption of the high-energy PL components.

In Table 8.2 the bi-exciton binding energy (E_{XX}) is also reported. This energy was estimated by considering the energy shift between the PL and ASE maxima. From Table 8.2 a decrease of E_{XX} with the CdS shell thickness emerges. This trend is consistent with the well-known differential potential barrier provided by a type-II hetero-structure such as CdSe-CdS to electrons and holes[40]. Namely, electrons tend to delocalize in the CdS material, thus reducing the wave function overlap.

For the CdSe-$Cd_{0.5}Zn_{0.5}S$ series higher E_{XX} values are registered, probably due to the better quantum confinement provided by this alloyed shell material. However, while passing from 2 to 4 ML E_{XX} increases, further shell growth strongly reduces the stabilization of the bi-exciton state. In fact, the sample CdSe-$Cd_{0,5}Zn_{0,5}S$ 6ML is the one exhibiting the lowest E_{XX}, probably due to a structural reason. In fact, from TEM analysis it is evident that their shape is far from the ideal sphericity, which is expected for large wurtzite-like nanocrystals. Models and experiments on highly anisotropic nanocrystals, such as quantum rods[195], demonstrate that ASE can be also blue-shifted with respect to the spontaneous PL.

The study of the optical gain threshold is performed through the analysis of the pump fluence necessary for activating ASE. For convenience the ASE activation fluence is usually considered as the gain threshold[179], even if this is just an approximation: ASE threshold is the condition where the ASE becomes the dominant (faster) mechanism depopulating the inverted gain state. Such an approximation is reinforced also by the fact that the ASE is red-shifted with respect to the PL (Figure 8.1). This peculiarity expedites the build-up of a gain regime, since a population inversion from single- to bi-exciton state occurs and, at the same time, losses due to the re-absorption are minimized.

In Figure 8.2 and Table 8.2 the threshold fluences versus the one-photon absorption cross section σ are presented. In Table 8.2 the stability of the ASE signal to irradiation is also reported as $t^{50\%}$, which represents the average irradiation time necessary to bleach the ASE signal down to the 50% of its initial value. Stability tests were conducted by pumping the films with a fluence slightly above the activation threshold. At least five tests per film were conducted, by focusing the beam each time on a different zone of the sample. For all the samples, a variability of only few minutes was detected. As expected, the stability increases with shell thickness.

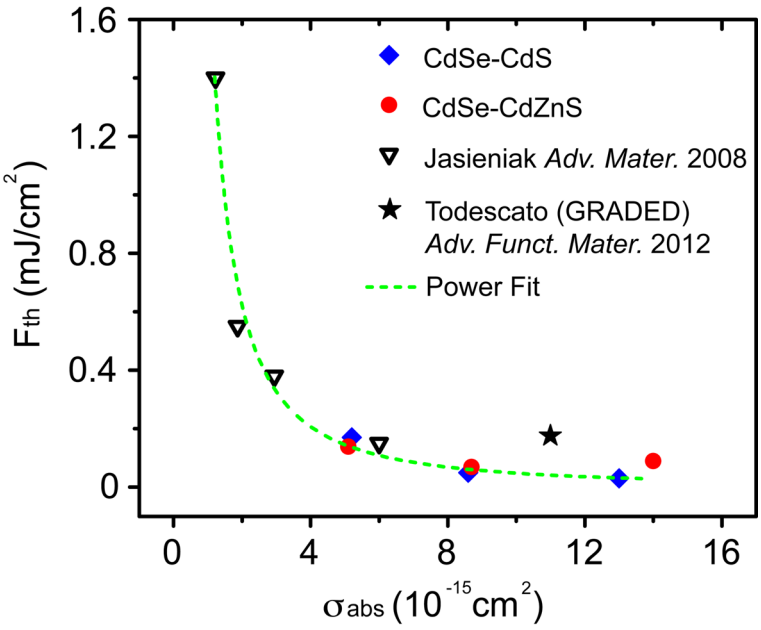

Figure 8.2: Threshold fluence versus abosroption cross setion at 400 nm optical pumping for CdSe-CdS (blue squares) and CdSe-$Cd_{0.5}Zn_{0.5}S$ series (red dots). The other symbols stand for results taken from literature[14,44]. The green dashed line is a power fit ($F=A*\sigma^{-B}$) of experimental and literature data.

In Figure 8.2 threshold values obtained in this work are compared with results from other similar works from the literature. ASE thresholds show a power law dependence, as expected since $F = <N>/\sigma$. However, the waveguide-based technique employed to measure thresholds and gain coefficients (see below) allows obtaining only effective values, *i.e.* waveguide losses and re-absorption should be taken into account when evaluating the intrinsic activation threshold. Due to the poor E_{XX}, ASE from CdSe-$Cd_{0.5}Zn_{0.5}S$ 6ML QDs is hindered by re-absorption losses, yielding a low signal to noise ratio (Figure 8.1.f) and an out of trend activation fluence (Figure 8.2 and Table 8.2).

Ideally, the average number of excitons per dot necessary to activate the optical gain is 1.55 e-h for CdSe QDs, as dictated by the Poisson statistics and degeneracy of the valence band[196,197]. The fit of the data reported in Figure 8.2 with a power law of the form $F=A*\sigma^{-B}$ is expected to yield A ~ 1.55 and B ~ 1, since $F = <N>/\sigma$[i]. However, this is not the case and, also at fixed B = 1, $<N>$ > 2.

8.2.2 ASE: Transmission configuration

The main contribution to the deviation from ideality just discussed comes, surprisingly, from the CdSe-CdS-$Cd_{0.5}Zn_{0.5}S$ graded core-shell QDs. The relative threshold fluence (F_{th} = 0.17 mJ/cm^2) was taken from Ref. [44]. In that work, graded QDs were embedded in ZrO_2 following the same protocol employed in this thesis and, despite the non-ideal ASE threshold fluence, one of

[i] For the fitting fluence was expressed in photons/cm^2 unities.

the lowest lasing thresholds ever registered (F_{th} = 0.07 mJ/cm²) from a QD device was obtained. The second order distributed feedback (DFB) microcavity employed may be responsible for this reduction, since it is well known from laser physics[198] than the lasing threshold is typically lower that the optical gain threshold. However, also the collection geometry may play a crucial role. In fact, differently from the ASE experiment, the output laser light in Ref. [44] was collected in a transmission configuration (Figure 3.7). Such collection geometry is expected to minimize the losses due to scattering and re-absorption that a waveguide configuration involves.

In Figure 8.3 the ASE spectra obtained from CdSe-CdS and CdSe-$Cd_{0.5}Zn_{0.5}S$ QDs are presented.

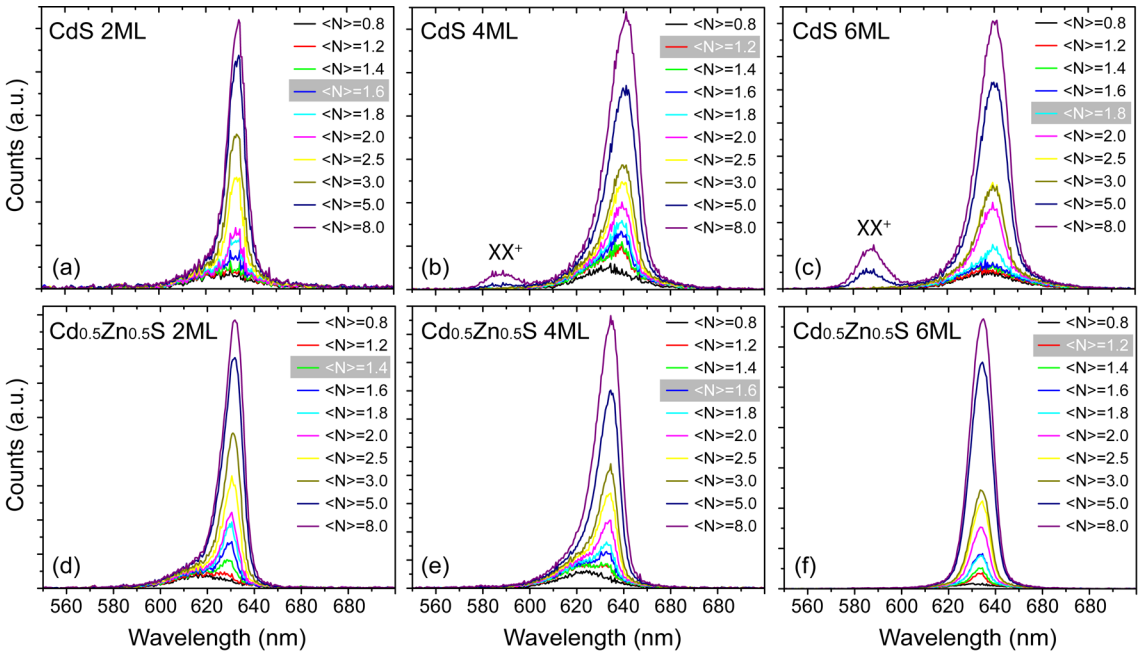

Figure 8.3: ASE evolution at increasing pump fluence for the (a-c) CdSe-CdS and (d-f) CdSe-$Cd_{0.5}Zn_{0.5}S$ core-shell QD series.

In Figure 8.3 the evolution of the ASE is monitored by increasing the average number of excitons generated per dot. For the samples, as highlighted in the relative figures, the ASE activation threshold occurs at $1 < \langle N \rangle < 2$, i.e. close to the ideal $\langle N \rangle = 1.55$.

It is worth noting also that, for the CdS series, a secondary peak at about 590 nm also appears when the pumping fluence exceeds <N> = 3 e-h. Such band has already been observed in literature[199,200] and is due to the emission from a "charged" bi-exciton state. The process is summarized in Figure 8.4.

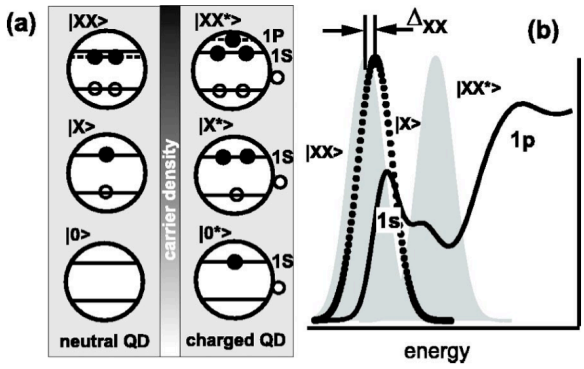

Figure 8.4: Schematic representation of the amplified spontaneous emission from a "charged" bi-exciton state. This figure has been adapted from Ref. [199].

This occurrence is consistent with the "hole-blockade" process predicted in the discussion of the TA results (Section 7.3). At increasing pump fluence the time constant τ_3, responsible for the delayed relaxation of the |1S> exciton, increases from 5 to 15 ps, since the hole transfer from shell to core material is obstructed by a Coulomb repulsive interaction. As already extensively discussed in the previous chapter, such "hole-blockade" phenomenon is imposed by the "quasi" type-II nature of the CdSe-CdS hetero-structure. |1S1S> bi-excitons localized in the core can interact with the hole "blocked" in the shell and form the bi-exciton equivalent of a positive "trion" (|$1S^+$>), which is the result of the interaction of a exciton with a hole. In the absence of any counteracting process, such as trapping at the core-shell interface, this |$1S1S^+$> can radiatively recombine.

Emission from the |$1S1S^+$> state is not observed in the CdSe-$Cd_{0.5}Zn_{0.5}S$ series, probably due to the presence of a more defective core-shell interface, which fosters the multi-exction Auger non-radiative recombination process.

Another possible explanation of this secondary band is the emission from a shell localized exciton, which was also detected in literature when characterizing CdSe-CdS "giant shell" QDs (shell thickness >20 MLs)[165]. Nevertheless, such hypothesis is ruled out here, since the spectral region of the XX^+ band does not match with any CdS state and the shell thickness is too low in the QDs under investigation.

8.2.3 Graded core-shell QDs: A comparative analyses

To demonstrate the crucial role of the collection geometry, the ASE of the same CdSe-CdS-$Cd_{0.5}Zn_{0.5}S$ graded core-shell QDs investigated in Ref. [43,44] has been characterized here by using the transmission configuration. The ASE spectra at increasing pump fluence of the graded QDs are reported in Figure 8.5.a, while all threshold fluences measured in this thesis are collected in Figure 8.5.b.

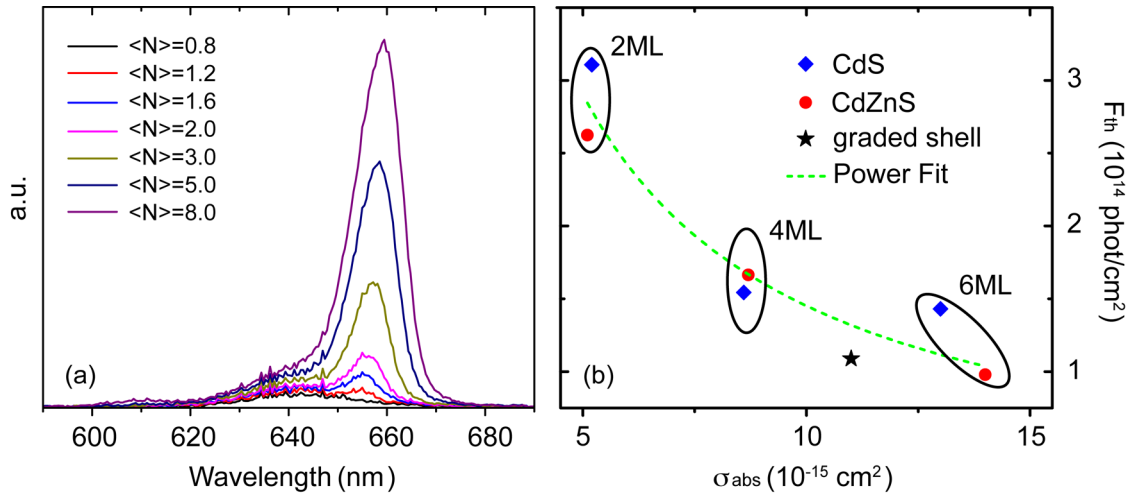

Figure 8.5: (a) ASE evolution at increasing pump fluence for CdSe-CdS-$Cd_{0.5}Zn_{0.5}S$ graded core-shell QDs embedded in ZrO_2 matrix. (b) Power law fit (green dashed line) on all the threshold fluences collected employing the transmission collection geometry versus the absorption cross-section.

The threshold fluence measured in this thesis from the hybrid ZrO_2-graded core-shell QDs films is 0.05 mJ/cm^2, therefore three times lower with respect to the one reported in Ref. [44] and comparable with the lasing threshold fluence reported in the same article. This demonstrates the importance of the intrinsic gain properties of the QDs in determining the performances of the final laser device.

The fit of the data collected in transmission configuration with the relation $F = \langle N \rangle / \sigma$ is also reported in Figure 8.5.b. Now, the extrapolated $\langle N \rangle$ is close to the theoretical expected threshold value (*i.e.* $\langle N \rangle = 1.5$).

Conclusions

In recent years, smart engineering of nanocrystalline heterostructures, known as core-shell QDs, has emerged as the most successful strategy for gaining control on detrimental processes such as carrier trapping at defects and non-radiative exciton decay, particularly Auger recombination. Such strategy is also known as "wave function engineering", which involves an effective control on the eigenfunctions of quantum-confined charges. To accomplish this, first of all a refined synthesis strategy is required. Synthesis however necessitates of a careful theoretical design of the nano-heterostructure, which must be guided by characterization tools sensitive to the exciton dynamics. Among the numerous prospective applications of semiconductor QDs in photonic technologies, this thesis demonstrates that light amplification is the one that makes the most of a detailed characterization of the exciton and multi-exciton dynamics, addressed to a careful design of the heterostructure.

Specifically, this thesis has provided experimental support to the idea that suitably engineered CdSe-$Cd_XZn_{1-X}S$ core-shell QDs can exhibit exceptionally favorable optical properties, such as high photoluminescence QY and optical gain efficiencies. Different CdSe-$Cd_XZn_{1-X}S$ core-shell QD series were characterized by means of steady-state and transient optical spectroscopy, with the aim of identifying the optimal shell composition that offers the best combination of high emission efficiency, photo-stability and gain activation threshold.

From conventional steady-state absorption and PL studies on the QDs under investigation it was possible to verify that different shell materials induce distinct exciton confinement, size dispersion and QY. The latter is of crucial relevance for any kind of light-emitting device and the QY values obtained provided empirical evidence that the CdSe emission efficiency is not improved (or even decreases) if the Zn concentration in the $Cd_XZn_{1-X}S$ shell is too high. This is due to the high mismatch between the CdSe and ZnS crystal lattice, which undermines the degree of epitaxy in the final heterostructure. Structural defectivity strongly affects the light-emitting performances in nanomaterials, as the probability of exciton-defect interaction is much higher than in bulk materials.

This preliminary observation stimulated the interest of finding a direct correlation between shell composition and structure. An all-optical approach, by means of Surface-enhanced Raman Scattering technique (SERS), was chosen in order to test the structural properties at conditions close to the final light-emitting device operation. This is advantageous with respect to more conventional structural characterization techniques, such as TEM and XRD, which have also

been employed to support the SERS results. With respect to conventional Raman technique, SERS offered the possibility to obtain (at RT) higher signal to noise Raman spectra with minimized residual fluorescence.

Before this thesis work, SERS has never been employed to this aim. As a local probe, such technique provided information about the structure at the core-shell interface. This was attained by monitoring the shift and the intensity of longitudinal and surface optical phonon modes relative to CdSe and shell materials. CdSe-CdS QDs were found to exhibit alloy formation with a radial extension of ~ 1 nm (*i.e.* 3 shell monolayers) and $CdSe_xS_{1-x}$ composition. On the other hand, at increased Zn concentration in the $Cd_XZn_{1-X}S$ shell, an abrupt interface limited to ~ 0.3 nm (*i.e.* 1 shell monolayers) was observed.

The unambiguous experimental evidence of the correlation between the core-shell interface structure and optical properties was detected with the use of transient optical spectroscopy. Exciton generation and recombination dynamics were probed in the nanosecond and picosecond regime by means of transient PL (ns) and transient absorption (ps) techniques. Regarding the ns regime, a modified version of a well-established charge-trapping kinetic model, based on charge-transfer, was employed to interpret ~ 10 to 100 ns long PL decays of QDs in their native colloidal dispersion. The recombination rates obtained by the application of such phenomenological model revealed a strong dependence on the core-shell interface. Correlation with SERS results has been discussed. Namely, the influence of a 3 monolayers thick $CdSe_xS_{1-x}$ alloyed layer at the CdSe-CdS core-shell interface on the exciton radiative and non-radiative exciton recombination rates was demonstrated. Moreover, the model was equally valid in identifying the abrupt nature of the interface between CdSe cores and a $Cd_XZn_{1-X}S$ shell at increasing Zn concentration. Notably, an explicit evidence of the pivotal role of the core-shell interface on tailoring the exciton recombination process is the necessity to consider a secondary trap distribution in the model. This second trap distribution was related to traps originating from strain release at the core-shell interface, probed by means of SERS experiments.

Sub-nanosecond exciton relaxation dynamics was obtained by the transient absorption characterization of the different core-shell QD series. Experiments were conducted at different pump fluences in order to investigate the dynamics that rules the optical gain regime, which is a multi-excitonic process in QDs and operates from the ps to the few nanosecond time-scale. By varying the pump fluence exciton and multi-exciton recombination rates were monitored below and above optical gain threshold. Despite the convolution of population effects and transient many-body Stark-effects complicates the interpretation of the experimental data, a global fitting procedure allowed to probe some peculiarities related to the shell composition. First of all CdS shell based QDs exhibited, at increasing pump fluence, a retardation of the relaxation dynamics, originating from a “hole-blockade” effect that limits the exciton transfer from shell to core. The “quasi type-II” nature of the CdSe-CdS heterostructure, *i.e.* the differential confinement of

electrons and holes provided by the CdS shell in the core, has been invoked to rationalize this behavior. A direct outcome of this effect is the detection of a secondary ASE signal when the QDs are deposited in thin films and pumped above the threshold fluence. Supported by previous works, this emission was related to an inter-material charged bi-exciton state, whose bi-exciton component is localized in the core while the charge is the "shell-bloked" hole. Due to the "hole-blockade", the lifetime is long enough to allow radiative recombination from this state. At the same time, the poor defectivity of the core-shell interface, thanks to the gradual composition provided by the $Cd_XZn_{1-X}S$ alloy, limits the Auger non-radiative recombination rate.

On the other hand, ZnS is not resonant with the pump beam (λ = 400 nm) and excitons are generated only in the CdSe core. Thus in this case the high excitation density in the core is influenced by the defective CdSe-ZnS core-shell interface, which causes an acceleration of the relaxation dynamics by a fast exciton trapping processes.

Transient absorption experiments were conducted on QDs with varying number of shell monolayers and, with exclusion of the first ML, a shell thickness independent trend was probed. Or, to put it better, this proves that the core-shell interface plays a crucial role also in the multi-exciton recombination process.

Finally, the amplified spontaneous emission of CdSe-$Cd_XZn_{1-X}S$ QDs has been characterized. To this aim, QDs were included in different solid-state matrices to form hybrid QD-doped thin films. Best results were obtained by using a sol-gel ZrO_2 matrix. ASE activation thresholds and stabilities to laser irradiation are measured and compared with CdSe QDs with a CdS-$Cd_XZn_{1-X}S$-ZnS graded shell. In such a graded heterostructure the choice of shell materials and relative thickness was engineered on the basis of the spectroscopic characterization. ASE threshold measured from the ZrO_2-graded QDs hybrid films is among the lowest obtained from a colloidal QD system. Therefore, results of this thesis demonstrates that a careful engineering of the core-shell structure, along with novel device architectures that enable also efficient electrical pumping, will pave the way for a new generation of QD laser devices.

References

(1) Prasad, N. P. *Nanophotonics*; 1st ed.; Wiley, 2004.

(2) Feldheim, D. L.; Colby, A. F. *Metal Nanoparticles: Synthesis, Characterization and Applications*; Feldheim, D. L.; Colby, A. F., Eds.; Marcel Dekker, 2002.

(3) Klimov, V. I. *Nanocrystal Quantum Dots*; Klimov, V. I., Ed.; 2nd ed.; CRC Press Taylor & Francis Group, 2010; Vol. 40, pp. 214–220.

(4) Reed, M. A.; Randall, J. N.; Aggarwal, R. J.; Matyi, R. J.; Moore, T. M.; Wetsel, A. E. Observation of Discrete Electronic States in a Zero-Dimensional Semiconductor Nanostructure.pdf. *Phys. Rev. Lett.* **1988**, *60*, 535–537.

(5) Ekimov, A. I.; Efros, A. L.; Onushchenko, A. A. Quantum Size Effect in Semiconductor Microcrystals. *Solid State Commun.* **1985**, *56*, 921–924.

(6) Brus, L. E. A Simple Model for the Ionization Potential, Electron Affinity, and Aqueous Redox Potentials of Small Semiconductor Crystallites. *J. Chem. Phys.* **1983**, *79*, 5566.

(7) Han, M.; Gao, X.; Su, J. Z.; Nie, S. Quantum-Dot-Tagged Microbeads for Multiplexed Optical Coding of Biomolecules. *Nat. Biotechnol.* **2001**, *19*, 631–635.

(8) Steckel, J. S.; Coe-Sullivan, S.; Bulović, V.; Bawendi, M. G. 1.3μm to 1.55μm Tunable Electroluminescence from PbSe Quantum Dots Embedded within an Organic Device. *Adv. Mater.* **2003**, *15*, 1862–1866.

(9) McBride, J.; Treadway, J.; Feldman, L. C.; Pennycook, S. J.; Rosenthal, S. J. Structural Basis for near Unity Quantum Yield Core/shell Nanostructures. *Nano Lett.* **2006**, *6*, 1496–1501.

(10) Khon, E.; Lambright, S.; Khon, D.; Smith, B.; O'Connor, T.; Moroz, P.; Imboden, M.; Diederich, G.; Perez-Bolivar, C.; Anzenbacher, P.; et al. Inorganic Solids of CdSe Nanocrystals Exhibiting High Emission Quantum Yield. *Adv. Funct. Mater.* **2012**, *22*, 3714–3722.

(11) Greytak, A. B.; Allen, P. M.; Liu, W.; Zhao, J.; Young, E. R.; Popović, Z.; Walker, B. J.; Nocera, D. G.; Bawendi, M. G. Alternating Layer Addition Approach to CdSe/CdS Core/shell Quantum Dots with near-Unity Quantum Yield and High on-Time Fractions. *Chem. Sci.* **2012**, *3*, 2028.

(12) Van Embden, J.; Jasieniak, J.; Mulvaney, P.; Embden, J. Van. Mapping the Optical Properties of CdSe/CdS Heterostructure Nanocrystals: The Effects of Core Size and Shell Thickness. *J. Am. Chem. Soc.* **2009**, *131*, 14299–14309.

(13) Leatherdale, C. A.; Mikulec, F. V; Bawendi, M. G. On the Absorption Cross Section of CdSe Nanocrystal Quantum Dots. *J. Phys. Chem. B* **2002**, *106*, 7619–7622.

(14) Jasieniak, J. J.; Fortunati, I.; Gardin, S.; Signorini, R.; Bozio, R.; Martucci, a.; Mulvaney, P. Highly Efficient Amplified Stimulated Emission from CdSe-CdS-ZnS Quantum Dot Doped Waveguides with Two-Photon Infrared Optical Pumping. *Adv. Mater.* **2008**, *20*, 69–73.

(15) Lesnyak, V.; Gaponik, N.; Eychmüller, A. Colloidal Semiconductor Nanocrystals: The Aqueous Approach. *Chem. Soc. Rev.* **2013**, *42*, 2905–2929.

(16) Pietryga, J. M.; Werder, D. J.; Williams, D. J.; Casson, J. L.; Schaller, R. D.; Klimov, V. I.; Hollingsworth, J. a. Utilizing the Lability of Lead Selenide to Produce Heterostructured Nanocrystals with Bright, Stable Infrared Emission. *J. Am. Chem. Soc.* **2008**, *130*, 4879–4885.

(17) Yang, W.; Li, J.; Zhang, Y.; Huang, P.-K.; Lu, T.-C.; Kuo, H.-C.; Li, S.; Yang, X.; Chen, H.; Liu, D.; et al. High Density GaN/AlN Quantum Dots for Deep UV LED with High Quantum Efficiency and Temperature Stability. *Sci. Rep.* **2014**, *4*, 5166.

(18) Liu, A. Y.; Zhang, C.; Norman, J.; Snyder, A.; Lubyshev, D.; Fastenau, J. M.; Liu, A. W. K.; Gossard, A. C.; Bowers, J. E. High Performance Continuous Wave 1.3 Mm Quantum Dot Lasers on Silicon. *Appl. Phys. Lett.* **2014**, *104*, 041104.

(19) Holmes, M. J.; Choi, K.; Kako, S.; Arita, M.; Arakawa, Y. Room-Temperature Triggered Single Photon Emission from a III-Nitride Site-Controlled Nanowire Quantum Dot. *Nano Lett.* **2014**, *14*, 982–986.

(20) Nanocrystallites, T. S.; Murray, C. B.; Noms, D. J.; Bawendi, M. G. Synthesis and Characterization of Nearly Monodisperse CdE (E = S, Se, Te) Semiconductor Nanocrystallites. *J. Am. Chem. Soc.* **1993**, *115*, 8706–8715.

(21) Dai, X.; Zhang, Z.; Jin, Y.; Niu, Y.; Cao, H.; Liang, X.; Chen, L.; Wang, J.; Peng, X. Solution-Processed, High-Performance Light-Emitting Diodes Based on Quantum Dots. *Nature* **2014**, *515*, 96–99.

(22) Dang, C.; Lee, J.; Breen, C.; Steckel, J. S.; Coe-Sullivan, S.; Nurmikko, A. Red, Green and Blue Lasing Enabled by Single-Exciton Gain in Colloidal Quantum Dot Films. *Nat. Nanotechnol.* **2012**, *7*, 335–339.

(23) Guilhabert, B.; Foucher, C.; Haughey, a-M.; Mutlugun, E.; Gao, Y.; Herrnsdorf, J.; Sun, H. D.; Demir, H. V; Dawson, M. D.; Laurand, N. Nanosecond Colloidal Quantum Dot Lasers for Sensing. *Opt. Express* **2014**, *22*, 7308–7319.

(24) Howes, P. D.; Chandrawati, R.; Stevens, M. M. Colloidal Nanoparticles as Advanced Biological Sensors. *Science (80-.).* **2014**, *346*, 1247390–1247390.

(25) Cheng, X.; Lowe, S. B.; Reece, P. J.; Gooding, J. J. Colloidal Silicon Quantum Dots: From Preparation to the Modification of Self-Assembled Monolayers (SAMs) for Bio-Applications. *Chem. Soc. Rev.* **2014**, *43*, 2680–2700.

(26) Clifford, J. P.; Konstantatos, G.; Johnston, K. W.; Hoogland, S.; Levina, L.; Sargent, E. H. Fast, Sensitive and Spectrally Tuneable Colloidal-Quantum-Dot Photodetectors. *Nat. Nanotechnol.* **2009**, *4*, 40–44.

(27) Deng, Z.; Jeong, K. S.; Guyot-Sionnest, P. Colloidal Quantum Dots Intraband Photodetectors. *ACS Nano* **2014**, *8*, 11707–11714.

(28) Chuang, C.-H. M.; Brown, P. R.; Bulović, V.; Bawendi, M. G. Improved Performance and Stability in Quantum Dot Solar Cells through Band Alignment Engineering. *Nat. Mater.* **2014**, *13*.

(29) Meinardi, F.; Colombo, A.; Velizhanin, K. a.; Simonutti, R.; Lorenzon, M.; Beverina, L.; Viswanatha, R.; Klimov, V. I.; Brovelli, S. Large-Area Luminescent Solar Concentrators Based on "Stokes-Shift-Engineered" Nanocrystals in a Mass-Polymerized PMMA Matrix. *Nat. Photonics* **2014**, *8*, 392–399.

(30) Zhang, W.; Feng, Y.; Zhang, H.; Zhon, X.; Zhong, X. Scalable Single-Step Noninjection Synthesis of High-Quality Core/shell Quantum Dots with Emission Tunable from Violet to near Infrared. *ACS Nano* **2012**, *6*, 11066–11073.

(31) Zhang, W.; Jin, C.; Yang, Y.; Zhong, X. Noninjection Facile Synthesis of Gram-Scale Highly Luminescent CdSe Multipod Nanocrystals. *Inorg. Chem.* **2012**, *51*, 531–535.

(32) Pan, J.; El-Ballouli, A. O.; Rollny, L.; Voznyy, O.; Burlakov, V. M.; Goriely, A.; Sargent, E. H.; Bakr, O. M. Automated Synthesis of Photovoltaic-Quality Colloidal Quantum Dots Using Separate Nucleation and Growth Stages. *ACS Nano* **2013**, *7*, 10158–10166.

(33) Jones, M.; Lo, S. S.; Scholes, G. D. Quantitative Modeling of the Role of Surface Traps in CdSe/CdS/ZnS Nanocrystal Photoluminescence Decay Dynamics. *Proc. Natl. Acad. Sci. U. S. A.* **2009**, *106*, 3011–3016.

(34) Quantum, C.; Photovoltaic, D. Charge Trapping Dynamics in PbS Devices. **2013**, 8771–8779.

(35) Minotto, A.; Todescato, F.; Fortunati, I.; Signorini, R.; Jacek, J. The Role of Core-Shell Interfaces on Exciton Recombination in CdSe – Cd X Zn 1-X S Quantum Dots. 1–33.

(36) Klimov, V. I.; Mikhailovsky, A. A.; McBranch, D. W.; Leatherdale, C. A.; Bawendi, M. G. Quantization of Multiparticle Auger Rates in Semiconductor Quantum Dots. *Science (80-.).* **2000**, *287*, 1011–1013.

(37) Frantsuzov, P.; Kuno, M.; Marcus, R. A.; Jank, O. Universal Emission Intermittency in Quantum Dots , Nanorods and Nanowires. *Nat. Phys.* **2008**, *4*, 519–522.

(38) Galland, C.; Ghosh, Y.; Steinbrück, A.; Hollingsworth, J. a; Htoon, H.; Klimov, V. I. Lifetime Blinking in Nonblinking Nanocrystal Quantum Dots. *Nat. Commun.* **2012**, *3*, 908.

(39) Xie, R.; Kolb, U.; Li, J.; Basche, T.; Mews, A. Synthesis and Characterization of Highly Luminescent CdSe-Core CdS/Zn0.5Cd0.5S/ZnS Multishell Nanocrystals. *J. Am. Chem. Soc.* **2005**, *127*, 7480–7488.

(40) García-santamaría, F.; Brovelli, S.; Viswanatha, R.; Hollingsworth, J. A.; Htoon, H.; Crooker, S. A.; Klimov, V. I. Breakdown of Volume Scaling in Auger Recombination in CdSe/CdS Heteronanocrystals: The Role of the Core-Shell Interface. *Nano Lett.* **2011**, *11*, 687–693.

(41) Todescato, F.; Minotto, A.; Signorini, R.; Jasieniak, J. J.; Bozio, R. Investigation into the Heterostructure Interface of CdSe-Based Core-Shell Quantum Dots Using Surface-Enhanced Raman Spectroscopy. *ACS Nano* **2013**, *7*, 6649–6657.

(42) Park, Y.; Bae, W. K.; Padilha, L. a; Pietryga, J. M.; Klimov, V. I.; Pietryga, M. Effect of the Core/shell Interface on Auger Recombination Evaluated by Single-Quantum-Dot Spectroscopy. *Nano Lett.* **2014**, *14*, 396–402.

(43) Signorini, R.; Fortunati, I.; Todescato, F.; Gardin, S.; Bozio, R.; Jasieniak, J. J.; Martucci, A.; Della Giustina, G.; Brusatin, G.; Guglielmi, M. Facile Production of up-Converted Quantum Dot Lasers. *Nanoscale* **2011**, *3*, 4109–4113.

(44) Todescato, F.; Fortunati, I.; Gardin, S.; Garbin, E.; Collini, E.; Bozio, R.; Jasieniak, J. J.; Della Giustina, G.; Brusatin, G.; Toffanin, S.; et al. Soft-Lithographed Up-Converted Distributed Feedback Visible Lasers Based on CdSe-CdZnS-ZnS Quantum Dots. *Adv. Funct. Mater.* **2012**, *22*, 337–344.

(45) Javaux, C.; Mahler, B.; Dubertret, B.; Shabaev, a; Rodina, a V; Efros, A. L.; Yakovlev, D. R.; Liu, F.; Bayer, M.; Camps, G.; et al. Thermal Activation of Non-Radiative Auger Recombination in Charged Colloidal Nanocrystals. *Nat. Nanotechnol.* **2013**, *8*, 206–212.

(46) Cragg, G. E.; Efros, A. L. Suppression of Auger Processes in Confined Structures. *Nano Lett.* **2010**, *10*, 313–317.

(47) Di Stasio, F.; Grim, J. Q.; Lesnyak, V.; Rastogi, P.; Manna, L.; Moreels, I.; Krahne, R. Single-Mode Lasing from Colloidal Water-Soluble CdSe/CdS Quantum Dot-in-Rods. *Small* **2014**, 1–7.

(48) Liao, Y.; Xing, G.; Mishra, N.; Sum, T. C.; Chan, Y. Low Threshold, Amplified Spontaneous Emission from Core-Seeded Semiconductor Nanotetrapods Incorporated into a Sol-Gel Matrix. *Adv. Mater.* **2012**, *24*, OP159–OP164.

(49) Guzelturk, B.; Kelestemur, Y.; Akgul, M. Z.; Sharma, V. K.; Demir, H. V. Ultralow Threshold One-Photon- and Two-Photon-Pumped Optical Gain Media of Blue-Emitting Colloidal Quantum Dot Films. **2014**, 6–10.

(50) Wang, X.; Ren, X.; Kahen, K.; Hahn, M. a; Rajeswaran, M.; Maccagnano-Zacher, S.; Silcox, J.; Cragg, G. E.; Efros, A. L.; Krauss, T. D. Non-Blinking Semiconductor Nanocrystals. *Nature* **2009**, *459*, 686–689.

(51) Brovelli, S.; Bae, W. K.; Meinardi, F.; Santiago González, B.; Lorenzon, M.; Galland, C.; Klimov, V. I. Electrochemical Control of Two-Color Emission from Colloidal Dot-in-Bulk Nanocrystals. *Nano Lett.* **2014**, *14*, 3855–3863.

(52) Chuang, C.-H.; Doane, T. L.; Lo, S. S.; Scholes, G. D.; Burda, C. Measuring Electron and Hole Transfer in Core/Shell Nanoheterostructures. *ACS Nano* **2011**, *5*, 6016–6024.

(53) Tschirner, N.; Lange, H.; Schliwa, A.; Biermann, A.; Thomsen, C.; Lambert, K.; Gomes, R.; Hens, Z. Interfacial Alloying in CdSe/CdS Heteronanocrystals: A Raman Spectroscopy Analysis. *Chem. Mater.* **2012**, *24*, 311–318.

(54) Margolin, G.; Barkai, E. Nonergodicity of Blinking Nanocrystals and Other Lévy-Walk Processes. *Phys. Rev. Lett.* **2005**, *94*, 080601.

(55) Margolin, G.; Protasenko, V.; Kuno, M.; Barkai, E. Photon Counting Statistics for Blinking CdSe-ZnS Quantum Dots: A Lévy Walk Process. *J. Phys. Chem. B* **2006**, *110*, 19053–19060.

(56) Petroff, P. M.; DenBaars, S. P. MBE and MOCVD Growth and Properties of Self-Assembling Quantum Dot Arrays in III-V Semiconductor Structures. *Superlattices Microstruct.* **1994**, *15*, 15.

(57) Germann, T. D.; Strittmatter, A.; Kettler, T.; Posilovic, K.; Pohl, U. W.; Bimberg, D. MOCVD of InGaAs/GaAs Quantum Dots for Lasers Emitting close to 1.3μm. *J. Cryst. Growth* **2007**, *298*, 591–594.

(58) Ekimov, A. I.; Efros, A. L. Nonlinear Optics of Semiconductor-Doped Glasses. *Phys. status solidi* **1988**, *150*, 627–633.

(59) Kim, J. Y.; Voznyy, O.; Zhitomirsky, D.; Sargent, E. H. 25th Anniversary Article: Colloidal Quantum Dot Materials and Devices: A Quarter-Century of Advances. *Adv. Mater.* **2013**, *25*, 4986–5010.

(60) Rogach, A. *Semiconductor Nanocrystal Quantum Dots: Synthesis, Assembly, Spectroscopy and Applications*; Springer, 2008; p. 383.

(61) Brus, L. E. Electron–electron and Electron-Hole Interactions in Small Semiconductor Crystallites: The Size Dependence of the Lowest Excited Electronic State. *J. Chem. Phys.* **1984**, *80*, 4403.

(62) Weller, H.; Schmidt, H. M.; Koch, U.; Fojtik, A.; Baral, S.; Henglein, A.; Kunath, W.; Weiss, K.; Dieman, E. Photochemistry of Colloidal Semiconductors. Onset of Light Absorption as a Function of Size of Extremely Small CdS Particles. *Chem. Phys. Lett.* **1986**, *124*, 557–560.

(63) LaMer, V. K.; Dinegar, R. H. Theory, Production and Mechanism of Formation of Monodispersed Hydrosols. *J. Am. Chem. Soc.* **1950**, *72*, 4847–4854.

(64) Murray, C. B.; Kagan, C. R.; Bawendi, M. G. Synthesis and Characterization of Monodisperse Nanocrystals and Close-Packed Nanocrystal Assemblies. *Annu. Rev. Mater. Reasearch* **2000**, *30*, 545–610.

(65) Sun, S. Monodisperse FePt Nanoparticles and Ferromagnetic FePt Nanocrystal Superlattices. *Science (80-.).* **2000**, *287*, 1989–1992.

(66) Peng, Z. A.; Peng, X. Formation of High-Quality CdTe, CdSe, and CdS Nanocrystals Using CdO as Precursor. *J. Am. Chem. Soc.* **2001**, *123*, 183–184.

(67) Pradhan, N.; Reifsnyder, D.; Xie, R.; Aldana, J.; Peng, X. Surface Ligand Dynamics in Growth of Nanocrystals. *J. Am. Chem. Soc.* **2007**, *129*, 9500–9509.

(68) Steigerwald, M. L.; Alivisatos, A. P.; Gibson, J. M.; Harris, T. D.; Kortan, R.; Muller, A. J.; Thayer, A. M.; Duncan, T. M.; Douglass, D. C.; Brus, L. E. Surface Derivatization and Isolation of Semiconductor Cluster Molecules. *J. Am. Chem. Soc.* **1988**, *110*, 3046–3050.

(69) Gaponik, N.; Talapin, D. V.; Rogach, A. L.; Hoppe, K.; Shevchenko, E. V.; Kornowski, A.; Eychmüller, A.; Weller, H. Thiol-Capping of CdTe Nanocrystals: An Alternative to Organometallic Synthetic Routes. *J. Phys. Chem. B* **2002**, *106*, 7177–7185.

(70) Qu, L.; Peng, X. Control of Photoluminescence Properties of CdSe Nanocrystals in Growth. *J. Am. Chem. Soc.* **2002**, *124*, 2049–2055.

(71) Hines, M. a.; Guyot-Sionnest, P. Synthesis and Characterization of Strongly Luminescing ZnS-Capped CdSe Nanocrystals. *J. Phys. Chem.* **1996**, *100*, 468–471.

(72) Reiss, P.; Protière, M.; Li, L. Core/Shell Semiconductor Nanocrystals. *Small* **2009**, *5*, 154–168.

(73) Wei, S.-H.; Zunger, A. Calculated Natural Band Offsets of All II–VI and III–V Semiconductors: Chemical Trends and the Role of Cation D Orbitals. *Appl. Phys. Lett.* **1998**, *72*, 2011.

(74) Mekis, I.; Talapin, D. V; Kornowski, A.; Haase, M.; Weller, H. One-Pot Synthesis of Highly Luminescent CdSe/CdS Core-Shell Nanocrystals via Organometallic and "Greener" Chemical Approaches. *J. Phys. Chem. B* **2003**, *107*, 7454–7462.

(75) Dabbousi, B. O.; Mikulec, F. V; Heine, J. R.; Mattoussi, H.; Ober, R.; Jensen, K. F.; Bawendi, M. G. (CdSe)ZnS Core - Shell Quantum Dots : Synthesis and Characterization of a Size Series of Highly Luminescent Nanocrystallites. *J. Phys. Chem. B* **1997**, *101*, 9463–9475.

(76) Ivanov, S. a.; Nanda, J.; Piryatinski, A.; Achermann, M.; Balet, L. P.; Bezel, I. V.; Anikeeva, P. O.; Tretiak, S.; Klimov, V. I. Light Amplification Using Inverted Core/Shell Nanocrystals: Towards Lasing in the Single-Exciton Regime. *J. Phys. Chem. B* **2004**, *108*, 10625–10630.

(77) Itzhakov, S.; Shen, H.; Buhbut, S.; Lin, H.; Oron, D. Type-II Quantum-Dot-Sensitized Solar Cell Spanning the Visible and Near-Infrared Spectrum. *J. Phys. Chem. C* **2012**, *117*, 22203–22210.

(78) Li, J. J.; Wang, Y. A.; Guo, W.; Keay, J. C.; Mishima, T. D.; Johnson, M. B.; Peng, X. Large-Scale Synthesis of Nearly Monodisperse CdSe/CdS Core/shell Nanocrystals Using Air-Stable Reagents via Successive Ion Layer Adsorption and Reaction. *J. Am. Chem. Soc.* **2003**, *125*, 12567–12575.

(79) Chen, Y.; Vela, J.; Htoon, H.; Casson, J. L.; Werder, D. J.; Bussian, D. a; Klimov, V. I.; Hollingsworth, J. a. "Giant" Multishell CdSe Nanocrystal Quantum Dots with Suppressed Blinking. *J. Am. Chem. Soc.* **2008**, *130*, 5026–5027.

(80) Bae, W. K.; Padilha, L. a; Park, Y.-S.; McDaniel, H.; Robel, I.; Pietryga, J. M.; Klimov, V. I. Controlled Alloying of the Core-Shell Interface in CdSe/CdS Quantum Dots for Suppression of Auger Recombination. *ACS Nano* **2013**, *7*, 3411–3419.

(81) Alivisatos, A. P. Cation Exchange Reactions in Ionic Nanocrystals. *Science (80-.).* **2004**, *306*, 1009–1012.

(82) Peng, X.; Manna, L.; Yang, W.; Wickham, J. Shape Control of CdSe Nanocrystals. *Nature* **2000**, *404*, 59–61.

(83) Manna, L.; Milliron, D. J.; Meisel, A.; Scher, E. C.; Alivisatos, a P. Controlled Growth of Tetrapod-Branched Inorganic Nanocrystals. *Nat. Mater.* **2003**, *2*, 382–385.

(84) Li, H.; Kanaras, A. G.; Manna, L. Colloidal Branched Semiconductor Nanocrystals: State of the Art and Perspectives. *Acc. Chem. Res.* **2013**, *46*, 1387–1396.

(85) Peng, Z. A.; Peng, X. Mechanisms of the Shape Evolution of CdSe Nanocrystals. *J. Am. Chem. Soc.* **2001**, *123*, 1389–1395.

(86) Peng, X. Mechanisms for the Shape-Control and Shape-Evolution of Colloidal Semiconductor Nanocrystals. *Adv. Mater.* **2003**, *15*, 459–463.

(87) Nanoplatelets, C.; Guzelturk, B.; Kelestemur, Y.; Olutas, M.; Delikanli, S.; Demir, H. V. Amplified Spontaneous Emission and Lasing in Colloidal Nanoplatelets. *ACS Nano* **2014**, *8*, 6599–6605.

(88) Kittel, C. *Introduction to Solid State Physics*; 8th ed.; Wiley, 2004.

(89) Ibach, H.; Lüth, H. *Solid-State Physics*; Springer Berlin Heidelberg: Berlin, Heidelberg, 2009.

(90) Sapoval, B.; Hermann, C.; Hermann, C. *Physics of Semiconductors*; Springer-Verlag, 1995.

(91) Grosso, G.; Parravicini, G. P. *Solid State Physics*; Academic Press, 2000.

(92) Klimov, V. I. Spectral and Dynamical Properties of Multiexcitons in Semiconductor Nanocrystals. *Annu. Rev. Phys. Chem.* **2007**, *58*, 635–673.

(93) Efros, A.; Rosen, M.; Kuno, M.; Nirmal, M.; Norris, D.; Bawendi, M. Band-Edge Exciton in Quantum Dots of Semiconductors with a Degenerate Valence Band: Dark and Bright Exciton States. *Phys. Rev. B* **1996**, *54*, 4843–4856.

(94) Robel, I.; Gresback, R.; Kortshagen, U.; Schaller, R.; Klimov, V. Universal Size-Dependent Trend in Auger Recombination in Direct-Gap and Indirect-Gap Semiconductor Nanocrystals. *Phys. Rev. Lett.* **2009**, *102*, 177404.

(95) Park, Y.; Bae, W. K.; Pietryga, J. M.; Klimov, V. I. Auger Recombination of Biexcitons and Negative and Positive Trions in Individual Quantum Dots. *ACS Nano* **2014**, *8*, 7288–7296.

(96) Galland, C.; Ghosh, Y.; Steinbrück, A.; Sykora, M.; Hollingsworth, J. a; Klimov, V. I.; Htoon, H. Two Types of Luminescence Blinking Revealed by Spectroelectrochemistry of Single Quantum Dots. *Nature* **2011**, *479*, 203–207.

(97) Minotto, A.; Todescato, F.; Fortunati, I.; Jasieniak, J. J.; Bozio, R. Role of Core – Shell Interfaces on Exciton Recombination in CdSe – Cd. **2014**.

(98) Padilha, L. a; Stewart, J. T.; Sandberg, R. L.; Bae, W. K.; Koh, W.-K.; Pietryga, J. M.; Klimov, V. I. Carrier Multiplication in Semiconductor Nanocrystals: Influence of Size, Shape, and Composition. *Acc. Chem. Res.* **2013**, *46*, 1261–1269.

(99) Einstein, A. On the Quantum Theory of Radiation. *Phys. Zeitschrift* **1917**, *18*, 121–128.

(100) Hall, R. N.; Fenner, G. E.; Kingsley, J. D.; Soltys, T. J. Coherent Light Emission From GaAs Junctions. *Phys. Rev. Lett.* **1962**, *9*, 366–369.

(101) Vahala, K. J. Optical Microcavities. *Nature* **2003**, *424*, 839–846.

(102) Wang, Z. M. *Quantum Dot Devices*; Springer, 2012.

(103) Malko, a. V.; Mikhailovsky, a. a.; Petruska, M. a.; Hollingsworth, J. a.; Klimov, V. I. Interplay between Optical Gain and Photoinduced Absorption in CdSe Nanocrystals. *J. Phys. Chem. B* **2004**, *108*, 5250–5255.

(104) García-santamaría, F.; Chen, Y.; Vela, J.; Schaller, R. D.; Hollingsworth, J. A.; Klimov, V. I.; Jennifer, A. Suppressed Auger Recombination in " Giant " Nanocrystals Boosts Optical. *Nano Lett.* **2009**, *9*, 3482–3488.

(105) Jasieniak, J.; Smith, L.; Embden, J. Van; Mulvaney, P.; Califano, M. Re-Examination of the Size-Dependent Absorption Properties of CdSe Quantum Dots. *J. Phys. Chem. C* **2009**, *113*, 19468–19474.

(106) Hoy, J.; Morrison, P. J.; Steinberg, L. K.; Buhro, W. E.; Loomis, R. a. Excitation Energy Dependence of the Photoluminescence Quantum Yields of Core and Core/Shell Quantum Dots. *J. Phys. Chem. Lett.* **2013**, *4*, 2053–2060.

(107) Demas, J. N.; Crosby, G. A. The Measurement of Photoluminescence Quantum Yields. A Review. *J. Phys. Chem.* **1971**, *75*, 991–1024.

(108) Würth, C.; Grabolle, M.; Pauli, J.; Spieles, M.; Resch-Genger, U. Relative and Absolute Determination of Fluorescence Quantum Yields of Transparent Samples. *Nat. Protoc.* **2013**, *8*, 1535–1550.

(109) Raman, C. V. A New Radiation. *Indian J. Phys.* **1928**, *2*, 387–398.

(110) Fleischmann, M.; Hendra, P. J.; McQuillan, A. J. Raman Spectra of Pyridine Adsorbed at a Silver Electrode. *Chem. Phys. Lett.* **1974**, *26*, 163–166.

(111) Jeanmaire, D. L.; Van Duyne, R. P. Surface Raman Spectroelectrochemistry Part I. Heterocyclic, Aromatic, and Amines Adsorbed on the Anodized Silver Electrode. *J. Electroanal. Chem. Interfacial Electrochem.* **1977**, *84*, 1–20.

(112) Moskovits, M. Surface Roughness and the Enhanced Intensity of Raman Scattering by Molecules Adsorbed on Metals. *J. Chem. Phys.* **1978**, *69*, 4159.

(113) Mie, G. Beiträge Zur Optik Trüber Medien, Speziell Kolloidaler Metallösungen. *Ann. Phys.* **1908**, *330*, 377–445.

(114) Maier, S. A. *Plasmonics: Fundamentals and Applications*; Springer, 2007.

(115) Meulenberg, R.; Jennings, T.; Strouse, G. Compressive and Tensile Stress in Colloidal CdSe Semiconductor Quantum Dots. *Phys. Rev. B* **2004**, *70*, 235311.

(116) Richter, H.; Wang, Z. P.; Ley, L. The One Phonon Raman Spectrum in Microcrystalline Silicon. *Solid State Commun.* **1981**, *39*, 625–629.

(117) Lange, H.; Artemyev, M.; Woggon, U.; Thomsen, C. Geometry Dependence of the Phonon Modes in CdSe Nanorods. *Nanotechnology* **2009**, *20*, 045705.

(118) Nesheva, D.; Kotsalas, I. .; Raptis, C.; Vateva, E. On the Structural Stability of Amorphous Se/CdSe Multilayers: A Raman Study. *J. Non. Cryst. Solids* **1998**, *224*, 283–290.

(119) Zielony, E.; Płaczek-Popko, E.; Henrykowski, a.; Gumienny, Z.; Kamyczek, P.; Jacak, J.; Nowakowski, P.; Karczewski, G. Laser Irradiation Effects on the CdTe/ZnTe Quantum Dot Structure Studied by Raman and AFM Spectroscopy. *J. Appl. Phys.* **2012**, *112*, 063520.

(120) Itoh, T.; Yoshida, K.; Biju, V.; Kikkawa, Y.; Ishikawa, M.; Ozaki, Y. Second Enhancement in Surface-Enhanced Resonance Raman Scattering Revealed by an Analysis of Anti-Stokes and Stokes Raman Spectra. *Phys. Rev. B* **2007**, *76*, 085405.

(121) Van Duyne, R. P.; Hulteen, J. C.; Treichel, D. a. Atomic Force Microscopy and Surface-Enhanced Raman Spectroscopy. I. Ag Island Films and Ag Film over Polymer Nanosphere Surfaces Supported on Glass. *J. Chem. Phys.* **1993**, *99*, 2101.

(122) Dieringer, J. a.; McFarland, A. D.; Shah, N. C.; Stuart, D. a.; Whitney, A. V.; Yonzon, C. R.; Young, M. a.; Zhang, X.; Van Duyne, R. P. Surface Enhanced Raman Spectroscopy: New Materials, Concepts, Characterization Tools, and Applications. *Faraday Discuss.* **2006**, *132*, 9.

(123) Le Ru, E. C.; Blackie, E.; Meyer, M.; Etchegoin, P. G. Surface Enhanced Raman Scattering Enhancement Factors: A Comprehensive Study. *J. Phys. Chem. C* **2007**, *111*, 13794–13803.

(124) Stiles, P. L.; Dieringer, J. a; Shah, N. C.; Van Duyne, R. P. Surface-Enhanced Raman Spectroscopy. *Annu. Rev. Anal. Chem.* **2008**, *1*, 601–626.

(125) Becker, W. *Advanced Time-Correlated Single Photon Counting Techniques*; Castleman, A. W.; Toennies, J. P.; Zinth, W., Eds.; Springer Series in Chemical Physics; Springer: Berlin, Heidelberg, 2005; Vol. 81.

(126) Mukamel, S. *Principles of Nonlinear Optical Spectroscopy*; Oxford University Press, 1999.

(127) Lanzani, G. *The Photophysics behind Photovoltaics and Photonics*; Wiley, 2012.

(128) Klimov, V.; McBranch, D.; Leatherdale, C.; Bawendi, M. Electron and Hole Relaxation Pathways in Semiconductor Quantum Dots. *Phys. Rev. B* **1999**, *60*, 13740–13749.

(129) Jasieniak, J.; Pacifico, J.; Signorini, R.; Chiasera, a.; Ferrari, M.; Martucci, a.; Mulvaney, P. Luminescence and Amplified Stimulated Emission in CdSe–ZnS-Nanocrystal-Doped TiO2 and ZrO2 Waveguides. *Adv. Funct. Mater.* **2007**, *17*, 1654–1662.

(130) Kogelnik, H.; Ramaswamy, V. Scaling Rules for Thin-Film Optical Waveguides. *Appl. Opt.* **1974**, *13*, 1857–1862.

(131) Van Embden, J.; Mulvaney, P. Nucleation and Growth of CdSe Nanocrystals in a Binary Ligand System. *Langmuir* **2005**, *21*, 10226–10233.

(132) Jasieniak, J.; Mulvaney, P. From Cd-Rich to Se-Rich--the Manipulation of CdSe Nanocrystal Surface Stoichiometry. *J. Am. Chem. Soc.* **2007**, *129*, 2841–2848.

(133) Davies, J. H. *The Physics of Low Dimensional Semiconductors. An Introduction*; Cambridge University Press, 1998.

(134) Zavelani-Rossi, M.; Lupo, M. G.; Tassone, F.; Manna, L.; Lanzani, G. Suppression of Biexciton Auger Recombination in CdSe/CdS Dot/rods: Role of the Electronic Structure in the Carrier Dynamics. *Nano Lett.* **2010**, *10*, 3142–3150.

(135) Antognazza, M. R.; Scotognella, F.; Miszta, K.; Dorfs, D.; Zanella, M.; Zavelani-Rossi, M.; Manna, L.; Lanzani, G.; Tassone, F. Steady-State Photoinduced Absorption of CdSe/CdS Octapod Shaped Nanocrystals. *Phys. Chem. Chem. Phys.* **2011**, *13*, 15326–15330.

(136) Comas, F.; Studart, N.; Marques, G. E. Optical Phonons in Semiconductor Quantum Rods. *Solid State Commun.* **2004**, *130*, 477–480.

(137) Trallero-Giner, C.; Debernardi, A.; Cardona, M.; Menéndez-Proupin, E.; Ekimov, A. I. Optical Vibrons in CdSe Dots and Dispersion Relation of the Bulk Material. *Phys. Rev. B* **1998**, *57*, 4664–4669.

(138) Campbell, I. H.; Fauchet, P. M. The Effects of Microcrystal Size and Shape on the One Phonon Raman Spectra of Crystalline Semiconductors. *Solid State Commun.* **1986**, *58*, 739–741.

(139) Szleifer, I.; Kramer, D.; Ben-Shaul, A.; Gelbart, W. M.; Safran, S. a. Molecular Theory of Curvature Elasticity in Surfactant Films. *J. Chem. Phys.* **1990**, *92*, 6800.

(140) Hwang, Y.; Shin, S.; Park, H.; Park, S.; Kim, U.; Jeong, H.; Shin, E.; Kim, D. Effect of Lattice Contraction on the Raman Shifts of CdSe Quantum Dots in Glass Matrices. *Phys. Rev. B. Condens. Matter* **1996**, *54*, 15120–15124.

(141) Zhang, J.-Y.; Wang, X.-Y.; Xiao, M.; Qu, L.; Peng, X. Lattice Contraction in Free-Standing CdSe Nanocrystals. *Appl. Phys. Lett.* **2002**, *81*, 2076.

(142) Dzhagan, V. M.; Valakh, M. Y.; Raevskaya, a. E.; Stroyuk, a. L.; Kuchmiy, S. Y.; Zahn, D. R. T. Characterization of Semiconductor Core–shell Nanoparticles by Resonant Raman Scattering and Photoluminescence Spectroscopy. *Appl. Surf. Sci.* **2008**, *255*, 725–727.

(143) Lu, L.; Xu, X.-L.; Liang, W.-T.; Lu, H.-F. Raman Analysis of CdSe/CdS Core-Shell Quantum Dots with Different CdS Shell Thickness. *J. Phys. Condens. Matter* **2007**, *19*, 406221.

(144) Dzhagan, V. M.; Valakh, M. Y.; Raevska, O. E.; Stroyuk, O. L.; Kuchmiy, S. Y.; Zahn, D. R. T. The Influence of Shell Parameters on Phonons in Core-Shell Nanoparticles: A Resonant Raman Study. *Nanotechnology* **2009**, *20*, 365704.

(145) Scamarcio, G.; Lugarà, M.; Manno, D. Size-Dependent Lattice Contraction in CdS1-xSex Nanocrystals Embedded in Glass Observed by Raman Scattering. *Phys. Rev. B* **1992**, *45*, 13792–13795.

(146) Dzhagan, V. M.; Valakh, M. Y.; Raevskaya, a E.; Stroyuk, a L.; Kuchmiy, S. Y.; Zahn, D. R. T. Resonant Raman Scattering Study of CdSe Nanocrystals Passivated with CdS and ZnS. *Nanotechnology* **2007**, *18*, 285701.

(147) Zhong, X.; Han, M.; Dong, Z.; White, T. J.; Knoll, W. Composition-Tunable ZnxCd1-X Se Nanocrystals with High Luminescence and Stability. *J. Am. Chem. Soc.* **2003**, *125*, 8589–8594.

(148) Lide, D. R. *Handbook of Chemistry and Physics*; 84th Editi.; CRC Press, 2003; p. 2616.

(149) Califano, M.; Gómez-Campos, F. M. Universal Trapping Mechanism in Semiconductor Nanocrystals. *Nano Lett.* **2013**, *13*, 2047–2052.

(150) Talapin, D. V.; Rogach, A. L.; Kornowski, A.; Haase, M.; Weller, H. Highly Luminescent Monodisperse CdSe and CdSe/ZnS Nanocrystals Synthesized in a Hexadecylamine–Trioctylphosphine Oxide–Trioctylphospine Mixture. *Nano Lett.* **2001**, *1*, 207–211.

(151) Carter, a. C.; Bouldin, C. E.; Kemner, K. M.; Bell, M. I.; Woicik, J. C.; Majetich, S. a. Surface Structure of Cadmium Selenide Nanocrystallites. *Phys. Rev. B* **1997**, *55*, 13822–13828.

(152) Eijt, S. W. H.; van Veen, A. T.; Schut, H.; Mijnarends, P. E.; Denison, A. B.; Barbiellini, B.; Bansil, A. Study of Colloidal Quantum-Dot Surfaces Using an Innovative Thin-Film Positron 2D-ACAR Method. *Nat. Mater.* **2006**, *5*, 23–26.

(153) Califano, M.; Franceschetti, A.; Zunger, A. Temperature Dependence of Excitonic Radiative Decay in CdSe Quantum Dots: The Role of Surface Hole Traps. *Nano Lett.* **2005**, *5*, 2360–2364.

(154) Gómez-Campos, F. M.; Califano, M. Hole Surface Trapping in CdSe Nanocrystals: Dynamics, Rate Fluctuations, and Implications for Blinking. *Nano Lett.* **2012**, *12*, 4508–4517.

(155) Jones, M.; Lo, S. S.; Scholes, G. D. Signatures of Exciton Dynamics and Carrier Trapping in the Time-Resolved Photoluminescence of Colloidal CdSe Nanocrystals. *J. Phys. Chem. C* **2009**, 18632–18642.

(156) Jones, M.; Scholes, G. D. On the Use of Time-Resolved Photoluminescence as a Probe of Nanocrystal Photoexcitation Dynamics. *J. Mater. Chem.* **2010**, *20*, 3533.

(157) Mooney, J.; Krause, M.; Saari, J.; Kambhampati, P. Challenge to the Deep-Trap Model of the Surface in Semiconductor Nanocrystals. *Phys. Rev. B* **2013**, *87*, 081201.

(158) Mooney, J.; Krause, M. M.; Saari, J. I.; Kambhampati, P. A Microscopic Picture of Surface Charge Trapping in Semiconductor Nanocrystals. *J. Chem. Phys.* **2013**, *138*, 204705.

(159) Marcus, R. A.; Sutin, N. Electron Transfers in Chemistry and Biology. *Biochim. Biophys. Acta - Rev. Bioenerg.* **1985**, *811*, 265–322.

(160) Verberk, R.; van Oijen, A.; Orrit, M. Simple Model for the Power-Law Blinking of Single Semiconductor Nanocrystals. *Phys. Rev. B* **2002**, *66*, 233202.

(161) Nirmal, M.; Dabbousi, B. O.; Bawendi, M. G.; Macklin, J. J.; Trautman, J. K.; Harris, T. D.; Brus, L. E. Fluorescence Intermittency in Single Cadmium Selenide Nanocrystals. *Nature* **1996**, *383*, 802–804.

(162) Kharchenko, V. A.; Rosen, M. Auger Relaxation Processes in Semiconductor Nanocrystals and Quantum Wells. *J. Lumin.* **1996**, *70*, 158–169.

(163) Mahler, B.; Spinicelli, P.; Buil, S.; Quelin, X.; Hermier, J.-P.; Dubertret, B. Towards Non-Blinking Colloidal Quantum Dots. *Nat. Mater.* **2008**, *7*, 659–664.

(164) Gong, K.; Zeng, Y.; Kelley, D. F. Extinction Coefficients, Oscillator Strengths and Radiative Lifetimes of CdSe, CdTe and CdTe/CdSe Nanocrystals. *J. Phys. Chem. C* **2013**, *117*, 20268–20279.

(165) Galland, C.; Brovelli, S.; Bae, W. K.; Padilha, L. a; Meinardi, F.; Klimov, V. I. Dynamic Hole Blockade Yields Two-Color Quantum and Classical Light from Dot-in-Bulk Nanocrystals. *Nano Lett.* **2013**, *13*, 321–328.

(166) Krasil'nik, Z. F.; Lytvyn, P.; Lobanov, D. N.; Mestres, N.; Novikov, A. V.; Pascual, J.; Valakh, M. Y.; Yukhymchuk, V. A. Microscopic and Optical Investigation of Ge Nanoislands on Silicon Substrates. *Nanotechnology* **2002**, *13*, 81–85.

(167) Zhong, X.; Feng, Y.; Knoll, W.; Han, M. Alloyed Zn(x)Cd(1-x)S Nanocrystals with Highly Narrow Luminescence Spectral Width. *J. Am. Chem. Soc.* **2003**, *125*, 13559–13563.

(168) Fisher, B. R.; Stott, N. E.; Bawendi, M. G. Emission Intensity Dependence and Single-Exponential Behavior In Single Colloidal Quantum Dot Fluorescence Lifetimes. **2004**, *11*, 143–148.

(169) Ebenstein, Y.; Mokari, T.; Banin, U. Fluorescence Quantum Yield of CdSe/ZnS Nanocrystals Investigated by Correlated Atomic-Force and Single-Particle Fluorescence Microscopy. *Appl. Phys. Lett.* **2002**, *80*, 4033.

(170) Lakowicz, J. R. *Principles of Fluorescence Spectroscopy*; 3rd Editio.; Springer: Singapore, 2006.

(171) Brovelli, S.; Schaller, R. D.; Crooker, S. a; García-Santamaría, F.; Chen, Y.; Viswanatha, R.; Hollingsworth, J. a; Htoon, H.; Klimov, V. I. Nano-Engineered Electron-Hole Exchange Interaction Controls Exciton Dynamics in Core-Shell Semiconductor Nanocrystals. *Nat. Commun.* **2011**, *2*, 280.

(172) Pal, B. N.; Ghosh, Y.; Brovelli, S.; Laocharoensuk, R.; Klimov, V. I.; Hollingsworth, J. a; Htoon, H. "Giant" CdSe/CdS Core/shell Nanocrystal Quantum Dots as Efficient Electroluminescent Materials: Strong Influence of Shell Thickness on Light-Emitting Diode Performance. *Nano Lett.* **2012**, *12*, 331–336.

(173) Jiang, Z.-J.; Kelley, D. F. Stranski–Krastanov Shell Growth in ZnTe/CdSe Core/Shell Nanocrystals. *J. Phys. Chem. C* **2013**, *117*, 6826–6834.

(174) Norris, D. J.; Sacra, A.; Murray, C. B.; Bawendi, M. Measurement of the Size Dependent Hole Spectrum in CdSe Quantum Dots. *Phys. Rev. Lett.* **1994**, *72*, 2612–2615.

(175) Mcguire, J. A.; Sykora, M.; Padilha, L. A.; Joo, J.; Pietryga, J. M.; Klimov, V. I. Spectroscopic Signatures of Photocharging due to Hot-Carrier Transfer in Solutions of Semiconductor Nanocrystals under Low-Intensity Ultraviolet Excitation. **2010**, *4*, 6087–6097.

(176) Saari, J. I.; Dias, E. a; Reifsnyder, D.; Krause, M. M.; Walsh, B. R.; Murray, C. B.; Kambhampati, P. Ultrafast Electron Trapping at the Surface of Semiconductor Nanocrystals: Excitonic and Biexcitonic Processes. *J. Phys. Chem. B* **2013**, *117*, 4412–4421.

(177) Tyagi, P.; Kambhampati, P. False Multiple Exciton Recombination and Multiple Exciton Generation Signals in Semiconductor Quantum Dots Arise from Surface Charge Trapping. *J. Chem. Phys.* **2011**, *134*, 094706.

(178) Wind, O.; Gindele, F.; Woggon, U.; Klingshirn, C. Gain Processes in CdSe Quantum Dots. *J. Cryst. Growth* **1996**, *159*, 867–870.

(179) Klimov, V. I.; Mikhailovsky, A. A.; Xu, S.; Malko, A.; Hollingworth, J. A.; Leatherdale, C. A.; Eisler, H.-J.; Bawendi, M. G. Optical Gain and Stimulated Emission in Nanocrystal Quantum Dots. *Science (80-.).* **2000**, *290*, 314–317.

(180) Sahin, M.; Koç, F. A Model for the Recombination and Radiative Lifetime of Trions and Biexcitons in Spherically Shaped Semiconductor Nanocrystals. *Appl. Phys. Lett.* **2013**, *102*, 183103.

(181) Christodoulou, S.; Vaccaro, G.; Pinchetti, V.; De Donato, F.; Grim, J. Q.; Casu, a.; Genovese, a.; Vicidomini, G.; Diaspro, a.; Brovelli, S.; et al. Synthesis of Highly Luminescent Wurtzite CdSe/CdS Giant-Shell Nanocrystals Using a Fast Continuous Injection Route. *J. Mater. Chem. C* **2014**, *2*, 3439.

(182) Brovelli, S.; Bae, W. K.; Galland, C.; Giovanella, U.; Meinardi, F.; Klimov, V. I. Dual-Color Electroluminescence from Dot-in-Bulk Nanocrystals. **2014**.

(183) Xu, S.; Mikhailovsky, a.; Hollingsworth, J.; Klimov, V. Hole Intraband Relaxation in Strongly Confined Quantum Dots: Revisiting the "phonon Bottleneck" Problem. *Phys. Rev. B* **2002**, *65*, 045319.

(184) Furis, M.; Hollingsworth, J. a; Klimov, V. I.; Crooker, S. a. Time- and Polarization-Resolved Optical Spectroscopy of Colloidal CdSe Nanocrystal Quantum Dots in High Magnetic Fields. *J. Phys. Chem. B B* **2005**, *109*, 15332–15338.

(185) Kambhampati, P. Unraveling the Structure and Dynamics of Excitons in Semiconductor Quantum Dots. *Acc. Chem. Res.* **2011**, *44*, 1–13.

(186) Van Stokkum, I. H. M.; Larsen, D. S.; van Grondelle, R. Global and Target Analysis of Time-Resolved Spectra. *Biochim. Biophys. Acta* **2004**, *1657*, 82–104.

(187) Van Wilderen, L. J. G. W.; Lincoln, C. N.; van Thor, J. J. Modelling Multi-Pulse Population Dynamics from Ultrafast Spectroscopy. *PLoS One* **2011**, *6*, e17373.

(188) Vandyshev, Y. V.; Dneprovskii, V. S.; Klimov, V. I. Nonlinear-Transmission Dynamics and Nonlinear Susceptibilities of Semiconducting Microcrystals (quantum Dots). *J. Exp. Theor. Phys.* **1992**, *74*, 144–150.

(189) Ledentsov, N. N. Quantum Dot Laser. *Semicond. Sci. Technol.* **2011**, *26*, 014001.

(190) Petruska, M. a.; Malko, a. V.; Voyles, P. M.; Klimov, V. I. High-Performance, Quantum Dot Nanocomposites for Nonlinear Optical and Optical Gain Applications. *Adv. Mater.* **2003**, *15*, 610–613.

(191) Olsson, Y. K.; Chen, G.; Rapaport, R.; Fuchs, D. T.; Sundar, V. C.; Steckel, J. S.; Bawendi, M. G.; Aharoni, A.; Banin, U. Fabrication and Optical Properties of Polymeric Waveguides Containing Nanocrystalline Quantum Dots. *Appl. Phys. Lett.* **2004**, *85*, 4469.

(192) Fortunati, I.; Bozio, R.; Jasieniak, J. J.; Antonello, A.; Martucci, A.; Giustina, G. Della; Brusatin, G.; Guglielmi, M. CdSe Core - Shell Nanoparticles as Active Materials for Up-Converted Emission. **2011**, 3840–3846.

(193) Todescato, F.; Chesman, A. S. R.; Martucci, A.; Signorini, R.; Jasieniak, J. J. Highly Luminescent and Temperature Stable Quantum Dot Thin Films Based on a ZnS Composite. *Chem. Mater.* **2012**, *24*, 2117–2126.

(194) Urlacher, C.; De Lucas, C. M.; Mugnier, J. Chemical and Physical Aspects of Sol—gel Process for Planar Waveguides Elaboration: Application to Zirconia Waveguides. *Synth. Met.* **1997**, *90*, 199–204.

(195) Xing, G.; Liao, Y.; Wu, X.; Chakrabortty, S.; Liu, X.; Yeoh, E. K. L.; Chan, Y.; Sum, T. C. Ultralow-Threshold Two-Photon Pumped Amplified Spontaneous Emission and Lasing from Seeded CdSe/CdS Nanorod Heterostructures. *ACS Nano* **2012**, *6*, 10835–10844.

(196) Crooker, S. a.; Barrick, T.; Hollingsworth, J. a.; Klimov, V. I. Multiple Temperature Regimes of Radiative Decay in CdSe Nanocrystal Quantum Dots: Intrinsic Limits to the Dark-Exciton Lifetime. *Appl. Phys. Lett.* **2003**, *82*, 2793.

(197) Malko, a. V.; Mikhailovsky, a. a.; Petruska, M. a.; Hollingsworth, J. a.; Htoon, H.; Bawendi, M. G.; Klimov, V. I. From Amplified Spontaneous Emission to Microring Lasing Using Nanocrystal Quantum Dot Solids. *Appl. Phys. Lett.* **2002**, *81*, 1303.

(198) Svelto, O. *Principles of Lasers*; 5th ed.; Springer, 2010.

(199) Achermann, M.; Hollingsworth, J.; Klimov, V. Multiexcitons Confined within a Subexcitonic Volume: Spectroscopic and Dynamical Signatures of Neutral and Charged Biexcitons in Ultrasmall Semiconductor Nanocrystals. *Phys. Rev. B* **2003**, *68*, 245302.

(200) Chan, Y.; Caruge, J.-M.; Snee, P. T.; Bawendi, M. G. Multiexcitonic Two-State Lasing in a CdSe Nanocrystal Laser. *Appl. Phys. Lett.* **2004**, *85*, 2460.

Achievements and Conferences:

PUBLICATIONS:

(1) Todescato, F.; Minotto, A.; Signorini, R.; Jasieniak, J. J.; Bozio, R. Investigation into the Heterostructure Interface of CdSe-Based Core-Shell Quantum Dots Using Surface-Enhanced Raman Spectroscopy. *ACS Nano* **2013**, *7*, 6649–6657.

(2) Minotto, A.; Todescato, F.; Fortunati, I.; Signorini, R.; Jasieniak, J. J.; Bozio, R. Role Of Core-Shell Interfaces on Exciton Recombination in CdSe-$Cd_xZn_{1-x}S$ QDs. *The Journal of Physical Chemistry C* **2014**, *118*, 24117-24126.

(3) Minotto, A.; Todescato, F.; Fortunati, I.; Signorini, R.; Jasieniak, J. J.; Bozio, R. Influence of Core-Chell Interfaces on Exciton and Multi-exciton Dynamics of CdSe–$Cd_xZn_{1-x}S$ Quantum Dots. *Proc. SPIE 9161, Nanophotonic Materials XI*, **2014**, 916103; doi:10.1117/12.2060973.

(4) Todescato, F.; Minotto, A.; Signorini, R.; Fortunati, I.; Jasieniak, J. J.; Bozio, R. Structural Engineering of Core/Shell Quantum Dots for Photonic Applications. *Submitted*

(5) Role of Core-Shell Interfaces on Multi-exciton Dynamics in CdSe–$Cd_xZn_{1-x}S$ Quantum Dots. *In preparation*

CONFERENCES:

(1) CFN Summer School 2012 on Nanophotonics – 10-13 September 2012 - Karlsruhe Institute of Technology (KIT) - Center for Functional Nanostructures (DFG) – POSTER: *"CdSe/$Cd_xZn_{1-x}S$ graded QDs: role of the outer shell on the optical properties".*

(2) Nanotechitaly 2013 – 27-28 Novembre 2013 - Venice (Italy) – POSTER: *"SERS Investigation on CdSe Based Core-Shell Quantum Dots Interfaces".*

(3) QD 2014 – 8th International conference on QDs – Pisa Conference Center – Pisa – 11-16 May 2014 – POSTER: *"The effect of core-shell interface on the optical properties of CdSe/$Cd_xZn_{1-x}S$ quantum dots".*

(4) Optics + Photonics 2014 - Nanophotonic Materials XI – 17-21 August 2014 San Diego Convention Center, San Diego, USA – TALK: "*Influence of core-shell interfaces on exciton and multi-exciton dynamics of CdSe-CdZnS quantum dots*".

Acknowledgements

Desidero ringraziare tutte le seguenti persone che nel corso di questi tre anni mi aiutato e permesso di portare a compimento il mio Lavoro di dottorato:

- In primis la mia famiglia, che mi ha permesso di arrivare a questo livello ultimo di educazione e formazione supportando tutte le mie scelte.
- Michi e Liqui, per la sopportazione, il supporto, il fritto misto piemontese e le passeggiate.
- Il mio supervisore, Dott.ssa Raffaella Signorini, per gli inestimabili consigli e l'aiuto sperimentale sia durante il periodo di tesi magistrale sia durante il mio percorso di dottorato. Un profondo ringraziamento va anche al Prof. Renato Bozio, per le utilissime discussioni e la disponibilità e alla Prof.ssa Camilla Ferrante per i preziosi consigli e il supporto nell'utilizzo delle tecniche spettroscopiche transienti. Ringrazio anche la Prof.ssa Elisabetta Collini per i preziosi consigli, il Dott. Robertino Pilot e il Prof. Danilo Pedron per l'aiuto sperimentale.
- Tutti i miei colleghi e compagni di ufficio e laboratorio (Alessia, Andrea, Anna, Betta, Bolz, Cate, Elena, Iaia, Maki, Marcello, Marco, Lucio, Nicola, Tode, Vere), in particolare il Dott. Francesco Todescato e la Dott.ssa Ilaria Fortunati per l'aiuto sperimentale e le sempre decisive disquisizioni sia tecniche sia ludiche.
- I collaboratori esterni: il Dott. Jacek J. Jasieniak (CSIRO, Clayton, Australia) per la sintesi dei quantum dots, il Prof. Giovanni Mattei per le immagini TEM, la Prof.ssa Giovanni Brusatin e la Dott.ssa Gioia Della Giustina per la preparazione delle matrici sol-gel e le misure XRD.